A window on stochastic processes and gamma-ray cosmology through spectral and temporal studies of AGN observed with H.E.S.S.

Jonathan Biteau

Thèse de Doctorat de l'École polytechnique

A window on stochastic processes and γ-ray cosmology through spectral and temporal studies of AGN observed with H.E.S.S.

Jonathan Biteau

Soutenue le 22 février 2013, devant le jury composé de :

Martin Lemoine,	Président
Fréderic Daigne,	Rapporteur
John Quinn,	Rapporteur
Régis Terrier,	Examinateur
Christian Stegmann,	Examinateur
Berrie Giebels,	Directeur de thèse

Laboratoire Leprince Ringuet, École polytechnique

Contents

Preamble

The second half of the twentieth century saw tremendous technical and technological developments led by world-wide collaborations of scientists and engineers. The scientific horizon expanded with, among others, the birth of the first large accelerators, the opening up of the sky from radio wavelengths to γ rays, and the advent of computing facilities. The greatest achievements of modern physics induced by these developments probably concern our understanding of the Universe, which, under the current state of the art, evolved from a primordial hot and dense plasma of elementary particles to form the stars and the galaxies, surrounded by dark matter and dark energy.

Among the most important of the fields that emerged is high-energy astrophysics, which aims at applying the laws of physics to the extreme and violent Universe in order to constrain its constituents and discover new laws. High-energy astrophysics is based on the measurements performed in X-ray astronomy, γ-ray astronomy, as well as on the studies of neutrinos, cosmic rays and gravitational waves. These observations make possible research on properties of matter under physical conditions that cannot be achieved in the laboratory and on distances and time-scales that by far exceed the human limitations. The questions raised by this field are at the cross-roads of astrophysics, cosmology, particle physics and fundamental physics, focussing on:

- the origin and nature of (extra)galactic cosmic rays,
- the search for dark matter particle candidates,
- the search for Lorentz invariance violation,
- the environment of black holes, neutron stars, supernovae,
- the particle acceleration in these astrophysical environments,
- the search for astrophysical neutrinos and gravitational waves,
- the nature of enigmatic transients (gamma-ray bursts, flares),

· the cosmological backgrounds and magnetic fields.

Parts of these vast questions are elucidated by experiments led by international collaborations. French institutes are particularly involved in experiments such as the γ-ray satellite *Fermi*, the ground based γ-ray telescope H.E.S.S. and the future array CTA. Other messengers than photons are under study, with neutrinos for ANTARES, cosmic-rays for AUGER and CODALEMA, and gravitational waves for VIRGO and the planned LISA. Research on the content and constituents of the Universe is carried out by AMS-02 for anti-matter, Edelweiss for dark matter particle candidates, as well as SCP, SNLS, SNFactory, Planck and the planned Snap and EUCLID for the density of dark matter and dark energy.

The studies developed in this manuscript exploit the results of *Fermi* and primarily of H.E.S.S. on phenomena occurring in the vicinity of the most massive black holes known in the Universe, hosted in active galactic nuclei. I purposely focus on these objects, called AGN, quasars or blazars as appropriate, and do not mention the other cosmic accelerators, which are now sufficiently numerous at high energy (tens of MeV up to hundreds of GeV) and very high energies (hundreds of GeV up to tens of TeV) to deserve a dedicated discussion. I describe in the first chapter the present state of the scientific knowledge regarding AGN. I then expose the characteristics of H.E.S.S. and explain how they can be used to discover new sources, such as the faint blazars 1ES 1312-423 and SHBL J001355.9-185406, detections which I have directly contributed to. The third chapter develops an important step in the advent of γ-ray cosmology, with the first detection of a cosmological background using very high energy γ rays from blazars. I study in chapter 4 one of the most striking property of blazars, their extreme variability, and I develop a model based on relativistic beaming and the generalized central limit theorem to explain their flux as a stochastic process. Based on these results and models, I finally summarize the scientific perspectives of the future ground-based instruments H.E.S.S. II and CTA.

Préambule

La seconde moitié du vingtième siècle a connu des développements techniques et technologiques extraordinaires, menés de concert par des collaborations internationales de chercheurs et d'ingénieurs. L'horizon de la science s'en est vu étendu, avec, entre autres, la naissance des premiers grands accélérateurs, l'ouverture de nouvelles fenêtres spectrales sur le ciel de la radio jusqu'aux rayons γ et l'avènement des grandes structures de calcul numérique. Les plus grandes avancées de la physique qui ont résulté de ces progrès concernent très certainement notre compréhension de l'Univers. Ce dernier, en l'état actuel des connaissances, a évolué depuis l'état de plasma dense et chaud de particules élémentaires pour former par la suite les étoiles et les galaxies, dans un milieu essentiellement constitué de matière noire et d'énergie noire.

L'astrophysique des hautes énergies est un des principaux domaines ayant émergé. Elle tente d'appliquer les lois de la physique à l'Univers violent, pour contraindre ses constituants et découvrir de nouvelles lois. Elle exploite les mesures réalisées en astronomie X et en astronomie γ, ainsi que les études de neutrinos, de rayons cosmiques et d'ondes gravitationnelles. À l'aide de ces observations, il devient possible d'étudier les propriétés de la matière dans des conditions inaccessibles sur Terre et sur des distances et des échelles de temps que l'Homme conçoit difficilement. Les questions que soulève ce domaine sont à la croisée des chemins entre astrophysique, cosmologie, physique des particules et physique fondamentale. En particulier, sont étudiés :

- l'origine et la nature des rayons cosmiques (extra)galactiques,
- la recherche d'hypothétiques particules de matière noire,
- la recherche de violation d'invariance de Lorentz,
- l'environnement des trous noirs, des étoiles à neutrons et des supernovae,

- l'accélération de particules en environnement astrophysique,
- la recherche de neutrinos d'origine astrophysique et d'ondes gravitationnelles,
- la nature des événements transitoires tels que les sursauts gamma ou les éruptions astrophysiques,
- les fonds diffus et champs magnétiques cosmologiques.

Des éléments de réponse à ces vastes questions ne peuvent être trouvés qu'à l'échelle de collaborations internationales. Les instituts français s'impliquent tout particulièrement dans des expériences telles que le satellite γ *Fermi*, le télescope γ H.E.S.S. et le futur grand réseau de télescopes CTA. D'autres messagers que les photons pourraient aussi être mis à profit, tels que les neutrinos d'ANTARES, les rayons cosmiques d'AUGER et de CODALEMA et les ondes gravitationnelles de VIRGO et du futur LISA. Une contribution à l'étude du contenu et des constituants de l'Univers est enfin apportée par la France dans des expérience telles qu'AMS-02 pour l'anti-matière, Edelweiss pour les particules de matière noire, mais aussi SCP, SNLS, SNFactory, Planck et les futurs Snap et EUCLID, pour l'étude des densités de matière et d'énergie noires.

Les travaux décris dans ce manuscrit tirent profit des observations de *Fermi* et surtout de H.E.S.S. Ils portent sur les phénomènes se déroulant au voisinage des trous noirs les plus massifs que l'on connaisse dans l'Univers, qui sont lovés au sein des noyaux actifs de galaxies. Je me limite volontairement à l'étude de ces objets, qu'on appelle AGN, blazars ou quasars selon les cas, et je ne fais pas mention des autres accélérateurs cosmiques. Ces derniers sont maintenant suffisamment nombreux à haute énergie (quelques dizaines de MeV jusqu'à des centaines de GeV) et à très haute énergie (quelques centaines de GeV jusqu'à des dizaines de TeV) pour mériter une discussion spécifique. Je décris dans le premier chapitre l'état actuel des connaissances sur les AGN. J'expose ensuite les caractéristiques de H.E.S.S. et montre comment elle peuvent servir la découverte de nouvelles sources, telles que les blazars de faible luminosité 1ES 1312-423 et SHBL J001355.9-185406, détéctions auxquelles j'ai directement contribué. Le troisième chapitre expose une étape marquante dans l'avènement de la cosmologie γ : la première détection d'un fond diffus cosmologique à l'aide

de rayons γ de très haute énergie provenant de blazars. J'étudie au chapitre 4 une des propriétés les plus surprenantes des blazars : leur extrême variabilité. Cela me permet de construire un modèle combinant focalisation relativiste et théorème de la limite centrale généralisé, et d'identifier le flux des blazars à un processus stochastique. À l'aide de ces résultats et de ces modèles, j'envisage enfin quelques unes des perspectives des prochaines générations de télescope γ, à savoir H.E.S.S. II et CTA.

Acronyms list

- **ACD**: Anti-coincidence dome
- **ADC**: Analogic to digital convertor
- **AGN**: Active galactic nucleus
- **ARS**: Analogic ring sampler
- **BLR**: Broad-line region
- **BLRG**: Broad-line radio galaxy
- **C.U.**: Crab unit
- **CIB**: Cosmic infrared background
- **CLT**: Central limit theorem
- **CMB**: Cosmic microwave background
- **COB**: Cosmic optical background
- **DFT**: Discrete Fourier transform
- **dof**: number of degrees of freedom
- **EBL**: Extragalactic background light (the COB and the CIB in this manuscript)
- **ECAL**: Electromagnetic calorimeter
- **EDF**: Electron distribution function
- **ELP**: Log parabola with an exponential cut off
- **EPWL**: Power law with an exponential cut off
- **FFT**: Fast Fourier transform
- **FoV**: field of view
- **FR I, FR II**: Fanaroff-Riley galaxy of type I and II
- **FR08**: EBL model of Franceschini et al., 2008 (baseline in this manuscript)
- **FSRQ**: Flat spectrum radio quasar
- **FT**: Fourier transform
- **GCLT**: Generalized central limit theorem
- **HDMVA**: Multivariate analysis in Ohm et al., 2009
- **HE**: High energy (20 MeV $< E <$ 100 GeV)

- **HSP, HBL**: High frequency synchrotron peaked blazars (resp. BL Lac objects)
- **IACT**: Imaging atmospheric Cherenkov telescope
- **IBL, ISP**: Intermediate frequency synchrotron peaked blazars (resp. BL Lac objects)
- **LBL, LSP**: Low frequency synchrotron peaked blazars (resp. BL Lac objects)
- **LP**: Log parabola
- **LST**: Large size telescope of CTA
- **MST**: Medium size telescope of CTA
- **NLR**: Narrow-line region
- **NLRG**: Narrow-line radio galaxy
- **OVV**: Optically violently variable (∼FSRQ)
- **pdf**: Probability density function
- **PM**: Photo multiplier
- **PMVA**: Multivariate analysis in Becherini et al., 2011
- **PSD**: Power spectral density
- **PSF**: Point spread function
- **PWL**: Power law
- **QSO**: Quasi stellar object (∼RQQ)
- **RLQ**: Radio loud quasar
- **RQQ**: Radio quiet quasar
- **SED**: Spectral energy distribution
- **SEPWL**: Power law with a super-exponential cut off
- **SSC**: Synchrotron self Compton
- **SST**: Small size telescope of CTA
- **Sy**: Seyfert Galaxy
- **TS**: Test statistics
- **VHE**: Very high energy (100 GeV $< E <$ 100 TeV)

CHAPTER 1

Very high energy blazars

1.1. Quasars, AGN and blazars

The year 1963 is one of the landmarks of extragalactic astronomy, with the discovery that quasi-stellar radio sources (quasars) are extragalactic objects. This triggered the meeting of astronomers, astrophysicists and physicists from general relativity in the first Texas Symposium, planting the seeds of the field of relativistic astrophysics.

I adopt in the following an historical approach to describe the various sub-classes of active galactic nuclei (AGN) and discuss the unification scheme that has emerged during the past fifty years. A more extensive discussion can be found in the excellent books of Kembhavi & Narlikar (1999) and Krolik (1999).

1.1.1. Half a century of quasar astronomy

Up to the end of the '20s, astronomical observations were performed exclusively in the optical band. The existence of extragalactic sources was established in 1924, with the work of Edwin Hubble (among others). In the beginning of the '40s, Carl Seyfert performed the first systematic spectroscopic study of spiral galaxies with bright nuclei (Seyfert 1943), now called AGN. The '40s also saw the pioneering work of Karl Jansky and Grote Reber, who performed the first observations of our galaxy in the radio band. In the '50s, scientists and engineers who had worked on radars during World War II took up the work of Jansky and Reber and discovered the first radio galaxies, such as the nearby Centaurus A, M 87 or Cygnus A. The emission of these objects was found to be polarized, indicating the non-thermal synchrotron origin of the emission (cf. Sect. 1.2.2.1).

1.1.1.1. *The year 1963: the birth of quasar astronomy and relativistic astrophysics*

The first quasars were discovered at the end of the '50s. Their name originates from the acronym QSRS, for quasi-stellar radio sources, because these objects have a very small angular extension and thus appear point like, as would stars. The nature of their astrophysical counterparts remained puzzling, but the collaboration of radio and optical astronomers created the breeding ground for the major discoveries of 1963. Quoting Maarteen Schmidt (Schmidt 1990):

"*The puzzle was suddenly resolved in the afternoon of February 5, 1963, while I was writing a brief article about the optical spectrum of 3C 273. Cyril Hazard had written up the occultation results for publication in Nature and suggested that the optical observations be published in an adjacent article. While writing the manuscript, I took another look at the spectra. I noticed that four of the six lines in the photographic spectra showed a pattern of decreasing strength and decreasing spacing from red to blue. For some reason, I decided to construct an energy-level diagram based on these lines. I must have made an error in the process which seemed to contradict the regular spacing pattern. Slightly irritated by that, I decided to check the regular spacing of the lines by taking the ratio of their wavelengths to that of the nearest line of the Balmer series. The first ratio, that of the 5630 line to H-β, was 1.16. The second ratio was also 1.16. When the third ratio was 1.16 again, it was clear that I was looking at a Balmer spectrum redshifted by 0.16.*"

A redshift of 0.16 indicated the extragalactic origin of 3C 273 and with an optical magnitude of 13, the luminosity of the object had to be tremendous! When, a few minutes latter, Maarteen Schmidt talked in the hallway with J. Greenstein, who was working on the spectrum of 3C 48, they immediately realized that the spectrum of the latter object corresponds to a redshift of 0.37, a gigantic cosmological distance for the epoch. One should recall that the usual galaxies that were known by then ranged up to a redshift of ~ 0.2. The four consecutive articles about these two quasars that were published in Nature (Hazard et al. 1963; Schmidt 1963; Oke 1963; Greenstein 1963) immediately caught the eye of theoreticians.

Schucking (1989) describes how, a few months later, I. Robinson (mathematician) and himself (from general relativity) were sitting by

a pool on a hot day of July, near Dallas, Texas, talking about the dull summer. L. Marshall, head of the Office of Scientific Personnel in the centre of gravity in Austin, suggested: "*Look you fellows. You've got a golden opportunity... a new division and new territory to branch into... Why don't you organize a little conference?*". They passed the next days thinking about it until E. Schucking said: "*You know, there are some new astronomical objects, observed by telescopes, and nobody knows quite what they are... Why don't we hold a conference on the subject?*"

The conference was held in December 1963 and a long series of "Texas Symposia" (originally financed by the university of Texas) was born, together with the field of relativistic astrophysics. Greenstein gave the main talk on 3C 273. Another major contribution to the conference was the newly discovered metric of R. Kerr (Kerr 1963), who studied the rotation of black holes, which happens to be one of the greatest energy reservoirs in the Universe. The self collapse of massive objects, which can lead to black hole formation as discussed in the following, was also pointed out a couple of months before by Hoyle & Fowler (1963), who realized that for large masses M, the thermonuclear energy $\propto M$ must be dominated by the gravitational energy $\propto M^2$.

1.1.1.2. *From quasars to the birth of blazars in 1978*

The end of the '60s saw the advent of X-ray astronomy with the detection of 3C 273, M 87 and Centaurus A (Friedman & Byram 1967; Bowyer et al. 1970), showing that quasars share properties in common with radio galaxies. In the beginning of the '70s, the first very long baseline interferometry observations were performed, enabling angular resolution below the milli-arcsec. Observations of the quasars 3C 273 and 3C 279 revealed structures moving with apparent speeds larger than the speed of light by factors of at least 2 and 3 (Cohen et al. 1971) and even by a factor as large as 10 according to Whitney et al. (1971). This apparent superluminal speed had been predicted by Rees (1966) with simple geometrical arguments, given that the true speed of the object is larger than $0.71c$ $(= c/\sqrt{2})$ and that the motion is almost co-linear with the line of sight.

The idea of a high-velocity emitting region moving toward the observer was recycled in 1978 for a different class of radio sources during the Pittsburgh Conference on BL Lac objects (Wolfe 1978). These

sources are named after BL Lacertae, originally thought to be a variable star in the constellation of Lacerta and later associated with a radio source (Schmitt 1968). BL Lacs usually show faint lines with respect to their non-thermal emission, complicating the measurement of their redshifts. One of the conclusions of the conference was the great resemblance between BL Lacs and flat spectrum radio quasars (FSRQs, also called OVVs for optically violently variables), the two classes exhibiting polarized and highly variable emission. The difference between these objects lies in the strong emission lines observed in FSRQs, with an equivalent width[1] of EW > 5Å. The after-dinner speaker of this conference, Ed Spiegel, created the name "blazar" to unite these two classes of object.

During this founding conference, Blandford & Rees (1978) explained that the continuum observed in blazars probably arose, as in radio galaxies, from synchrotron radiation. The fast variability, however, should imply a tiny emitting region invoking what is now known as the causality argument: the emission of a region of size R can not vary on time scales shorter than the time needed to cross the region at the speed of light, i.e. R/c. The high luminosity observed from such a small region would result in large synchrotron self absorption (see Sect. 1.2.2.1) and large electron scattering that would imply no polarization. The problem can be resolved by imposing a relativistic boost on the emitting region (see Sect. 1.1.2.1), which shortens the observed time scales and enhances the emission for a direction of motion in close alignment with the line of sight.

The late '70s also saw the advent of charge coupled device (CCD) cameras, which enabled the resolution, in the optical band, of the cores of nearby elliptical radio galaxies such as M 87. The bright core emission, as shown in Fig. 1, serves as a natural bridge with the nuclei of Seyfert galaxies, all of them belonging to the class of AGN.

Large X-ray surveys began in the '80s, in particular with the Einstein observatory (HEAO-2, Giacconi et al. 1979). The common properties of radio galaxies, Seyfert galaxies, quasars and blazars progressively led to the conclusion that they must host an AGN, powered

[1]The equivalent width (EW) of a line is defined as the integral under the curve $|F_\lambda - F_0|/F_0$, where F_0 is the flux of the continuous (non-thermal) emission and F_λ the total flux (line + continuum). This quantity thus highly depends on the state of a variable source (on F_0), a high state reducing EW. FSRQs in high states have thus the same properties as BL Lac objects.

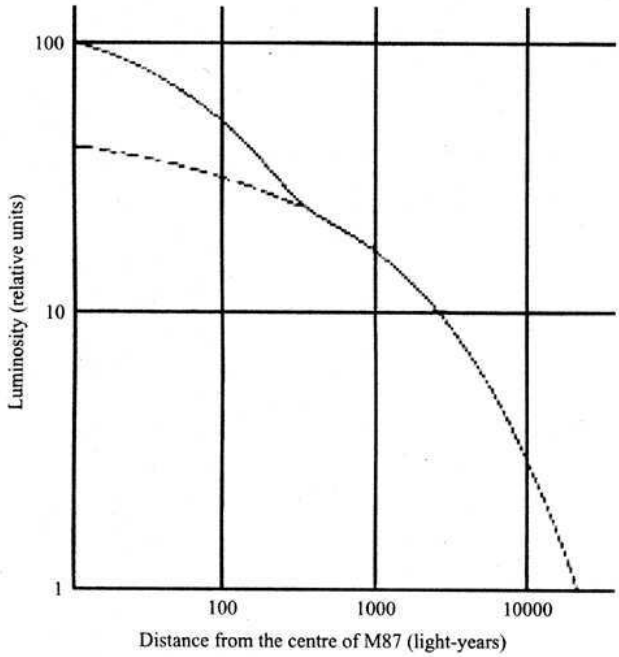

FIGURE 1. Luminosity profile of M87 showing that the emission is dominated by the bright active nucleus below a hundred light years. *Extracted from Kembhavi & Narlikar (1999).*

by gravitational energy, which can outshine the emission of the whole galaxy, be it spiral (for Seyferts) of elliptical (for the others).

1.1.1.3. *The properties of AGN*

In their classic book, Burbidge & Burbidge (1967) list the criteria (established by Maarten Schmidt) that an object must fulfil to be identified as a quasar. These criteria are compared in Table 1 with the "ingredients" that compose an AGN, taken from in the menu of Krolik (1999). Apart from radio emission, which is now known to characterize a minority of AGN, the properties initially defining quasars largely describe the entire class of AGN. These are extragalactic sources (i.e. have what was considered a large redshift in the '60s) and are point-like objects on optical photographic plates. They used to be selected

by their large UV flux that, being of non-thermal origin, differentiates them from stars. This technique has been successful for discovering quasars with a rather weak radio emission, so-called radio-quiet quasars (RQQ, also QSO), which distinguishes them from the radio-loud quasars (RLQ) that were originally discovered.

More generally, AGN have broad-band spectra that can extend from radio wavelengths up to γ rays for the most energetic objects. Their luminosity can range from 1% up to 10^4 times that of a typical galaxy[2]. Most of the AGN, but not all of them (e.g. BL Lac objects), have prominent emission lines, in contrast with stars or galaxies that usually exhibit weak absorption lines. The most common lines are the Ly α and the Balmer series of hydrogen (originally used for 3C 273), but also the doublet at 1549Å of CIV, the line at 5007Å of OIII and the K_α X-ray line of iron at 6.4 keV.

Unlike normal galaxies, AGN are variable sources. The usual variation is on the order of $\sim$ 10% on the $\sim$year time scale and their emission is weakly polarized (linear polarization on the order of 1%), but strongly enough to distinguish them from stars or galaxies (typically 0.5% linearly polarized). A minority are strongly variable and much more polarized ($\sim$ 10% in linear polarization), most of these being bright blazars. Following the schematic arrangement of Krolik (1999), one can distinguish the sub-varieties of AGN as a function of their radio loudness, of the width of their emission lines and of their variability/polarization, as in Fig. 2.

I already mentioned BL Lacs and FSRQs, the two sub-classes of blazars, which are radio-loud, variable, polarized objects. They are distinguished by the widths of their emission lines with those of the BL Lacs usually being weak to non-existant and those of FSRQs being stronger and broader. Seyfert (Sy) galaxies, which are non-variable unpolarized radio-quiet objects, can also be divided into two classes based on the width of their emission lines with type 2 and type 1 objects having narrow and broad lines, respectively. Their radio-loud equivalents are the narrow and broad lines radio galaxies (NLRG and BLRG). Note that, while BLRG and Sy 1 have particularly bright optical emission, their optically faint equivalents are the so-called RLQ and RQQ.

[2]The luminosity of a galaxy is typically on the order of 10^{44} erg s^{-1}.

Schmidt's criteria for quasars ('60s)	Krolik's ingredients for AGN ('90s)	Occurrence in AGN	Comments
Large redshift	Extragalactic	All	If measurable redshift
Star-like object	Very small angular size	Many	Wavelength dependent
Large UV flux	$\gtrsim$ Galactic luminosity	Many	Malmquist bias
	Broad-band continuum	Most	
Broad emission lines	Strong emission lines	Most	Sometimes narrow
Variable	Variable, weakly polarized	Most	$\sim 1\%$ linear polarization
	Strongly variable, polarized	Minority	Usually radio and γ rays
Radio emission	Radio emission	Minority	Mostly very weak
			Sometimes extended

TABLE 1. Comparison of the criteria of M. Schmidt to select quasars with the ingredients of J. Krolik that compose an AGN.

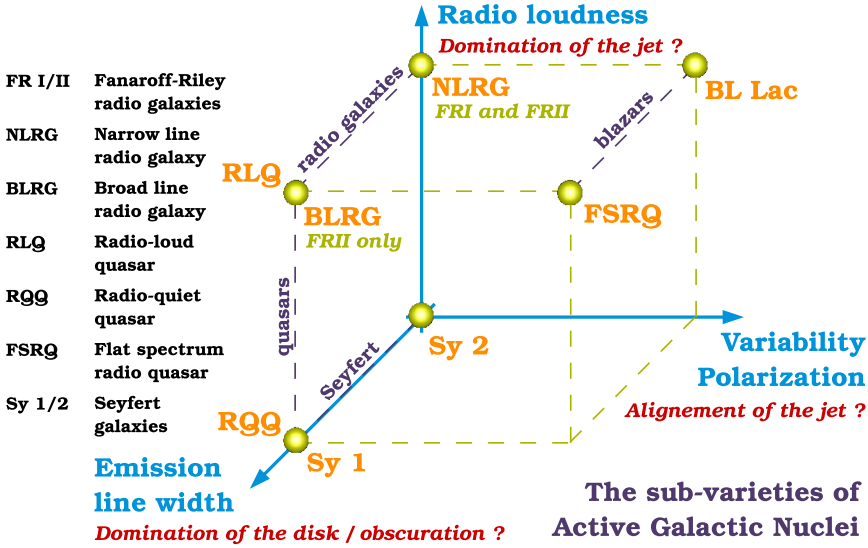

FIGURE 2. Principal sub-varieties of AGN, ordered as a function of their relative power in the radio band, of the width of their emission lines and of their variability and polarization. *Adapted from Krolik (1999).*

A common classification of radio galaxies was established by Fanaroff & Riley (1974) and this is still widely used today. FR I galaxies are characterized by a distance between their two brightest spots smaller than half the size of the whole structure and FR II have more distant brightest spots. As shown in Fig. 3 with Centaurus A and Cygnus A, FR II galaxies tend to have more collimated and fainter jets than FR Is and exhibit very bright terminal hot spots. This morphological distinction is remarkably correlated with the radio luminosity of the object, FR IIs being brighter than FR Is. Ledlow & Owen (1996) showed that the radio luminosity that divides the two classes roughly goes as the square of the optical luminosity of the host, indicating an apparent link between the host and the giant jetted structures on Mpc

scales[3]. When resolved, the jets of FSRQs mostly exhibit FR II-like structures while those of BL Lacs can belong to either class (Ledlow & Owen 1996; Antonucci 2011).

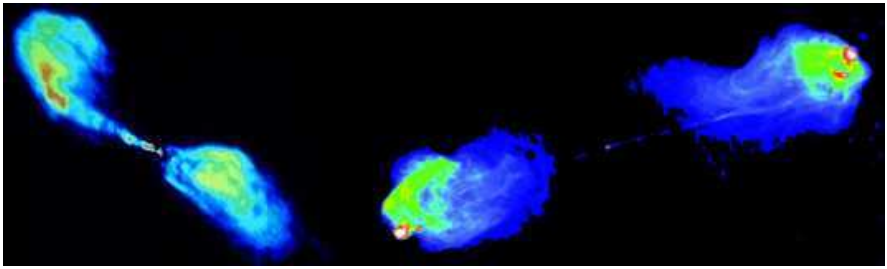

FIGURE 3. *Left:* FR I radio galaxy Centaurus A. *Right:* FR II radio galaxy Cygnus A.

1.1.2. The components of an AGN

A global picture of the various ingredients necessary to understand the sub-classes of AGN emerged in the '90s. I discuss these ingredients and the current unification scheme in the following sections.

1.1.2.1. *The jetted emission*

The large scale Mpc structures observed in radio galaxies such as Centaurus A and Cygnus A, and also the jet of the FR I M 87 in the optical band (reported since the '20s) point back to their central source of power down to the smallest scales. Very long baseline interferometry has revealed since the '70s the continuity of jets down to the kpc and pc scales, but the sub-pc scale, presumably where the most energetic radiation is emitted, usually remains un-resolved. Note however that, recently, the emission of M 87 has been resolved in the radio band down to 5 mpc (Doeleman et al. 2012).

The discovery of superluminal motion (introduced in Sect. 1.1.1.2) in the jets of the FSRQs 3C 273 and 3C 279 by Cohen et al. (1971) and Whitney et al. (1971), which had been theorized by Rees (1966), can be be explained by arguments that are purely geometric, as shown

[3]A parsec (pc) corresponds to 3.26 light years $= 3.09 \times 10^{16}$ m.

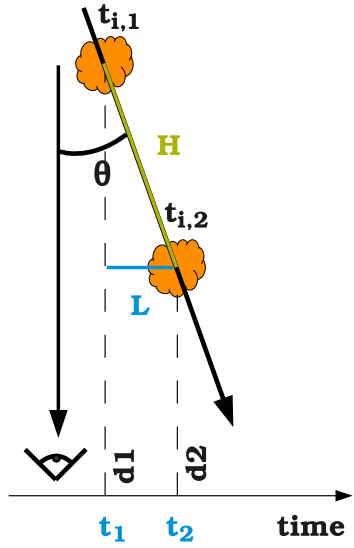

FIGURE 4. Schematic view of the motion of an emitting region along a direction at angle θ from the line of sight. The signal emitted at $t_{i,1}$ (resp. $t_{i,2}$) travels for d_1/c (resp. d_2/c) before arriving at t_1 (resp. t_2). A displacement of L is observed between t_1 and t_2, for an effectively travelled distance of H.

in Fig. 4. The apparent velocity $v_{\rm app}$ is given by Eq. (1.1):

$$v_{\rm app} = \frac{L}{t_2 - t_1} = \frac{L}{(t_{i,2} + \frac{d_2}{c}) - (t_{i,1} + \frac{d_1}{c})} = \frac{L}{(t_{i,2} - t_{i,1}) - \frac{d_1 - d_2}{c}} \tag{1.1}$$

where the only hypothesis is that the signal travels at the speed of light c. The "true" velocity of the emitting region is $v_i = H/(t_{i,2} - t_{i,1})$. Then using Eq. (1.1), the apparent velocity is:

$$v_{\rm app} = \frac{H \sin\theta}{H/v_i - H\cos\theta/c} = \frac{v_i \sin\theta}{1 - \frac{v_i}{c}\cos\theta} \tag{1.2}$$

Calling $\beta = v_i/c$, and using $t = \tan\theta/2$, Eq. (1.1) can be re-written with standard trigonometry $v_{\rm app}/c = 2\beta t/\left[(1-\beta) + (1+\beta)t^2\right]$, so that after a bit of algebra:

$$v_{\rm app} = kc \Leftrightarrow \left[(1+\beta)t - \beta/k\right]^2 = (\beta/k - 1/\gamma) \times (\beta/k + 1/\gamma) \tag{1.3}$$

where $\gamma = 1/\sqrt{1-\beta^2}$ is the Lorentz factor of the region. The left hand term is positive and the equation in t admits at least one solution if $\beta/k \geq 1/\gamma$. Superluminal motion $v_{\rm app} \geq c$ (i.e. $k \geq 1$) is then possible as long as $\gamma\beta \geq v_{\rm app}/c$. A direct consequence of the previous equation is $\gamma \geq v_{\rm app}/c$, which proves that, even for moderate superluminal motions, the true velocity is relativistic.

This relativistic motion yields anisotropic emission. It also enhances the energy of the photons and the intensity of the radiation when the region is moving toward the observer. The textbook derivation of this effect, called the relativistic Doppler effect, is based on the velocity transformation. I propose here a simple framework based on the transformation of the energy of an emitted photon. I assume isotropic emission at the energy $E_{\rm iso}$ in the emitting region frame (orange cloud in Fig. 4) and I call the associated four-momentum $[E_{\rm iso}, p_{x,\ {\rm iso}}, p_{y,\ {\rm iso}}, p_{z,\ {\rm iso}}]$. The observer receives photons with an energy E in his own rest frame. Since only the photons travelling along the line of sight are received, the observed four-momentum can be written $[E, p_x = E, p_y = 0, p_z = 0]$, where x is the direction of the line of sight (I adopt here the convention $c = 1$). These two four-momenta are related with a Lorentz boost γ of the emitting region and a rotation of θ from the direction of motion, i.e.:

$$\begin{bmatrix} E \\ E \\ 0 \\ 0 \end{bmatrix} = \begin{bmatrix} 1 & & & \\ & \cos\theta & \sin\theta & \\ & -\sin\theta & \cos\theta & \\ & & & 1 \end{bmatrix} \begin{bmatrix} \gamma & \gamma\beta & & \\ \gamma\beta & \gamma & & \\ & & 1 & \\ & & & 1 \end{bmatrix} \begin{bmatrix} E_{\rm iso} \\ p_{x,\ {\rm iso}} \\ p_{y,\ {\rm iso}} \\ p_{z,\ {\rm iso}} \end{bmatrix}$$

or inversely

$$\begin{bmatrix} E_{\rm iso} \\ p_{x,\ {\rm iso}} \\ p_{y,\ {\rm iso}} \\ p_{z,\ {\rm iso}} \end{bmatrix} = \begin{bmatrix} \gamma & -\gamma\beta & & \\ -\gamma\beta & \gamma & & \\ & & 1 & \\ & & & 1 \end{bmatrix} \begin{bmatrix} 1 & & & \\ & \cos\theta & -\sin\theta & \\ & \sin\theta & \cos\theta & \\ & & & 1 \end{bmatrix} \begin{bmatrix} E \\ E \\ 0 \\ 0 \end{bmatrix}$$

which reads:

(1.4)

$$[E_{\rm iso}, p_{x,\ {\rm iso}}, p_{y,\ {\rm iso}}, p_{z,\ {\rm iso}}] = [\gamma E(1-\beta\cos\theta), \gamma E(\cos\theta - \beta), E\sin\theta, 0]$$

The time-like component can be used to define the Doppler factor δ as the ratio of the received and emitted energies:

$$\delta = \frac{E}{E_{\rm iso}} = \frac{1}{\gamma(1-\beta\cos\theta)} \tag{1.5}$$

The Doppler factor is thus the quantity by which the energy is enhanced in the observer frame and its maximal value is $\delta_{\max} = 1/\gamma(1-\beta) \sim 2\gamma$ (where $\sim$ corresponds to the ultra-relativistic limit $\beta \to 1$). With the energy being enhanced by δ, so too is the frequency. Time, which is the inverse of frequency, is then contracted by a factor δ.

The Doppler factor also affects the beaming of the radiation. Indeed, following Eq. (1.4), $p_{x,\,\mathrm{iso}} \geq 0$ corresponds to $\cos\theta \geq \beta$, i.e. $1-\theta^2/2 \geq 1-\gamma^{-2}/2$ in the ultra-relativistic limit, which reads $\theta \leq 1/\gamma$. Thus the front hemisphere of the emission is transformed into a cone of half-opening angle $\theta = 1/\gamma$.

Finally, the effect on the specific intensity I_ν per unit solid angle can be derived, as in Rybicki & Lightman (1979), using what could be called a relativistic Liouville's theorem, i.e. the invariance of the number of particles per phase volume $\mathrm{d}\mathcal{N}/\mathrm{d}^3x\mathrm{d}^3p$ under a Lorentz transformation. Since the energy density per unit solid angle $u_\nu \mathrm{d}\nu$ is linked to the specific intensity via $u_\nu \mathrm{d}\nu = I_\nu \mathrm{d}\nu/c$ and can easily be expressed as a function of the previous Lorentz invariant, the specific intensity reads:

$$\frac{I_\nu}{c}\mathrm{d}\nu = u_\nu \mathrm{d}\nu = h\nu \times \frac{\mathrm{d}\mathcal{N}}{\mathrm{d}^3x\mathrm{d}^3p} \times p^2\mathrm{d}p \tag{1.6}$$

Using $p = h\nu/c$, the number of particles per phase volume is proportional to I_ν/ν^3, which consequently is a Lorentz invariant. Thus, even considering a flux intensity independent of the energy $I_\nu \propto \nu^0$, the flux is enhanced by a factor δ^3. The enhancement of the flux ($\times\delta^3$) together with the shortening of the variation time scale ($/\delta$), within an angle $\theta < 1/\gamma$, explain the properties of the brightest and most rapidly variable objects among the jetted AGN: the blazars, which are thought to have a jet closely aligned with the line of sight.

1.1.2.2. *The super-massive black hole and the accretion disk*

The domination of gravitational energy for high-luminosity systems was first discussed by Hoyle & Fowler (1963), Salpeter (1964) and Zel'dovich (1964). Lynden-Bell (1969) reached a similar conclusion, with a *reductio ad absurdum* argument that is particularly enlightening. What if we assume that the prime process feeding the giant lobes observed in radio galaxies is of nuclear origin and thus that the nuclear energy released by the system dominates over the gravitational binding

energy? Given that the total energy in the lobes can be estimated to an equivalent of $10^7 M_\odot c^2$, where $M_\odot$ is the mass of the sun ($\sim 2\times10^{33}$ g), and since the efficiency of nuclear processes is below the percent level (0.7% for hydrogen fusion), the engine powering these giant structures should have at least a mass $M > 10^9\ M_\odot$. The typical time scales of variation of the optical flux observed by that time were on the order of ~ 10 hours. This imposes a maximum size on the system on the order of $R < 10$ light hours and a lower limit on the gravitational energy in the system can then be computed as $GM^2/R > 3\times10^8 M_\odot c^2$. But the gravitational energy is then at least 30 times[4] larger than the energy supposedly released by nuclear processes and gravitation should then have been able to power the observed structures. Lynden-Bell then concludes that such a system "*will collapse and finally fall within its Schwarzschild radius and be lost from view*"[5].

Gravitational collapse is one of the major processes considered in the formation of super-massive black holes ($M \gtrsim 10^6\ M_\odot$). These objects are believed to lie in the centres of the majority of galaxies, if not all. The most convincing argument has certainly been raised by Rees (1978) with his famous flow chart, reproduced in Fig. 5. The aim of this flow chart is to show that, given the high luminosity of AGN, a large amount of material must have been involved in their formation and "*the almost inevitable endpoint [...] [is] the collapse of a large fraction of its total mass to a black hole*" (Rees 1984).

It was realized at the end of the '70s that gravitational energy could be quite efficiently converted around black holes. Considering the accretion by a non-rotating black hole, the binding energy of the last circular orbit for a test particle of mass m is $\frac{\sqrt{8}}{3}mc^2$, a process extracting the remaining energy would have an efficiency of $1-\frac{\sqrt{8}}{3} = 5.7\%$. For a maximally rotating black hole, the efficiency of conversion of the energy of the accreted matter energy goes up to 42%, sixty times larger than for hydrogen fusion. Blandford & Payne (1982) proposed a mechanism tapping this energy reservoir based on the magnetic field anchored in the disk, which can generate a magneto-hydrodynamic

[4]Even assuming that the observed variations come from a boosted region of Doppler factor δ, the gravitational energy can not be neglected unless $\delta \gg 30$.

[5]The Schwarzschild radius R_S of a system of mass M is simply defined as the size for which the escape velocity equals the speed of light, $v_{\rm esc} = c$. For a test mass m with the simple classical argument $\frac{1}{2}mv_{\rm esc}^2 = GmM/R_S$, one gets $R_S = 2GM/c^2$.

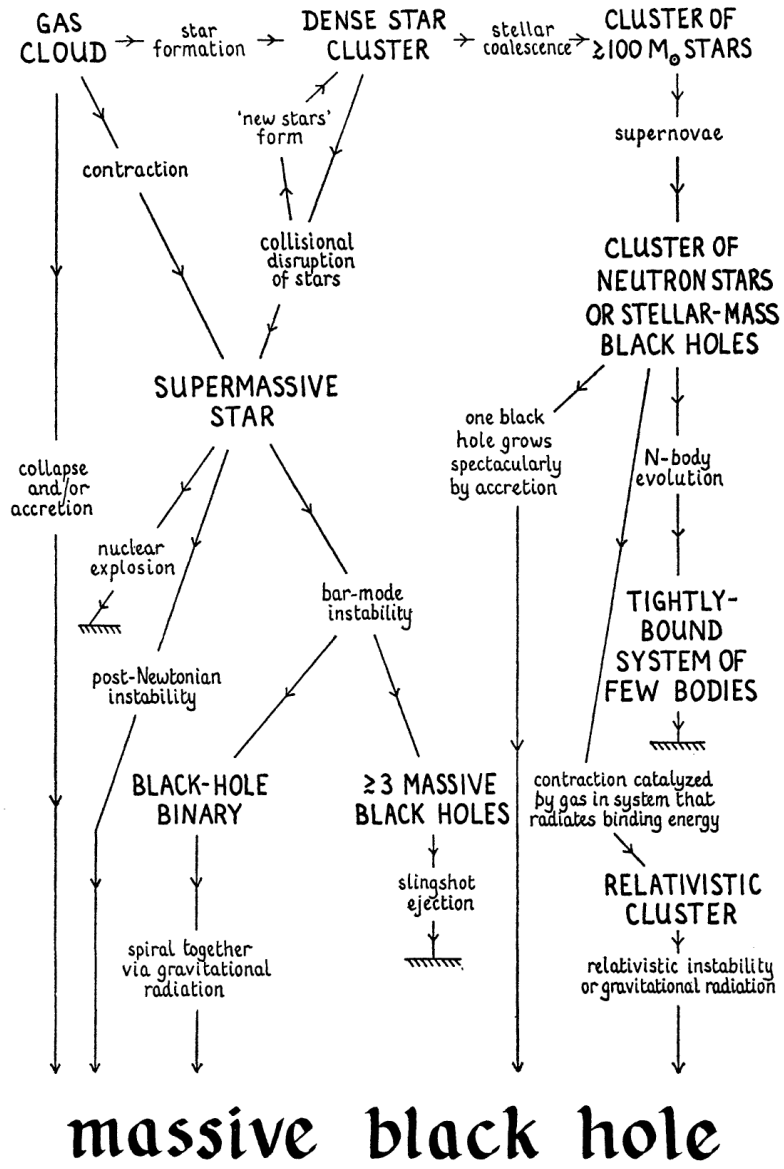

FIGURE 5. Possible modes of formation of a supermassive black hole in an AGN. *Extracted from Rees (1978).*

wind along the rotation axis (Ferrari 1998). The power extracted from the accreted material would then be:

$$\mathcal{L}_{\rm BP} \sim B_d^2 R_{\rm disk}^2 \sqrt{\frac{GM}{R_{\rm disk}}} \sim 2\times 10^{46} \left(\frac{B_d}{10^3{\rm G}}\frac{M}{10^9 M_{\rm o}}\right)^2 \ {\rm erg\ s^{-1}} \tag{1.7}$$

where the inner radius of the accretion disk is assumed to be $R_{\rm disk} \sim 5R_S$. Using Eq.(5.6) in Blandford & Payne (1982), the typical efficiency of the process is on the order of 12%.

One can compare this power to the Eddington luminosity $\mathcal{L}_E$, which is the maximal steady state luminosity of a spherical system powered by accretion. One assumes that the gravitational force exerted on electron-proton pairs in a fully ionized plasma is balanced by the radiation pressure of an inner shining object when the luminosity attains the critical value $\mathcal{L}_E$. The radiation pressure mostly acts on the electrons, and is accounted for using the Thomson cross section σ_T, while the gravitational force mostly acts on the protons of mass $m_p \sim 1800 m_e$ and one assumes that the plasma remains locally neutral so that charges are not separated. The Eddington luminosity is then:

$$\mathcal{L}_E = \frac{2\pi m_p c^3}{\sigma_T} R_S \sim 1.26\times 10^{47} \left(\frac{M}{10^9 M_{\rm o}}\right) \ {\rm erg\ s^{-1}} \tag{1.8}$$

The power could also in principle be extracted from the black hole itself. The energy of a rotating black hole (Kerr 1963) of mass M has indeed two components: one due to its spin and an "irreducible" mass that goes down $M/\sqrt{2}$ for a maximal rotation. The rotation energy could be extracted by slowing down the black hole and the efficiency of such a process would be $E_{\rm spin}/E_{\rm tot} = (Mc^2 - Mc^2/\sqrt{2})/Mc^2 \sim 29\%$. Nonetheless, it is not easy to build a realistic astrophysical scenario able to extract all of this energy. Blandford & Znajek (1977) proposed a scenario where the black hole is seen has a resistive sphere (though with a small surface resistivity on the order of $\sim 100\ \Omega$). In an ambient magnetic field B_0, power can be extracted using a current flow between the equator and the poles, with a maximum value of:

$$\mathcal{L}_{\rm BZ} \sim B_0^2 \left(\frac{J}{J_{\rm max}}\right)^2 \left(\frac{R_S}{2}\right)^2 c \sim 3\times 10^{46} \left(\frac{B_0}{10^4{\rm G}}\frac{M}{10^9 M_{\rm o}}\frac{J}{0.5 J_{\rm max}}\right)^2 \ {\rm erg\ s^{-1}} \tag{1.9}$$

In this equation B_0 is the magnetic field close to the black hole, which is assumed here to be ten times larger[6] than the magnetic field at $R_{\rm disk}$, which is used in Eq. (1.7). By slowing down the black hole from a maximal spin $J = J_{\rm max}$ to $J = 0$, a fraction of 9.2% of the rest energy can be extracted (Rees 1984). This scenario is based on a strong magnetic field and the most natural explanation for its origin would be the accretion disk that feeds the black hole with matter and "frozen-in" magnetic lines.

The mechanisms of Blandford & Znajek (1977) and Blandford & Payne (1982) do not exceed the limiting Eddington luminosity and both generate jetted outflows that are sufficiently powerful to explain the giant structures observed in radio or the emission at higher energies. They provide a direct link between the black hole and the jet or between the accretion disk and the jet, where rotating magnetic fields are a crucial ingredient, but distinctive signatures of these mechanisms are not yet clearly identified. A recent review of the various processes at play in the ejection and collimation of jets as well as the tremendous efforts of simulations and observations ongoing on this topic can be found in Pudritz et al. (2012).

1.1.2.3. *The geometric unification scheme*

AGN are thought to host a black hole, which is fed by an accretion disk. As discussed in Sect. 1.1.1.3, AGN are usually divided in radio-loud and radio-quiet objects, the latter not exhibiting jets. Both subclasses can exhibit emission lines, believed to emerge from the photo-ionization of a small region of dense, fast moving clouds (the broad line region, BLR) and of a larger zone with slower moving clouds (the narrow line region, NLR).

NLRGs and radio-quiet Seyfert 2 do not exhibit broad lines. Rowan-Robinson (1977) assumed that, instead of being absent, BLR are hidden, or obscured by dust. Observing the polarized light from the Seyfert 2 prototype NGC 1068, Antonucci & Miller (1985) found a spectrum very similar to a Seyfert 1. This is understood as light being scattered and polarized by electrons in the material above the nucleus (see e.g. the review of Shields 1999) and it confirms the "hidden" BLR hypothesis. An extra ingredient in the AGN unification scheme was

[6]The solutions studied by Blandford & Payne (1982) correspond to a self similar magnetic field $B \propto R^{-5/4}$.

added: a dusty torus or a wrapped disk obscuring the light of type 2 objects.

The unification scheme that has emerged combining these ingredients (black hole, disk, jet, torus and clouds) is usually attributed to Antonucci (1993) and Urry & Padovani (1995). As shown in Fig. 6, it is based on orientation effects compared to the line of sight.

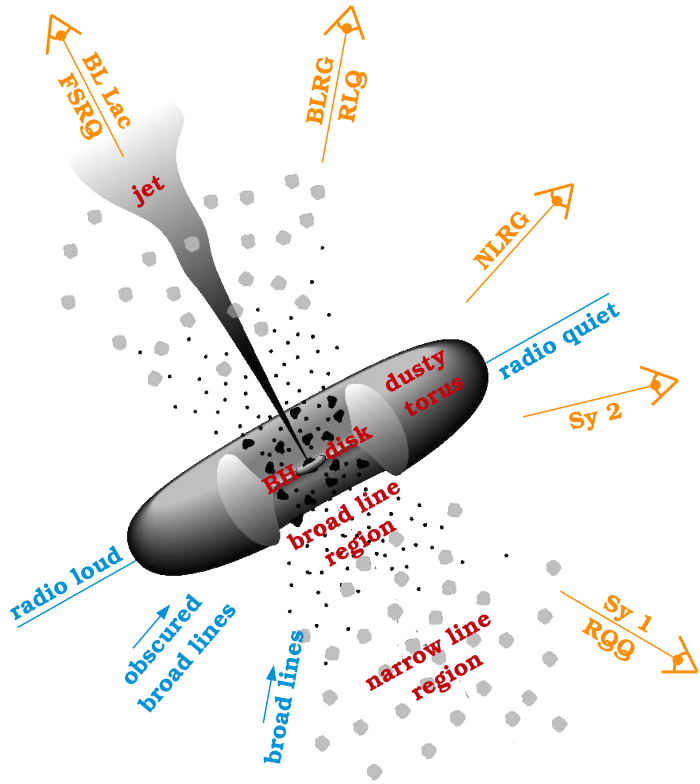

FIGURE 6. Unification scheme of AGN. The acronyms for the different sub-classes of AGN are given in Fig. 2. *Adapted from Urry & Padovani (1995)* .

1.2. Jetted emission of blazars

1.2.1. Transferring the jet energy to particles

The mechanisms launching the jet and the processes converting the jet energy into particle kinetic energy are thought to be related to the matter content of the jet. It is widely accepted that at least half of the electromagnetic spectrum of AGN is radiated by electrons, but for the plasma to remain neutral, they must have a positive counterpart: positrons (in which case one speaks of pair plasma) or ions/protons (referred to as protons or normal matter in the following).

1.2.1.1. *The jet content*

The matter content of the jet is usually thought to be linked to the mechanism responsible for the launch of the jet. Processes tapping the black hole rotational energy (e.g. Blandford-Znajek) are often assumed to yield pair plasma jets while the content of outflows originating from rotating disks (e.g. Blandford-Payne) is assumed to be extracted from the disk itself and should therefore be an electron-proton plasma.

But the variety of astrophysical scenarios is far more complex. As discussed before, the magnetic field embedding the black hole may be partly fed from the disk, conveying normal matter together with the lines (McKinney & Gammie 2004; De Villiers et al. 2005). The opposite can also happen if a very small amount of matter is loaded on the magnetic field lines anchored in the disk. In this case, the interaction of the disk emission with the magnetic field could produce a pair plasma (a possibility that has not been yet deeply investigated according to Spruit 2010).

Whatever the power source, either black hole rotation or accretion, and whatever one jet contains, either pair plasma or normal matter, an efficient process must convert the energy at the base of the jet into particle kinetic energy. Depending on the author, the energy at the base of the jet is referred to as "centrifugal" or "magnetic" and the use of "Poynting flux" is widespread. Spruit (2010) argues that these quantities are in general equivalent. If one considers the frame co-rotating with the power source, then the matter flow is parallel to the magnetic field lines and the Lorentz force $\propto \mathbf{v} \times \mathbf{B}$ is null - only the centrifugal force drives the flow. In an inertial frame there is no centrifugal force but it is the azimuthal component of the magnetic field that drives the flow, hence the magnetic energy denomination. These two equivalent

forces can be seen as participating in the conversion of electromagnetic energy into kinetic energy. Indeed, in magneto hydrodynamics, as in simple vacuum electrodynamics, $\mathbf{E} = \mathbf{v} \times \mathbf{B}$, and the Poynting flux reads, in cgs:

$$\mathbf{\Pi} = \frac{c}{4\pi}\mathbf{E} \times \mathbf{B} = \mathbf{v}_\perp \frac{B^2}{4\pi} \tag{1.10}$$

where $\mathbf{v}_\perp$ is the component of the flow velocity that is orthogonal to the magnetic field. Eq. (1.10) shows that the Poynting flux in magneto hydrodynamics is the flux of magnetic energy advected with the fluid in a direction orthogonal to the magnetic field. Spruit (2010) observes that the Poynting flux plays a role similar to a flux of enthalpy in regular hydrodynamics. In analogy with Bernoulli's theorem, the sum of the enthalpy ($\propto B^2$) and kinetic energy of the fluid ($\propto v^2$) is conserved. The increasing particle energy along the jet is progressively extracted from the magnetic field.

The fraction of the magnetic energy going into kinetic energy is model dependent. Standard scenarios assume that the jet is axisymmetric (rotational symmetry around the jet axis) and the maximum bulk Lorentz factor achieved is $\Gamma_\infty \sim \sigma^{1/3}$, where σ is the ratio of the magnetic and kinetic energy at the base of the jet (calling B_0 and ρ_0 the magnetic field and the particle density at the base of the jet, $\sigma = \frac{B_0^2}{8\pi}/\frac{1}{2}\rho_0 c^2$). If all the energy was converted, by definition of σ, one would get $\Gamma_{\max} = \sigma$. Defining the efficiency η of the process as the ratio between the achieved particle energy and the maximal one, one gets

$$\eta = \frac{\Gamma_\infty \rho c^2}{\Gamma_{\max} \rho c^2} \sim \sigma^{-2/3} = \frac{1}{\Gamma_\infty^2} \tag{1.11}$$

The conversion of Poynting flux to the flow of particles is then efficient for mildly relativistic flows and inefficient for high velocity flows. This conclusion is drawn for axisymmetric, i.e. 2D flows. 3D modelling of the system including kinking modes/reconnection (cf. next subsection) can be much more efficient, with values of up to 50% for Lorentz factors of ~ 20, being reached after a distance from the base of the jet of $10^2 - 10^3\ R_S$ (Giannios & Spruit 2006; Komissarov et al. 2007).

Despite the high efficiency of the above-mentioned magnetic dissipation processes (see also Blandford 2002), the acceleration of particles

remains mostly attributed to shocks (Blandford & Rees 1974; Begelman et al. 1984), the efficiency of which is still a matter of debate. The simulations of the latter tend to produce broad distributions of particle Lorentz factors while the former are still limited (potentially by numerical constraints).

To support the large energetics of giant radio lobes, there should be a fraction of protons in the jet. Sikora et al. (2005) argue that a scenario involving shocks favours such a proton domination of the energy flux. Authors, such as Marscher (2006), suggest an intermediate picture where reconnection-like scenarios, which are more likely linked to pairs and can be much more efficient, would occur in an initial phase and feed the shocks with already energized particles. The interested reader can also refer to the theoretical work of Petrosian (2012) and the simulations of Sironi & Spitkovsky (2009) where turbulence acts as the injector of particles in the shock.

1.2.1.2. *Acceleration processes*

An acceleration process extracts energy from the medium and feeds it to the particles. This can be done through a scattering of the particles off irregularities in the magnetic fields or simply through reflections on "magnetic walls". The generic equation to study the evolution over time t of a distribution of particles' energy, or equivalently of a Lorentz factor distribution $N(\gamma)$, is the Fokker-Planck equation:

$$\frac{\partial N}{\partial t}(\gamma,t) + \frac{\partial}{\partial \gamma}\left[\dot{\gamma} N(\gamma,t)\right] = Q(\gamma,t) - \frac{N(\gamma,t)}{t_{\rm esc}} \tag{1.12}$$

where the diffusion term is neglected. In Eq. (1.12), $Q(\gamma,t)$ is the source term, $t_{\rm esc}$ is the time needed for the particle to escape the region and $\dot{\gamma}$ is the energy loss/gain term. The latter includes the acceleration of particles (positive contribution), characterized by a time scale $t_{\rm acc}$, as well as the various radiative losses (negative contributions) that I discuss in Sect. 1.2.2.1[7]. I assume here for the sake of simplicity that the loss processes are slow compared to the acceleration ones, so that there is only one contribution to the loss/gain term: $\dot{\gamma} = \gamma/t_{\rm acc}$. Assuming that no source injects particles when the steady state is reached, Eq. (1.12) reads, after a development of the derivative of the loss/gain

[7]For the sake of clarity, the acceleration and escape times are assumed independent of γ, but an integral solution can be derived in a more general context

term:

$$\gamma \frac{\mathrm{d}N(\gamma)}{\mathrm{d}\gamma} = -N(\gamma) \times \left(1 + \frac{t_{\mathrm{acc}}}{t_{\mathrm{esc}}}\right) \tag{1.13}$$

which is solved for a particle spectrum $N(\gamma) \propto 1/\gamma^{1+t_{\mathrm{acc}}/t_{\mathrm{esc}}}$, i.e. a power law of index $1 + t_{\mathrm{acc}}/t_{\mathrm{esc}}$. A process that accelerates particles at high energies (hard spectrum, i.e. small index) is thus a process for which the ratio $t_{\mathrm{acc}}/t_{\mathrm{esc}}$ is as small as possible, i.e. a process that has a fast acceleration rate.

In the late '40s, Enrico Fermi designed a mechanism which stochasticly accelerates charged particles through collisions with magnetized clouds of randomly oriented velocity U (Fermi 1949). Following Begelman et al. (1984), for a relativistic particle of speed c, each bounce yields an energy change $|\Delta\gamma/\gamma| \propto U/c$ with an increase when the collision is head on and a decrease when the cloud is moving away. The head-on collisions are more frequent and the energy increase is favoured by an amount U/c, so that the acceleration time is $t_a \propto (c/U)^2$. Since the clouds are slower than the speed of light $c/U < 1$, this quadratic process (called the second order Fermi process) is quite slow. He then designed in the beginning of the '50s (Fermi 1954), a first order process with $t_a \propto c/U$, where only head-on collisions occur in a "contracting magnetic bottle" (Petrosian 2012). The latter is faster and thus much more efficient.

Acceleration by shocks can be as efficient as a first-order Fermi process, in which case authors speak of diffusive shock acceleration (see e.g. Drury 1983), or as a second-order Fermi process, called stochastic shock acceleration (see e.g. Petrosian 2012, for a recent approach). Not until recently has magnetic reconnection been recognized as a first order Fermi process, as discussed in the following. Both mechanisms are triggered by an initial disturbance in the medium. If the disturbance travels faster than the speed of sound, a shock is formed and the particles are accelerated as they cross the front. In a highly-magnetized plasma, the magnetic field lines are anchored with - "frozen in" - the matter and they become tangled as the flow advects them. If the resistivity of the plasma is not null, Joule dissipation locally causes a heating of the matter which conveys magnetic lines. Reconnection of opposite direction lines thus occurs, which can efficiently accelerate particles.

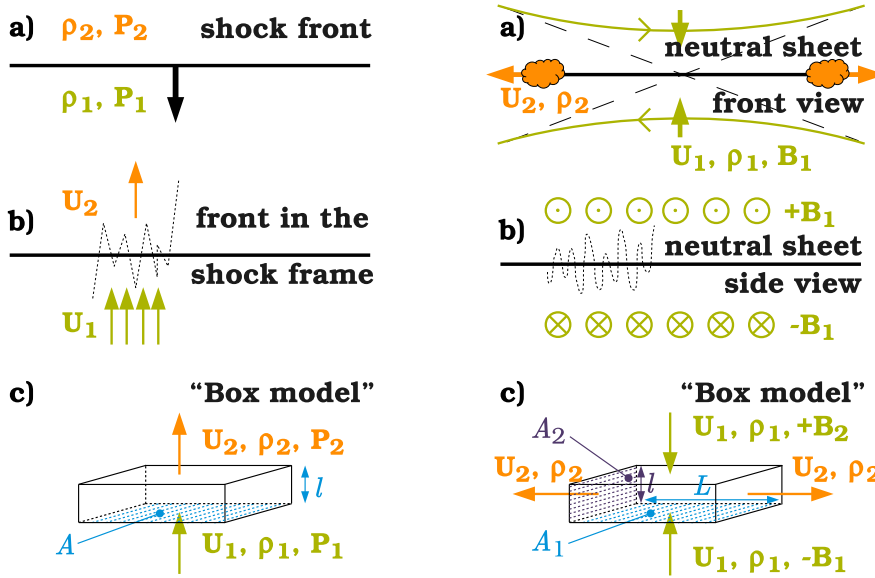

FIGURE 7. Schematic view of shock acceleration (left) and magnetic reconnection acceleration (right) in panels a). Panels b) show the reflections of the particle on inhomogeneities or on the magnetic "walls" with the dashed line. Panels c) show simplified views as box models. *Adapted from Drury et al. (1999); Drury (2012).*

I show in Fig. 7 a schematic view of the two acceleration processes. In the following, I adapt the "box model" approach and derive the acceleration and escape times in these two scenarios. A more detailed discussion and a more rigorous approach can be found in Drury et al. (1999); Drury (2012) and references therein. The escape rates are in both cases determined by the speed of the outflow and the typical scale involved (l for shocks, L for reconnection). The flow leaves the box from two sides for reconnection, hence the factor of 2 in the velocity (first line of Table 2).

The acceleration rate corresponds to the velocity change on each side of the box. Since only one direction of motion is accounted for and since the particles' motion is assumed to be isotropic, only a third of the particles are effectively accelerated at this rate (the same classic

	Shock acceleration	Magnetic reconnection
Escape rate	$\frac{1}{t_{\rm esc}} = \frac{U_2}{l}$	$\frac{1}{t_{\rm esc}} = \frac{2U_2}{L}$
Acceleration rate	$\frac{1}{t_{\rm acc}} = \frac{1}{3}\frac{\lvert U_1 - U_2\rvert}{l}$	$\frac{1}{t_{\rm acc}} = \frac{1}{3}\lvert\frac{2U_1}{l} - \frac{2U_2}{L}\rvert$
Ratio	$\frac{t_{\rm acc}}{t_{\rm esc}} = \frac{3}{\lvert\frac{U_1}{U_2} - 1\rvert}$	$\frac{t_{\rm acc}}{t_{\rm esc}} = \frac{3}{\lvert\frac{U_1 L}{U_2 l} - 1\rvert}$
Mass flux conservation	$\rho_1 U_1 A = \rho_2 U_2 A$	$2\rho_1 U_1 A_1 = 2\rho_2 U_2 A_2$
Power law index	$1 + \frac{t_{\rm acc}}{t_{\rm esc}} = 1 + \frac{3}{\lvert r-1\rvert}$	$1 + \frac{t_{\rm acc}}{t_{\rm esc}} = 1 + \frac{3}{\lvert r-1\rvert}$

TABLE 2. Derivation of the index of the power-law distribution of the accelerated particles for the "box models" of the shock acceleration (second column) and magnetic reconnection (third column). In both cases the compression ratio is defined as $r = \rho_2/\rho_1$.

argument as in the kinetic theory of gases). One can then simply compute the ratio of these rates and combine it with the conservation of mass flux, as in the third and fourth lines of Table 2, to obtain the index of the electron power law. The compression ratio $r = \rho_2/\rho_1$ is particularly useful, and in both cases:

$$N(\gamma) \propto 1/\gamma^{1+\frac{3}{\lvert r-1\rvert}} \tag{1.14}$$

The compression ratio can be derived precisely in the case of a strong shock, for a perfect gas. Using the conservation of energy flux, the conservation of momentum flux and assuming a mono-atomic gas one gets $r = 4$, which yields a power law of index 2 for shocks. The case of magnetic reconnection is less constrained. Indeed the conservation of momentum flux is trivial since the total input and output momenta are null. With the sole constraint of the conservation of energy flux, one cannot derive r. Drury (2012) argues that, for reconnections, one expects a much denser output medium than the input one, yielding $r \gg 1$ and an index tending towards 1.

These very simple derivations of indices are in good agreement with particle-in-cells simulations, e.g. Zenitani & Hoshino (2001); Drake et al. (2006) for magnetic reconnection and Sironi & Spitkovsky (2009) for shock acceleration. In this simple approach, the energy dependency of the time scales is not explicitly taken into account and the maximum energy to which particles can be accelerated is determined by the escape time[8], presumably decreasing with energy, and by the radiative losses, which are discussed in the following.

1.2.2. Radiation of the accelerated particles

1.2.2.1. *From particles to photons*

The processes that convert the energy of a particle into γ rays can be divided into two sub-classes: the matter-matter interactions and the matter-field interactions.

γ rays produced by matter-matter interactions in astrophysical environments could come from hadronic processes, mostly from photo production of pions, i.e. interactions of protons with ambient photons (from the jet itself or from its environment in the case of AGN): $p + \gamma \rightarrow p + \pi^0$. π^0 have a life time of $\sim 10^{-16}$ s and decay, with a branching ratio of 99%, into two γ rays of ~ 135 MeV$/2 = 67.5$ MeV in the particle rest frame. After integration over the pitch angle and after Lorentz transformation, the γ-ray spectrum produced by hadronic interactions is almost identical to that of the parent population at the highest energies, i.e. above the bulk emission around 67.5 MeV that constitutes a smoking gun of these interactions. Another smoking gun would be the detection on Earth of neutrinos of astrophysical origin from an equivalent channel such as $p + \gamma \rightarrow n + \pi^+$. Indeed a charged pion decays with probab 99.99% into a muon and the associated neutrino and the muon itself decays into an electron and associated neutrinos: $\pi^+ \rightarrow \nu_\mu + \mu^+ \rightarrow \nu_\mu + \bar{\nu}_\mu + \nu_e + e^+$.

The production of γ rays can also originate from matter-antimatter annihilation. The first channel to consider is the annihilation of positrons with electrons producing, in the centre-of-mass frame, two γ rays emitted back-to-back with energies $m_e c^2 = 511$ keV. This emission line, broadened by relative motion, tracks the areas where the density of matter is large, such as the galactic plane, and can, for instance, be

[8]Note that the size of the magnetic reconnection region is *a priori* smaller than that of a shock, which should yield a smaller maximum energy.

studied with the INTEGRAL satellite (see e.g. Knödlseder et al. 2005). The counterpart of this annihilation process is pair creation by two photons, which is responsible for the absorption of γ rays during their propagation, discussed in Sect. 1.3.2. Besides the annihilation of electrons, any particle-antiparticle pair can produce γ rays, each of them carrying half of the total energy in the centre-of-mass frame. Such annihilations can be exploited in the search for dark matter, which represents 23% of the energy content of the Universe. Weakly interacting massive particles (WIMPs) are one of the leading dark matter particle candidates and they could annihilate producing lines between 10 GeV and a few TeV (Drees & Gerbier 2012). An apparent excess around ~ 130 GeV (e.g. Su & Finkbeiner 2012; Weniger 2012) near the Galactic centre has recently triggered some excitement but has not yet been confirmed by the *Fermi*-LAT collaboration and could still be of systematic origin.

When considering the interaction of matter with an electromagnetic field, or equivalently with a photon, one must account for synchrotron losses for a magnetic field, Compton scattering for a collision with a photon and bremsstrahlung when the Coulomb field of a nucleus is involved. The latter, combined with pair creation in the field of a nucleus, explains the development of atmospheric showers, discussed in Sect. 1.3.1.1. Synchrotron emission of electrons is the most favoured process to explain the emission of AGN from radio to X rays. It has also been invoked for proton emission at higher energy (Aharonian 2000). Depending on the modelling (Mücke & Protheroe 2001), this process could even dominate over photo production of pions, eliminating the neutrino smoking gun for proton acceleration (but see also Cerruti et al. 2012, for a mixed model). The synchrotron emission has a counterpart, synchrotron self absorption, which occurs when the brightness of a synchrotron source becomes high enough to heat up the emitting population. Below a critical frequency, the emitting region becomes opaque to its own radiation or "optically thick" and the emitted spectrum follows a power law $E\frac{dN}{dE} \propto E^{5/2}$.

The most favoured process to explain the γ-ray emission of AGN is Compton scattering. In its usual formulation, it consists of the "collision" of a photon with an electron in a frame where the electron is at rest. The final state consists of a photon that has lost a fraction of its energy and an electron with a recoil energy. If the incoming

photon energy is negligible compared to the mass of the electron, the collision is almost elastic and the scattering occurs in the so-called Thomson regime where no direction is preferred. At higher photon energy, in the so-called Klein-Nishina regime, the recoil of the electron becomes non negligible, the angular distribution of the outgoing particles is increasingly front sided and the interaction cross section drops. In astrophysics, one usually considers the frame where an energetic electron transfers its energy to a low-energy photon and the process is called inverse Compton. If the electron has a Lorentz factor γ and the photon has an energy $h\nu$ in the observer frame, then the photon has an energy $\sim \gamma h\nu$ in the electron frame. In the Thomson regime $\gamma h\nu \ll m_e c^2$, the outgoing photon energy remains $\gamma h\nu$ while in the Klein-Nishina regime, the electron transfers almost all of its energy to the photon $\gamma h\nu = m_e c^2$. Back in the observer frame, the outgoing photon has then an energy $\gamma^2 h\nu$ in the Thomson regime and an energy $\gamma m_e c^2$ in the Klein-Nishina limit. A natural origin of the Comptonized photon field is the synchrotron radiation of the electrons, in which case the emission scenario is called synchrotron self Compton (see Band & Grindlay 1985), which I discuss in the next subsection. When the photon field does not come primarily from the electrons themselves, one speaks of external Compton. Though presumably less important in BL Lacs and potentially dominant in FSRQs, external photon fields, e.g. from the BLR or from the accretion disk (see e.g. Dermer & Schlickeiser 1993; Sikora et al. 1994), can also be scattered by the electrons.

1.2.2.2. *The synchrotron self Compton model*

I consider an electron of energy $\gamma m_e c^2$, moving at an angle θ with respect to the magnetic field of norm B. The particle loses energy via synchrotron processes and emits radiation at the frequency ν, or equivalently emits photons of energy $h\nu$. The synchrotron energy losses per frequency band and per unit solid angle for a Lorentz factor γ are defined as:

$$\begin{aligned}\frac{\mathrm{d}P_{\rm sync}}{\mathrm{d}\Omega}(\nu,\gamma,\theta) &= \frac{\mathrm{d}}{\mathrm{d}\Omega\mathrm{d}\nu}\left(-m_e c^2 \dot{\gamma}_{\rm sync}\right) = \frac{\mathrm{d}}{\mathrm{d}\Omega\mathrm{d}\nu}\left(-\frac{\mathrm{d}E}{\mathrm{d}t}_{\rm sync}\right) \\ &= 2\sigma_{\rm T} c\gamma^2 \times U_B \times f(\nu)\frac{\sin^2\theta}{2\pi} \qquad (1.15)\end{aligned}$$

where $U_B = B^2/8\pi$ is the magnetic energy density (in cgs) and $\sigma_{\rm T} = \frac{8\pi}{3}\left[\frac{e^2}{m_e c^2}\right]^2$ is the Thomson cross section. I normalize the function $f(\nu)$ to unity so that $\int_0^\infty f(\nu)d\nu = 1$ and:

$$f(\nu) = \frac{9\sqrt{3}}{8\pi}\frac{1}{\nu_C}F\left(\frac{\nu}{\nu_C}\right) \tag{1.16}$$

where the critical angular frequency is defined with $2\pi\nu_C = \frac{3}{2}\frac{eB}{m_e c}\gamma^2\sin\theta$. The function F is linked to the modified Bessel function $K_{5/3}$ via $F(x) = x\int_x^\infty K_{5/3}(t)\mathrm{d}t$ and can be found in the GNU scientific library, for computational purposes. Assuming that the magnetic field is tangled with matter and that the emission of the synchrotron radiation is isotropic in the emitting region frame (sometimes called a "blob"), the total synchrotron energy losses are:

$$P_{\rm sync}(\nu,\gamma) = \int \mathrm{d}\Omega \frac{\mathrm{d}P_{\rm sync}}{\mathrm{d}\Omega}(\nu,\gamma,\theta) = \frac{4}{3}\sigma_{\rm T} c\gamma^2 \times U_B \times f(\nu) \tag{1.17}$$

The other losses that I consider here come from the interaction of the electron with a field of photons through inverse Compton. Assuming an isotropic field of photons of energies $h\nu_0 = \epsilon_0 m_e c^2$ and averaging over the arrival direction of the electron:

$$P_{\rm IC}(\nu,\gamma) = \frac{4}{3}\sigma_{\rm T} c\gamma^2 \times m_e c^2 \int \mathrm{d}\epsilon_0 n(\epsilon_0)\epsilon_0 \times g(\nu,\gamma,\nu_0) \tag{1.18}$$

where $n(\epsilon_0)$ is the density of photons per energy band, so that $n_{\rm ph} = \int \mathrm{d}\epsilon_0 n(\epsilon_0)$ is the number of photons per unit volume and that the quantity $U_{\rm ph} = m_e c^2 \int \mathrm{d}\epsilon_0 n(\epsilon_0)\epsilon_0$ is the photon energy density. Like $f(\nu)$ for the synchrotron radiation, I normalize $g(\nu,\gamma,\nu_0)$ to unity, i.e. $\int_0^\infty \mathrm{d}\nu g(\nu,\gamma,\nu_0) = 1$. I simply define this function as $g(\nu,\gamma,\nu_0) = 6x^2(1-x)/\nu$, with $x = \frac{\nu/\nu_0}{4\gamma^2} \in [0;1]$, in the Thomson scattering limit and for an ultra-relativistic electron (derived from Eq.(7.26b) in Rybicki & Lightman 1979). To account for the reduction of the cross section for non-facing collisions derived by Klein and Nishina, Jones (1968) computed an approximated expression that reads (with my definition of g and a bit of algebra):

$$g(\nu,\gamma,\nu_0) = \frac{9x^2}{\nu}\left[2\kappa\ln\kappa + (1-\kappa)\times(1+2\kappa+\gamma\epsilon_0 x)\right] \tag{1.19}$$

where $\kappa^{-1} = x^{-1} - 1$ and $\kappa \geq 1/4\gamma^2$ for kinematic reasons.

Eq. (1.18) and Eq. (1.17) are remarkably similar. After integration over the frequency (f and g are normalized to unity), both losses are proportional to $\gamma^2 B^2$ and the ratio of the total inverse Compton over synchrotron losses for a single particle is simply the ratio of the photon field over magnetic field energies $U_{\rm ph}/U_B$.

Instead of a single electron, I now deal with a distribution, say e.g. a power law $n_e(\gamma) \propto \gamma^{-p}$, where n_e is the number of electrons per unit volume. The spectral luminosity, in energy per unit time per frequency band, is derived by integrating over the volume of emission and over the electron distribution. For a spherical homogeneous emission region of radius R, assuming that its light crossing time is small with respect to the radiative time scales:

(1.20)
$$L_{\rm sync}(\nu) = \frac{4\pi}{3} R^3 \times \frac{3}{2} \frac{1 - \frac{2}{\tau^2}\left[1 - e^{-\tau}(1+\tau)\right]}{\tau} \int {\rm d}\gamma n_e(\gamma) P_{\rm sync}(\nu, \gamma)$$

where the middle expression characterizes the synchrotron self absorption and tends to one for a null optical depth. Using Gould (1979), the latter reads:

$$\tau(\nu) = \frac{1}{4\pi} \frac{R \times (c/\nu)^2}{m_e c^2} \int {\rm d}\gamma \left\{ -\gamma^2 \frac{\rm d}{{\rm d}\gamma} \left[\frac{n_e(\gamma)}{\gamma^2} \right] \right\} P_{\rm sync}(\nu, \gamma) \quad (1.21)$$

In the SSC model, the field of photons which is "Comptonized" by the electrons is the very field that they create through synchrotron losses. Since $n(\epsilon_0)$ varies in the emission region (Gould 1979), an average corrective factor $\alpha_{corr} = 3/4$ is applied (as in Kataoka 1999; Sanchez 2010), so that the photon field energy density and the synchrotron power are linked with:

(1.22)
$$m_e c^2 n(\epsilon_0)\epsilon_0 {\rm d}\epsilon_0 = \alpha_{\rm corr} \frac{R}{c} \times \frac{1 - e^{\frac{\tau(\nu_0)}{2}}}{\frac{\tau(\nu_0)}{2}} \times \left[\int {\rm d}\gamma' n_e(\gamma') P_{\rm sync}(\nu_0, \gamma') \right] {\rm d}\nu_0$$

The inverse Compton luminosity then reads:

$$L_{\rm IC}(\nu) = \frac{4}{3}\pi R^3 \times \frac{3}{2} \frac{1 - \frac{2}{\tau_{ee}^2}\left[1 - e^{-\tau_{ee}}(1+\tau_{ee})\right]}{\tau_{ee}} \times \sigma_T R \int {\rm d}\gamma n_e(\gamma) \gamma^2$$
$$\int {\rm d}\nu_0 \frac{1 - e^{-\frac{\tau(\nu_0)}{2}}}{\frac{\tau(\nu_0)}{2}} g(\nu, \gamma, \nu_0) \int {\rm d}\gamma' n_e(\gamma') P_{\rm sync}(\nu_0, \gamma') \quad (1.23)$$

where the absorption factor takes into account the pair creation. Following Coppi & Blandford (1990), the associated optical depth is well approximated by:

$$\tau_{ee}(\nu) = 0.2\sigma_T R \times n\left(\frac{m_e c^2}{h\nu}\right) \tag{1.24}$$

The observed flux $F(\nu_{\rm obs})$ (in energy per unit time per unit area per frequency band) accounts for the luminosity distance of the source D_L, $F(\nu_{\rm obs}) = L_{\rm obs}(\nu_{\rm obs})/4\pi D_L^2$, and also for its redshift, dividing the frequency by $1+z$. The Doppler effect increases the frequency by a factor δ, $\nu_{\rm obs} = \delta\nu/(1+z)$, and enhances the flux normalization by a factor δ^3, as in Sect. 1.1.2.1[9]. The observed flux is, therefore:

$$F(\nu_{\rm obs}) = \delta^3 \frac{1}{4\pi D_L^2} \times L_{\rm tot}\left(\frac{(1+z)\nu_{\rm obs}}{\delta}\right) \times e^{-\tau_{\rm EBL}(h\nu_{\rm obs})} \tag{1.25}$$

where $L_{\rm tot} = L_{\rm sync} + L_{\rm IC}$ is the total SSC luminosity. The last term quantifies the transparency of the Universe to γ rays, discussed in Sect. 1.3.2.

1.2.2.3. *The delta approximations and equipartition*

I discuss in the following the SSC modelling by imposing null opacities $\tau(\nu) = \tau_{ee}(\nu) = 0$ and exploiting delta approximations. The first delta approximation is very common and is based on the fact that the function $F(x)$ in Eq. (1.16) is maximum for $x = 0.29$. With my appropriate normalization of $f(\nu)$, I thus assume that $f(\nu) = \delta(\nu - \gamma^2\nu_B)$, where δ is the Dirac function and $\nu_B = 0.29\nu_C/\gamma^2 \propto B$. Then from Eq. (1.17) and Eq. (1.20), the synchrotron luminosity $L^\delta_{\rm sync}$ in the delta approximation reads:

$$\begin{aligned} L^\delta_{\rm sync}(\nu) &= \frac{4\pi}{3}R^3 \times \frac{4}{3}\sigma_{\rm T} c \times U_B \times \int {\rm d}\gamma n_e(\gamma)\gamma^2 \delta(\nu - \gamma^2\nu_B) \\ &= \frac{4\pi}{3}R^3 \times \frac{4}{3}\sigma_{\rm T} c \times U_B \times \int {\rm d}\gamma n_e(\gamma)\gamma^2 \delta(\gamma - \sqrt{\nu/\nu_B}) \times \frac{1}{2\gamma\nu_B} \\ &= \frac{4\pi}{3}R^3 \times \frac{4}{3}\sigma_{\rm T} c \times \frac{U_B}{2\nu_B} \times \sqrt{\frac{\nu}{\nu_B}} n_e\left(\sqrt{\frac{\nu}{\nu_B}}\right) \end{aligned} \tag{1.26}$$

[9] I assume here that the angular size of the emitting region is smaller than the inverse of the jet Lorentz factor.

where the transition from the first to the second line exploits the transformation of the Dirac function under a change of variable, i.e. $\delta(x)dx = \delta(h(x))h'(x)dx$.

I can apply the same procedure to the inverse Compton, assuming a Dirac distribution for the function g (this is a less common delta approximation which I use for the sake of clarity and ease of comprehension). Localizing analytically the maximum of g with its full expression in the Klein-Nishina regime is not straightforward and I use its simple expression in the Thomson regime, which peaks at $2\gamma^2\nu_0$, so that $g(\nu,\gamma,\nu_0) = \delta(\nu - 2\gamma^2\nu_0)$. Using Eq. (1.17) and Eq. (1.23), the inverse Compton luminosity in the delta approximation and assuming null optical depths is then:

$$\begin{aligned} L^{\delta}_{\rm IC}(\nu) &= \frac{4\pi}{3}R^3 \times \sigma_T R \times \frac{4}{3}\sigma_{\rm T} c \times U_B \times \int {\rm d}\gamma n_e(\gamma)\gamma^2 \int {\rm d}\nu_0 \delta(2\gamma^2\nu_0 - \nu) \times \\ &\qquad \int {\rm d}\gamma' n_e(\gamma')\gamma'^2 \delta(\gamma'^2\nu_B - \nu_0) \\ &= \frac{4\pi}{3}R^3 \times \sigma_T R \times \frac{4}{3}\sigma_{\rm T} c \times \frac{U_B}{4\nu_B} \times \int {\rm d}\gamma n_e(\gamma) \sqrt{\frac{\nu}{2\gamma^2\nu_B}} n_e\left(\sqrt{\frac{\nu}{2\gamma^2\nu_B}}\right) \\ &= \frac{\sigma_T R}{2} \int {\rm d}\gamma n_e(\gamma) L^{\delta}_{\rm sync}\left(\frac{\nu}{2\gamma^2}\right) \end{aligned} \tag{1.27}$$

I show in Eq. (1.27) that assuming an electron distribution function (EDF) peaking at $\bar{\gamma}$, $n_e(\gamma) = n_{e,0}\delta(\gamma - \bar{\gamma})$, the inverse Compton luminosity is simply the synchrotron luminosity, scaled up by a factor $n_{e,0}\sigma_T R/2$, and shifted to frequencies $2\bar{\gamma}^2$ times larger.

As shown in Sect. 1.2.1.2, a power-law EDF is expected from acceleration processes, which reads $n_e(\gamma) = n_{e,0}\gamma^{-p}$ for $\gamma \in [1;\gamma_{\rm max}]$. Then from Eq. (1.26):

$$\begin{aligned} L^{\delta}_{\rm sync}(\nu) &= \frac{4\pi}{3}R^3 \times \frac{4}{3}\sigma_{\rm T} c \times \frac{U_B}{2\nu_B} \times n_{e,0} \times \left(\frac{\nu}{\nu_B}\right)^{-\frac{p-1}{2}} \quad \text{for } \nu \in [\nu_B; \gamma^2_{\rm max}\nu_B] \\ &\propto n_{e,0} \times R^3 \times B^{\frac{p+1}{2}} \times \nu^{-\frac{p-1}{2}} \end{aligned} \tag{1.28}$$

And using Eq. (1.27)

$$L^{\delta}_{\rm IC}(\nu) = \frac{\sigma_T R}{2} \times \frac{4\pi}{3} R^3 \times \frac{4}{3}\sigma_{\rm T} c \times \frac{U_B}{2\nu_B} \times n^2_{e,0} \times \left(\frac{\nu}{2\nu_B}\right)^{-\frac{p-1}{2}} \times \int_{\max\left(1, \frac{1}{\gamma_{\max}}\sqrt{\frac{\nu}{2\nu_B}}\right)}^{\min\left(\gamma_{\max}, \sqrt{\frac{\nu}{2\nu_B}}\right)} \frac{{\rm d}\gamma}{\gamma}$$

$$\propto n^2_{e,0} \times R^4 \times B^{\frac{p+1}{2}} \times \nu^{-\frac{p-1}{2}} \tag{1.29}$$

Eq. (1.29) and Eq. (1.28) show that, for an EDF index p, the observed luminosity is a power law of index $(p-1)/2$. This can be seen on the spectral energy distribution (SED) shown in Fig. 8, for an EDF index $p = 2$. By convention, the luminosity multiplied by the frequency (or equivalently the energy) is plotted as a function of the energy, so that the integral below the curve per logarithmic energy increment is the integrated luminosity ($\int {\rm d}\nu\ L(\nu) = \int {\rm d}\ln\nu\ \nu L(\nu)$). The synchrotron emission extends from radio to X rays and the γ-ray luminosity originates from inverse Compton scattering. Depending on the location of the peak of their synchrotron emission, blazars are usually divided in low, intermediate and high synchrotron peaked objects (LSP, ISP and HSP, with frontiers typically at 10^{14} and 10^{15} Hz). The denomination LBL, IBL and HBL is also usually employed for the specific case of BL Lac objects.

The dependence of the SSC luminosity on the magnetic field $\propto B^{\frac{p+1}{2}}$ can be used to constrain the energy budget necessary to produce a synchrotron luminosity $\mathcal{L}_{\rm sync} = \int_{\nu_1}^{\nu_2} {\rm d}\nu L_{\rm sync}(\nu)$, measured in the frequency band $[\nu_1, \nu_2]$. The parent electrons are distributed between $\gamma_1 = \sqrt{\nu_1/\nu_B}$ and $\gamma_2 = \sqrt{\nu_2/\nu_B}$, as in Eq. (1.26), and assuming for simplicity a purely leptonic jet, the energy in matter is:

$$U_e = m_e c^2 \int_{\gamma_1}^{\gamma_2} d\gamma n_e(\gamma)\gamma \propto n_{e,0} \left[\left(\frac{\nu}{\nu_B}\right)^{\frac{2-p}{2}}\right]_{\nu_1}^{\nu_2} \propto n_{e,0} B^{\frac{p-2}{2}} \tag{1.30}$$

The total energy density is then $U_{\rm tot} = U_e + U_B$, where $U_B \propto B^2$ is the magnetic energy density. Instead of following the sometimes fuzzy textbook approach, I derive the minimum energy budget with the technique of the Lagrange multiplier (called here λ), imposing the

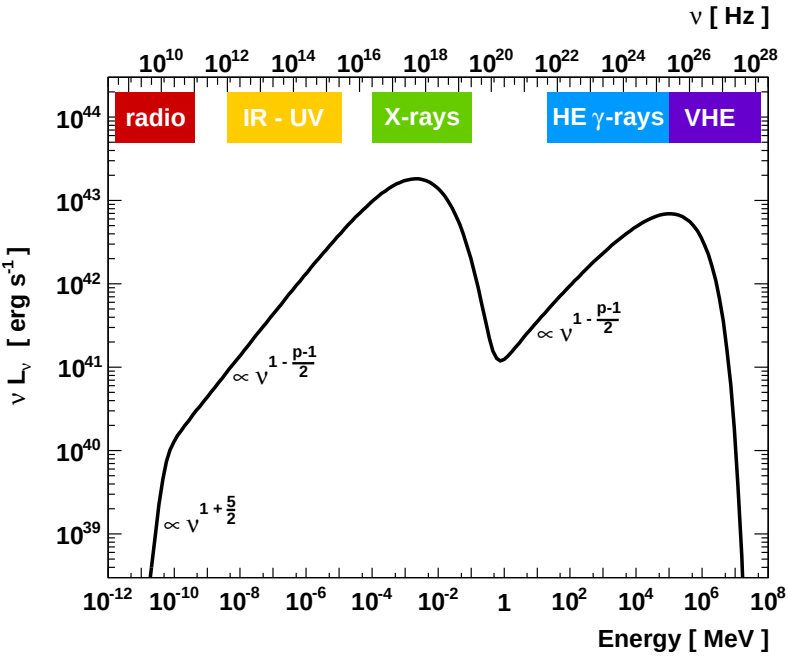

FIGURE 8. SED of an emitting region within an SSC model, for an HBL with a synchrotron emission (low-energy bump) peaking in X rays. The break in the radio wavelengths is due to synchrotron self absorption. The high-energy bump comes from inverse-Compton scattering off the synchrotron photon field.

constraint of a fixed observed luminosity $\mathcal{L}_{\rm sync,0}$. The quantity to minimize is then:

$$U_{\rm tot}(n_{e,0}, B) = U_e + U_B - \lambda\,(\mathcal{L}_{\rm sync} - \mathcal{L}_{\rm sync,0}) \tag{1.31}$$

where the relevant parameters are the magnetic field and the EDF normalisation, which is proportional to the density of electrons for a fixed index. The minimization as a function of λ, $\partial U_{\rm tot}/\partial\lambda = 0$, naturally yields a luminosity equal to the observed luminosity $\mathcal{L}_{\rm sync} = \mathcal{L}_{\rm sync,0}$. The minimization as a function of the two other parameters yields,

using Eq. (1.28):

$$0 = \frac{\partial U_{\rm tot}}{\partial B}(n_{e,0}, B) = \frac{p-2}{2} \times \frac{U_e}{B} + 2 \times \frac{U_B}{B} - \lambda \frac{p+1}{2} \frac{\mathcal{L}_{\rm sync}}{B}$$
$$0 = \frac{\partial U_{\rm tot}}{\partial n_{e,0}}(n_{e,0}, B) = \frac{U_e}{n_{e,0}} - \lambda \frac{\mathcal{L}_{\rm sync}}{n_{e,0}}$$

i.e., extracting the Lagrange multiplier from the second equation and injecting in the first:

$$U_e = \frac{4}{3} U_B \tag{1.32}$$

which corresponds to a quasi equipartition between the energy in matter and in the magnetic field. Note that if I had used a fixed inverse Compton luminosity ($\propto n_{e,0}^2$), the equation would depend on the index of the EDF, but the proportionality coefficient would remain close to unity. A minimum energy budget thus imposes a rough equality of the matter energy and of the magnetic field energy, a condition which is, surprisingly, violated in blazars as briefly discussed in Chapter 2.3.2.2.

1.3. Observing blazars at high and very high energies

γ rays are the preferential messengers of the non-thermal Universe. Unlike charged particles, they are not deviated by intergalactic magnetic fields, whatever their energy, and unlike neutrinos their interaction with matter allows a large number of them to be detected on Earth or in space, as discussed in Sect. 1.3.1. γ-ray astronomy is nonetheless limited by a horizon, set by the extragalactic background light, which the messengers interact with. The problem can actually be reversed and one can use γ rays to probe this diffuse cosmological component, otherwise difficult to measure, as discussed in Sect. 1.3.2.

1.3.1. γ-ray astronomy in space and on Earth

I focus in the following on the emission of AGN at high (HE, 20 MeV $< E <$ 100 GeV) and very high energy (VHE, 100 GeV $< E <$ 100 TeV).

1.3.1.1. *Principles*

The detection of γ rays in space is based on pair conversion, which is the dominant interaction process of a photon with matter above the MeV energy scale. Satellites like the Large Area Telescope of *Fermi*

(*Fermi*-LAT) are based on three sub-detectors: a tracker, an electromagnetic calorimeter (ECAL), and an anti-coincidence dome (ACD), as shown in Fig. 9.

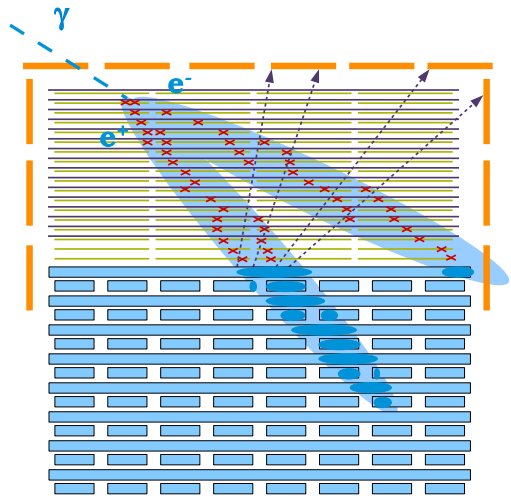

FIGURE 9. Schematic view of a pair-conversion satellite like *Fermi*-LAT. A segmented anti-coincidence dome (ACD, in orange) shields the detector from charged particles. A γ ray passes through the ACD and creates an electron-positron pair in the conversion layers (thin purple lines) of the tracker. The showers leave hits (red crosses) in the active layers (in yellow) of the tracker and deposit part of their energy in the crystals of the electromagnetic calorimeter (ECAL, in blue). Charged particles (dashed purple arrows) can "back-splash" when the shower enters the ECAL, triggering the ACD.

The ACD is a segmented plastic scintillator that sends a veto when a charged particle passes through. It enables a reduction of the background of protons and electrons typically by a factor of 10^3. The segmentation of the ACD, combined with the tracker information, enables

the identification of the outgoing charged particles and avoids a systematic veto which would reduce the trigger rate if the ACD was monolithic. The tracker is made of an active material, typically silicon, and a high Z conversion material (e.g. lead or tungsten) which initiates the shower development and, above all, provides the direction of the incident particle. The ECAL ($\lesssim 10X_0$, where X_0 is the radiation length) is made of crystals, typically CsI or NaI, that convert the energy of the ionising shower into optical light, which the crystal mildly absorbs. To convert this light into an electrical signal, photo-diodes based on semi-conductors are employed.

Space-based γ-ray detectors can achieve an effective area on the order of a square meter in the HE band and cover a large fraction of the sky (1/5 for *Fermi*-LAT) with a duty cycle of almost 100%. At the high-energy limit of HE band, the showers are less and less contained in the ECAL and the bandwidth of the detector is increasingly saturated, implying a drastic reduction of the energy and angular resolution. Moreover, with astrophysical fluxes decreasing as power laws, large effective areas are needed to collect a significant amount of events. For example, considering the reasonably bright source PKS 2155-304 studied in Aharonian et al. (2009), one gets an HE photon rate above 200 MeV of 4 $\mathrm{m}^{-2}\ \mathrm{h}^{-1}$ and a VHE photon rate above 200 GeV of $2 \times 10^{-3}\ \mathrm{m}^{-2}\ \mathrm{h}^{-1}$. Practically speaking, the cost and logistics of launching a detector with a collection area of more than about 1 m^2 are prohibitive. So, although space-based detectors are sensitive enough to detect sources (a handful of events per hours), as we go to higher energies, a large collection area, only achievable on Earth, is necessary in order to compensate for the rapidly falling source spectra.

This can be done using the atmosphere as a calorimeter. Indeed, though less dense than the crystals of pair-conversion satellite, the atmosphere represents a total of $\sim 20X_0$. VHE γ rays initiate atmospheric electromagnetic showers typically 20 km above sea level. An electromagnetic shower is composed of γ rays that create pairs of electron/positrons. These leptons lose energy, emitting bremsstrahlung photons, down to the critical energy of 83 MeV (in air), where ionization losses become dominant. This avalanche is almost axisymmetric for electromagnetic processes. On the contrary, hadronic showers are

composed of nuclear fragments, nucleons, mesons (π and K), electromagnetic sub-showers (coming from $\pi^0 \rightarrow \gamma\gamma$), muons and neutrinos that can carry a large transverse momentum. These showers have irregular shapes, which can be discriminated from γ-induced showers with imaging instruments.

This imaging can be performed using the Cherenkov radiation emitted by the charged particles of the shower. This radiation is emitted inside a dielectric medium traversed by a particle moving faster than the local speed of light c/n, where n is the refractive index of the medium, and is beamed on a cone of angle θ, with $\cos\theta = 1/n$. The atmosphere absorbs this radiation below 300 nm, but above, a light pool of blue light (differential Cherenkov spectrum $\propto \lambda^{-2}$) illuminates for a few nanoseconds a circular area of $\sim 10^5$ m^2 on the ground. Cherenkov light thus tracks back the shower development in a natural calorimeter, the atmosphere.

Using a reflector, one can focus the image of the shower onto a fast camera. The nano-second resolution avoids contamination from the night sky background, which typically accounts for 10^8 photoelectrons per second per pixel, for an experiment such as H.E.S.S. (Funk et al. 2004). The trigger energy threshold of imaging atmospheric Cherenkov telescopes (IACTs), defined at the maximum of the trigger rate[10], is around 100 GeV, depending on the observational conditions and the source spectrum. For example, at large zenith angles, the showers are observed through a large atmospheric column depth, which absorbs part of the Cherenkov light and increases the energy threshold. In the focal plane of the telescope, the Cherenkov emission can be represented as an ellipse for an electromagnetic shower, as shown in Fig. 10. The reconstruction of the major axis of the ellipse only locates the shower in a 2D plane (the actual direction corresponds to a single point on this axis) and stereoscopy helps to break the degeneracy by intersecting planes from different viewing angles (right panel on Fig. 10). For a set of observational parameters (impact parameter of the shower, zenith angle, optical efficiency, off-axis angle), the cumulated charge within the ellipse can be converted into an equivalent energy of the primary using look-up tables that are based on simulations of the shower development and of the instrument. The effective area covered with this

[10]Note that the analysis energy threshold, defined at a given percentage of the nominal acceptance, is larger than the trigger threshold by a factor of ~ 2.

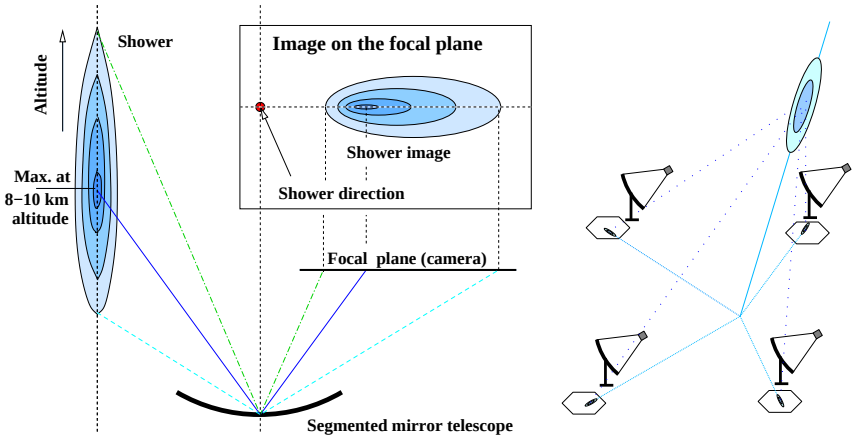

FIGURE 10. *Left panel*: Imaging of an atmospheric shower. In the focal plane, the shower direction corresponds to the red point shown on the major axis of the ellipse. Single-telescope observations only enable the reconstruction of this axis in the camera frame, i.e. of a plane containing the direction of the shower in the atmosphere. *Extracted from Völk & Bernlöhr (2009). Right panel*: Schematic representation of the stereoscopic technique: the intersection of the planes containing the shower enables the reconstruction of its direction.

technique is on the order of the size of the Cherenkov light pool on the ground ($\sim 10^5$ m^2). The telescopes have, nonetheless, a limited field of view (a few degrees) and have access to less than half of the sky, in contrast with space-based detectors. The duty cycle of IACT is relatively low ($\sim 10\%$) as they can operate only on clear moonless nights.

1.3.1.2. *From SAS 2 and Whipple to Fermi-LAT and H.E.S.S.*

One could consider that the birth of γ-ray astronomy coincides with the launch of the small astronomy satellite 2 (SAS-2) and the start of operation of the Whipple observatory in the beginning of the '70s. SAS-2 detected the first sources of γ rays at tens of MeV, coincident with

galactic pulsars (the Crab, Vela and Geminga). After twenty years of operation, the use of imaging allowed the Whipple γ-ray telescope to detect the Crab Nebula at TeV energies (Weekes et al. 1989). By that time, Europe had stepped into the field with the launch of the COS-B satellite, which revealed 25 sources in the first map of the galactic plane, as well as the first extragalactic source of γ rays: the very 3C 273 that triggered the creation of the first Texas Symposium.

SAS-2 and COS-B were mostly based on spark-chamber technology. EGRET, on board the Compton gamma-ray observatory (CGRO), was moreover constituted of an electromagnetic calorimeter (in NaI) of $8X_0$. During its ten years of operation, EGRET detected hundreds of sources, with at least 66 of them identified at a high confidence level as AGN (Hartman et al. 1999). 1992 is a particularly important year for both space and terrestrial extragalactic γ-ray astronomy, with the discovery by EGRET of 3C 279 at HE (Hartman et al. 1992) and the discovery at VHE of Mrk 421 with the Whipple telescope (Punch et al. 1992). The '90s also saw the advent of the second generation γ-ray observatories with experiments such as HEGRA (Daum et al. 1997), a pioneer of stereoscopy, and CAT (Barrau et al. 1998), a pioneer of fast and finely pixelated cameras. One should also cite other Cherenkov experiments such as the Telescope Array, CANGAROO, the Crimean Observatory and the Durham mark 6 (Yamamoto et al. 1999; Enomoto et al. 2002; Stepanian et al. 1982; Armstrong et al. 1999), all of whom contributed to the establishment of the field.

The third-generation satellites and Cherenkov telescopes emerged in the second part of the '2000s, leaving an observational gap, initially supposed to be filled with AGILE, which was eventually launched in 2007. *Fermi*-LAT, launched one year later, is equipped with similar technology, i.e. silicon tracker and crystal electromagnetic calorimeter, but has a sensitivity almost ten times larger than AGILE. In its second catalogue, *Fermi*-LAT announced almost 2000 sources, more than half of them being AGN (Nolan et al. 2012). The characteristics of the past and present γ-ray satellites are shown in Table 3. The third generation IACTs are represented by H.E.S.S., MAGIC and VERITAS, who are the current main actors of VHE γ-ray astronomy. They have detected, as of September 2012, about 150 VHE sources[11], 50 of them being AGN, as shown in Table 4. One could be surprised that the HE sky is

[11] http://tevcat.uchicago.edu/

Mission	Launch	Life time [years]	Area [m^2]	Energy range [GeV]	Detections
SAS-2	1972	0.6	0.064	0.02 – 0.3	3
COS-B	1975	7	0.005	0.03 – 3	25 (1 AGN: 3C 273)
EGRET	1991	9	0.15	0.02 – 30	~ 270 ($\gtrsim 65$ AGN)
AGILE	2007	> 5	0.15	0.03 – 50	$\gtrsim 50$ ($\gtrsim 15$ AGN)
Fermi-LAT	2008	> 4	1.0	0.02 – 300	$\gtrsim 1900$ ($\gtrsim 1100$ AGN)

TABLE 3. Comparison of the past and current HE γ-ray satellites. The first, second and third columns give the name of the on-board experiments and the year when the satellite was launched, as well as the duration of operation. The fourth and fifth columns give the maximum effective area and the energy range covered. The last column shows the number of sources detected.

IACT	Start	Life time years	$A_{\rm tel}$ [m^2]	$N_{\rm tel}$	$N_{\rm pix/tel}$	FoV [deg]	$E_{\rm th}$ [GeV]	Detections
Whipple	1968	~ 30	75	1	379	2.3	300	10 (5 AGN)
HEGRA	1992	10	9	5	271	4.3	500	9 (5 AGN)
CAT	1996	5	18	1	600	4.8	250	4 (3 AGN)
H.E.S.S.	2003	> 9	107	4	960	5.0	100	$\gtrsim 100$ ($\gtrsim 20$)
MAGIC	2004	> 8	234	2	574	3.5	60	$\gtrsim 40$ ($\gtrsim 25$)
VERITAS	2007	> 5	106	4	499	3.5	100	$\gtrsim 35$ ($\gtrsim 20$)

TABLE 4. Comparison of past and current IACT. The first, second and third columns give the name of the experiment, the year when the arrays started operation and the life time of the experiment. The fifth and fourth columns show the number of telescopes and the area of individual telescopes. The sixth and seventh columns give the number of pixel and the field of view of the cameras. The last columns gives the threshold energy of the arrays and the number of sources detected.

mostly populated with AGN while the VHE sky does not seem to be. Sky surveys performed by satellites are complete, in the sense that the whole sky is covered with a similar exposure, while the observations of the VHE sky are pointed toward probable sources. Because of its location near the tropic of Capricorn, H.E.S.S. can survey the galactic plane (e.g. Aharonian et al. 2006a) and thus has observed almost two

thirds of the known VHE emitters. If only MAGIC or VERITAS were operating, one can see from Table 4 that the fraction of AGN among the detected sources would be similar at HE and VHE.

1.3.2. Universe transparency to γ rays

Photons may be the best astronomical messengers because they are not deviated by magnetic fields and because they do not have extremely small interaction cross sections, which enables their detection. These interactions are, nonetheless, responsible for the existence of a horizon, i.e. a maximum observational distance or look-back time, for γ-ray astronomy. Even though such high-energy photons had not been observed by then, it was realized in the '60s that the pair-creation process is responsible for the absorption of γ rays along their propagation on cosmological distances (Nikishov 1962; Jelley 1966; Gould & Schréder 1967). Assuming an isotropic target photon field, the cross section peaks when the product of the energy of the γ ray, E, and of the target photon, ϵ, equals $(2m_e c^2)^2 \sim 1\ \mathrm{MeV}^2$ (see e.g. Herterich 1974; Aharonian & Neronov 2005). Thus a γ ray of $E = 1$ TeV preferentially interacts with a photon of energy $\epsilon = 1$ eV, i.e. of wavelength $\lambda = hc/\epsilon \sim 2\pi \times 0.197 \times (\epsilon/1\ \mathrm{eV})^{-1} \sim 1.2\mu\mathrm{m} \times (\epsilon/1\ \mathrm{eV})^{-1}$.

The relevant target photon field at these wavelengths is the diffuse electromagnetic component of the Universe second only to the cosmic microwave background (CMB) in intensity. This is called the extragalactic background light (EBL). The first component of the EBL is the cosmic optical background (COB), which is the integrated optical emission from stars and galaxies since the end of the dark ages. The second component is the cosmic infrared background (CIB) and consists of the UV-optical light reprocessed by dust in the IR band. The total brightness of these components ($I = \int \mathrm{d}\lambda\ I_\lambda = \int \mathrm{d}\ln\lambda\ \lambda I_\lambda$) can be estimated to $\sim 5\%$ of the brightness of the CMB (cf. boxes in Fig. 11), but precise measurements remain difficult.

1.3.2.1. *EBL optical depth*

Calling $n(\epsilon, z)$ the density of photons at the redshift z and at the energy ϵ per energy band ($\int \mathrm{d}\epsilon\ n(\epsilon, z)$ is a number of photons per unit volume), the absorption of γ rays of observed energy E emitted by a

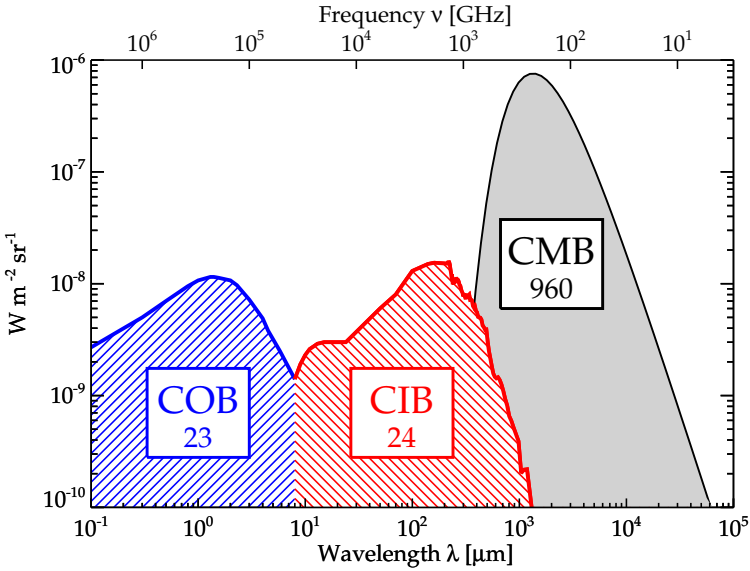

FIGURE 11. Schematic spectral energy distribution of the most intense electromagnetic cosmic backgrounds, extracted from Dole et al. (2006a). An estimation of the approximate brightness of the two components of the EBL, the cosmic optical background (COB) and the cosmic infrared background (CIB), are given in the boxes in nW m^{-2} sr^{-1}.

source at a redshift z is characterized by the optical depth:

(1.33)
$$\tau\,(E,z) = \int_0^z \mathrm{d}z' \frac{\mathrm{d}l}{\mathrm{d}z}(z') \int_0^{+\infty} \mathrm{d}\epsilon\, n(\epsilon,z') \int_{-1}^{1} \mathrm{d}\mu \frac{1-\mu}{2} \sigma_{ee}(\epsilon, E\times(1+z'), \mu)$$

In Eq. (1.33), the distance L is cosmological, hence the integration over redshift where

(1.34)
$$\frac{\mathrm{d}l}{\mathrm{d}z}(z) = \frac{c}{H_0(1+z)} \frac{1}{\sqrt{\Omega_\Lambda + \Omega_m (1+z)^3}}$$

for a flat Universe, i.e. a Universe where the sum of matter and dark energy density is unity, $\Omega_m + \Omega_\Lambda = 1$. The second integration is performed over the energy of the target photons at the redshift z' and the last integration is performed in the centre-of-mass frame over the angle

θ between the target photon and the γ ray that had, at this epoch, an energy $E \times (1+z')$, using $\mu = \cos\theta$. The pair-creation cross section is given by Bethe and Heitler:

(1.35)

$$\sigma_{ee}(\epsilon_1, \epsilon_2, \mu) = \frac{3}{16}\sigma_{\rm T}(1-\beta^2)\left[2\beta(\beta^2-2) + (3-\beta^4)\ln\left(\frac{1+\beta}{1-\beta}\right)\right]\Theta(\epsilon-\epsilon_{\rm th})$$

where Θ is the Heaviside function, $\epsilon_{\rm th} = 2m_e^2c^4/(1-\mu)\epsilon_2$ is the threshold energy and $\beta^2 = 1-\epsilon_{\rm th}/\epsilon_1$.

The less constrained term in Eq. (1.33) is the density of EBL photons, which relies on a modelling of the emission of optical light throughout the cosmic history. Assuming this quantity known, a fraction $\exp(-\tau(E,z))$ of the flux is "absorbed". I show in Fig. 12 the lines of iso-absorption in the plane redshift versus γ-ray energy within the modelling of Franceschini et al. (2008) (FR08 hereafter), which is representative of the state of the art of EBL modelling, as discussed in Sect. 1.3.2.2.

The most distant blazars detected so far at VHE (such as 3C 279, PG 1553+113 or KUV 00311-1938) are presumably located at redshifts of $z \geq 0.5$ and one can notice that their differential flux at 1 TeV is dramatically reduced (by a factor $\gtrsim 500$) in comparison to the intrinsic emission. For $z = 0.1$, the average redshift of the currently detected VHE blazars, the optical depth is equal to one at an energy of ~ 1 TeV. An inflection in the absorption can be seen between $\sim$ 1 TeV and ~ 5 TeV. This is due to the fast decrease of the target optical photons between ~ 1 μm and ~ 5 μm, as shown in Fig. 11. Above ~ 5 TeV, the increasing contribution of the CIB results in a shortening of the γ-ray horizon or, equivalently, in a sharp cut off of the γ-ray flux.

1.3.2.2. *EBL modelling*

Modelling the EBL photon density $n(\epsilon, z)$ is a complex task, and an excellent review of the various approaches and of the constraints can be found in Hauser & Dwek (2001).

Backward-evolution models exploit the local population of galaxies and extrapolate their emission to higher redshift with an empirical $(1+z)^\gamma$ dependence of the luminosity for the various types of sources. The model of FR08 is a good representation of the state of the art of such methods. These authors used the information from surveys carried out by ground-based observatories in optical and near-IR wavelengths

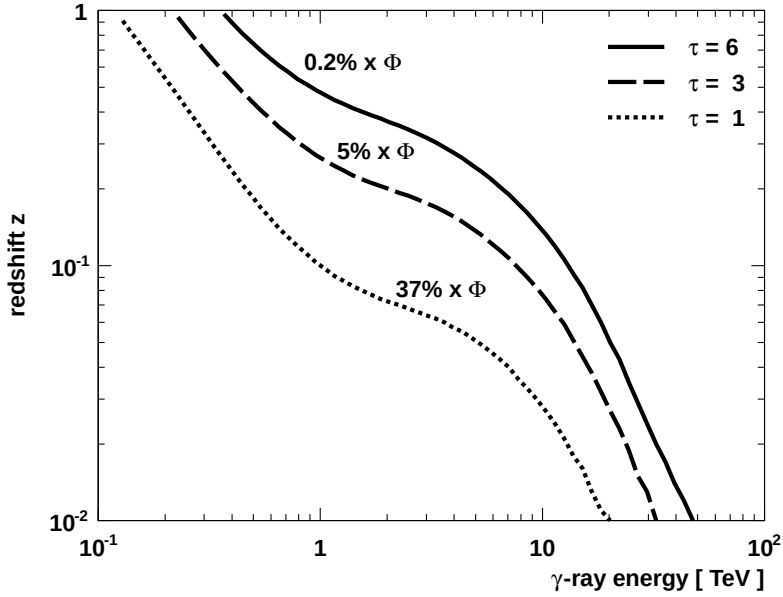

FIGURE 12. Horizon of the γ-ray Universe for the modelling of FR08. The contours $\tau = 1, 3, 6$ are shown in the plane of redshift versus γ-ray energy. They correspond to an absorption of 63%, 95% and 99.8% of the flux.

as well as data from the space telescopes HST, ISO and Spitzer to derive a minimal level of EBL photons.

Forward-evolution models rely on large libraries of astronomical data. The SED of galaxies are fitted at various epochs and their cumulative spectral contribution to the EBL is thus computed. The model of Domínguez et al. (2011), exploiting a survey of 6000 galaxies from $z = 0.2$ to $z = 1$, is a recent example of these approaches. The propagation of the uncertainty in the SEDs of the observed galaxies allowed a 1σ confidence band on the EBL density to be derived by these authors.

Semi-analytical models may be the most challenging class regarding the computational effort. The formation of structures, e.g. within a ΛCDM cosmology, is simulated and outputs, such as the star formation rate density or the evolution of the luminosity density vs redshift, can be compared to the observational constraints. The most recent

contribution of the group of Primack to this class of models can be found in Gilmore et al. (2012), where the five year release of WMAP results is used.

The present, i.e. $z = 0$, EBL SEDs derived with these different types of models are compared in Fig. 13, extracted from Gilmore et al. (2012), where I add the model of FR08 as a solid light blue line. Though the methods are fundamentally different, the models of the COB derived by these groups are in close agreement between 0.5 μm and 10 μm ($=10^5$Å). For the CIB, an uncertainty of a factor ~ 3 on the peak amplitude remains between the lower and upper models.

1.3.2.3. *Direct measurements, Galaxy counts and constraints from γ rays*

The satellite COBE is well known for its instruments DMR (differential microwave radiometer) and FIRAS (far infra red absolute spectrometer) which revealed the detailed map and the beautiful blackbody spectrum of the CMB. The third instrument DIRBE (diffuse infrared background experiment) may be less known but it was designed to probe the EBL between 1.25 and 240 μm (Hauser & Dwek 2001). Unfortunately, direct measurements can be contaminated by foregrounds, e.g. by the zodiacal light or by the galactic light, which results in an overestimation of the diffuse background. Other constraints must thus be found to derive more than an upper limit on the COB intensity.

Strict lower limits can be derived from integrated galaxy counts (see, e.g., Madau & Pozzetti 2000; Fazio et al. 2004; Dole et al. 2006b, for more details). The idea is to cumulate the brightness of galaxies and to correct for the low-luminosity sources missing from the survey. The lower limits derived from source counts in the near IR domain can be down to one order of magnitude below the limits from direct measurements .

Strong constraints on the EBL density have also been derived using extragalactic γ-ray sources. The main limitation so far is in the knowledge of the intrinsic VHE spectrum, i.e. the spectrum emitted by the source before absorption. Indeed, in principle, if one perfectly knew the observed and the emitted spectra, one could reconstruct the amount of absorption in between and thus derive the density of targets. But the intrinsic spectrum varies from one source to another, and, often, over time for individual sources, so strong hypotheses must be made. Assuming that the intrinsic photon index can not be harder than 1.5

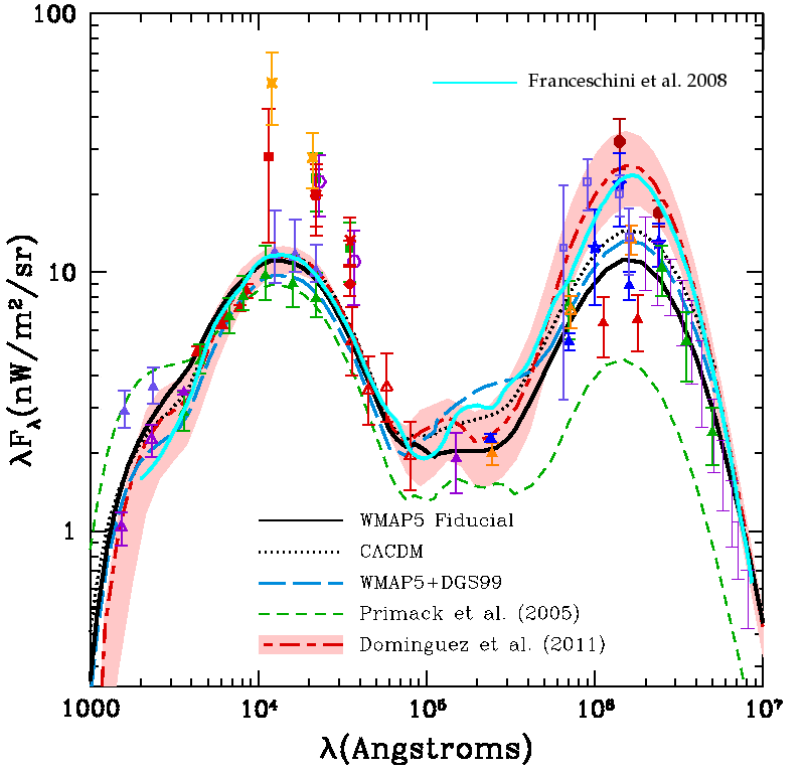

FIGURE 13. Models of the present EBL Spectral Energy Distribution. The first four models described in the legend are semi-analytical models. The forward evolution model of Domínguez et al. (2011) and the associated uncertainties are shown with the dashed red line and the filled area. The backward evolution model of FR08 is added as a solid light blue line. *Adapted from Gilmore et al. (2012).*

(corresponding to the canonical EDF index of $p = 2$), stringent upper limits on the EBL opacity to γ rays have been derived by Aharonian et al. (e.g. 2006b); Mazin & Raue (e.g. 2007). More recently, studies exploiting the *Fermi*-LAT measurements as templates for the intrinsic spectrum have been performed (Georganopoulos et al. 2010; Orr

et al. 2011; Meyer et al. 2012). Current models of the EBL are in close agreement with these limits and converge on a peak value of the stellar component $\lambda F_\lambda \sim 12$ nW m^{-2} sr^{-1}, yielding a consistent value for the opacity to γ rays.

1.3.2.4. *Concluding remark*

I can not help but concluding this chapter with the almost prophetic statement of Gould & Schréder (1967) concerning the VHE constraints on the EBL.

"*Observations of cosmic photons in the region* 10^{12} *to* 10^{13} eV *would be of great value, since in this region absorption due to the cosmic optical photons is important. In fact, this may provide a means of determining the optical photon density and of testing cosmological models. The technique of observing shower Cherenkov radiation would probably be most useful here; however, apparently it can only be used to determine high-energy photon fluxes from discrete sources. Some slight indications that quasars may be such sources has come from observations* [...]".

I discuss in Chapter 2 the detections at VHE of these "quasars" that are now known as AGN and I focus in particular on the contribution of H.E.S.S. to this field. I then overcome the limitations of the methods employed so far at VHE to constrain the EBL and perform the first VHE measurement of the COB, using H.E.S.S. data, i.e. "10^{12} to 10^{13} eV cosmic photons". I then focus in Chapter 4 on the intrinsic properties of AGN and mostly on the extreme variability seen in VHE blazars. Finally, I draw some perspectives on VHE astronomy of blazars in Chapter 5.

Bibliography

Aharonian, F., Akhperjanian, A. G., Anton, G., et al. 2009, ApJ, 696, L150

Aharonian, F., Akhperjanian, A. G., Bazer-Bachi, A. R., et al. 2006a, ApJ, 636, 777

Aharonian, F., Akhperjanian, A. G., Bazer-Bachi, A. R., et al. 2006b, Nature, 440, 1018

Aharonian, F. & Neronov, A. 2005, ApJ, 619, 306

Aharonian, F. A. 2000, New A, 5, 377

Antonucci, R. 1993, ARA&A, 31, 473

Antonucci, R. 2011, arXiv:1101.0837

Antonucci, R. R. J. & Miller, J. S. 1985, ApJ, 297, 621

Armstrong, P., Chadwick, P. M., Cottle, P. J., et al. 1999, Experimental Astronomy, 9, 51

Band, D. L. & Grindlay, J. E. 1985, ApJ, 298, 128

Barrau, A., Bazer-Bachi, R., Beyer, E., et al. 1998, Nuclear Instruments and Methods in Physics Research A, 416, 278

Begelman, M. C., Blandford, R. D., & Rees, M. J. 1984, Reviews of Modern Physics, 56, 255

Blandford, R. D. 2002, in Lighthouses of the Universe: The Most Luminous Celestial Objects and Their Use for Cosmology, ed. M. Gilfanov, R. Sunyeav, & E. Churazov, 381

Blandford, R. D. & Payne, D. G. 1982, MNRAS, 199, 883

Blandford, R. D. & Rees, M. J. 1974, MNRAS, 169, 395

Blandford, R. D. & Rees, M. J. 1978, in BL Lac Objects, ed. A. M. Wolfe, 328–341

Blandford, R. D. & Znajek, R. L. 1977, MNRAS, 179, 433

Bowyer, C. S., Lampton, M., Mack, J., & de Mendonca, F. 1970, ApJ, 161, L1

Burbidge, G. R. & Burbidge, E. M. 1967, Quasi-stellar objects

Cerruti, M., Zech, A., Boisson, C., & Inoue, S. 2012, arXiv:1210.5024

Cohen, M. H., Cannon, W., Purcell, G. H., et al. 1971, ApJ, 170, 207
Coppi, P. S. & Blandford, R. D. 1990, MNRAS, 245, 453
Daum, A., Hermann, G., Hess, M., et al. 1997, Astroparticle Physics, 8, 1
De Villiers, J.-P., Hawley, J. F., Krolik, J. H., & Hirose, S. 2005, ApJ, 620, 878
Dermer, C. D. & Schlickeiser, R. 1993, ApJ, 416, 458
Doeleman, S. S., Fish, V. L., Schenck, D. E., et al. 2012, Science
Dole, H., Lagache, G., Puget, J.-L., et al. 2006a, å, 451, 417
Dole, H., Lagache, G., Puget, J.-L., et al. 2006b, A&A, 451, 417
Domínguez, A., Primack, J. R., Rosario, D. J., et al. 2011, MNRAS, 410, 2556
Drake, J. F., Swisdak, M., Che, H., & Shay, M. A. 2006, Nature, 443, 553
Drees, M. & Gerbier, G. 2012, arXiv:1204.2373
Drury, L. O. 1983, Reports on Progress in Physics, 46, 973
Drury, L. O. 2012, MNRAS, 422, 2474
Drury, L. O., Duffy, P., Eichler, D., & Mastichiadis, A. 1999, A&A, 347, 370
Enomoto, R., Hara, S., Asahara, A., et al. 2002, Astroparticle Physics, 16, 235
Fanaroff, B. L. & Riley, J. M. 1974, MNRAS, 167, 31P
Fazio, G. G., Ashby, M. L. N., Barmby, P., et al. 2004, ApJS, 154, 39
Fermi, E. 1949, Physical Review, 75, 1169
Fermi, E. 1954, ApJ, 119, 1
Ferrari, A. 1998, ARA&A, 36, 539
Franceschini, A., Rodighiero, G., & Vaccari, M. 2008, A&A, 487, 837
Friedman, H. & Byram, E. T. 1967, Science, 158, 257
Funk, S., Hermann, G., Hinton, J., et al. 2004, Astroparticle Physics, 22, 285
Georganopoulos, M., Finke, J. D., & Reyes, L. C. 2010, ApJ, 714, L157
Giacconi, R., Branduardi, G., Briel, U., et al. 1979, ApJ, 230, 540
Giannios, D. & Spruit, H. C. 2006, A&A, 450, 887
Gilmore, R. C., Somerville, R. S., Primack, J. R., & Domínguez, A. 2012, MNRAS, 422, 3189
Gould, R. J. 1979, A&A, 76, 306
Gould, R. J. & Schréder, G. P. 1967, Physical Review, 155, 1408
Greenstein, J. L. 1963, Nature, 197, 1041

Hartman, R. C., Bertsch, D. L., Bloom, S. D., et al. 1999, ApJS, 123, 79
Hartman, R. C., Bertsch, D. L., Fichtel, C. E., et al. 1992, ApJ, 385, L1
Hauser, M. G. & Dwek, E. 2001, ARA&A, 39, 249
Hazard, C., Mackey, M. B., & Shimmins, A. J. 1963, Nature, 197, 1037
Herterich, K. 1974, Nature, 250, 311
Hoyle, F. & Fowler, W. A. 1963, Nature, 197, 533
Jelley, J. V. 1966, Physical Review Letters, 16, 479
Jones, F. C. 1968, Physical Review, 167, 1159
Kataoka, J. 1999, PhD thesis, University of Tokyo
Kembhavi, A. K. & Narlikar, J. V. 1999, Quasars and active galactic nuclei : an introduction
Kerr, R. P. 1963, Physical Review Letters, 11, 237
Knödlseder, J., Jean, P., Lonjou, V., et al. 2005, A&A, 441, 513
Komissarov, S. S., Barkov, M. V., Vlahakis, N., & Königl, A. 2007, MNRAS, 380, 51
Krolik, J. H. 1999, Active galactic nuclei : from the central black hole to the galactic environment
Ledlow, M. J. & Owen, F. N. 1996, AJ, 112, 9
Lynden-Bell, D. 1969, Nature, 223, 690
Madau, P. & Pozzetti, L. 2000, MNRAS, 312, L9
Marscher, A. P. 2006, in American Institute of Physics Conference Series, Vol. 856, Relativistic Jets: The Common Physics of AGN, Microquasars, and Gamma-Ray Bursts, ed. P. A. Hughes & J. N. Bregman, 1–22
Mazin, D. & Raue, M. 2007, A&A, 471, 439
McKinney, J. C. & Gammie, C. F. 2004, ApJ, 611, 977
Meyer, M., Raue, M., Mazin, D., & Horns, D. 2012, arXiv:1202.2867
Mücke, A. & Protheroe, R. J. 2001, Astroparticle Physics, 15, 121
Nikishov, A. I. 1962, Soviet Physics JETP, 14, 393
Nolan, P. L., Abdo, A. A., Ackermann, M., et al. 2012, ApJS, 199, 31
Oke, J. B. 1963, Nature, 197, 1040
Orr, M. R., Krennrich, F., & Dwek, E. 2011, ApJ, 733, 77
Petrosian, V. 2012, Space Sci. Rev., 49
Pudritz, R. E., Hardcastle, M. J., & Gabuzda, D. C. 2012, Space Sci. Rev., 169, 27

Punch, M., Akerlof, C. W., Cawley, M. F., et al. 1992, Nature, 358, 477
Rees, M. J. 1966, Nature, 211, 468
Rees, M. J. 1978, The Observatory, 98, 210
Rees, M. J. 1984, ARA&A, 22, 471
Rowan-Robinson, M. 1977, ApJ, 213, 635
Rybicki, G. B. & Lightman, A. P. 1979, Radiative processes in astrophysics, ed. Rybicki, G. B. & Lightman, A. P.
Salpeter, E. E. 1964, ApJ, 140, 796
Sanchez, D. A. 2010, PhD thesis, École polytechnique
Schmidt, M. 1963, Nature, 197, 1040
Schmidt, M. 1990, The discovery of quasars, ed. B. Bertotti, R. Balbinot, & S. Bergia, 347
Schmitt, J. L. 1968, Nature, 218, 663
Schucking, E. L. 1989, Physics Today, 42, 46
Seyfert, C. K. 1943, ApJ, 97, 28
Shields, G. A. 1999, PASP, 111, 661
Sikora, M., Begelman, M. C., Madejski, G. M., & Lasota, J.-P. 2005, ApJ, 625, 72
Sikora, M., Begelman, M. C., & Rees, M. J. 1994, ApJ, 421, 153
Sironi, L. & Spitkovsky, A. 2009, ApJ, 707, L92
Spruit, H. C. 2010, in Lecture Notes in Physics, Berlin Springer Verlag, Vol. 794, Lecture Notes in Physics, Berlin Springer Verlag, ed. T. Belloni, 233
Stepanian, A. A., Fomin, V. P., Neshpor, Y. I., Vladimirsky, B. M., & Zyskin, Y. L. 1982, in Very High Energy Gamma Ray Astronomy, ed. P. V. Ramana Murthy & T. C. Weekes, 43
Su, M. & Finkbeiner, D. P. 2012, arXiv:1206.1616
Urry, C. M. & Padovani, P. 1995, PASP, 107, 803
Völk, H. J. & Bernlöhr, K. 2009, Experimental Astronomy, 25, 173
Weekes, T. C., Cawley, M. F., Fegan, D. J., et al. 1989, ApJ, 342, 379
Weniger, C. 2012, J. Cosmology Astropart. Phys., 8, 7
Whitney, A. R., Shapiro, I. I., Rogers, A. E. E., et al. 1971, Science, 173, 225
Wolfe, A. M., ed. 1978, Pittsburgh Conference on BL Lac Objects, University of Pittsburgh, Pittsburgh, Pa., April 24-26, 1978, Proceedings

Yamamoto, T., Chamoto, N., Chikawa, M., et al. 1999, in International Cosmic Ray Conference, Vol. 5, International Cosmic Ray Conference, 275
Zel'dovich, Y. B. 1964, Soviet Physics Doklady, 9, 195
Zenitani, S. & Hoshino, M. 2001, ApJ, 562, L63

CHAPTER 2

AGN targeted with H.E.S.S.

Although located in the southern hemisphere to observe the Galactic plane and its centre, H.E.S.S. dedicates more than 40% of its observation time to AGN, and in particular to blazars.

In this chapter, I briefly describe the H.E.S.S. array, which has now been operating for nearly ten years, and I expose the principles of the data analysis. After a discussion of the strategy for AGN observations and a highlight of the detections made by H.E.S.S., I analyse H.E.S.S. AGN observations that did not result in detections. I finally focus on 1ES 1312-423 and SHBL J001355.9-185406, two objects that are representative of the faintest blazars detected so far at VHE, with fluxes below a percent of the flux of the Crab Nebula at these energies.

2.1. Targeting AGN with H.E.S.S.

During the past ten years, the H.E.S.S. experiment, operated by a collaboration of 35 institutions from 12 countries across the world, has contributed significantly to revealing a VHE extragalactic sky dominated by AGN. I focus here on the H.E.S.S. capabilities and strategy in terms of AGN observations.

2.1.1. The H.E.S.S. experiment

The High Energy Stereoscopic System (H.E.S.S.) is an array of four Cherenkov telescopes located 1800 m above sea level in the Khomas Highland, Namibia (23°16'18" S, 16°30'01" E). The choice of this site was motivated by the quality of the sky in terms of "light pollution", the nearest city Windhoek being located 110 km away from the site, of cloud cover, typically below 20% eighty percent of the time, and of air pollution, mostly coming from aerosols, whose concentration is certainly reduced by the proximity of the ocean (see Louedec & Will 2012, for a discussion of these factors). The geographic area is in the well

of the south Atlantic anomaly, resulting in a low magnetic field[1] (total amplitude of ~ 0.3 G vs $\sim 0.4 - 0.5$ G for MAGIC and VERITAS.), that barely deviates the charged particles in the atmospheric showers and facilitates the reconstruction of the primary parameters.

2.1.1.1. *The* H.E.S.S. *array*

During its first phase, the H.E.S.S. array was composed of four telescopes, CT1, CT2, CT3 and CT4, placed at the four corners of a 120 m side square. This distance is an optimum between a large collection area and the coincident detection of events by several telescopes, limited by the size of the Cherenkov light pool from a shower. The second phase of H.E.S.S., H.E.S.S. II, has recently been inaugurated. The fifth larger telescope, CT5, can be seen under construction in Fig. 1. The expected impact on VHE astronomy of blazars is discussed in Chapter 5.1.1.

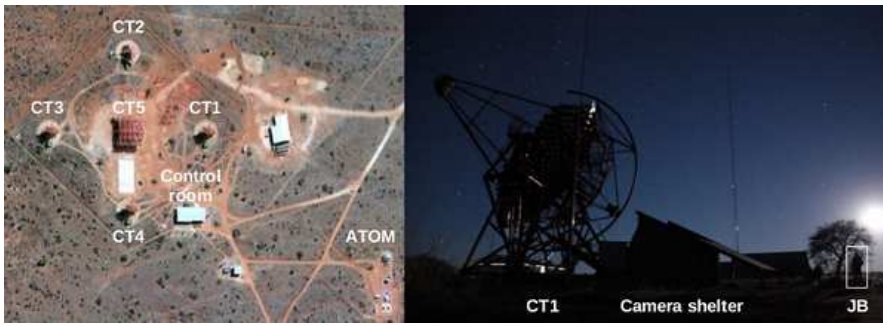

FIGURE 1. *Left panel*: Satellite view of the H.E.S.S. site, extracted from Google maps in September 2012. *Right panel*: Picture of CT1 and myself during a moon rise.

Each of the four telescopes of H.E.S.S. I consists of a 13 m diameter reflector and of a camera with fast electronics, mounted on a dish of steel, for an overall weight of ~ 60 t per telescope. An alt-azimuth mounting enables the telescopes to point toward any direction in the sky in less than 2 min with a positioning accuracy of ~ 30 arcsec.

[1]The amplitude of the magnetic field given here is just indicative, noting that only the transverse component plays a role.

The optical reflector of each telescope is composed of 380 mirror facets of 60 cm diameter (Bernlöhr et al. 2003), which are motorized with three actuators for the alignment (Cornils et al. 2003). The alignment procedure is performed by imaging stars with a CCD camera placed at the centre of the dish. Each mirror has a typical reflectivity of 70% and focuses the light on the camera placed at a focal distance $f = 15$ m. The arrangement of the mirrors on a spherical surface of radius f (Davies-Cotton mounting) reduces the geometrical aberrations (e.g. coma aberration), at the price of anisochronism of the arrival time on the focal point of an initially plane wave (typical deviation of 1.4 ns).

The large field of view of 5° in diameter seen by the cameras allows the showers, which typically cover 1 to 2° in the sky, to be fully contained in the focal plane. Each camera (1.6 m diameter, 1.5 m depth, $\sim$ 0.9 t) is composed of 960 pixels, the photomultipliers (PM), that observe 0.16° of the sky, providing fine imaging of the showers. Winston cones are placed in front of each PM to reduce the dead space, maximizing the light collection, and to limit the solid angle covered by each pixel (reducing e.g. the albedo light). A flat-fielding LED and a diffuser are placed at the centre of the dish to cross calibrate the response of the PMs and of the Winston cones.

In addition to the H.E.S.S. telescopes, several instruments of smaller scale are present on site. The atmospheric monitoring equipment includes one radiometer per telescope, a scanning radiometer and a weather station. LEDs are installed 30 km away from the site and 500 m higher in altitude (on the Gamsberg mountain). These systems monitor the wind speed, the cloud coverage, the temperature and pressure of the atmosphere. A LIDAR measures the concentration of aerosols as a function of altitude. This information is currently only used for data selection. The Automatic Telescope for Optical Monitoring (ATOM, Hauser et al. 2004) also operates on site, as shown in Fig. 1. ATOM monitors the sky in the B and R bands and is used to trigger H.E.S.S. observations of blazars when they are brighter at optical wavelengths.

2.1.1.2. *Data acquisition and calibration*

The electronics of the cameras is housed in 60 drawers, which are clusters of 16 PMs (Vincent et al. 2003), this modular design easing maintenance operations. For each drawer, a dedicated slow-control card monitors the temperature, controls the high voltage and sets the

trigger threshold of the PMs. The signal from each PM is sent to low gain and high gain channels that amplify the signals spanning 1-150 photoelectrons (p.e.) and 20-2000 p.e, respectively. These two amplification channels send the signals to an analogic ring sampler (ARS) that can store a total of 16 signals of 16 ns, with a 1 ns sampling rate. A third channel is dedicated to the trigger system which identifies shower-like signatures in the camera, thus reducing the false-detection rate. When triggering, the signal of the ARS is converted by an analogic to digital convertor (ADC) and is transmitted to the central unit of the camera.

At the level of the cameras, the trigger is based on correlating the signal from neighbouring PMs. A minimum signal of 4 p.e. in at least 3 nearby PMs within 1.3 ns enables the rejection of the noise arising from the night sky background and results in an event rate of ~ 1 kHz per single camera (Funk et al. 2004). The coincident detection with at least two telescopes enables the rejection of isolated muons or of localized showers and reduces the trigger rate down to $300 - 400$ Hz. The dead time of the instrument is 0.45 ms, corresponding to maximum event rate of ~ 2 kHz. This is not a limiting factor, but it still obstructs a fraction of $\sim 10\%$ of the acquisition time.

The events are packed in data sets called "runs", which correspond, for historical reasons, to observations of 28 min. Every month, these data sets are shipped to Europe on magnetic bands for calibration and analysis. The calibration of the data allows us to convert the electronic signal, measured in ADC counts, to a physical number of Cherenkov photons. An extensive discussion of this complex task, as well as of the different analysis techniques, can be found in de Naurois (2012). Briefly, the first step is the determination of the electronic pedestals, using dedicated observation runs where the lids of the cameras are closed. The gain is then calibrated with dedicated runs that use the optical signal of a pulsed LED placed in the camera shelter (the low and high gains can be inter-calibrated in their overlapping range of p.e.). A flat-fielding coefficient is then applied to account for the relative efficiencies of the Winston cones and of the photocathodes of the PMs. Finally, the number of p.e. derived with the previous steps can be converted to a number of Cherenkov photons via a global efficiency factor. This factor is computed with the Cherenkov rings that are recorded from atmospheric muons passing through the telescope.

2.1.1.3. *Data analysis*

The reconstruction of the parameters of the atmospheric shower enables us to derive two important properties of the γ ray that initiated it: the energy and the direction. The values of the parameters or the quality of the fit can also be used to reject the events due to hadronic showers, which are a thousand times more frequent. These showers are indeed characterized by large deviations to the ellipsoid-like structure expected from electromagnetic showers. Without test beams of VHE γ rays, a comparison with simulations of the detector response and of the shower development in the atmosphere, e.g. with KASCADE (Kertzman & Sembroski 1994) or CORSIKA (Heck et al. 1998), is necessary to establish the rejection cuts and to determine the performance of the analysis chain (energy and angular bias/resolution, acceptance).

Three main analysis techniques have been developed so far, with the addition of multi-variate strategies that combined the previous complementary informations (see e.g. Becherini et al. 2011; Ohm et al. 2009, called in the following PMVA and HDMVA, respectively). The historical analysis method is based on the Hillas parameters (Hillas 1985), which are the width and length of the ellipse, the direction of the major axis and the position of the barycentre of the charges in the camera frame. The discrimination between hadron-like showers and electromagnetic-like showers is then based on the fact that hadronic widths and lengths have wider distributions than their electromagnetic equivalent. A refined method, the *3D Model* analysis, assumes that the showers are Gaussian photo-spheres and computes the charge expected in each pixel of the cameras for a given set of parameters. A maximum likelihood method is then employed to compare the predicted and observed numbers of p.e. per pixel and the quality of the fit is used as a discriminating parameter. With the assumption of rotational symmetry, this method improves the background rejection compared to the Hillas method. The *Model* analysis (de Naurois & Rolland 2009) compares pre-computed images derived from a semi-analytical modelling and rejects the background using the goodness of the fit. This analysis is twice as sensitive as the Hillas technique[2] and is particularly efficient in the low-energy range of atmospheric γ-ray astronomy (typically $\lesssim 500$ GeV).

[2]Note that a factor of 2 in sensitivity corresponds to a multiplication of the effective area, i.e. of the number of telescopes, by a factor of 2^2.

The set of γ-like events selected with the analysis method includes a fraction of hadronic events and a fraction of (almost) irreducible background from electrons or $\pi^0 \rightarrow \gamma + \gamma$ showers. The background subtraction technique aims at estimating the excess of "true" γ-ray events at the test position, in the so-called ON region, compared to the number of events arising from the background, estimated in so-called OFF regions, where presumably no source is present. For point-like sources such as the AGN observed with H.E.S.S.[3], the reflected background technique is usually employed to estimate the excess of "true" γevents. The ON region is defined as a disk of radius $R \sim 0.1^{\circ}$, the exact value depending on the series of cuts performed. For each run, OFF regions of the same size and located at the same distance from the telescope axis in the camera frame are used to estimate the background. This ensures that the acceptance of the telescope is the same in the ON and the OFF regions. Calling α the inverse of the number of OFF regions and $N_{\rm ON}$ and $N_{\rm OFF}$ the total numbers of γ-like events in the ON and OFF regions respectively, the excess is then simply defined as the number of events in the ON region minus the average number of events in the background regions, i.e. $N_{\rm XS} = N_{\rm ON} - \alpha N_{\rm OFF}$. The significance of the excess can then be computed through a propagation of uncertainties. Assuming a Gaussian distribution of events ($\sigma_N = \sqrt{N}$) the significance is $S = N_{\rm XS}/\sigma_{N_{\rm XS}} = (N_{\rm ON} - \alpha N_{\rm OFF})/\sqrt{N_{\rm ON} + \alpha^2 N_{\rm OFF}}$. This simple Gaussian propagation of uncertainties holds as long as the uncertainties are small compared to the numbers. The more sophisticated estimator of Li & Ma (1983), based on a likelihood ratio test with the null hypothesis $N_{\rm ON} = \alpha N_{\rm OFF}$ and on Poisson distributions of events, is generally employed by the community.

H.E.S.S. is typically able to detect the Crab Nebula, the brightest source of the VHE sky (on average), at the $S = 5\sigma$ significance level in 20 s, a source at a tenth of the Crab Nebula flux in 20 min and a source at 1% of the Crab Nebula flux in 20 hours of observation.

2.1.1.4. *Spectral and morphological analysis*

The first physical observable that can be derived from a VHE detection is the spectrum of a source. The natural functional form of a non-thermal spectrum such as those measured at VHE is a power law

[3]The Point Spread Function (PSF) of H.E.S.S. has typically a width of 0.1°.

$\phi(E) = \phi_0 E^{-\Gamma}$, where ϕ is the flux of photons per energy band (differential flux, $\mathrm{d}N/\mathrm{d}E$), where E is the energy of the γray, and where ϕ_0 and Γ are the normalization and photon index. The aim of the spectral analysis is to provide a best fit estimation of these parameters for N_{ON} and N_{OFF} measured in various energy bins (typically of size of 0.1 in log scale). The expected excess of photons $\hat{N}_\gamma$ is related to the observation time T_{ON}, the effective area $\mathcal{A}_{eff}(\hat{E})$ (tabulated and derived from simulations) and the expected spectrum $\hat{\phi}(\hat{E}, \Omega)$ (spectral hypothesis) according to $\hat{N}_\gamma = T_{on} \int_{E_{min}}^{E_{max}} \hat{\phi}(\hat{E}, \Omega) \mathcal{A}_{eff}(\hat{E}) \mathrm{d}\hat{E}$, where $[E_{min}, E_{max}]$ is the energy range of the detected γ rays and where Ω is a set of parameters such as ϕ_0 and Γ for a power law. The measured energy E is only an estimation of the true energy $\hat{E}$ and the energy resolution function $\mathcal{R}(E, \hat{E})$ (derived from simulations) can be taken into account using Eq. (2.1):

$$\hat{N}_\gamma = T_{on} \int_{E_{min}}^{E_{max}} \mathrm{d}E \int_0^{+\infty} \mathrm{d}\hat{E} \quad \hat{\phi}(\hat{E}, \Omega)\ \mathcal{A}_{eff}(\hat{E})\ \mathcal{R}(E, \hat{E}) \tag{2.1}$$

Integrations over experimental parameters such as time, zenith or off-axis angles are implicitly included in Eq. (2.1) to determine the expected excess.

Piron et al. (2001) developed a maximum likelihood method that fully accounts for the limited energy resolution of Cherenkov experiments, yielding a leakage of events toward high-energy bins, as well as the Poisson statistics of the signal and background events. The maximization of the likelihood enables the determination of the spectral parameters and of an equivalent[4] χ^2.

The light curve, i.e. the variations of the normalization of the flux (or of the integral flux) as a function of time, can similarly be derived with a maximum likelihood method, where one usually fixes the index to its global best fit value.

The angular extension of AGN at VHE is smaller than the PSF of H.E.S.S., so, they are considered as point sources. Similarly to the

[4]For a given set of spectral parameters, the likelihood normalization $\mathcal{L}_0$ is obtained, mathematically speaking, by replacing in each energy bin the number of observed events with the number of expected ones. Then $\mathcal{L}/\mathcal{L}_0 = 1$ when the expected and observed numbers of events are equal, i.e. $\chi^2 = -\ln \mathcal{L}/\mathcal{L}_0 = 0$ when there is a perfect match between the model and the data.

spectral fitting procedure, a likelihood method has been developed for morphological studies, using the number of events in bins of the θ^2 distribution (angular distance between the direction of the source and of the event), or in bins of the sky map for non axisymmetrical shapes.

2.1.2. Observation strategy

IACTs such as H.E.S.S. have a field of view of about 5°. Full-sky surveys are for the moment out of question given the sensitivity of the instrument and the limited number of dark nights with good conditions. This means that targets must be selected that can be detected in a reasonable amount of time and that will provide scientifically compelling results.

2.1.2.1. *Time allocated to AGN observations*

I show in Fig. 2 the observation time[5] that is dedicated to AGN and to other types of sources on a yearly basis (from September 2004 to August 2012). On average, AGN are observed 40% of the time, which represents for H.E.S.S. about 300 hours per year. Observing AGN is thus a primary goal of H.E.S.S., together with the Galactic plane survey.

The average repartition of the observation time over the periods of the year, where a period is defined by the slot between two successive full moons (hence the period P13 occurring every three years), is shown in Fig. 3. With the rainy season spanning January to March and with the increase of the dark-time duration up to the summer solstice, the distribution of the observation time peaks in June-July. The AGN season is a bit delayed with a peak in August-September (cf. dark filled histogram), mostly because the priority galactic targets are less visible at this time of the year.

With an average observation time dedicated to AGN of about 20 hours per month ($\sim$ time needed to detect 1% C.U.[6] at the 5σ level), a tough selection of the potential VHE targets must be performed.

---

[5]The values are extracted from the on-line analysis tool. After calibration and data selection, the effective number of hours used for the data analysis can be reduced by a fraction as large as several tenths (see e.g. Aharonian et al. 2006a).

[6]The Crab units C.U. hereafter refer to the spectrum derived by Aharonian et al. (2006a) from Crab Nebula observations, i.e. a power law of index $\Gamma = 2.63$ and flux a 1 TeV $\phi_0 = 3.45 \times 10^{-11}$ cm^{-2} s^{-1} TeV^{-1}

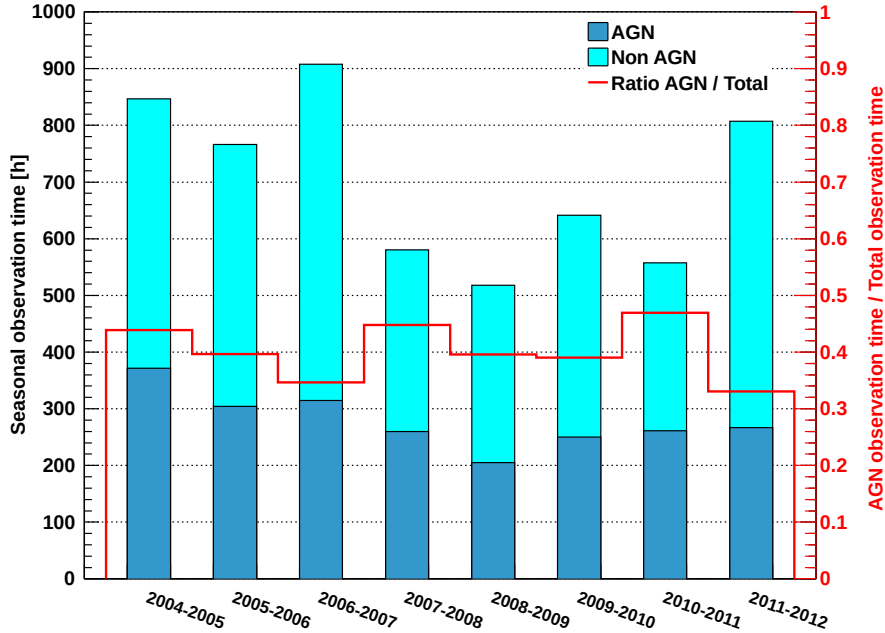

FIGURE 2. Raw observation time that H.E.S.S. dedicated to AGN (filled dark blue) and to other sources (filled light blue) from September 2004 to August 2012. The fraction of time dedicated to AGN observations is shown with the empty red histogram.

2.1.2.2. *Selection of the targets*

Attempts to systematically select good VHE AGN candidates begun before the advent of the third generation Cherenkov telescopes (H.E.S.S., MAGIC and VERITAS). In particular, Costamante & Ghisellini (2002) pointed out the importance of the X-ray and radio counterparts of the candidate VHE emitters. Within a simple SSC framework, commonly used to model AGN emission, one expects the TeV γrays to be the Comptonized counterpart of IR-optical photons interacting with electrons that radiate the X-ray synchrotron spectrum. The optical emission of nearby AGN ($z \lesssim 0.3$, Sbarufatti et al. 2005) is usually

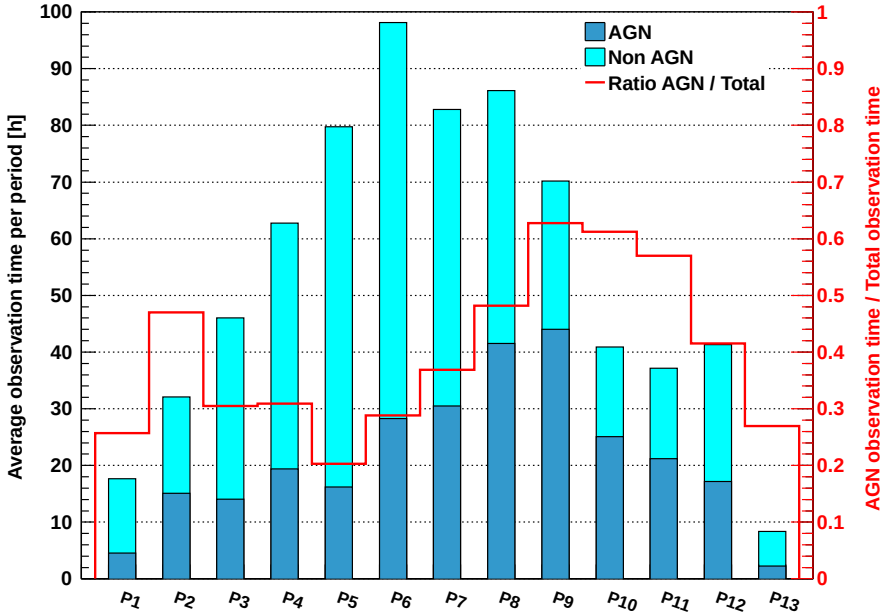

FIGURE 3. Repartition of the observation time per period of the year, averaged over the eight years shown in the left panel.

contaminated by the host galaxy[7], the radio emission is thus used by these authors as a proxy for the population of target photons, while the density of electrons is probed with the X-ray emission.

Large X-ray and radio fluxes, such as shown in the top-right corner of Fig. 4 for selected BL Lac objects, thus hint at potential VHE emission. When Costamante & Ghisellini (2002) published their list of 33 candidates, only five extragalactic emitters had been detected: Mrk 501, Mrk 421, PKS 2155-304, 1ES 1426+428 and 1ES 2344+514. Ten years later (in September 2012), a total of 48 BL Lacs objects have been detected (34 HBLs, 4 IBLs, 4 LBLs), a third of which (14 HBLs, 1 IBLs, 1 LBLs) were listed in the early work of these authors.

[7]Note however that, using the recent WISE survey, D'Abrusco et al. (2012) established selection criteria based on the IR properties of the candidate blazars.

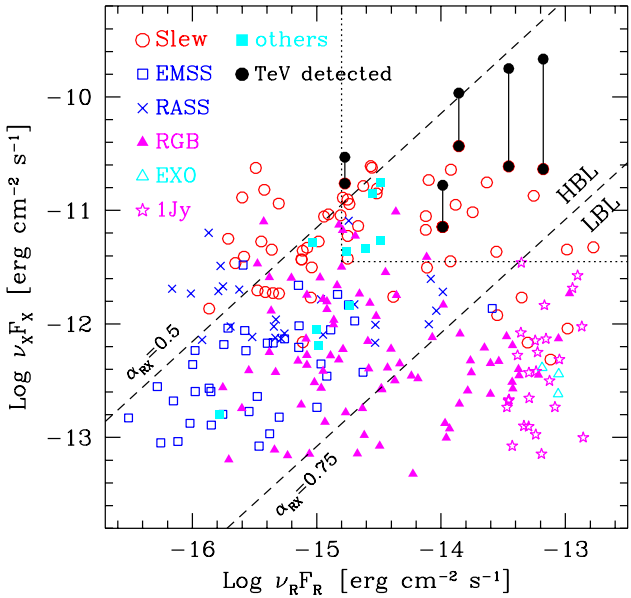

FIGURE 4. X-ray flux at 1 keV vs radio flux at 5 GHz for the BL Lacs of the surveys shown in the legend. At the time of this publication (in 2002), only five VHE AGN had been detected, and the authors proposed the 33 candidates in the top-right corner as good candidates for TeV emission. 16 of them have now been detected. *Extracted from Costamante & Ghisellini (2002).*

The radio and X-ray fluxes probe the synchrotron component and indirectly constrain the second bump of the emission at higher energies. A direct view of this component has been made possible by the all-sky monitoring of the *Fermi*-LAT, with an unprecedented sensitivity. The extrapolation of the HE fluxes pinpoints the candidate VHE sources, which are selected as bright and hard HE emitters. The brightness and hardness of the blazars listed in the Second Catalogue of Active Galactic Nuclei of *Fermi*-LAT (2LAC, Ackermann et al. 2011) are shown in Fig. 5. While FSRQs are intrinsically bright sources at HE,

they have a softer spectrum than BL Lacertae and thus usually a fainter extrapolation at VHE. They also are on average more distant (peak of the distribution at $z_{\text{peak 2LAC}} \sim 1$ in the 2LAC) than BL Lac objects ($z_{\text{peak 2LAC}} \sim 0.2$) and any potential VHE emission would be largely attenuated by the EBL absorption, complicating their detection with arrays such H.E.S.S., at least in its first phase.

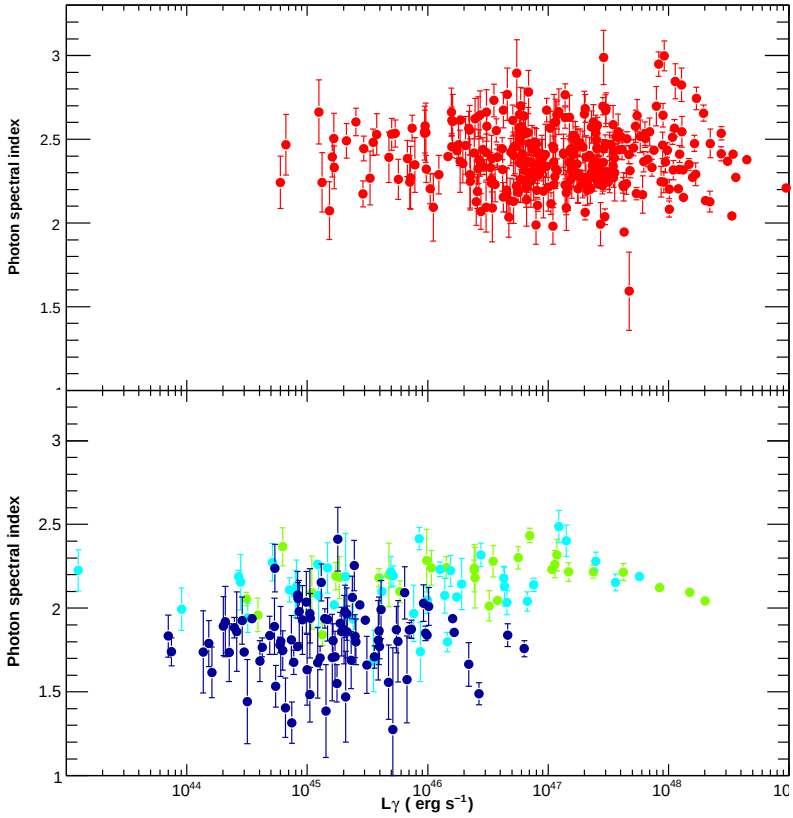

FIGURE 5. Photon index vs γ-ray luminosity in the HE band as detected with the *Fermi*-LAT. The top panel shows the FSRQs while the bottom panel shows the BL Lac objects (HBL in blue on the left, IBL in light blue in the centre, LBL in green on the right). *Extracted from Ackermann et al. (2011).*

The bright HBLs detected with *Fermi*-LAT constitute a class of primary interest for VHE observatories with their hard intrinsic spectra. LBLs and IBLs remain a minority of the VHE detected blazars with their brighter but softer spectra.

The criterion based on the synchrotron emission or on the HE spectrum are intimately linked, as illustrated by the correlation between the HE spectral index and the location of the synchrotron peak shown in Fig. 6. This corresponds to the so-called blazar sequence (Fossati et al. 1998), where a fainter-when-bluer shift of the synchrotron component is correlated with an increase of the ratio of the inverse Compton to synchrotron emission (Ghisellini et al. 1998).

2.1.2.3. *Scientific goals*

Detecting new AGN improves step-by-step the understanding of the mechanisms responsible for their TeV emission but the number of detected sources remains too small to allow for a detailed population study. Increasing the number of sources not only allow trends to be drawn but also proves highly valuable when using AGN as lighthouses to probe the EBL (cf. the study I performed in Chapter 3).

The goal of VHE observations is not only to increase the number of detections but also to carry out long-term campaigns that aim to refine spectral characteristics and study the evolution of the AGN emission as a function of time (see e.g. Abramowski et al. 2012, for the long-term observation campaign on the radio galaxy M87).

Not unlike philatelists, VHE observers are more and more willing to pay great sums (in term of hours) to add a rare stamp to their collection. Rarity can be ephemeral, when e.g. announcing the most distant (currently KUV 00311-1938, announced at the Gamma2012 conference) or the faintest (see e.g. 1ES 1312-423 and SHBL J001355.9-185406 in the following) AGN ever detected at VHE, but these detections are strong signals sent to other astronomical communities of the increasing capabilities of VHE observatories.

Opening windows on new types of objects, such as LBL or IBL, or even on the so far not detected Seyfert Galaxies (see e.g. Lenain et al. 2010, for NGC 1068 and NGC 4945) enables the test of extrapolations of models established for known VHE emitters, as well as fundamentally different emission scenarios predicting a VHE counterpart.

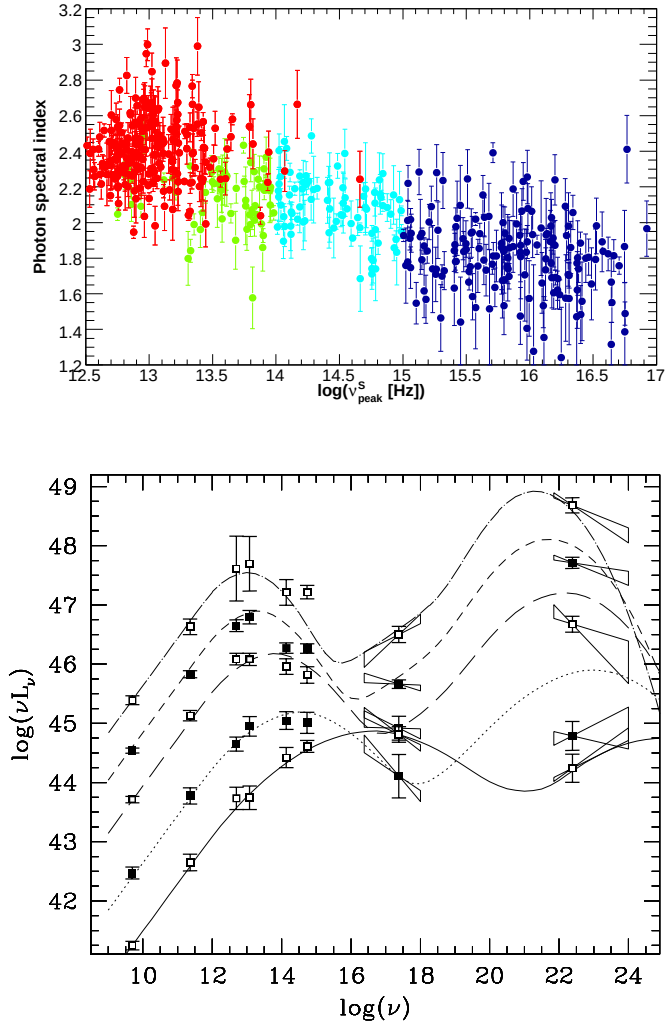

FIGURE 6. *Top:* Photon index vs frequency of the peak of the synchrotron component for the blazars detected with *Fermi*-LAT (cf. Fig. 5 for the color code). *Extracted from Ackermann et al. (2011). Bottom:* Spectral energy distributions of different types of blazars. From top left to bottom right: FSRQs, LBLs, IBLs and HBLs. *Extracted from Fossati et al. (1998).*

2.2. AGN observed at VHE

After a summary in Sect. 2.2.1 of the AGN detected at VHE as of September 2012, I analyse in Sect. 2.2.2 the H.E.S.S. fields of view where the candidate VHE AGN have not passed the detection threshold.

2.2.1. Detected AGN

2.2.1.1. *Status of the AGN detections at VHE in September 2012*

I show in Fig. 7 the evolution of the number of AGN detected at VHE from the first detection of Mrk 421 by Punch et al. (1992) up to the latest announcement at the Gamma2012 conference in July 2012.

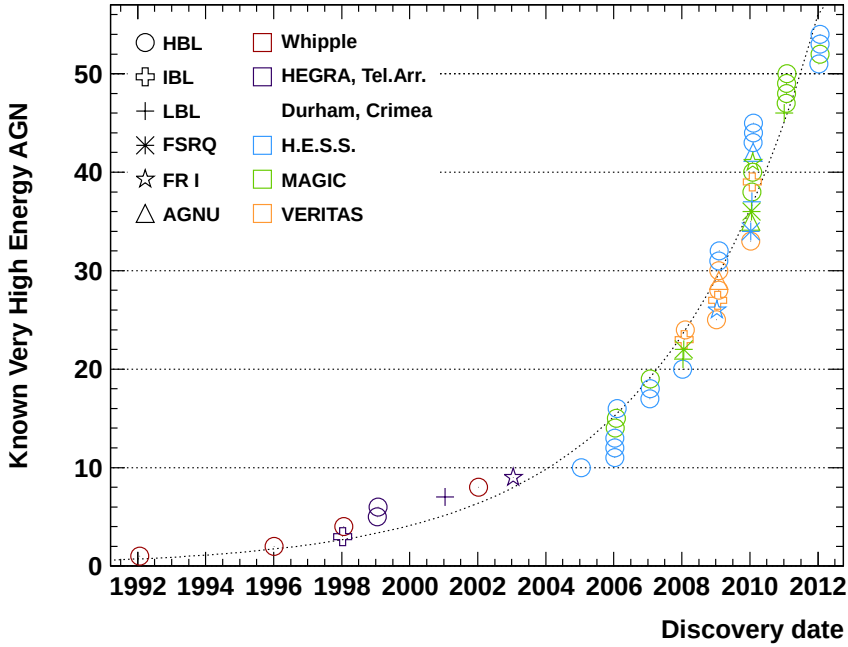

FIGURE 7. Number of AGN detected at VHE as a function of time up to September 2012. *Information retrieved from TeVCat - http://tevcat.uchicago.edu/.*

Up to the advent of the third generation IACT, one can keep track of the individual detections. The first extragalactic sources, the two nearby monsters Mrk 421 (Punch et al. 1992) and Mrk 501 (Quinn et al. 1996) were discovered by the Whipple observatory and were followed by the questionable detections of the IBL 3C 66A and of the LBL BL Lacerta by the Crimean Observatory (Neshpor et al. 1998, 2001). The latter discovery has been fiercely debated because of the simultaneous non-detection by HEGRA, which was observing the source with a similar sensitivity. Note also that the flux reported by the MAGIC collaboration ten years later is two order of magnitudes below the estimation of the Crimean observatory (Albert et al. 2007). At the same epoch, the groups of Whipple, Durham and Telescope Array reported the detection of the four bright ($>$ tenths of C.U.) and variable HBLs 1ES 2344+514 (Catanese et al. 1998), PKS 2155-304 (Chadwick et al. 1999), 1ES 1959+650 (Nishiyama 1999) and H 1426+428 (Horan et al. 2002). The last, but not least, legacy of the second generation instruments is the 4σ evidence of a signal from the FR I radio galaxy M 87, reported by the HEGRA collaboration (Aharonian et al. 2003). The firm detection of this source and of its variability could only be confirmed (Aharonian et al. 2006e) with the third generation instruments.

Since 2005, H.E.S.S., MAGIC and VERITAS have discovered 45 of the 54 VHE AGN that are currently known. Noticeable landmarks are the detection of the distant HBL PG 1553+113 by H.E.S.S. (Aharonian et al. 2006c), with a redshift estimated to ~ 0.5 that remains uncertain (see the discussion in Abdo et al. 2010). The detections of the HBLs 1ES 1101-232 and H 2356-309 by H.E.S.S. set the first constraining limits on the EBL (Aharonian et al. 2006d). MAGIC then discovered in 2008 the LBL S5 0716+714 (Teshima & MAGIC Collaboration 2008) and the FSRQ 3C 279 (Teshima & MAGIC Collaboration 2008) while VERITAS announced the discovery of the IBL W Comae (Acciari et al. 2008). 2009 marks the discovery of the FR I radio galaxy Centaurus A by H.E.S.S. (Aharonian et al. 2009c), widely highlighted as a potential source of ultra-high-energy cosmic rays.

The 54 AGN detected at VHE are largely dominated by a total of 37 HBLs. Four IBL have so far been detected, the above mentioned 3C 66A and W Comae, but also PKS 1424+240 (Ong 2009a) and 1ES 1440+122 (Ong 2010), announced by VERITAS. I already discussed the observations of the LBLs BL Lacertae and S5 0716+714.

Two other blazars of this type can be added to the list PKS 1514-421 (Hofmann 2010a), aka AP Lib, discovered by H.E.S.S., and 1ES 1215+303, discovered by MAGIC (Mariotti 2011) in the same field of view as the HBL 1ES 1218+304. In addition to 3C 279, the FSRQs PKS 1510-089 and 4C +21.35 have been detected by H.E.S.S. (Wagner & H.E.S.S. Collaboration 2010) and MAGIC (Aleksić et al. 2011a), respectively. Finally, besides M 87 and Centaurus A, the radio galaxy NGC 1275 has been monitored by MAGIC since 2010 (Mariotti & MAGIC Collaboration 2010).

The careful reader has certainly noticed that, among the 54 sources, three objects are missing. These are AGN of unknown type: the potential BL Lac object VER J0521+211 (Ong 2009b), coincident with the radio-loud galaxy RGB J0521.8+2112, the object IC 310 (Mariotti 2010) detected by MAGIC and the potential HBL IGR J19443+2117 (H.E.S.S. Collaboration et al. 2011) detected in the Galactic plane.

2.2.1.2. *The contribution of* H.E.S.S.

H.E.S.S. has so far discovered 20 AGN, i.e. almost half of the 45 AGN discovered with the third generation instruments. I list in Table 1 the sources routinely monitored by the collaboration.

The first extragalactic source ever detected in the VHE energy domain, Mrk 421, is observable by H.E.S.S. at large zenith angles (Aharonian et al. 2005a), yielding a high-energy threshold around 1 TeV but also, with a large effective area at higher energies, photons up to ~ 40 TeV.

PKS 2005-489 and H 2356-309 are two blazars at the $\sim 2\%$ C.U., detected by H.E.S.S. since it went into operation (Aharonian et al. 2006b, 2005b). While the latter does not show any sign of spectral variability (H.E.S.S. Collaboration, Abramowski et al. 2010a), an intensive observation campaign on the former revealed significant variations (H.E.S.S. Collaboration, Acero et al. 2010; H.E.S.S. Collaboration, Abramowski et al. 2011).

A dedicated study of 1ES 1101-232 did not reveal significant flux variations over the observation period between 2004 and 2005 (Aharonian et al. 2007d). Together with H 2356-309, this source enabled us to set stringent limits on the EBL which were confirmed by the spectra of 1ES 0229+200 and 1ES 0347-121 (Aharonian et al. 2007a,b).

PKS 2155-304 is the brightest extragalactic source in the Southern sky and has been widely studied with H.E.S.S. (Aharonian et al.

#	Object	z	Type	Discoverer
1	Cen A	0.002	FR I	H.E.S.S.
2	M 87	0.004	FR I	HEGRA
3	Markarian 421	0.031	HBL	Whipple
4	PKS 1514-241	0.049	LBL	H.E.S.S.
5	PKS 1440-389	0.065	HBL	H.E.S.S.
6	PKS 0548-322	0.069	HBL	H.E.S.S.
7	PKS 2005-489	0.071	HBL	H.E.S.S.
8	RGB J0152+017	0.08	HBL	H.E.S.S.
9	SHBL J001355.9-185406	0.095	HBL	H.E.S.S.
10	1ES 1312-423	0.105	HBL	H.E.S.S.
11	PKS 2155-304	0.116	HBL	Durham
12	1ES 0229+200	0.14	HBL	H.E.S.S.
13	1RXS J101015.9-311909	0.143	HBL	H.E.S.S.
14	H 2356-309	0.165	HBL	H.E.S.S.
15	1ES 1101-232	0.186	HBL	H.E.S.S.
16	1ES 0347-121	0.188	HBL	H.E.S.S.
17	PKS 0301-243	0.266**	HBL	H.E.S.S.
18	1ES 0414+009	0.287	HBL	H.E.S.S.
19	PKS 1510-089	0.361	FSRQ	H.E.S.S.
20	PKS 0447-439	-	HBL	H.E.S.S.
21	PG 1553+113	-	HBL	H.E.S.S.
22	IGR J19443+2117	-	-	H.E.S.S.
23	KUV 00311-1938	>0.506**	HBL	H.E.S.S.

TABLE 1. AGN detected by H.E.S.S. up to September 2012. The redshifts are extracted from SIMBAD and NED (**: redshift from Pita et al. 2012).

2005c,d, 2007c, 2009b,a; H.E.S.S. Collaboration, Abramowski et al. 2010b; H.E.S.S. Collaboration et al. 2012). It exhibited a spectacular flux outburst in July 2006 (Aharonian et al. 2007c).

I discuss the discovery of 1ES 1312-423 and SHBL J001355.9-185406 in Sect. 2.3. They are representative of the class of HBLs detected by H.E.S.S. such as PKS 1440-389 (Hofmann 2010a), PKS 0548-322 (Aharonian et al. 2010), RGB J0152+017 (Aharonian et al. 2008b), 1RXS J101015.9-311909 (HESS Collaboration et al. 2012), 1ES 0414+009

(The HESS Collaboration et al. 2012) or the recently announced PKS 0301-243 (Gamma2012 conference).

Finally, the sources PKS 0447-439 (Raue et al. 2009) and KUV 00311-1938 (Gamma2012) are known by the community mostly because of their redshifts. The former was claimed to be located at $z > 1.246$ by Landt (2012), which triggered wild discussions on the transparency of the Universe to γrays, but the spectral line responsible for this redshift estimation has rapidly been identified as due to telluric absorption (Pita et al. 2012; Fumagalli et al. 2012). Given the lower limit on the redshift of the latter, it currently is the most distant source detected at VHE.

2.2.2. Signals compatible with background fluctuations

The H.E.S.S. collaboration does not spend all its observation time on monitoring already detected sources, which explains its successful contributions to the field. After almost ten years of observation, a large amount of data where no signal is apparent have been "hidden away in the cupboards", despite two publications of upper limits on the fluxes expected from the targeted AGN.

A total of 63 hours of observations performed in 2003-2004 on 19 AGN led Aharonian et al. (2005e) to derive upper limits between 0.4 and 5.1% C.U.. The second upper-limit paper (Aharonian et al. 2008a) listed 14 upper limits between 0.9% and 4.9% C.U., based on 94 hours of observations spanning 2005-2007. I analyse here, for the third AGN upper-limit paper, a total of 400 hours of data taken up to December 2011 and I derive upper limits on 47 targets.

2.2.2.1. *List of targets and data analysis*

I select all the observations of AGN away from the galactic plane (galactic latitude $> 10^{o}$), as listed in Table 2. The name of the target is given in the first column, its right ascension and declination are shown in the second and third columns. The redshift and the category of the source are given in columns 4 and 5. These were extracted crossing the informations of the public databases such as NED, SIMBAD and of catalogues such as the 2FGL or the Roma BZCAT, unless stated otherwise in the table. I only analyse the sources for which the size of the dataset (in term of hours of observation) is larger than that previously published in Aharonian et al. (2005e, 2008a). Thus the limits on 1ES 0145+138, EXO 0556.4-3838, RGB J0812+026, RGB J1117+202, Q J22548-2725, NGC 3783, BWE 0210+116, 3C 273, HS 2250+1926,

Object	α_{J2000} [h m s]	δ_{J2000} [d m s]	z	Type
IIIZw 2	00 10 31.2	+10 58 12	0.09	Sy I
1FGL J0022.2-1850	00 22 16.8	-18 51 00	<1.38*	BL Lac
2FGL J0048.8-6347	00 48 52.8	-63 48 00	-	-
PKS 0048-097	00 50 40.8	-09 28 48	1.53	BL Lac
1FGL J0051.4-6242	00 51 31.2	-62 42 36	<1.12*	BL Lac
RGB J0109+182	01 09 07.2	+18 16 12	0.14	BL Lac
2FGL J0211.2+1050	02 11 14.4	+10 50 24	-	BL Lac
2EG J0216+1107	02 16 00.0	+11 07 12	-	-
2FGL J0229.3-3644	02 29 21.6	-36 43 48	2.11	FSRQ
RBS 334	02 37 33.6	-36 03 36	0.41**	BL Lac
RBS 0413	03 19 52.8	+18 45 36	0.19	BL Lac
RBS 421	03 25 40.8	-16 46 12	0.29	BL Lac
1ES 0323+022	03 26 14.4	+02 25 12	0.15	BL Lac
QSO B0331-362	03 33 12.0	-36 19 48	0.31	BL Lac
2FGL J0334.3-3728	03 34 19.2	-37 28 12	<1.34*	BL Lac
PKS 0352-686(**)	03 52 57.6	-68 31 12	0.09	BL Lac
2FGL J0426.6+0509c	04 26 40.8	+05 09 00	1.33	FSRQ
3C 120	04 33 12.0	+05 21 00	0.03	Sy I
2FGL J0505.8-0411	05 05 48.0	-04 12 00	1.48	FSRQ
1FGL J0506.9-5435	05 06 57.6	-54 36 00	<1.07*	BL Lac
1ES 0507-040	05 09 38.4	-04 00 36	0.31	BL Lac
2FGL J0515.0-4411	05 15 00.0	-44 12 00	-	-
2FGL J0516.5-4601	05 16 33.6	-46 01 12	0.19	FSRQ
Pictor A	05 19 50.4	-45 46 48	0.03	Sy I
2FGL J0537.7-5716	05 37 43.2	-57 16 12	1.55*	AGN
2FGL J0540.4-5415	05 40 26.4	-54 15 00	1.19	FSRQ
BZB J0543-5532	05 43 57.6	-55 31 48	0.27**	BL Lac
1ES 0715-259	07 18 04.8	-26 08 24	0.47	BL Lac
RBS 1049	11 54 04.8	-00 10 12	0.25	BL Lac
1ES 1218+30.4	12 21 21.6	+30 10 48	0.18	BL Lac
2FGL J1226.0+2953	12 26 04.8	+29 54 00	-	-
3C 279	12 56 12.0	-05 47 24	0.54	FSRQ
1ES 1332-295	13 35 28.8	-29 50 24	0.26	BL Lac
PKS 1345+125	13 47 33.6	+12 17 24	0.12	Sy II
2FGL J1351.4+1115	13 51 28.8	+11 15 36	0.40	BL Lac
1ES 1440+122	14 42 48.0	+12 00 36	0.16	BL Lac
2FGL J1959.1-4245	19 59 09.6	-42 45 36	2.17	FSRQ
PKS 2004-447	20 07 55.2	-44 34 48	0.24	Sy I
RBS 1752	21 31 36.0	-09 15 36	0.45	BL Lac
PG 2209+184	22 11 52.8	+18 42 00	0.07	Sy I
2FGL J2219.1+1805	22 19 12.0	+18 05 24	1.80	FSRQ
RBS 1888	22 43 43.2	-12 31 12	0.23	BL Lac
3EG J2248+1745	22 48 57.6	+17 46 12	-	-
NGC 7469	23 03 16.8	+08 52 12	0.02	Sy I
PMN J2345-1555	23 45 12.0	-15 55 12	0.62	FSRQ
1ES 2343-151	23 45 38.4	-14 49 12	0.22	BL Lac
2FGL J2347.9-1629	23 47 55.2	-16 29 24	0.58	FSRQ

TABLE 2. Selected observations from 2003 to December 2011. A * indicates that the redshift is extracted from Rau et al. (2012) while ** refers to Pita et al. (2012).

PKS 2316-423 and PKS 0558-504 that are published therein are not recomputed.

I also selected the AGN and unidentified sources from the 2FGL in the same fields of view as the H.E.S.S. targets. The results of the analysis, performed with the *Model++ Std cuts* analysis (de Naurois & Rolland 2009), are shown in Table 3. A large offset ($> 0.7^{o}$) of the source with respect to the camera centre (column 4) indicates that the object is in the same field of view as another target. Similar information can be extracted from the difference between the observed time (column 2) and the time corrected for the acceptance (column 5), which is large for sources far from the centre of the field of view. As previously mentioned, the zenith angle shown in column 3 is correlated with the energy threshold given in column 6. The number of ON events, OFF events and the normalization of the OFF events (inverse of the number of regions used) are given in column 7, 8 and 9. The excess and significance of detection are shown in the last two columns.

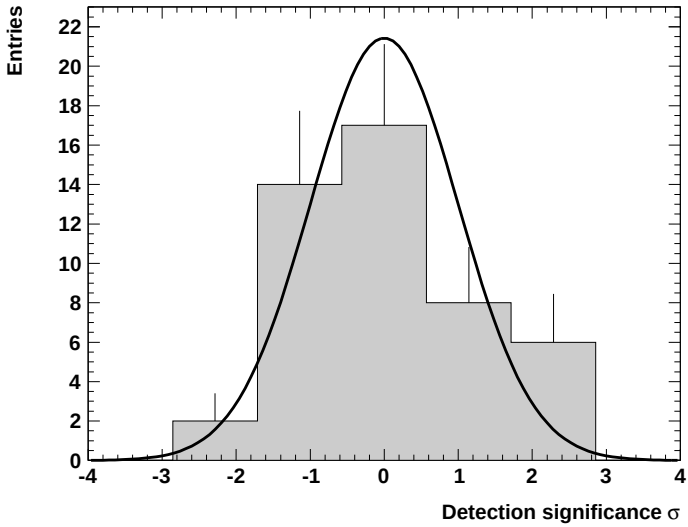

FIGURE 8. Distribution of the detection significance of the targets listed in Table 1.

I show in Fig. 8 the distribution of the significance of the individual detections, which is in good agreement with a normal distribution zero

Object	T [h]	Z_{obs} °	offset °	T_{corr} [h]	E_{th} [TeV]	ON	OFF	Norm	XS	S [σ]
IIIZw 2	13.1	37	0.5	12.0	0.39	51	633	0.083	-1.7	-0.2
1FGL J0022.2-1850	61.5	13	2.1	15.4	0.24	104	6348	0.018	-13.1	-1.2
2FGL J0048.8-6347	8.0	40	1.2	4.9	0.58	23	431	0.033	8.8	2.1
PKS 0048-097	44.3	19	1.9	14.8	0.26	76	3418	0.023	-3.2	-0.4
1FGL J0051.4-6242	8.0	40	0.5	7.4	0.58	10	193	0.083	-6.1	-1.6
RGB J0109+182	4.1	42	0.5	3.8	0.71	10	144	0.083	-2.0	-0.6
2FGL J0211.2+1050	7.4	43	1.5	3.6	0.48	18	518	0.027	4.2	1.1
2EG J0216+1107	7.4	43	1.2	4.7	0.48	15	543	0.038	-5.7	-1.3
2FGL J0229.3-3644	6.1	14	1.8	2.0	0.39	7	421	0.021	-1.8	-0.6
RBS 334	6.1	14	0.5	5.6	0.35	26	293	0.083	1.6	0.3
RBS 0413	4.1	43	0.5	3.7	0.71	10	102	0.083	1.5	0.5
RBS 421	14.4	9	0.5	13.3	0.29	92	1153	0.083	-4.1	-0.4
1ES 0323+022	10.0	27	0.5	9.3	0.26	78	985	0.083	-4.1	-0.4
QSO B0331-362	30.6	19	1.1	20.6	0.24	109	3166	0.038	-12.6	-1.1
2FGL J0334.3-3728	24.7	18	1.6	11.4	0.26	84	2656	0.025	16.6	1.9
PKS 0352-686	15.0	47	0.5	14.2	0.71	36	423	0.083	0.8	0.1
2FGL J0426.6+0509c	11.9	30	1.7	5.1	0.29	47	2137	0.023	-1.8	-0.3
3C 120	11.9	30	0.5	11.1	0.29	108	1008	0.083	24.0	2.4
2FGL J0505.8-0411	8.3	21	1.1	5.8	0.29	54	1306	0.035	7.9	1.1
1FGL J0506.9-5435	2.1	32	0.5	2.0	0.95	2	41	0.083	-1.4	-0.8
1ES 0507-040	8.3	21	0.5	7.7	0.32	52	614	0.083	0.8	0.1
2FGL J0515.0-4411	20.9	29	1.8	7.4	0.24	61	2877	0.021	0.1	0.0
2FGL J0516.5-4601	20.9	29	0.8	17.1	0.26	132	2123	0.056	12.8	1.1
Pictor A	20.9	29	0.5	19.4	0.29	134	1367	0.083	20.1	1.8
2FGL J0537.7-5716	8.8	33	2.0	2.7	0.35	19	1103	0.019	-1.8	-0.4
2FGL J0540.4-5415	8.8	33	1.5	4.7	0.35	26	1303	0.027	-8.9	-1.6
BZB J0543-5532	8.8	33	0.5	8.1	0.39	49	652	0.083	-5.3	-0.7
1ES 0715-259	5.7	13	1.9	1.9	0.32	15	788	0.021	-1.4	-0.4
RBS 1049	4.3	30	0.5	3.9	0.39	17	253	0.083	-4.1	-0.9
1ES 1218+30.4	2.3	56	0.5	2.1	1.41	12	85	0.083	4.9	1.6
2FGL J1226.0+2953	2.3	56	1.2	1.4	1.41	10	147	0.031	5.4	2.1
3C 279	5.5	26	0.5	5.0	0.29	35	475	0.075	-0.5	-0.1
1ES 1332-295	10.1	25	0.7	8.4	0.26	54	1059	0.054	-2.9	-0.4
PKS 1345+125	7.9	37	0.7	6.7	0.53	22	351	0.056	2.5	0.5
2FGL J1351.4+1115	7.9	37	1.6	3.6	0.48	7	531	0.026	-6.6	-2.0
1ES 1440+122	11.2	37	0.5	10.4	0.29	66	650	0.083	11.8	1.5
2FGL J1959.1-4245	12.9	33	2.1	2.7	0.39	8	994	0.016	-8.1	-2.2
PKS 2004-447	25.6	33	0.5	23.5	0.39	110	1139	0.083	15.1	1.4
RBS 1752	25.1	16	0.5	23.1	0.29	149	2023	0.083	-19.6	-1.5
PG 2209+184	8.8	42	0.5	8.1	0.64	19	286	0.083	-4.8	-1.0
2FGL J2219.1+1805	8.8	42	1.9	2.6	0.64	7	529	0.019	-3.2	-1.1
RBS 1888	7.9	14	0.5	7.3	0.22	74	916	0.077	3.5	0.4
3EG J2248+1745	17.3	43	1.8	5.8	0.48	36	1069	0.024	10.0	1.8
NGC 7469	7.9	33	0.5	7.4	0.32	79	772	0.083	14.7	1.7
PMN J2345-1555	21.0	15	1.0	15.9	0.22	147	3775	0.037	6.4	0.5
1ES 2343-151	21.0	15	0.7	18.4	0.22	156	2629	0.066	-18.5	-1.4
2FGL J2347.9-1629	21.0	15	1.6	9.6	0.20	104	3593	0.025	15.1	1.5

TABLE 3. Results of H.E.S.S. observations of selected AGN

centred, with a standard deviation of one and where the area of the Gaussian is set to the area of the histogram. This agreement does not suggest the presence of a significant amount of detectable sources among the studied set of targets.

2.2.2.2. *VHE upper limits*

I perform the spectral analysis assuming a photon index $\Gamma = 3$ and I show in the fourth column of Table 4 the 99.9% limit on the integral flux above the threshold energy according to the statistics of Feldman & Cousins (1998). Limits as low as 0.3% C.U. are derived and 41 of the 47 upper limits are the most constraining ever published. Two of the six left (NGC 7469 and 3C 120) are slightly above the constraints derived with H.E.S.S. in Aharonian et al. (2005e) due to large downward fluctuations (-2σ) in the previous dataset and to the $\sim 1\sigma$ significances derived in this study.

Object	z	E_{th} [TeV]	$I(>E_{th})$ [$\times 10^{-12}$ cm^{-2} s^{-1}]	Crab [%]	$\mathcal{P}(\chi^2)$ [%]	MJD-50000
IIIZw 2	0.09	0.39	0.58	0.6^U	22	3943-44,3953,4267,4270,4272,4274-76,4279,4320, 4322-26, 4328,4331-33
1FGL J0022.2-1850	<1.38*	0.24	0.72	0.3^U	64	3589-90,3592,3594-95,3597-98,3623,3625-27,3637-39, 3641-44,4353,4358,4360-61,4363-64,4378-86,4391
2FGL J0048.8-6347	-	0.58	1.02	2.0^U	50	5833-37
PKS 0048-097	1.53	0.26	0.78	0.4^U	69	4023,4050-57,4321-26,4328,4331-35,4349,4350, 4352-53,4357,4359-60,4363,4374,4378-79,4381-85, 5058,5060,5063-65,5067-68
1FGL J0051.4-6242	<1.12*	0.58	0.27	0.5^U	32	5833-37
RGB J0109+182	0.14	0.71	0.47	1.3^U	15	5093,5095
2FGL J0211.2+1050	-	0.48	1.00	1.4^U	39	3966-69,3971-72,3974,3976-78
2EG J0216+1107	-	0.48	0.42	0.6^U	63	3966-67,3969,3971-72,3974,3976-78
2FGL J0229.3-3644	2.11	0.39	1.02	1.0^U	67	5444,5446,5448-52
RBS 334	0.41**	0.35	1.24	1.1^U	31	5444,5446,5448-52
RBS 0413	0.19	0.71	0.61	1.7^D	22	5446,5448-51,5482-83
RBS 421	0.29	0.29	0.79	0.5^U	98	4715,4717,4720,4815,4818-20,4822-30
1ES 0323+022	0.15	0.26	1.13	0.6^U	84	3267-68,3675-77,3996-4000
QSO B0331-362	0.31	0.24	0.69	0.3^U	12	4653-61,5064,5090-94,5112,5115-18,5150,5154, 5415-19,5421-28,5442-44,5446,5448-51,5482,5497, 5500-01,5503-07,5771,5773,5775-77,5779,5781-83, 5853-54,5885,5887-91,5893,5909-10,5912,5917
2FGL J0334.3-3728	<1.34*	0.26	1.65	0.9^U	14	3589-90,3592,3597-98,3623,3625-27,3637-38,3641-44, 4353,4358,4360-61,4363-64,4378-86,4391
PKS 0352-686	0.09	0.71	0.35	0.9^U	43	5483-84,5499-5502,5504-08,5510-12,5526-27,5529, 5532-37
2FGL J0426.6+0509c	1.33	0.29	1.33	0.8^U	30	3315-17,3352-54,5834-39,5841-43,5867-68
3C 120	0.03	0.29	2.10	1.3	73	3315-18,3352-54,5834-43,5867-68
2FGL J0505.8-0411	1.48	0.29	1.93	1.2^U	45	4439,4441-46,4450
1FGL J0506.9-5435	<1.07*	0.95	0.49	2.1^U	87	5867-68
1ES 0507-040	0.31	0.32	1.20	0.9^U	69	4439,4441-46,4450
2FGL J0515.0-4411	-	0.24	1.71	0.8^U	27	3268-70,3273,3318-19,3350,3352-53,4050-53,

TABLE 4. Spectral and temporal analysis results. Superscripts ^{U} and ^{D} indicate the most constraining upper limits ever published or targets detected by another VHE experiment.

Object	z	E_{th} [TeV]	$I(>E_{th})$ [$\times 10^{-12}$ cm^{-2} s^{-1}]	Crab [%]	$\mathcal{P}(\chi^2)$ [%]	MJD-50000
						4055-56,4059-62,4496,4498-99,4819-20,4823
2FGL J0516.5-4601	0.19	0.26	1.53	0.8^U	89	3268-70,3273,3318-19,3350,3352-53,4051-53, 4055-56,4059-62,4496,4499,4819-20,4823
Pictor A	0.03	0.29	1.36	0.9^U	12	3268-70,3273,3318-19,3350,3352-53,4050-53, 4055-56,4059-62,4496,4498-99,4819-20,4823
2FGL J0537.7-5716	1.55*	0.35	1.55	1.3^U	78	5911,5914,5917,5922-25
2FGL J0540.4-5415	1.19	0.35	0.77	0.7^U	27	5911,5914,5917,5922-25
BZB J0543-5532	0.27**	0.39	0.75	0.8^U	25	5911,5914,5917,5922-25
1ES 0715-259	0.47	0.32	1.56	1.1^U	96	4140-44,4146,4148
RBS 1049	0.25	0.39	0.84	0.9^U	22	5320-23
1ES 1218+30.4	0.18	1.41	0.79	6.5^D	19	3875-76
2FGL J1226.0+2953	-	1.41	1.06	8.7^U	90	3875-76
3C 279	0.54	0.29	1.57	1.0^D	40	4118-21,4501,4855,4858-59,4861
1ES 1332-295	0.26	0.26	1.31	0.7^U	45	3929-35
PKS 1345+125	0.12	0.53	0.57	1.0^U	21	4938-41,4944-46,4948-49,4952
2FGL J1351.4+1115	0.40	0.48	0.34	0.5^U	40	4938-41,4944-46,4948-49,4952
1ES 1440+122	0.16	0.29	1.53	1.0^D	47	3109,3119,4995-99,5002-03,5005-06
2FGL J1959.1-4245	2.17	0.39	0.60	0.6^U	95	5358-59,5362,5365,5367,5369,5386,5389-91,5393-94, 5396-97,5413,5415-16,5419,5421-23
PKS 2004-447	0.24	0.39	0.82	0.8^U	26	5358-59,5361-62,5364-67,5369-70,5386-87,5389-90, 5391-96,5413-16,5418-24
RBS 1752	0.45	0.29	0.46	0.3^U	37	4625-32,4653-56,4728-39
PG 2209+184	0.07	0.64	0.27	0.6^U	52	4373,4375-76,4378-79,4381-86
2FGL J2219.1+1805	1.80	0.64	0.39	0.9^U	47	4374,4376-79,4381-86
RBS 1888	0.23	0.22	1.95	0.8^U	94	3207-10,3914-18
3EG J2248+1745	-	0.48	0.98	1.4^U	99	4292-96,4298-04,5004-09
NGC 7469	0.02	0.32	1.67	1.2	70	3202,3206,3211-12,4019-20,4022-23
PMN J2345-1555	0.62	0.22	1.54	0.6^U	47	3211-13,3590,3592-95,3597-98,5495-96,5498-99
1ES 2343-151	0.22	0.22	0.82	0.3^U	20	3212-13,3590,3592-93,3594-95,3597-98,5495-96, 5498-99
2FGL J2347.9-1629	0.58	0.20	2.93	1.0^U	88	3211-12,3590,3592-93,3594-95,3597-98,5495-96, 5498-99

TABLE 5. Continuation of Table 4.

The four others are detected by other Cherenkov telescopes and have photon indices compatible with $\Gamma = 3$. RBS 0413 is detected by VERITAS (Aliu et al. 2012) at 1% C.U. (compared to the upper limit of 1.7% derived here). 1ES 1218+30.4 is detected by MAGIC (Albert et al. 2006) and VERITAS (Acciari et al. 2009, 2010) and is a known variable source with reported fluxes from 6% to 20% C.U. (upper limit of 6.5% derived here above the high threshold energy of 1.4 TeV). MAGIC has also detected 3C 279 (Aleksić et al. 2011b) at 0.5% C.U. (upper limit of 1.0% here) and VERITAS reports a flux of 1% C.U. for 1ES 1440+122 (Wystan Benbow for the VERITAS Collaboration 2011), marginally suggesting a variability of this source (upper limit of 1.0% C.U. derived herein).

I carried out a search for transient emission deriving the light curves of the 47 targets on a nightly time scale, as shown in the last column of Table 4. No deviations from a constant fit are seen, with χ^2 probabilities above 12%, suggesting no detectable flaring periods of emission.

2.2.2.3. *Multi-wavelength overview*

Some of the limits derived in the previous section can be directly exploited in a multi-wavelength context. I select the 2FGL sources for which the extrapolated *Fermi*-LAT flux is twice larger[8] than the upper limit derived from the H.E.S.S. observations. As shown in Table 6, when including the EBL absorption the list of constraining upper limits shrinks dramatically, leaving one constrained, known-redshift, HE source: BZB J0543-5532 ($z = 0.27$). For this source, we can conclude that the maximum of the second component of the emission is below the energy threshold of H.E.S.S.. For the others, refined spectroscopic measurements will allow for more definite conclusions.

2.3. The blazars 1ES 1312-423 and SHBL J001355.9-185406

1ES 1312-423 and SHBL J001355.9-185406 are two examples of the faintest HBLs detected by IACT to date. These two objects were detected in X rays at the beginning of the 90s with the Einstein observatory (Gioia et al. 1990) and with ROSAT (1RXS J001356.6-185408, Voges et al. 1996), respectively. Their classification was refined with

[8]A fiducial value of two corresponds to the average EBL absorption between 500 GeV and 1 TeV for a source situated at $z \sim 0.1$

Object	z	E_{th} [TeV]	I($> E_{th}$) [% C.U.]	$I_{2LAC}(> E_{th})$ [% C.U.]	$I^{EBL}_{2LAC}(> E_{th})$ [% C.U.]
2FGL J1351.4+1115	0.40	0.48	0.5	40	0.2
1FGL J0022.2-1850	<1.38*	0.24	0.3	24	2.8
1FGL J0051.4-6242	<1.12*	0.58	0.5	37	0.5
BZB J0543-5532	0.27**	0.39	0.8	25	1.4
1FGL J0506.9-5435	<1.07*	0.95	2.2	65	0.2
RBS 334	0.41**	0.35	1.1	13	0.2
PKS 0048-097	0.64*	0.26	0.4	3.6	0.05
2FGL J0334.3-3728	<1.34*	0.26	0.9	7.3	1.0
RBS 1049	0.25	0.39	0.9	5.0	0.4
PMN J2345-1555	0.62	0.22	0.6	2.7	0.1
RBS 421	0.29	0.29	0.5	1.8	0.2
RBS 1752	0.45	0.29	0.3	1.0	0.04

TABLE 6. Comparison of the high energy extrapolation from the 2FGL with H.E.S.S. upper limits. Only the objects with constraining limits are selected. $I_{2FGL}(> E_{th})$ and $I^{EBL}_{2FGL}(> E_{th})$ are the 2FGL measurements extrapolated above E_{th}, taking into account the EBL absorption for the second quantity, with an optical depth 27% larger than that of FR08 as in Chapter 3. When only an upper limit on the redshift is available, a value of $z = 0.3$ is assumed to derive these extrapolations.

their optical spectra, indicating BL Lac objects (Stocke et al. 1991; Schwope et al. 2000, respectively).

Based on their X-ray and radio emissions, Wolter et al. (1998) and Giommi et al. (2005) refined their classification as HBLs. Given the proximity of these objects - 1ES 1312-423 is located at $z = 0.105$ (Rector et al. 2000) and SHBL J001355.9-185406 is located at $z = 0.095$ (Jones et al. 2009) - Stecker et al. (1996) and Costamante & Ghisellini (2002) highlighted them as good TeV candidates.

A dedicated observation campaign was performed by H.E.S.S. on the blazar SHBL J001355.9-185406 and its discovery was consequently announced in Hofmann (2010b). The case of 1ES 1312-423 is more unusual. This source benefited from the very long period of observation dedicated to its neighbour, the radio galaxy Centaurus A (Aharonian et al. 2009c), located 2^o away.

2.3.1. H.E.S.S. data

2.3.1.1. *Detection of the TeV emission*

SHBL J001355.9-185406 was observed with H.E.S.S. between the 6 July 2008 and the 17 December 2011 (MJD 54653-55912). I used a standard-quality selection of the data within ParisAnalysis[9]. I restricted the analysis to runs in common with the list obtained for the HDMVA analysis. This yields a total of 44.6 hours live time for an average offset in the camera field of view of 0.5°. Accounting for the decrease of acceptance with the off-axis angle results in a corrected live time of 41.5 hours. With the *Model++ Std cuts* analysis, an excess of 153.5γ, for $N_{\rm ON} = 830$, $N_{\rm OFF} = 8190$ and an OFF normalization of 0.083, is detected at the 5.5σ significance level at the test position $\alpha_{\rm J2000} = 00^{\rm h}\,13^{\rm m}\,56^{\rm s}$ and $\delta_{\rm J2000} = -18^\circ\,54'\,06''$. With an average zenith angle of 12.9°, the energy threshold, computed at 20% of the nominal acceptance, is $E_{\rm th} = 310$ GeV. I show in Fig. 9 and Fig. 10 the H.E.S.S. sky map around SHBL J001355.9-185406 and the so-called θ^2-distribution[10]. I performed a morphological study of the source assuming a photon index $\Gamma = 3$. Fitting a point-like source convolved with the PSF to the sky map yields a best fit position at $\alpha_{\rm J2000} = 00^{\rm h}\,13^{\rm m}\,52^{\rm s} \pm 23^{\rm s}_{\rm stat}$ and $\delta_{\rm J2000} = -18^\circ\,53'\,29'' \pm 22''_{\rm stat}$, 0.02° away from the test position. Fitting a Gaussian convolved with the PSF results in a slightly extended source $\delta\theta = 0.03 \pm 0.01^\circ$ at the same position, compatible with the systematic uncertainty on the PSF for such a soft source (the PSF narrows with increasing energy).

The observations for which 1ES 1312-423 is in the field of view of the cameras span MJD 53111 - MJD 55383 (16 April 2004 - 6 July 2010). I also used a standard-quality selection and analysed the runs in common with other tools, for multiple cross checks. The total of 147.1 hours is not representative of the exposure on this source, since, with an average offset in the camera field of view of 1.9°, the acceptance correction yields an effective exposure of 48.4 hours. With an average zenith angle of 23.9° and an acceptance as a function of energy flatter than that of SHBL J001355.9-185406 due to the larger offset, the energy threshold at 20% of the nominal acceptance is 210 GeV. The source is detected at the 6.3σ level with the *Model++ Std cuts* analysis,

[9]ParisAnalysis is the software associated to the *Model++* analysis.

[10]I recall that θ^2 is the squared angular distance between the arrival direction of the γrays and the test position.

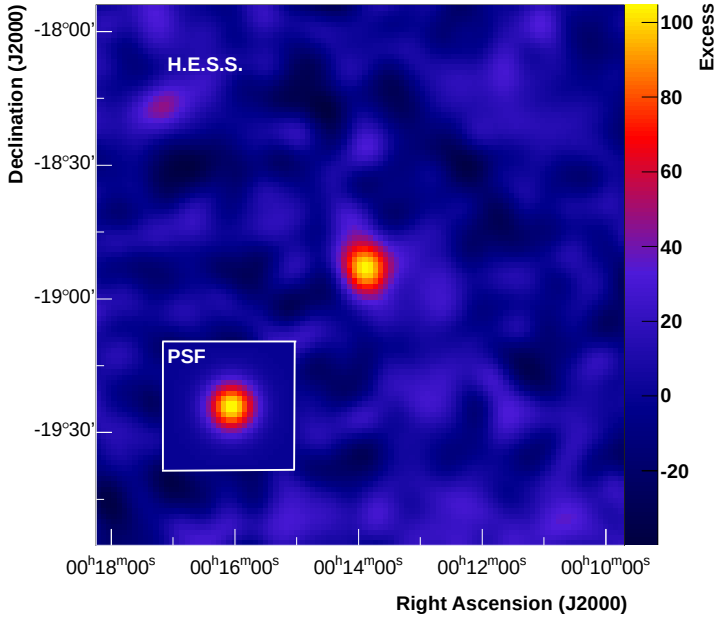

FIGURE 9. Sky map of the excess events detected with H.E.S.S. around the position of SHBL J001355.9-185406, smoothed with the PSF, which is averaged over the observation runs for a photon index $\Gamma = 3$ and is shown in the bottom left inset.

corresponding to an excess of 164.0 events ($N_{\mathrm{ON}} = 770$, $N_{\mathrm{OFF}} = 30084$, $\alpha = 0.020$). The morphological analysis of the source, assuming an index $\Gamma = 3$, yields a best fit position at $\alpha_{\mathrm{J2000}} = 13^{\mathrm{h}}\,15^{\mathrm{m}}\,03^{\mathrm{s}} \pm 22^{\mathrm{s}}_{\mathrm{stat}}$ and $\delta_{\mathrm{J2000}} = -42^{\circ}\,35'\,39'' \pm 16''_{\mathrm{stat}}$, 0.02^{o} away from the radio position (referenced in Mao 2011). A Gaussian of best fit width 0.02^{o} convolved with the PSF is not preferred at more than the 1.2σ level to a point-like source emission by a likelihood ratio test. The wide excess sky map in Fig. 11 shows the H.E.S.S. joint observations of 1ES 1312-423 and Centaurus A. The θ^2-distribution around the direction of 1ES 1312-423 is shown in Fig. 12.

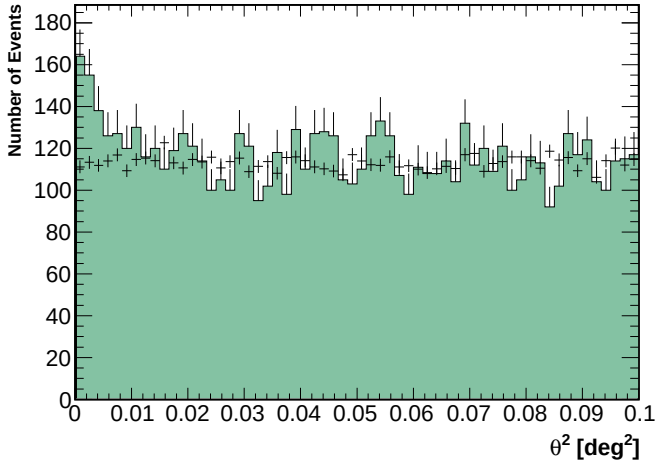

FIGURE 10. Distribution of the squared angular between the arrival direction of the γrays and the direction of SHBL J001355.9-185406. The filled histogram shows the ON events while the background derived from the OFF regions is shown with crosses.

2.3.1.2. *Spectral and temporal analysis*

The top panels of Fig. 13 show the differential energy spectrum of SHBL J001355.9-185406 and 1ES 1312-423. Power-law spectra represent reasonably well the data with reduced χ^2 of 25.1/19 ($\mathcal{P}_{\chi^2} = 15.7\%$) and 16.8/23 ($\mathcal{P}_{\chi^2} = 82.0\%$), respectively. Despite the residuals at the low and high-energy ends of the spectra, more complex models (cf. discussion in the next chapter) such as the log-parabola or the exponential cut-off power law are not favoured, with an improvement below the 1σ level (as given by a likelihood ratio test).

The spectra of these two VHE sources are characterized by a flux at 1 TeV of $\phi_{\rm SHBL}(1\ {\rm TeV}) = (1.16{\pm}0.45_{\rm stat}{\pm}0.23_{\rm sys}){\times}10^{-13}\ {\rm cm}^{-2}\ {\rm s}^{-1}\ {\rm TeV}^{-1}$, $\phi_{\rm 1ES}(1\ {\rm TeV}) = (1.07 \pm 0.36_{\rm stat} \pm 0.21_{\rm sys}) \times 10^{-13}\ {\rm cm}^{-2}\ {\rm s}^{-1}\ {\rm TeV}^{-1}$ and photon indices $\Gamma_{\rm SHBL} = 3.45 \pm 0.50_{\rm stat} \pm 0.2_{\rm sys}$, $\Gamma_{\rm 1ES} = 3.26 \pm 0.46_{\rm stat} \pm 0.2_{\rm sys}$. These fluxes at 1 TeV are equivalent to 3 milli-C.U., making these sources some of the faintest ones ever detected at VHE. I study in Appendix A the impact of the specific observation conditions

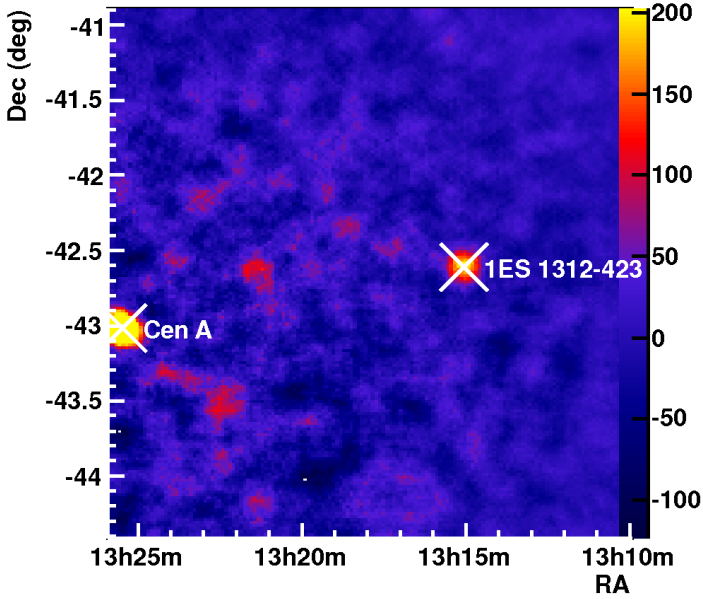

FIGURE 11. Sky map of the excess events detected with H.E.S.S. for observations centred on Centaurus A. 1ES 1312-423 is located in a gradient of acceptance as reflected by the background contrast decreasing with the distance to Centaurus A. The maximum of the color axis is set to 200 events per pixel of $0.1^{\circ} \times 0.1^{\circ}$.

of 1ES 1312-423 on the spectral reconstruction and show that the resulting uncertainty is negligible compared to the quoted systematic uncertainty.

SHBL J001355.9-185406 is detected with the *Model ++* analysis and with PMVA, the latter yielding compatible best fit parameters with a flux at 1 TeV of $(1.54 \pm 0.45) \times 10^{-13}$ cm^{-2} s^{-1} TeV^{-1} and an index of 2.8 ± 0.3. These two analyses rely on the same calibration. The lower sensitivity of the analyses exploiting a different calibration only enables a marginal detection of the source at the 3σ to 4σ depending on the analysis cuts, too low to derive a spectrum.

1ES 1312-423 is detected at the 5σ level with the HDMVA analysis, yielding a compatible flux level and an index of 2.5 ± 1.0, with a large statistical uncertainty. A 6σ detection is achieved with PMVA. and the

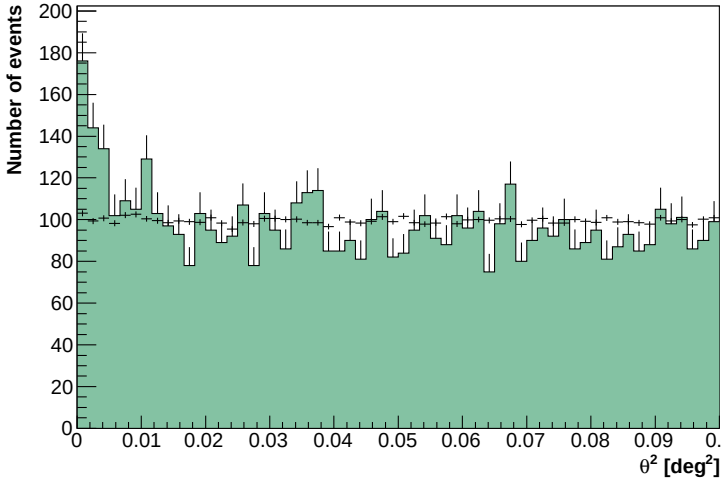

FIGURE 12. Distribution of the squared angular between the arrival direction of the γrays and the direction of 1ES 1312-423. The filled histogram shows the ON events while the background derived from the OFF regions is shown with crosses.

best fit parameters are $\phi_{\rm 1ES}^{\rm MVA}(1\ {\rm TeV}) = (1.89{\pm}0.58){\times}10^{-13}\ {\rm cm}^{-2}\ {\rm s}^{-1}\ {\rm TeV}^{-1}$ and $\Gamma_{\rm 1ES}^{\rm MVA} = 2.85 \pm 0.47$, compatible at the 1σ level with the values derived with the *Model ++* analysis. For the publications of the discovery of these sources, the *Model++* analysis was chosen for SHBL J001355.9-185406 and the MVA analysis was chosen for 1ES 1312-423.

I show in the bottom panels of Fig. 13 the light curves of SHBL J001355.9-185406 and 1ES 1312-423 above the threshold energies of 310 GeV and 210 GeV, respectively, on a period-by-period time scale. This binning, which I implemented in ParisAnalysis, is particularly adapted to H.E.S.S. observations, which are performed between two successive full moons. I carried out a search for variability (that I also implemented in ParisAnalysis) using the normalized excess variance (see e.g. Vaughan et al. 2003). This quantity is an estimator of the variance in the light curve normalized to the average flux and is obtained by subtracting the variance due to the uncertainties from the observed variance. A negative value implies that the statistical uncertainties dominate over the

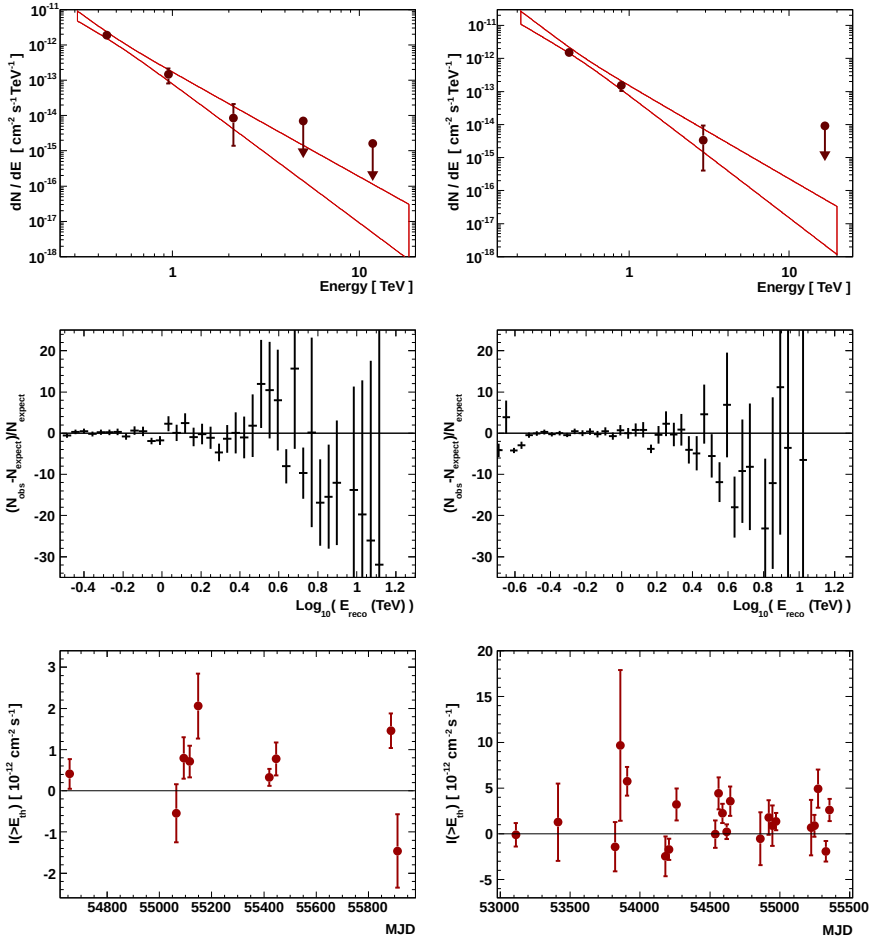

FIGURE 13. *Top panel:* Differential energy spectrum of SHBL J001355.9-185406 (left) and 1ES 1312-423 (right). *Middle panel:* Residuals of the spectra, i.e. normalized difference between the expected and measured numbers of events in each energy bin, logarithm of the reconstructed energy *Bottom panel:* Light curves of SHBL J001355.9-185406 (left) and 1ES 1312-423 (right) on the period, i.e. $\sim$ monthly, time scale.

intrinsic variations. For each of the two light curves, the normalized excess variance is compatible with zero at the 2σ level and I derived an upper limit at the 99% level using the method of Feldman & Cousins (1998). I obtain $V_{NXS}^{\rm SHBL} < 2.57$ and $V_{NXS}^{\rm 1ES} < 2.16$, which translates for the fractional variance (the square root of V_{NXS}, i.e. an estimator of the R.M.S. normalized to the flux) to values of 1.6 and 1.5. This indicates that average variations of the flux below the level of $\pm 150\%$ would not be detectable given the faintness of the sources and the sensitivity of the instrument.

2.3.2. Broad band SEDs

2.3.2.1. *Multi-wavelength data*

The discovery of a new source at VHE is team work, involving multi-wavelength experts in various astronomical fields. The analyses of the *Fermi*-LAT data at HE were performed by D. Sanchez, in collaboration with J. Perkins for 1ES 1312-423. The X-ray data acquired during dedicated observations with *Swift*-XRT (Burrows et al. 2005) were analysed by B. Giebels. The details of the analysis methods are given in the two publications and I only summarize the results hereafter.

The two sources are detected at the 6σ level in 3.5 years of *Fermi*-LAT observations, with rather hard HE spectra (photon indices of $\Gamma_{\rm SHBL}^{HE} = 1.96 \pm 0.20$ and $\Gamma_{\rm 1ES}^{HE} = 1.44 \pm 0.42$). The X-ray spectra exhibit significant curvature, with a log-parabola being preferred over a power law for both SHBL J001355.9-185406 and 1ES 1312-423, at the 3 and 8σ level, respectively.

The observations of *Swift*-XRT were accompanied with *Swift*-UVOT observations in the UV band. These data were analysed by S. Kaufmann and D. Horan for SHBL J001355.9-185406 and 1ES 1312-423, respectively. As mentioned in Sect. 2.1.1.1, ATOM also routinely observes the AGN targeted with H.E.S.S. and these data were calibrated by J.P. Lenain and G. Cologna. For 1ES 1312-423, radio observations were performed by R. Ojha with ATCA (Wilson et al. 2011; Stevens et al. 2012, Australia Telescope Compact Array).

In addition to these new data, the literature and public database NED and VizieR were searched for archival data in the radio to UV bands. The broad band SEDs of 1ES 1312-423 and SHBL J001355.9-185406 are shown in Fig. 14 and Fig. 15, respectively.

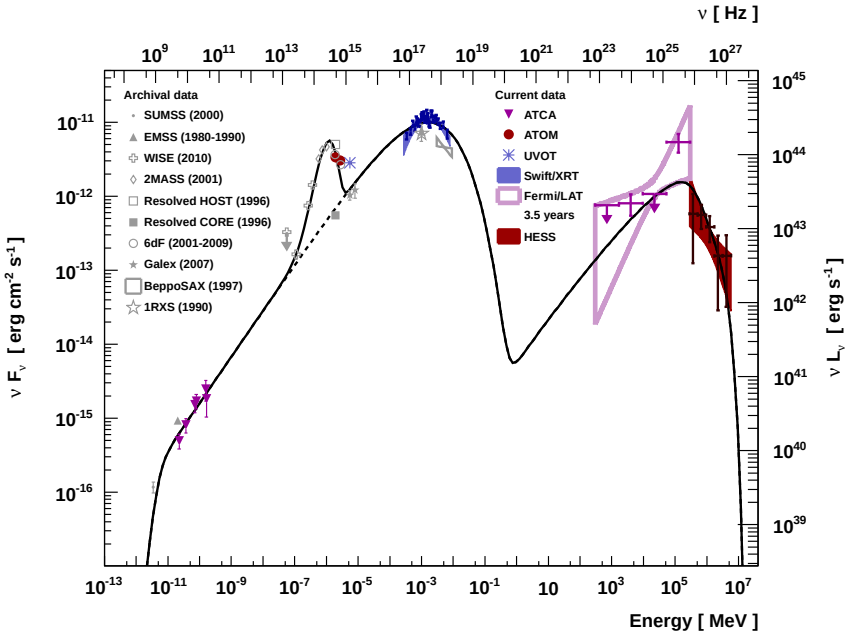

FIGURE 14. Broad-band spectral energy distribution of 1ES 1312-423. The data acquired/analysed for the publication of the VHE and HE discovery of this source are shown in the top right legend while the grey points, listed in the top left legend, correspond to archival data. The non-thermal emission is modelled within a SSC scenario (dashed line) and the thermal emission with black body spectrum - the sum being shown as the continuous line.

2.3.2.2. *Modelling of the emission*

I performed the modelling of the emission 1ES 1312-423 with a standard, one zone, homogeneous, time-independent SSC code that I developed from scratch[11]. Note that for both sources, the emission of

[11] A noticeable difference between my code and the codes developed by D. Sanchez or J. Kataoka, as described in their PhD manuscripts, is the use of the `gsl_sf_synchrotron_1 (double x)` function of the GNU Scientific Library, which significantly reduces the computation time of the program compared to the integration of the modified Bessel function $K_{5/3}$.

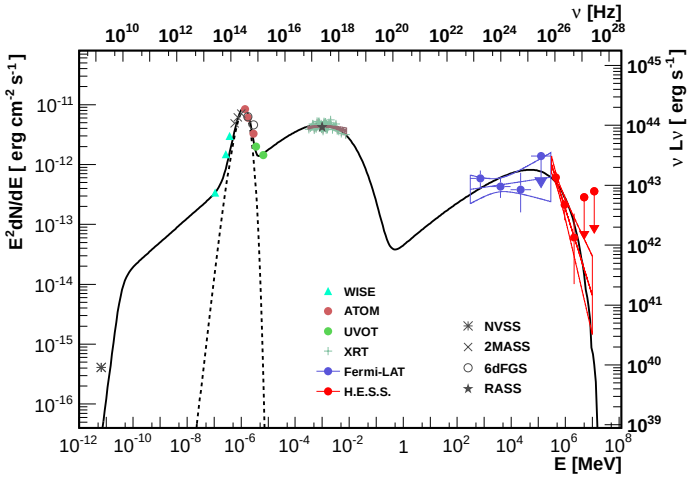

FIGURE 15. Broad-band spectral energy distribution of SHBL J001355.9-185406. The data acquired/analysed for the publication of the VHE and HE discovery of this source are shown in the bottom left legend while the grey points, listed in the bottom right legend, correspond to archival data. The IR to UV emission is modelled with a black-body spectrum (dashed line) while the non-thermal emission is modelled within a SSC scenario. The sum of the host and AGN contributions are shown as the continuous line. *Courtesy of D. Sanchez.*

the host galaxy from IR to UV is modelled with a simple black body spectrum as in Katarzyński et al. (2003).

As e.g. in Giebels et al. (2007), the population of radiating electrons is described by an EDF $n(\gamma) = n_0 \gamma^{-p} \exp(-\gamma/\gamma_{\rm cut})$, where $\gamma = E/m_e c^2$ is the Lorentz factor of the electrons, p is the electron index, n_0 a normalization factor and $\gamma_{\rm cut} m_e c^2$ a characteristic energy above which the electron population sharply drops. These electrons radiate in a spherical region of size R, a blob of plasma, which is filled with a constant tangled magnetic field B and which is assumed to move with a bulk Doppler factor δ, in the observer frame.

I already discussed in Sect. 1.2.2.2 the influence of SSC parameters on the synchrotron and inverse Compton bumps of the SED. For the modelling of the emission of 1ES 1312-423, I exploit the fact that the

Usual set	Description		New set	Description
B	Magnetic field	$=$	B	Magnetic field
δ	Doppler factor	$=$	δ	Doppler factor
R	Region size	$\neq$	νL_s	Sync. peak amplitude
n_0	EDF normalization	$\neq$	u_e/u_B	Equipartition factor
$\gamma_{\rm cut}$	EDF cut off	$\neq$	E_s	Sync. peak energy
p	EDF index	$=$	p	EDF index

TABLE 7. Parametrization of the SSC model. The conventional parameters are given on the left and the set of parameters that ease the modelling procedure is described on the right.

peak of the synchrotron component is tightly constrained by the X-ray measurement. The index of the EDF is also constrained by the radio to X-ray continuum, in particular with the optical measurement of Falomo & Ulrich (2000), who resolved the AGN (filled square in Fig. 14) and the host galaxy (total emission represented with an empty square in Fig. 14).

To account for these constraints on the index and on the synchrotron peak, I use the parameters described in Table 7. The peak of the synchrotron emission is defined by its amplitude νL_s which is proportional to $n_0\delta^4R^3B^2$ and by its peak energy[12] $E_s \propto B\delta\gamma_{\rm cut}^2$. Instead of parametrizing the EDF with its normalization, I use its integral via the equipartition factor u_e/u_B, which is the ratio of electron kinetic to magnetic energy density. This dimensionless factor enables a straightforward determination of the relative contributions of matter and electromagnetic field to the energy budget.

For a fixed set of B, δ, E_s, νL_s and u_e/u_B, the conventional parameters can be retrieved using $\gamma_{\rm cut} \propto \sqrt{E_s/B\delta}$, followed by $n_0 = (u_e/u_B) \times (B^2/4\pi)/m_ec^2 \int_1^{+\infty} \gamma^{-p} \exp(-\gamma/\gamma_{\rm cut})$ (in CGS unit for the magnetic energy) and $R \propto (\nu L_s/n_0\delta^4B^2)^{1/3}$. The dependence of the model on this new set of parameters for a fixed EDF index and a fixed location of the synchrotron peak $\{E_s, \nu L_s\}$ is shown in Fig. 16.

With all of the other parameters fixed, increasing the equipartition factor increases the EDF normalization and thus the amplitude of the

[12]The peak energy occurs at the maximum of $\gamma^3 n(\gamma)$, i.e. at $\gamma_{3p} = (3-p)\gamma_{\rm cut}$. I consider the EDF index p fixed by the data in the following.

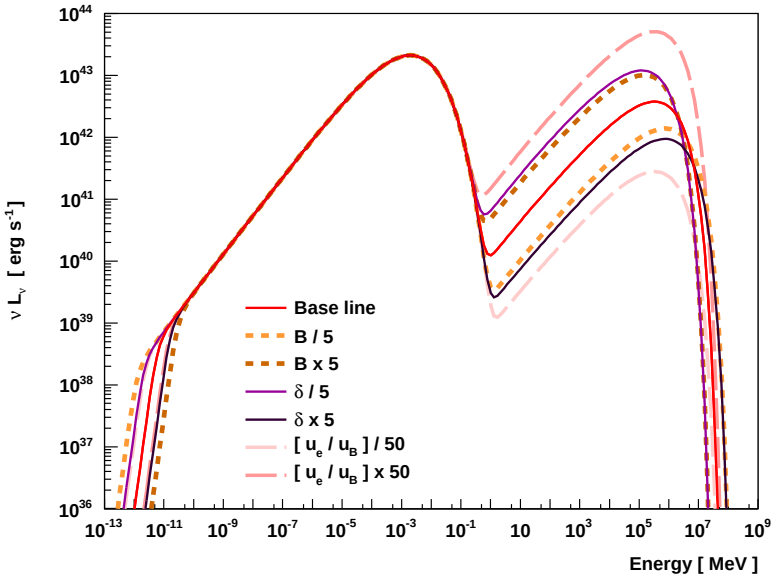

FIGURE 16. SSC model parametrized with the magnetic field B, the Doppler factor δ and the equipartition factor u_e/u_B for a fixed synchrotron peak location $\{E_s, L_s\}$ and EDF index p. The magnetic field and the Doppler factor have almost exactly opposite effects, characterized by a shift in energy and amplitude of the Compton component peak while the equipartition factor only impacts the amplitude of this bump. Note that the EBL absorption is not included for these curves.

Compton component without shifting its position. An increase in the magnetic field increases the amplitude of the Compton component, as with the conventional set of parameters, but shifts the peak toward low energies, because of the decrease of $\gamma_{\rm cut}$ (cf. previous paragraph). The Doppler factor has the opposite effect with an increased value shifting the peak to higher energies and reducing its amplitude. This is due to the decrease in the size of the emission region (cf. previous paragraph), which impacts the synchrotron and Compton components by factors of R^3 and R^4 (resp.) within the conventional parametrization.

The degeneracy of SSC models is easily demonstrated with this set of parameters where the magnetic field and the inverse of the Doppler factor have a similar effect on the emission[13]. This degeneracy could in principle be broken with the low-energy part of the spectrum which is governed by synchrotron self absorption. The observations in the radio domain are nonetheless usually interpreted as the superposition of the core emission and of more extended structures. They can thus only be used as upper limits on the modelled flux, imposing a lower limit on the magnetic field.

To break the degeneracy, I require that the magnetic energy and the electron kinetic energy be as close to each other as possible, which ensures a small energy budget. I also impose a Doppler factor as small as possible to comply with the Lorentz factor of $\Gamma \sim 3-4$ usually inferred for blazars, either from the radio observation or from the statistics of beamed object within the radio galaxies/BL Lac unification scheme (cf. bulk Lorentz factor crisis Henri & Saugé 2006). Note that this approach (minimisation of δ and of the difference between u_e and u_B) by consequence yields the maximal size allowed for the emission region. With these constraints, the SED of 1ES 1312-423 shown in Fig. 14 is well represented by the parameters given in Table 8.

index p	$\gamma_{\rm cut}$	u_{e^-}/u_B	B mG	δ	R $\times 10^{17}$ cm
1.75	8.8×10^5	40	10	7	2.6

TABLE 8. Parameters of the one zone SSC model of 1ES 1312-423.

The Doppler factor of 7 corresponds to a minimum Lorentz factor of $\Gamma_{\rm min} = \delta/2 = 3.5$, in agreement with the other constraints on this class of objects. The system is matter-dominated and clearly out of equipartition, by more than an order of magnitude. The rather low minimum magnetic field of 10 mG is on the order of the values derived for PKS 2155-304 during the multi-wavelength campaign reported in Aharonian et al. (2009b). The maximum size of the emission region

[13]Note that the slight difference in the high-energy end of the broad band spectrum between increasing the Doppler factor by α or decreasing the magnetic field by α is certainly due to γ-γ internal absorption and Klein-Nishina suppression.

is equivalent to 80 mpc, which corresponds to the typical size of the BLR.

Finally, note that the model adopted for the EDF is self consistent. Indeed a break in the index of $\Delta p = 1$ is expected at the electron energy for which the cooling time equals the time needed to escape the region, typically R/c to $R/(c/3)$ (cf. e.g. Tavecchio et al. 1998). Here the cooling of the electrons is dominated by the synchrotron emission (of larger amplitude than the Compton component), which reads $t_{\rm cool} = \left[\frac{4}{3}\,\frac{\sigma_T c}{m_e c^2}\,\gamma\,u_B\right]^{-1} \sim R/c$. This corresponds to the maximum energy of the electrons at $\sim \gamma_{\rm cut}$ and the $\Delta p = 1$ break can be neglected in comparison with the EDF cut off.

Similar parameters are derived for the emission of SHBL J001355.9-185406, with a magnetic field of 50 mG, a Doppler factor of 10, an EDF cut off at $\gamma_{\rm cut} = 6 \times 10^5$, an emission region of 15 mpc and a system out of equipartition by a factor of 50. This tendency for SSC models to be dominated by matter rather than by magnetic fields (Böttcher 2007) has also been observed for the bright BL Lac objects Mrk 421 and Mrk 501 (Mankuzhiyil et al. 2012).

2.3.2.3. *Conclusion on the observations of AGN with* H.E.S.S.

The observation campaigns carried out during the past decade by H.E.S.S. on the South hemisphere extragalactic sky have discovered almost 40% of the 54 AGN detected so far at VHE. H.E.S.S. observations also resulted in stringent constraints on the VHE emission of half a hundred targets, as derived herein.

While SSC modellings are usually in good agreement with the SEDs of HBLs, they are not favoured when considering objects peaking at lower energies, such as FSRQs or the recently discovered LBL AP Lib (Hofmann 2010a). HBLs though seem to require out-of-equipartition systems with weakly-magnetized emission regions. The matter-dominated SSC modelling is not necessarily at odds with a magnetically dominated jet, since as noted by Giannios (2012), acceleration mechanisms such as efficient reconnection may result in a heat-dominated (or particle-dominated) plasma.

Deep field exposures and enhanced analysis techniques are revealing objects as faint as a few milli-C.U. and the growing number of detected sources is paving the road for the next generation instruments, discussed in Chapter 5. Generalizing simple modellings such as performed

for 1ES 1312-423 and SHBL J001355.9-185406 to a whole population of VHE HBLs will certainly enable the identification of tendencies for important quantities such as the equipartition factor, improving our understanding of the properties of the plasma conveyed in the jets of AGN.

Bibliography

Abdo, A. A., Ackermann, M., Ajello, M., et al. 2010, ApJ, 708, 1310

Abramowski, A., Acero, F., Aharonian, F., et al. 2012, ApJ, 746, 151

Acciari, V. A., Aliu, E., Arlen, T., et al. 2009, ApJ, 695, 1370

Acciari, V. A., Aliu, E., Beilicke, M., et al. 2010, ApJ, 709, L163

Acciari, V. A., Aliu, E., Beilicke, M., et al. 2008, ApJ, 684, L73

Ackermann, M., Ajello, M., Allafort, A., et al. 2011, ApJ, 743, 171

Aharonian, F., Akhperjanian, A., Beilicke, M., et al. 2003, A&A, 403, L1

Aharonian, F., Akhperjanian, A. G., Anton, G., et al. 2010, A&A, 521, A69

Aharonian, F., Akhperjanian, A. G., Anton, G., et al. 2009a, A&A, 502, 749

Aharonian, F., Akhperjanian, A. G., Anton, G., et al. 2009b, ApJ, 696, L150

Aharonian, F., Akhperjanian, A. G., Anton, G., et al. 2009c, ApJ, 695, L40

Aharonian, F., Akhperjanian, A. G., Aye, K.-M., et al. 2005a, A&A, 437, 95

Aharonian, F., Akhperjanian, A. G., Aye, K.-M., et al. 2005b, A&A, 436, L17

Aharonian, F., Akhperjanian, A. G., Aye, K.-M., et al. 2005c, A&A, 430, 865

Aharonian, F., Akhperjanian, A. G., Barres de Almeida, U., et al. 2007a, A&A, 475, L9

Aharonian, F., Akhperjanian, A. G., Barres de Almeida, U., et al. 2007b, A&A, 473, L25

Aharonian, F., Akhperjanian, A. G., Barres de Almeida, U., et al. 2008a, A&A, 478, 387

Aharonian, F., Akhperjanian, A. G., Barres de Almeida, U., et al. 2008b, A&A, 481, L103

Aharonian, F., Akhperjanian, A. G., Bazer-Bachi, A. R., et al. 2007c, ApJ, 664, L71
Aharonian, F., Akhperjanian, A. G., Bazer-Bachi, A. R., et al. 2006a, A&A, 457, 899
Aharonian, F., Akhperjanian, A. G., Bazer-Bachi, A. R., et al. 2006b, A&A, 455, 461
Aharonian, F., Akhperjanian, A. G., Bazer-Bachi, A. R., et al. 2006c, A&A, 448, L19
Aharonian, F., Akhperjanian, A. G., Bazer-Bachi, A. R., et al. 2006d, Nature, 440, 1018
Aharonian, F., Akhperjanian, A. G., Bazer-Bachi, A. R., et al. 2005d, A&A, 442, 895
Aharonian, F., Akhperjanian, A. G., Bazer-Bachi, A. R., et al. 2005e, A&A, 441, 465
Aharonian, F., Akhperjanian, A. G., Bazer-Bachi, A. R., et al. 2007d, A&A, 470, 475
Aharonian, F., Akhperjanian, A. G., Bazer-Bachi, A. R., et al. 2006e, Science, 314, 1424
Albert, J., Aliu, E., Anderhub, H., et al. 2006, ApJ, 642, L119
Albert, J., Aliu, E., Anderhub, H., et al. 2007, ApJ, 666, L17
Aleksić, J., Antonelli, L. A., Antoranz, P., et al. 2011a, ApJ, 730, L8
Aleksić, J., Antonelli, L. A., Antoranz, P., et al. 2011b, A&A, 530, A4
Aliu, E., Archambault, S., Arlen, T., et al. 2012, ApJ, 750, 94
Becherini, Y., Djannati-Ataï, A., Marandon, V., Punch, M., & Pita, S. 2011, Astroparticle Physics, 34, 858
Bernlöhr, K., Carrol, O., Cornils, R., et al. 2003, Astroparticle Physics, 20, 111
Böttcher, M. 2007, Ap&SS, 309, 95
Burrows, D. N., Hill, J. E., Nousek, J. A., et al. 2005, Space Sci. Rev., 120, 165
Catanese, M., Akerlof, C. W., Badran, H. M., et al. 1998, ApJ, 501, 616
Chadwick, P. M., Lyons, K., McComb, T. J. L., et al. 1999, Astroparticle Physics, 11, 145
Cornils, R., Gillessen, S., Jung, I., et al. 2003, Astroparticle Physics, 20, 129
Costamante, L. & Ghisellini, G. 2002, A&A, 384, 56
D'Abrusco, R., Massaro, F., Ajello, M., et al. 2012, ApJ, 748, 68

de Naurois, M. 2012, Very High Energy astronomy from H.E.S.S. to CTA. Opening of a new astronomical window on the non-thermal Universe (TEL), http://tel.archives-ouvertes.fr/tel-00687872
de Naurois, M. & Rolland, L. 2009, Astroparticle Physics, 32, 231
Falomo, R. & Ulrich, M.-H. 2000, A&A, 357, 91
Feldman, G. J. & Cousins, R. D. 1998, Phys. Rev. D, 57, 3873
Fossati, G., Maraschi, L., Celotti, A., Comastri, A., & Ghisellini, G. 1998, MNRAS, 299, 433
Fumagalli, M., Furniss, A., O'Meara, J. M., et al. 2012, arXiv:1207.3592
Funk, S., Hermann, G., Hinton, J., et al. 2004, Astroparticle Physics, 22, 285
Ghisellini, G., Celotti, A., Fossati, G., Maraschi, L., & Comastri, A. 1998, MNRAS, 301, 451
Giannios, D. 2012, arXiv:1211.0296
Giebels, B., Dubus, G., & Khélifi, B. 2007, A&A, 462, 29
Gioia, I. M., Maccacaro, T., Schild, R. E., et al. 1990, ApJS, 72, 567
Giommi, P., Piranomonte, S., Perri, M., & Padovani, P. 2005, A&A, 434, 385
Hauser, M., Möllenhoff, C., Pühlhofer, G., et al. 2004, Astronomische Nachrichten, 325, 659
Heck, D., Knapp, J., Capdevielle, J. N., Schatz, G., & Thouw, T. 1998, CORSIKA: a Monte Carlo code to simulate extensive air showers.
Henri, G. & Saugé, L. 2006, ApJ, 640, 185
H.E.S.S. Collaboration, Abramowski, A., Acero, F., et al. 2011, A&A, 529, A49
H.E.S.S. Collaboration, Abramowski, A., Acero, F., et al. 2012, A&A, 539, A149
HESS Collaboration, Abramowski, A., Acero, F., et al. 2012, arXiv:1204.1964
H.E.S.S. Collaboration, Abramowski, A., Acero, F., Aharonian, F., et al. 2011, A&A, 533, A110
H.E.S.S. Collaboration, Abramowski, A., Acero, F., Aharonian, F., et al. 2010a, A&A, 516, A56
H.E.S.S. Collaboration, Abramowski, A., Acero, F., Aharonian, F., et al. 2010b, A&A, 520, A83
H.E.S.S. Collaboration, Acero, F., Aharonian, F., Akhperjanian, A. G., et al. 2010, A&A, 511, A52
Hillas, A. M. 1985, in International Cosmic Ray Conference, Vol. 3,

International Cosmic Ray Conference, ed. F. C. Jones, 445–448
Hofmann, W. 2010a, The Astronomer's Telegram, 2743, 1
Hofmann, W. 2010b, The Astronomer's Telegram, 3007
Horan, D., Badran, H. M., Bond, I. H., et al. 2002, ApJ, 571, 753
Jones, D. H., Read, M. A., Saunders, W., et al. 2009, MNRAS, 399, 683
Katarzyński, K., Sol, H., & Kus, A. 2003, A&A, 410, 101
Kertzman, M. P. & Sembroski, G. H. 1994, Nuclear Instruments and Methods in Physics Research A, 343, 629
Landt, H. 2012, MNRAS, 423, L84
Lenain, J.-P., Ricci, C., Türler, M., Dorner, D., & Walter, R. 2010, A&A, 524, A72
Li, T.-P. & Ma, Y.-Q. 1983, ApJ, 272, 317
Louedec, K. & Will, M. 2012, arXiv:1207.3534
Mankuzhiyil, N., Ansoldi, S., Persic, M., et al. 2012, ApJ, 753, 154
Mao, L. S. 2011, New A, 16, 503
Mariotti, M. 2010, The Astronomer's Telegram, 2510, 1
Mariotti, M. 2011, The Astronomer's Telegram, 3100, 1
Mariotti, M. & MAGIC Collaboration. 2010, The Astronomer's Telegram, 2916, 1
Neshpor, Y. I., Chalenko, N. N., Stepanian, A. A., et al. 2001, Astronomy Reports, 45, 249
Neshpor, Y. I., Stepanyan, A. A., Kalekin, O. P., et al. 1998, Astronomy Letters, 24, 134
Nishiyama, T. 1999, in International Cosmic Ray Conference, Vol. 3, International Cosmic Ray Conference, 370
Ohm, S., van Eldik, C., & Egberts, K. 2009, Astroparticle Physics, 31, 383
Ong, R. A. 2009a, The Astronomer's Telegram, 2084, 1
Ong, R. A. 2009b, The Astronomer's Telegram, 2260, 1
Ong, R. A. 2010, The Astronomer's Telegram, 2786, 1
Piron, F., Djannati-Atai, A., Punch, M., et al. 2001, A&A, 374, 895
Pita, S., Goldoni, P., Boisson, C., et al. 2012, arXiv:1208.1785
Punch, M., Akerlof, C. W., Cawley, M. F., et al. 1992, Nature, 358, 477
Quinn, J., Akerlof, C. W., Biller, S., et al. 1996, ApJ, 456, L83
Rau, A., Schady, P., Greiner, J., et al. 2012, A&A, 538, A26

Raue, M., Behera, B., Charbonnier, A., et al. 2009, The Astronomer's Telegram, 2350, 1

Rector, T. A., Stocke, J. T., Perlman, E. S., Morris, S. L., & Gioia, I. M. 2000, AJ, 120, 1626

Sbarufatti, B., Treves, A., & Falomo, R. 2005, ApJ, 635, 173

Schwope, A., Hasinger, G., Lehmann, I., et al. 2000, Astronomische Nachrichten, 321, 1

Stecker, F. W., de Jager, O. C., & Salamon, M. H. 1996, ApJ, 473, L75

Stevens, J., Edwards, P. G., Ojha, R., et al. 2012, arXiv:1205.2403, Proceedings of Fermi and Jansky: Our Evolving Understanding of AGN, St Michaels, MD, November 10-12, 2011, edited by R. Ojha, D. J. Thompson and C. Dermer, eConf C1111101 (2011)

Stocke, J. T., Morris, S. L., Gioia, I. M., et al. 1991, ApJS, 76, 813

Tavecchio, F., Maraschi, L., & Ghisellini, G. 1998, ApJ, 509, 608

Teshima, M. & MAGIC Collaboration. 2008, The Astronomer's Telegram, 1500, 1

The HESS Collaboration, Abramowski, A., Acero, F., et al. 2012, arXiv:1201.2044

Vaughan, S., Edelson, R., Warwick, R. S., & Uttley, P. 2003, MNRAS, 345, 1271

Vincent, P., Denanca, J.-P., Huppert, J.-F., et al. 2003, in International Cosmic Ray Conference, Vol. 5, International Cosmic Ray Conference, 2887

Voges, W., Aschenbach, B., Boller, T., et al. 1996, IAU Circ., 6420, 2

Wagner, S. J. & H.E.S.S. Collaboration. 2010, in AAS/High Energy Astrophysics Division, Vol. 11, AAS/High Energy Astrophysics Division #11, 27.06

Wilson, W. E., Ferris, R. H., Axtens, P., et al. 2011, MNRAS, 416, 832

Wolter, A., Comastri, A., Ghisellini, G., et al. 1998, A&A, 335, 899

Wystan Benbow for the VERITAS Collaboration. 2011, arXiv:1110.0040

CHAPTER 3

Spectral studies: first EBL measurement at VHE

In this chapter, I perform the first detection of the EBL imprint in the VHE spectra of blazars. After a presentation of the methods and datasets in Sect. 3.1, I perform in Sect. 3.2 the analysis that has enabled this detection. I use the measurement of the EBL to derive the intrinsic spectra of the brightest blazars detected with H.E.S.S. in Sect. 3.3 and discuss their consistency in a multi-wavelength context.

3.1. Spectral modelling and datasets

The spectrum of VHE blazars that is measured on Earth can be described with the two terms given in Eq. (3.1):

$$\phi(E, z) = \phi_{\rm int}(E) \times \exp(-\tau(E, z, n)) \tag{3.1}$$

where ϕ is the measured flux, E is the γ-ray energy and z is the redshift of the source.

The first term $\phi_{\rm int}$ is the intrinsic spectrum, which is presumably independent of cosmic evolution factors for local ($z \leq 0.3$) blazars (see Reimer 2007, for distant FSRQs). The second term, which is extrinsic to the source, quantifies the EBL absorption of γ rays. The optical depth τ for a γ ray of energy E emitted at a redshift z depends on the density n of target EBL photons. There is a growing consensus on the modelling of the COB density n, as discussed in Chapter 1.3.2, and I consider in the following that its overall SED is known within a multiplicative constant close to unity.

3.1.1. Intrinsic spectrum

I parametrize the intrinsic spectra with the most natural functional forms that can be expected for a non-thermal emission. The simplest energy dependence of such an emitted spectrum is the power law, a

linear function in log-log scale:

$$\text{PWL}: \quad \phi_{\text{PWL}}(E) = \phi_0 (E/E_0)^{-\Gamma} \tag{3.2}$$

which is defined with the normalization factor ϕ_0 and the photon index Γ. E_0 is the reference energy, which can be fixed e.g. to 1 TeV or to the de-correlation energy. In the latter case, the correlation between the best fit parameters is minimum but their determination requires a larger computational time since the reference energy is iteratively[1] computed.

To account for intrinsic curvature, one can go to the next order of complexity using the log-parabola, which is the equivalent of the parabola in log-log scale:

$$\text{LP}: \quad \phi_{\text{LP}}(E) = \phi_0 (E/E_0)^{-\alpha - \beta \log(E/E_0)} \tag{3.3}$$

where α is the photon index at E_0 and β parametrizes the curvature, i.e. $\log \phi_{\text{LP}}(E) = \log \phi_0 - \alpha \log(E/E_0) - \beta \log^2(E/E_0)$.

As for a Taylor expansion, one could imagine that the next step would be to use the functional form that corresponds to the cubic polynomial in log-log scale:

$$\text{LCubic}: \quad \phi_{\text{LCubic}}(E) = \phi_0 (E/E_0)^{-\alpha - \beta \log(E/E_0) - \gamma \log^2(E/E_0)} \tag{3.4}$$

and so on.

There are two strong arguments against such a procedure. First, the emission of blazars is expected to smoothly vary over the VHE range and one does not expect the inflection point that would inevitably occur at $\log(E/E_0) = -\beta/3\gamma$ for a cubic form. Secondly, the modelling of an exponential cut off, which is expected on theoretical grounds (intrinsic cut off or Klein-Nishina suppression), would require a high polynomial order and thus a large number of free parameters, unreasonably widening the parameter space.

To overcome these issues, I use the exponential cut-off power-law model:

$$\text{EPWL}: \quad \phi_{\text{EPWL}}(E) = \phi_0 (E/E_0)^{-\Gamma} \exp(-E/E_{\text{cut}}) \tag{3.5}$$

[1] An educated guess of the value of the de-correlation energy as a function of the initial parameters is made at the beginning of the fitting procedure and is compared to the de-correlation energy that is computed at the end of the first step. If the difference is not negligible compared to the energy resolution, the reference energy is fixed to the previously computed de-correlation energy and the fit is performed again.

where $E_{\rm cut}$ is the cut-off energy.

The next order models (i.e. with an extra parameter) are the exponential cut-off log parabola:

$$\text{ELP}: \quad \phi_{\rm ELP}(E) = \phi_0 (E/E_0)^{-\alpha-\beta\log(E/E_0)} \exp(-E/E_{\rm cut}) \tag{3.6}$$

and the super exponential cut-off power law:

$$\text{SEPWL}: \quad \phi_{\rm EPWL}(E) = \phi_0 (E/E_0)^{-\Gamma} \exp\left(-(E/E_{\rm cut})^{\epsilon}\right) \tag{3.7}$$

where $\epsilon > 0$ parametrizes the sharpness of the cut off.

One can note that the ELP model presents an inflection point for $\beta < 0$ at $\log(E/E_0) = \log(-2\beta)$. Nonetheless, this model has the advantage of being nested[2] to the LP and to the EPWL models.

In the following, though the parameters are left free to vary in non-physical ranges (e.g. $\beta < 0$ for the LP when a convex spectrum is not expected), I check *a posteriori* that the best fit values of the parameters converge in physical regions. In any case, allowing a wider parameter range to be probed results in larger statistical uncertainties which attests of the conservativeness of the approach.

I show in Fig. 1 the energy dependence of the five models that are used in this study, for a given set of parameters.

3.1.2. EBL absorption

If the absorption of γ rays by the EBL followed a simple exponential cut-off function of energy, it could hardly be disentangled from an intrinsic cut off such as shown in Fig. 1. The detection of the EBL imprint in γ-ray spectra relies on a very specific characteristic: a non concave energy dependence with inflection points, as well as a redshift dependence of the absorption. The extragalactic spectra measured with H.E.S.S. typically span 200 GeV to 10 TeV, a population of γ rays which preferentially interacts with the EBL photons between 0.2 μm and 10 μm, i.e. the bulk of the photons of the COB.

[2] A complex model is nested to a simpler one if a continuous change of its parameters result in the simpler one, e.g. the LP and the PWL models are nested ($\beta \to 0$).

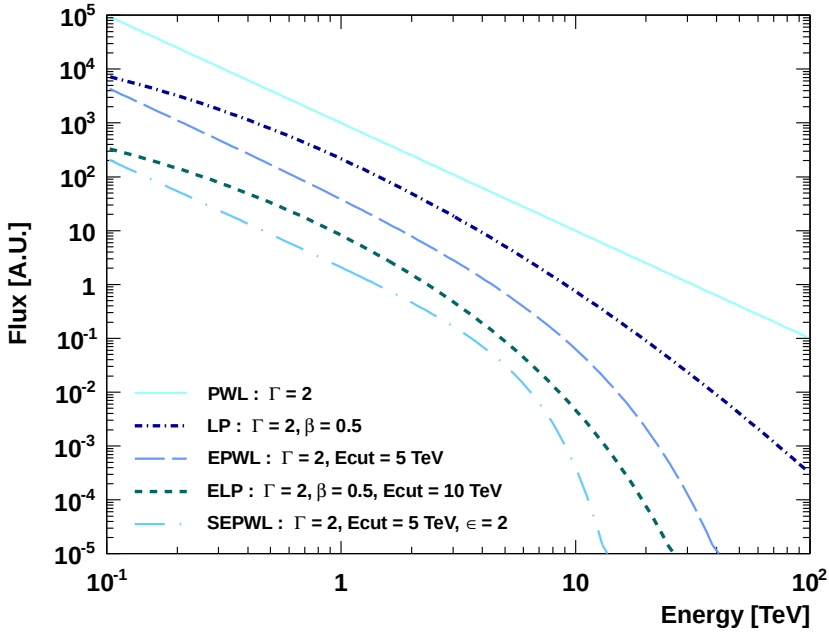

FIGURE 1. Modelling of the intrinsic spectrum. The five models are shown for a given set of parameters.

In the following, I use the optical depth derived by FR08, which has the technical advantage of being finely sampled[3] in redshift ($\mathrm{d}z = 10^{-3}$) and energy (50 logarithmic steps between 20 GeV and 170 TeV). The FR08 EBL absorption $\exp(-\tau)$ as a function of the γ-ray energy is shown for different redshifts in Fig. 2.

In the following, the spectra measured with H.E.S.S. are parametrized as in Eq. (3.8):

$$\phi(E, z) = \phi^{\alpha}_{\mathrm{int}}(E) \times \exp(-\alpha \times \tau(E, z, n_{\mathrm{FR008}})) \tag{3.8}$$

The intrinsic spectrum is modeled either with a PWL, a LP, an EPWL, an ELP or a SEPWL as described in Eq. (3.2), Eq. (3.3), Eq. (3.5), Eq. (3.6) and Eq. (3.7), respectively. The template of FR08 is used for the EBL optical depth, a choice which marginally impacts the analysis, as is quantified in the following.

[3]A table of the optical depth for redshifts between 10^{-3} and 1 can be found at http://www.astro.unipd.it/background/.

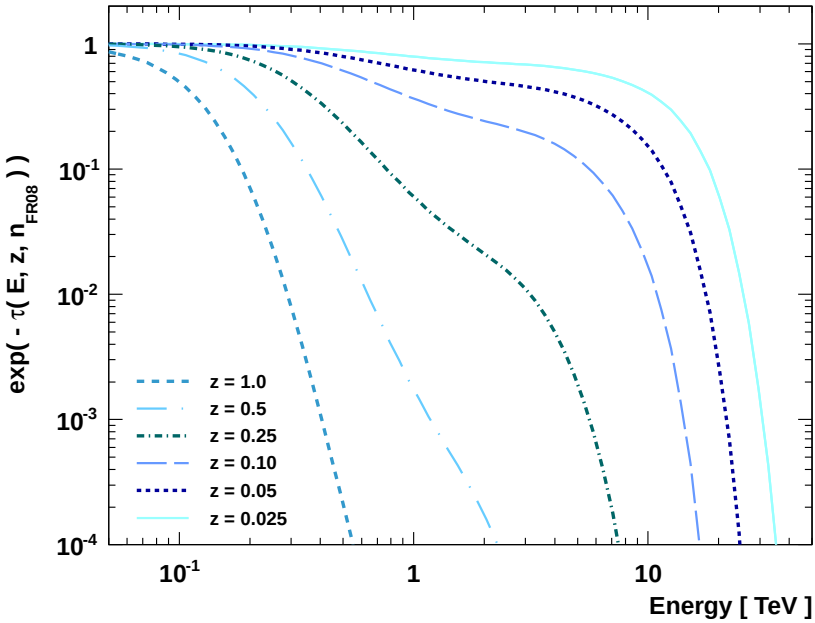

FIGURE 2. EBL absorption vs γ-ray energy for various redshifts, as modeled by FR08.

Eq. (3.8) mainly differs from Eq. (3.1) by the factor α, originally used in Abdo et al. (2010) to set an upper limit on the high-z EBL. In the following, I call α the EBL optical depth normalization or simply the EBL normalization. This parameter is the quantity that quantifies the "amount" of template absorption that is present in H.E.S.S. spectra. Writing the "true" Universe optical depth to γ rays $\tau(E, z, n)$ and assuming[4] $\tau(E, z, n) \propto n$, one can express α as:

$$\alpha = < \frac{\tau(E, z, n)}{\tau(E, z, n_{\mathrm{FR008}})} >_{E,z} \sim < \frac{n(\lambda, z)}{n_{\mathrm{FR008}}(\lambda, z)} >_{\lambda,z} \tag{3.9}$$

where the $<>_X$ operator is the average over X.

This parametrization of the EBL absorption with a multiplicative factor remains valid as long as the deviations to the model of FR08 as

[4]Note that there are integrations over redshift, EBL photon energy and pitch angle, so the approximation consist in assuming that the corrective multiplicative factor α barely depends on these quantities.

a function of energy and redshift are small, i.e. as long as α remains close to one, which can be checked *a posteriori*.

3.1.3. Datasets

For this study, I compile one of the largest dataset used so far in a VHE publication. With a total acceptance corrected live time of $\sim$ 380 hours, this dataset corresponds to almost twice the amount of data published in Aharonian et al. (2006a) for the H.E.S.S. Galactic survey. Particular attention is paid to variable sources.

3.1.3.1. *Data selection*

The datasets analyzed in this study are listed in Table 1. The detailed list of the observation runs, which are selected with standard quality cuts and intersected with the run-lists established with the tool associated to HDMVA, can be found in Appendix B.3.

These datasets are analyzed with *Model++ Loose cuts* (de Naurois & Rolland 2009) and result in a total excess of $\sim$ 74 000 γ rays from the brightest blazars observed by H.E.S.S.. I define the energy threshold as the energy for which the acceptance reaches 10% of its nominal value. This set of cuts results in an energy threshold that is lower than that derived with the conventional Hillas method (see Chapter 2.1.1.3), allowing the non EBL-absorbed part of the spectrum to be partially probed (cf. column 4 in Table 1). This yields an improved reconstruction of the intrinsic spectrum as well as of the EBL imprint.

3.1.3.2. *Subsets on highly significant sources*

Blazars such as PKS 2155-304 can exhibit spectral variations correlated with the flux at VHE, as shown in H.E.S.S. Collaboration, Abramowski et al. (2010) and as discussed in Chapter 4.1. A smearing of these variations would increase the variance from energy bin to energy bin and reduce the quality of the fit (as measured e.g. by the χ^2 probability) as well as the accuracy of the measurement.

To minimize this effect, the datasets on PKS 2155-304, Mrk 421 and PKS 2005-489 are divided in sub-sets of similar excess and flux range (in log-scale). Assuming a power-law spectrum in a reduced energy range ($0.2 - 1$ TeV for PKS 2155-304 and PKS 2005-489, $1 - 5$ TeV for Mrk 421), I perform the division sorting the runs by flux level and plotting the cumulated excess as a function of the flux.

Source	z	LT h	N_γ	σ	$E_{\rm min} - E_{\rm max}$ TeV
Mrk 421 (*1*)	0.031	4.8	3381	96.7	$0.95 - 41$
Mrk 421 (*2*)	0.031	3.9	5548	135	$0.95 - 37$
Mrk 421 (*3*)	0.031	2.6	5156	134	$0.95 - 45$
PKS 2005-489 (*1*)	0.071	68.6	1540	25.3	$0.16 - 37$
PKS 2005-489 (*2*)	0.071	17.6	910	28.9	$0.18 - 25$
PKS 2155-304 (*2008*)	0.116	24.0	5279	99.2	$0.13 - 19$
PKS 2155-304 (*1*)	0.116	7.1	3499	93.0	$0.13 - 5.7$
PKS 2155-304 (*2*)	0.116	6.0	3470	116	$0.13 - 9.3$
PKS 2155-304 (*3*)	0.116	5.7	9555	186	$0.13 - 14$
PKS 2155-304 (*4*)	0.116	2.5	4606	132	$0.18 - 4.6$
PKS 2155-304 (*5*)	0.116	3.4	11901	219	$0.13 - 5.7$
PKS 2155-304 (*6*)	0.116	1.2	6494	166	$0.15 - 5.7$
PKS 2155-304 (*7*)	0.116	1.2	8253	191	$0.20 - 7.6$
1ES 0229+200	0.14	55.1	670	12.6	$0.29 - 25$
H 2356-309	0.165	88.5	1642	21.2	$0.11 - 34$
1ES 1101-232	0.186	56.8	1268	17.8	$0.12 - 23$
1ES 0347-121	0.188	31.9	604	13.5	$0.13 - 11$

TABLE 1. VHE blazars detected by H.E.S.S. used for this study of the EBL. The data sets on highly variable sources are divided into smaller subsets which are indexed in column 1 and correspond to restricted flux ranges. The redshifts of the sources are given in column 2. The acceptance corrected live time (in hours), photon excess, detection significance and energy range of the spectra (in TeV) are given in column 3, 4, 5 and 6, respectively.

The basic spectral analysis of the seven subsets that I obtained for PKS 2155-304, assuming a power-law spectrum in the $0.2 - 1$ TeV range, is in good agreement with the independent analysis published in H.E.S.S. Collaboration, Abramowski et al. (2010), as shown in Fig. 3. The slight differences between the two analyses (e.g. point at $\Phi \sim 10^{-9}$ cm^{-2} s^{-1}) can be attributed to the different versions of the calibration, to a different run selection and to the different grouping of

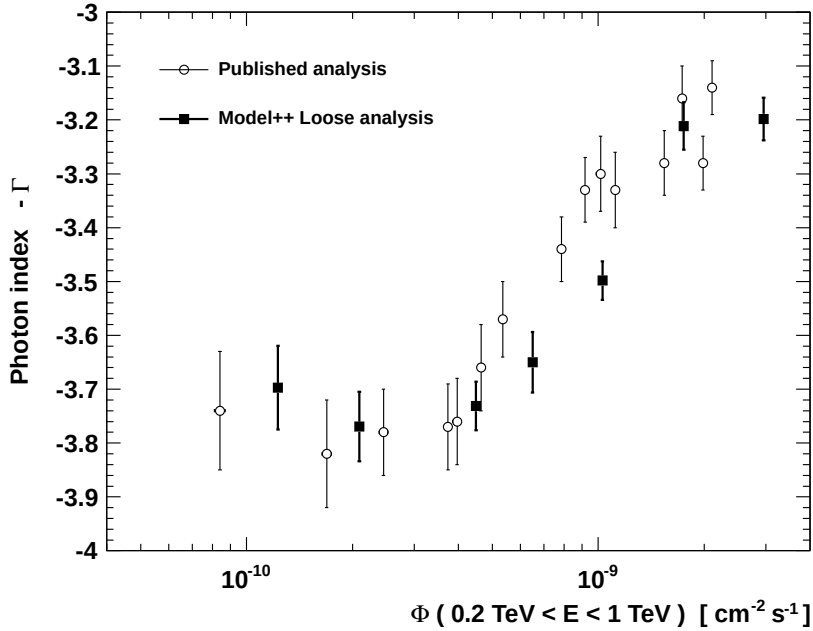

FIGURE 3. Photon Index -Γ vs integral flux in the 0.2 − 1 TeV energy range. The filled black points show the spectral parameters of datasets *1* to *7* on PKS 2155-304 while the empty circles show the published data.

runs. All the spectra analyzed in this study are found in good agreement with those previously published.

3.2. Analysis and discussion

3.2.1. Spectral analysis

The spectral model given by $\phi(E,z) = \phi_{\rm int}^{\alpha}(E)\mathrm{e}^{-\alpha\tau(E,z)}$ is fitted to the datasets for the smooth intrinsic models described in the previous sections and fixing α to eleven values between 0 and 2.5. The intrinsic spectral parameters are left free during the fitting procedure and a different set of best fit parameters is achieved for each value α. The fit relies on the forward-folding method described in Piron et al. (2001). The likelihood $\mathcal{L}$ of each set of best fit parameters can be converted into an equivalent $\chi^2 = -2\log\mathcal{L}$, given the proper normalization of the

likelihood. The associated number of degrees of freedom dof is then simply obtained subtracting the number of parameters of the model from the number of energy bins used in the fit and the conventional χ^2 probability $\mathcal{P}(\chi^2, dof)$ can be determined.

3.2.1.1. *Selection of the intrinsic model*

For each dataset, the likelihood and χ^2 probability profiles of the various smooth intrinsic models as a function of the parameter α are compared to select the most appropriate intrinsic model. I show in Fig. 4 the example of the profiles of the PWL, LP and EPWL models for the dataset on 1ES 0229+200.

The top panel shows the likelihood profile of the three models. One can note that the likelihood of the LP is not larger than the likelihood of the PWL for any α, while the EPWL is marginally larger for α close to zero.

For a given α, the improvement of the fit for two nested models can easily be quantified, in term of Gaussian standard deviation, as the square root of the difference between the $2\log\mathcal{L}$ (likelihood ratio test). In the case of the EPWL, the improvement compared to the PWL for $\alpha = 0$ is on the order of $\sqrt{0.5} \sim 0.7\sigma$ and is not considered as significant. This kind of reasoning is the usual way of selecting the model: one imposes a threshold on the significance of the improvement and selects the most complex model if it passes the threshold, otherwise the simpler model is chosen. Such likelihood ratio tests work as long as the models are nested but the approach would be meaningless if one wanted to compare e.g. a LP and a EPWL. Moreover, the higher the significance threshold, the simpler the intrinsic model and such an approach would partially neglect the intrinsic curvature and would overestimate the curvature due to the EBL absorption.

To circumvent these problems and fully account for intrinsic curvature, the model with the largest χ^2 probability is selected, as shown on the bottom panel of Fig. 4. In simple cases such as for the dataset on 1ES 0229+200, the profiles for the SEPWL and ELP models are not computed: they are not expected to improve the quality of the fit since the LP or the EPWL models do not improve the fit in comparison with the PWL hypothesis. They must be checked when the EPWL or the LP model are preferred to the PWL and they become crucial when there is an ambiguity between the LP and EPWL models. Such an

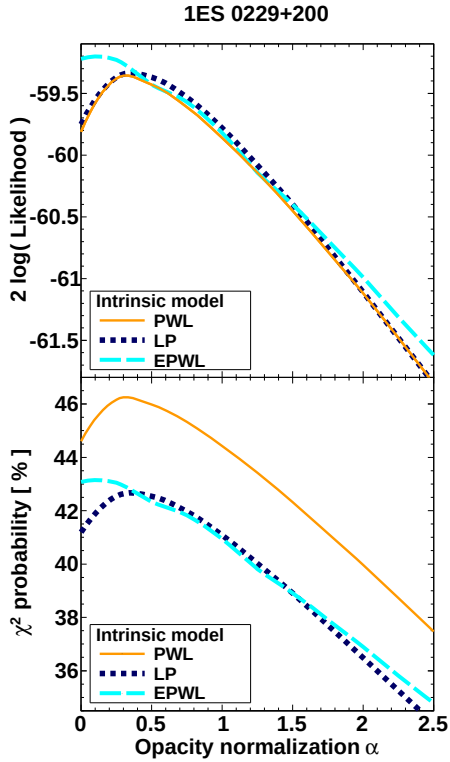

FIGURE 4. *Top panel:* Likelihood profiles, as a function of the optical depth normalization for the different intrinsic models which are detailed in the legend. *Bottom panel:* Corresponding χ^2 probabilities as a function of the optical depth normalization. The PWL is the spectral model chosen to describe the spectrum of 1ES 0229+200.

ambiguity occurs when the difference between the maximum χ^2 probabilities of the two models is small (typically less than a percent), as e.g. shown in Fig. 5. In such a case, the model of the third order (LP and SEPWL) with the maximum χ^2 probability is chosen, the SEPWL in the case of PKS 2155-304 (*5*).

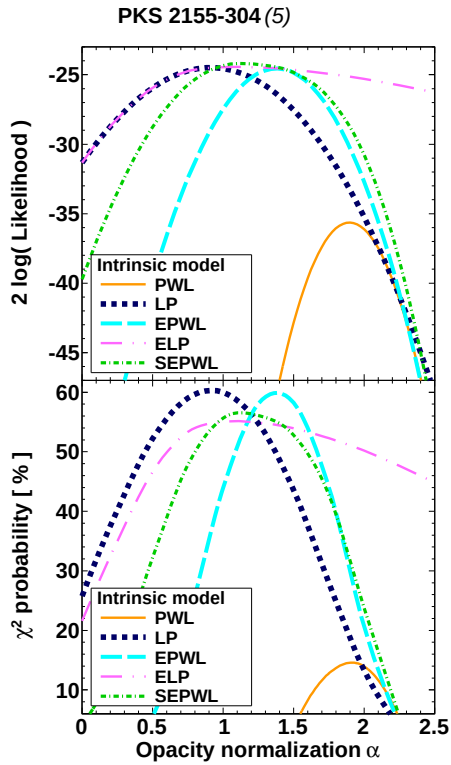

FIGURE 5. *Top panel:* Likelihood profiles, as a function of the optical depth normalization for the different intrinsic models which are detailed in the legend. *Bottom panel:* Corresponding χ^2 probabilities as a function of the optical depth normalization. The SEPWL is the spectral model chosen to describe the spectrum of PKS 2155-304 (*5*).

3.2.1.2. *Combined likelihood profile*

The selected intrinsic models are given in Table 2. The minimum χ^2 achieved as function of α for each dataset indicates that the spectral modelling is a good representation of the data and that a large enough number of intrinsic parameters is used (most of the reduced χ^2 are smaller than one). The dataset number *2* on Mrk 421 is the only marginally good fit with a reduced χ^2 of ~ 1.5 and an associated

probability of 3%, most probably indicating a scatter due to spectral variability. Given the significance of its contribution to the final result, I did not perform a finer division of this dataset as a function of the flux level.

Source	Model	$\chi^2_{\rm min}$	dof	$\chi^2_{\alpha_0}$	$\mathcal{P}_{\alpha_0}$	$\sqrt{\Delta\chi^2}$
Mrk 421 (*1*)	ELP	21.3	31	21.5	89.8%	0.4σ
Mrk 421 (*2*)	ELP	45.6	30	46.8	2.6%	1.1σ
Mrk 421 (*3*)	ELP	34.8	28	34.8	17.5%	0.2σ
PKS 2005-489 (*1*)	PWL	49.0	60	49.5	83.1%	0.7σ
PKS 2005-489 (*2*)	LP	31.5	46	31.8	94.5%	0.5σ
PKS 2155-304 (*2008*)	ELP	21.5	37	21.9	97.7%	0.6σ
PKS 2155-304 (*1*)	PWL	31.8	31	32.3	40.2%	0.7σ
PKS 2155-304 (*2*)	SEPWL	24.9	28	25.3	61.1%	0.6σ
PKS 2155-304 (*3*)	SEPWL	35.2	31	35.2	27.6%	0.3σ
PKS 2155-304 (*4*)	SEPWL	18.0	21	19.1	57.9%	1.0σ
PKS 2155-304 (*5*)	SEPWL	24.3	27	24.3	61.4%	0.3σ
PKS 2155-304 (*6*)	LP	27.8	21	29.2	10.9%	1.2σ
PKS 2155-304 (*7*)	SEPWL	11.2	13	13.6	40.3%	1.5σ
1ES 0229+200	PWL	59.4	60	60.1	47.2%	0.8σ
H 2356-309	LP	69.0	61	70.2	19.7%	1.1σ
1ES 1101-232	PWL	60.1	69	62.6	69.3%	1.6σ
1ES 0347-121	ELP	31.7	35	31.7	62.8%	0.2σ

TABLE 2. Spectral models used to derive the likelihood profile for each dataset. The minimum χ^2 as a function of α and the number of degrees of freedom *dof* are given in the third and fourth columns. The χ^2 for the best fit EBL optical depth normalization $\alpha_0 = 1.27$ and the associated probability are shown in column five and six. The last column indicates the deviation of each dataset to the best fit EBL normalization in Gaussian standard deviation.

To quantify the deviation to the null hypothesis $\alpha = 0$ (i.e. no EBL imprint in these datasets), I define the Test Statistic as the likelihood ratio test:

$$\mathrm{TS} = 2\log\mathcal{L}(\alpha) - 2\log\mathcal{L}(\alpha = 0) \tag{3.10}$$

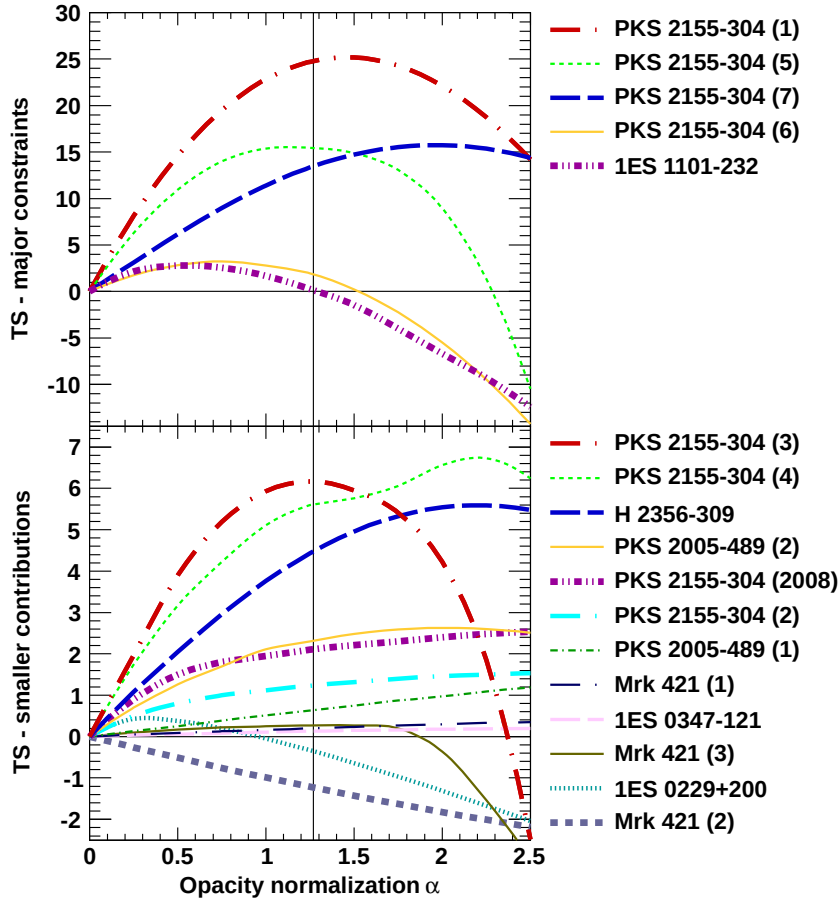

FIGURE 6. Test statistic as a function of the normalized EBL optical depth for the intrinsic spectral models described in Table 2. The TS profiles are sorted by contribution to the measurement. The top panel shows the most constraining data sets while the bottom panel shows the less constraining contributions. The vertical line indicates the best fit value derived in this study. Note the different scale on the vertical axis in the upper and the lower panel.

The profiles of the TS as a function of α are shown for each dataset in Fig. 6. The major constraints are shown in the top panel while the smaller contributions are shown in the bottom panel. The datasets number *1, 5, 7* on PKS 2155-304 significantly contribute to the rejection of the null hypothesis $\alpha = 0$ with a maximum TS of 25 ($\sim 5\sigma$) for the first one and of ~ 15 ($\sim 4\sigma$) for the last ones. The dataset number *6* on PKS 2155-304 and the dataset on 1ES 1101-232 significantly contribute to the rejection of large EBL normalization with difference between their maximal TS and the TS at $\alpha = 2.5$ of 15 ($\sim 4\sigma$). Such a contribution from PKS 2155-304 is expected since this source represents the largest reservoir of γ rays in this study ($\sim$ 53 000 photons over the $\sim$ 74 000). Interestingly, high EBL models ($\alpha \gtrsim 2$) are rejected in this study using solely data from 1ES 1101-232 (at the 3σ level), without having to limit the spectral hardness as was done in (Aharonian et al. 2006b) on the same source.

I show in Fig. 7 the sum of the TS profiles as a function of α. A maximum TS of 77.3 is achieved for $\alpha_0 = 1.27$. The model of FR08, scaled up by a factor $\alpha_0 = 1.27$, is thus preferred at the $\sqrt{77.3} \sim 8.8\sigma$ level to no EBL absorption. The deviation to the FR08 modelling, $\alpha = 1$, is of 1.8σ, showing *a posteriori* the validity of this approach with α_0 close to one (cf. discussion in Sect. 3.1.2). The Gaussian statistical uncertainty, computed at ΔTS$= 1$, yields $\alpha_0 = 1.27^{+0.18}_{-0.15}$.

To check that there is no significant deviation at the single dataset level, I show in Fig. 6 the best fit EBL normalization with a vertical line. The deviations are quantified with a likelihood ratio test, where the null hypothesis, the best fit EBL normalization, is compared to the maximum of the profile. The last column of Table 2 shows a good overall consistency, with maximum deviations below 1.6σ.

A cross check has been performed by D. Sanchez with HDMVA. The derived likelihood profile is shown with a gray dashed line in Fig. 6 and is maximum for an EBL normalization of $1.24^{+0.09}_{-0.22}$, in close agreement with the nominal value of α_0, though a smaller statistical significance of detection $\sqrt{33.9} \sim 5.8\sigma$ is achieved. This difference of sensitivity can

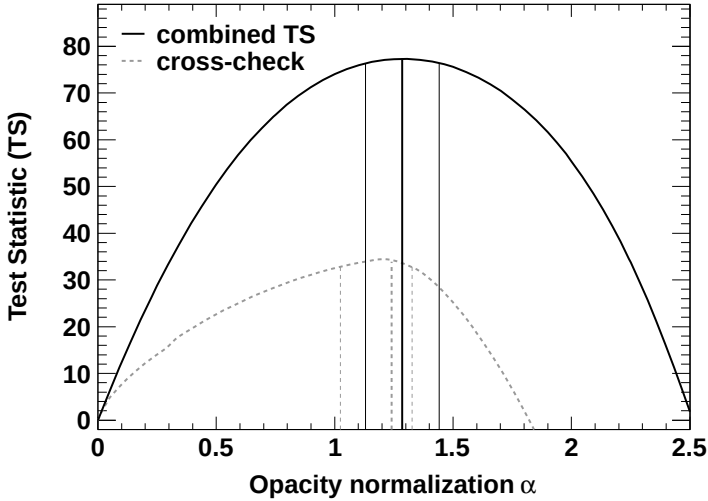

FIGURE 7. Combined test statistic as a function of the normalized EBL optical depth. The result obtained with the *Model analysis* is shown with a black line and the cross check performed with the MVA analysis is shown with the dashed gray line. The best fit value and 1σ statistical uncertainties are shown with the vertical lines.

be attributed to the much larger energy range[5] covered by the analysis that I performed.

3.2.1.3. *Residuals and redshift dependence*

The detection and measurement of the EBL absorption are only significant using the combination of several datasets and a deviation from

[5]TS is proportional to square of the χ^2, i.e., assuming a constant χ^2/dof, TS $\propto dof^2$. One can approximate in this case the dof by the number of bins (cf. values in Table 2 to compare to three free parameters on average) and the number of bins is proportional to the logarithmic difference between the maximum and minimum energies, hence TS $\propto (\sum_{\rm datasets} \log({\rm E_{max}}/{\rm E_{min}}))^2$. The expected ratio of TS for the *Model++* energy range and the MVA range from this formula is then of 2.5. This means that using the MVA energy ranges with the *Model ++* datasets would result in a maximum TS of $77.3/2.5 \sim 31$ similar to the maximum TS of 34 obtained with the MVA analysis.

the EBL template absorption can not be evaluated on the individual residuals.

For each dataset, I computed the number of photons detected in each energy bin, N_{mes}, and the expected excess from the intrinsic spectra $N_{th,\alpha=0} = N_{th}(\alpha_0) \times e^{\alpha_0 \tau}$. To avoid large statistical uncertainties preventing the assessment of any deviation from the model, I summed both quantities for three groups of sources with similar redshifts. I use the datasets on Mrk 421 and PKS 2005-489 for the low redshift, with an average of $z = 0.051$ (weight of one per source). The datasets on PKS 2155-304 ($z = 0.116$) are used for the intermediate range and the four other datasets for the high redshifts, with an average of $z = 0.170$. Fig. 8 shows the expected EBL absorption for each group (solid lines) and the "residuals" to this expected absorption $N_{mes}/N_{th,\alpha=0}$ as a function of energy. Abrupt changes in the amplitude of the statistical uncertainties (e.g. around 1 TeV for the low redshift group: Mrk 421 / PKS 2005-489) are due to the grouping of the data sets, which cover different energy ranges (the data sets on Mrk 421 start at $\sim$ 1 TeV when those on PKS 2005-489 start at $\sim$ 200 GeV).

To investigate the redshift dependence of the EBL normalized opacity, I compute the total TS profile for the three above mentioned groups of sources. The TS of Mrk 421 and PKS 2005-489 is maximum at $\alpha(z_1) = 1.61^{+0.48}_{-1.06}$, with an average redshift of $z_1 = 0.051$. The TS of the eight datasets on PKS 2155-304 ($z_2 = 0.116$) peaks at $\alpha(z_2) = 1.36 \pm 0.17$. With the four other datasets, a maximal TS is obtained for $\alpha(z_3) = 0.71^{+0.46}_{-0.29}$, corresponding to a mean redshift $z_3 = 0.170$.

The fit of a linear function on the decreasing trend of the EBL normalization yields $\chi^2/dof = 0.41/1$, which does not significantly improve the fit with regards to a constant fit $\chi^2/dof = 1.83/2$ (a likelihood ratio test prefers the linear fit only at the 1.1σ level). I therefore neglect any deviation to the redshift dependence of the EBL modelling in the following.

3.2.1.4. *Systematic uncertainties and other cross checks*

I carried out an extensive investigation of the systematic uncertainties arising from the method and from the limited knowledge of the instrument. I identified four sources of systematics on the normalized EBL opacity: the analysis chain, the choice of intrinsic model and of the EBL template, as well as the uncertainty on energy scale, related to

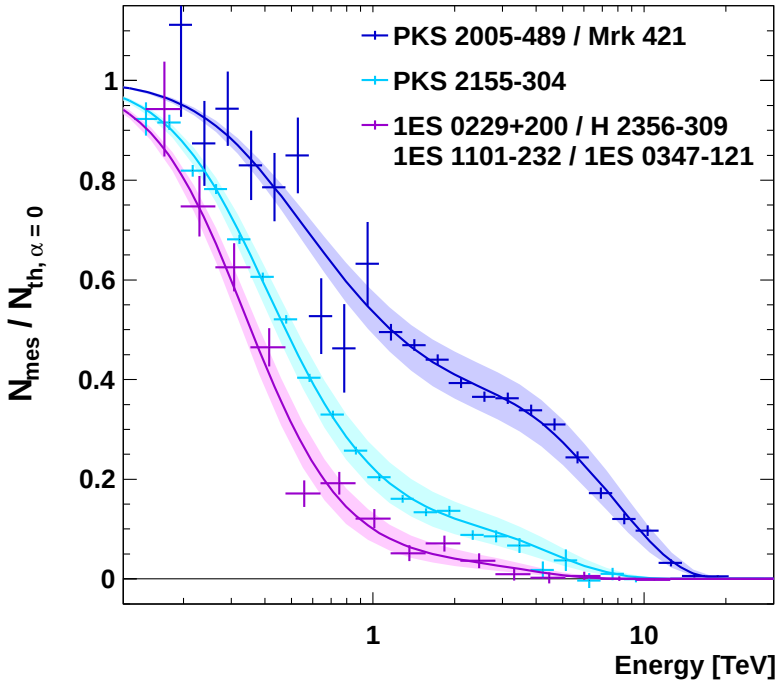

FIGURE 8. Observed number of γ rays over number of events expected for a null EBL absorption as a function of energy. The datasets are grouped by similar redshift and the detected and expected numbers of γ rays are summed in each energy bin. The best fit EBL absorption is represented by the solid lines for the redshifts of the three groups of datasets. The shaded area represents the $\pm 1\sigma$ statistical uncertainty on the best fit EBL normalization. Note the linear y-axis scale.

the limited knowledge of the atmosphere. These sources of systematic uncertainty and their impact on the EBL normalization are listed in Table 3.

I briefly summarize the different methods I developed to estimate the uncertainties, while the full discussion can be found in Appendix B.1.

Sources of systematics	Estimated systematics
Analysis chain	0.21
Intrinsic model	0.10
EBL model	0.06
Energy scale	0.05
Total	**0.25**

TABLE 3. Sources of systematics and estimated uncertainties on the normalized EBL optical depth $\alpha_0 = 1.27^{+0.18}_{-0.15\ \mathrm{stat}}$.

I investigated the quality of the reconstruction of the EBL normalization with the analysis chain using Monte-Carlo simulated events. I first absorbed power-law spectra for a redshift $z = 0.1$ and for EBL normalizations between 0 and 2. For simulated observational parameters similar to those of PKS 2155-304, the simulated EBL normalizations differ from the reconstructed ones at the percent level, way below the systematic uncertainty estimated in the following.

I performed another set of simulations imposing a poor background estimation, this factor being the key point of a good spectral reconstruction. I estimate the maximum systematic uncertainty due to a bad knowledge of the background to a value of 0.21. To investigate the presence of a point-to-point systematic uncertainty which would mimic the EBL effect, I also measured the amount of EBL absorption in the spectrum of the brightest galactic source, the Crab Nebula. The absolute value of the EBL normalization for this source is well below the systematic uncertainty on the analysis chain.

I also investigated the procedure involved in the choice of the intrinsic spectral model (criteria on the χ^2 probability). I show in Appendix B.1.1 that, as expected, this criteria is conservative with regards to the estimation of the significance of the detection. Imposing arbitrary intrinsic modelling for each dataset, I estimate the systematic uncertainty due to the intrinsic model to 0.10.

I checked a reasonable range of models using the "theoretical" limits derived in the concurrent modelling of Domínguez et al. (2011). The choice of the EBL model impacts the reconstruction of the EBL optical depth with a rather small uncertainty of 0.06, due to the convergence on the predicted shape.

Finally, I modeled the effect of the atmosphere as a shift of 10% in the energy scale[6] of the reconstructed events (absorption of the Cherenkov light), yielding a systematic of 0.05.

The quadratic sum of the above-mentioned factors yields a total systematic uncertainty $\sigma_{\rm sys}(\alpha_0) = 0.25$, which is comparable to the statistical uncertainty derived on the normalized EBL.

3.2.2. Discussion of the detection

In the following sections, I discuss the detection of the EBL imprint and the measurement of its normalization in light of the current knowledge on the COB spectral energy distribution. I also compare this measurement to the recent detection announced by the *Fermi*-LAT collaboration.

3.2.2.1. *SED of the Cosmic Optical Background*

As discussed in Chapter 1.3.2, a γ ray of energy E^* preferentially produces an electron-positron pair by interacting with an EBL photon of energy $\epsilon^* = (2m_e c^2)^2/E^*$, where the * refers to the referential in which the interaction occurs. This referential is indeed linked to the epoch when the pair is created. Calling z' the corresponding redshift, $\epsilon*$ and E^* are decreased by a factor $(1+z')$ in the observer frame. The relation between the γ-ray energy and the probed EBL wavelength becomes, in the observer frame:

$$(\lambda_{\rm EBL}/1\ \mu{\rm m}) = 1.187 \times (E/1\ {\rm TeV}) \times (1+z')^2 \tag{3.11}$$

with $z' < z$, where z is the redshift of the source and where E is the γ-ray energy in the observer frame.

Thus, the minimal wavelength range probed by each dataset, for a source at a redshift z spanning $[E_{\rm min}, E_{\rm max}]$ is $1.187\ \mu{\rm m}\ \times\ [(1+z)^2\ E_{\rm min}, E_{\rm max}]$. These ranges, given in Table 4, only take into account the peak of the pair-creation cross section. Accounting for the width of this quantity would result in a larger wavelength coverage.

The detection of an EBL flux density scaled up by a factor α_0 being based on all the datasets, the measurement is only valid in the overlap of the probed wavelength ranges, as shown in a schematic way in Fig. 9. This intersection corresponds to the wavelength range $[1.2, 5.5]\ \mu$m,

[6] 10% is a conservative value compared to the 5% estimated by Meyer et al. (2010), who used the Crab Nebula spectrum measured with *Fermi*-LAT and IACT as an inter-calibrator.

Source	z	$E_{\rm min} - E_{\rm max}$ TeV	$\lambda_{\rm min} - \lambda_{\rm max}$ μm
Mrk 421 (*1*)	0.031	$0.95 - 41$	$1.2 - 49$
Mrk 421 (*2*)	0.031	$0.95 - 37$	$1.2 - 44$
Mrk 421 (*3*)	0.031	$0.95 - 45$	$1.2 - 53$
PKS 2005-489 (*1*)	0.071	$0.16 - 37$	$0.22 - 44$
PKS 2005-489 (*2*)	0.071	$0.18 - 25$	$0.25 - 30$
PKS 2155-304 (*2008*)	0.116	$0.13 - 19$	$0.30 - 23$
PKS 2155-304 (*1*)	0.116	$0.13 - 5.7$	$0.19 - 6.8$
PKS 2155-304 (*2*)	0.116	$0.13 - 9.3$	$0.19 - 11$
PKS 2155-304 (*3*)	0.116	$0.13 - 14$	$0.19 - 17$
PKS 2155-304 (*4*)	0.116	$0.18 - 4.6$	$0.19 - 5.5$
PKS 2155-304 (*5*)	0.116	$0.13 - 5.7$	$0.27 - 6.8$
PKS 2155-304 (*6*)	0.116	$0.15 - 5.7$	$0.19 - 6.8$
PKS 2155-304 (*7*)	0.116	$0.20 - 7.6$	$0.22 - 9.0$
1ES 0229+200	0.14	$0.29 - 25$	$0.45 - 30$
H 2356-309	0.165	$0.11 - 34$	$0.18 - 40$
1ES 1101-232	0.186	$0.12 - 23$	$0.20 - 27$
1ES 0347-121	0.188	$0.13 - 11$	$0.22 - 13$

TABLE 4. EBL wavelengths probed with the datasets used in this study (column four). The redshift of the sources and the energy ranges of the datasets are given in column 2 and 3

where 1.2 μm (resp. 5.5 μm) is the counterpart of the low (resp. high) energy bound of the Mrk 421 (resp. PKS 2155-304) data sets. Given the significance level of the detection ($\sim 9\sigma$), the datasets can be organized in two groups probing low and high wavelengths, respectively, as shown in the bottom panel of Fig. 9. The EBL normalizations and the EBL wavelength ranges derived for this low and high ranges are given in Table 5.

I scale up the EBL flux density of FR08 by these normalization factors in the appropriate wavelength ranges and compare them to various independent constraints in Fig. 10. The systematic uncertainty is quadratically added to the statistical uncertainty on the best fit measurement for the intermediate energy range, and on the low and high-energy measurements for the rest of the SED. One can notice that the

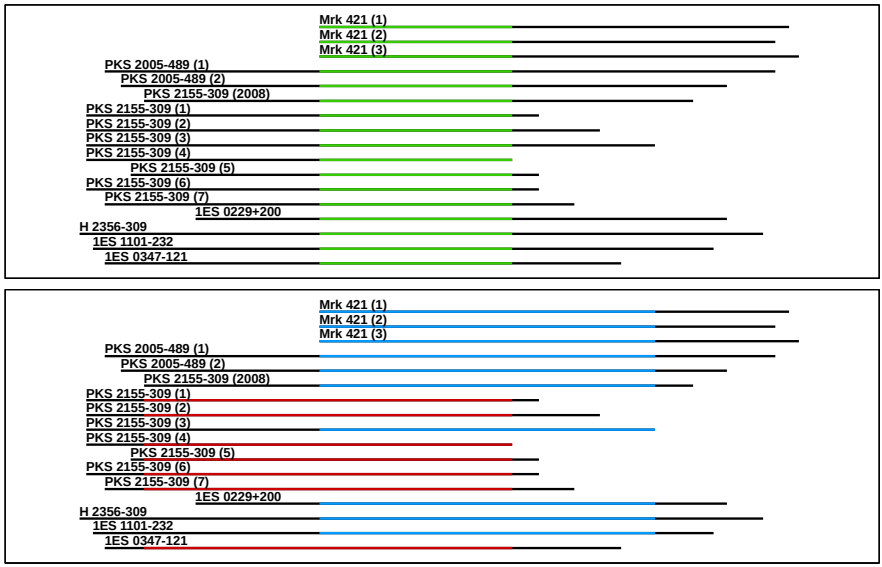

FIGURE 9. Schematic representation of the EBL wavelength ranges probed by the various datasets. *Top panel*: the measurement of the EBL normalization with the full dataset is valid in the overlap, shown as the green area. *Bottom panel*: division of the datasets in two groups, probing low (red) and high (blue) wavelengths, respectively.

low and high wavelength ranges fully cover the first peak of the EBL, the COB, as well as the onset of the CIB. The intersection of these two contours is in close agreement with the full measurement, as expected from the absence of deviation at the single dataset level. Direct measurements and galaxy counts are shown as full downward and empty upward pointing triangles. The measurement of the EBL derived with H.E.S.S. lies in between these data, comforting their status of upper and lower limits, respectively. An overall good agreement is also found with the upper limit derived by Meyer et al. (2012), who combined the spectra of objects observed both at high energies (by *Fermi*-LAT) and at very high energies (by H.E.S.S., MAGIC and VERITAS). The marginal tension found around the peak value does not exceed the 1σ level.

$\tau_{\rm measured}/\tau_{\rm FR08}$	$\lambda_{\rm min}$ – $\lambda_{\rm max}$	$\lambda F_\lambda(\lambda_{\rm min})$ – $\lambda F_\lambda(\lambda_{\rm max})$
	μm	nW m^{-2} sr^{-1}
$1.27^{+0.18}_{-0.15}$	1.2 – 5.5	$14.8^{+2.1}_{-1.7}$ – $4.0^{+0.6}_{-0.5}$
$1.34^{+0.19}_{-0.17}$	0.30 – 5.5	3.1 ± 0.4 – $4.2^{+0.6}_{-0.5}$
$1.05^{+0.32}_{-0.28}$	1.2 – 17	$12.2^{+3.7}_{-3.3}$ – $3.2^{+1.0}_{-0.8}$

TABLE 5. Measured normalization of the EBL optical depth, corresponding to the 1σ (statistical) contours shown in Fig. 10. The second column indicates the wavelength range where this measurement is valid and the third column shows the corresponding flux densities. The first line corresponds to the full data set. The second and third lines indicate the value derived with smaller data sets focussed on specific energy ranges. The systematic uncertainty on the measurements listed in the first column is 0.25.

Finally, I measure a COB peak flux density of $\lambda F_\lambda = 15.0^{+2.1}_{-1.8} \pm 2.8_{\rm sys}$ nW m^{-2} sr^{-1} at 1.4 μm, propagating the uncertainties on the factor α_0. This value is compatible with the previous constraints on the EBL flux density derived with H.E.S.S. data in Aharonian et al. (2006b), where a peak EBL flux density of 14 ± 4 nW m^{-2} sr^{-1} is stated imposing intrinsic spectra described by power laws of index 1.5. I show in Sect. 3.3 that this assumption is valid within the statistical and systematic uncertainties for the sources used in this paper H 2356-309 and 1ES 1101-232, as well as for the two sources used to confirm this limit, 1ES 0347-121 and 1ES 0229+200.

3.2.2.2. *Comparison with the detection of the Fermi*-LAT

M. Ajello announced the "discovery of the EBL attenuation in the spectra of *Fermi* blazars" at the Gamma 2012 conference, on behalf of the *Fermi*-LAT collaboration. For this publication in Science (The Fermi-LAT Collaboration 2012), they fit the spectra of a total of ~ 50

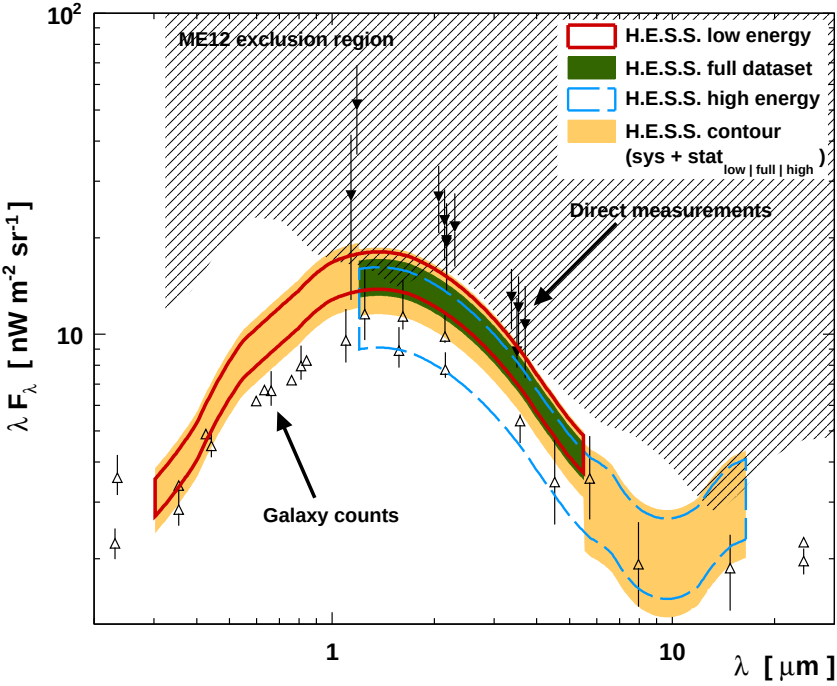

FIGURE 10. Flux density of the Extragalactic Background Light versus wavelength. The 1σ (statistical) contours derived for three energy ranges are described in the top-right legend. Lower limits based on galaxy counts and direct measurements are respectively shown with empty upward and filled downward pointing triangles (extracted from Gilmore et al. 2012). The region excluded by Meyer et al. (2012) with VHE spectra is represented by the dashed area.

"non-variable" BL Lacs with the same parametrization of the EBL optical depth as the one used in this study, assuming an intrinsic log-parabolic spectrum. They have a direct access to the non-absorbed part of the spectrum below the pair creation threshold. The parameters of the log-parabola are fitted with this non-absorbed part of the spectrum and then fixed when fitting the EBL absorption. This log-parabolic assumption may be one of the weakness of their approach, since an

exponential cut-off power law could reproduce the EBL absorption for the distant sources that are studied (cf. absence of inflection points for $z = 1.0$ in Fig. 2) but one of the strength of their work lies in the variety of studied EBL models.

The models for which the EBL absorption is the most significantly detected by this analysis are the model of FR08 and of Domínguez et al. (2011). Binning the datasets by redshift and using the model of FR08, they obtain a 2σ effect for $z < 0.2$, a 2.5σ effect between $0.2 < z < 0.5$ and a significant detection at the 5σ level between $0.5 < z < 1.6$. This work and the study I performed are fully complementary, the former probing high redshifts and the latter probing the local Universe, as shown on Fig. 11.

3.3. Intrinsic spectra of H.E.S.S. blazars

Using the EBL normalization measured in the previous section, I derive in this section the time-averaged intrinsic spectrum of the blazars 1ES 0229+200, H 2356-309, 1ES 1101-232 and 1ES 0347-121. I also study the intrinsic spectral variations of Mrk 421, PKS 2005-489 and PKS 2155-304. A comparison with the measurement of *Fermi*-LAT at HE comforts the reliability of the EBL measurement.

3.3.1. Spectral analysis

For the study of the EBL normalization, I purposely chose complex intrinsic models, maximizing the χ^2 probability, to fully account for intrinsic curvature and to avoid an overestimation of the EBL absorption. Assuming now that the EBL normalization is measured at $\alpha_0 = 1.27$, I derive the spectra in a more conventional way, yielding simpler intrinsic models than previously derived. The spectral parameters and the covariance matrices can be found in Appendix B.2.

3.3.1.1. *Single dataset sources*

Power-law models successfully describe the spectra of 1ES 0229+200, H 2356-309, 1ES 1101-232 and 1ES 0347-121, with the log-parabola and exponential cut-off power law not preferred by a likelihood ratio test by more than 2σ. The intrinsic fluxes at 1 TeV and the intrinsic photon indices of these four sources are given in Table 6. The systematic uncertainty on the intrinsic parameters arise from the limited knowledge of the detector and from the uncertainty on the EBL normalization. The latter systematics is estimated fixing the EBL normalization to

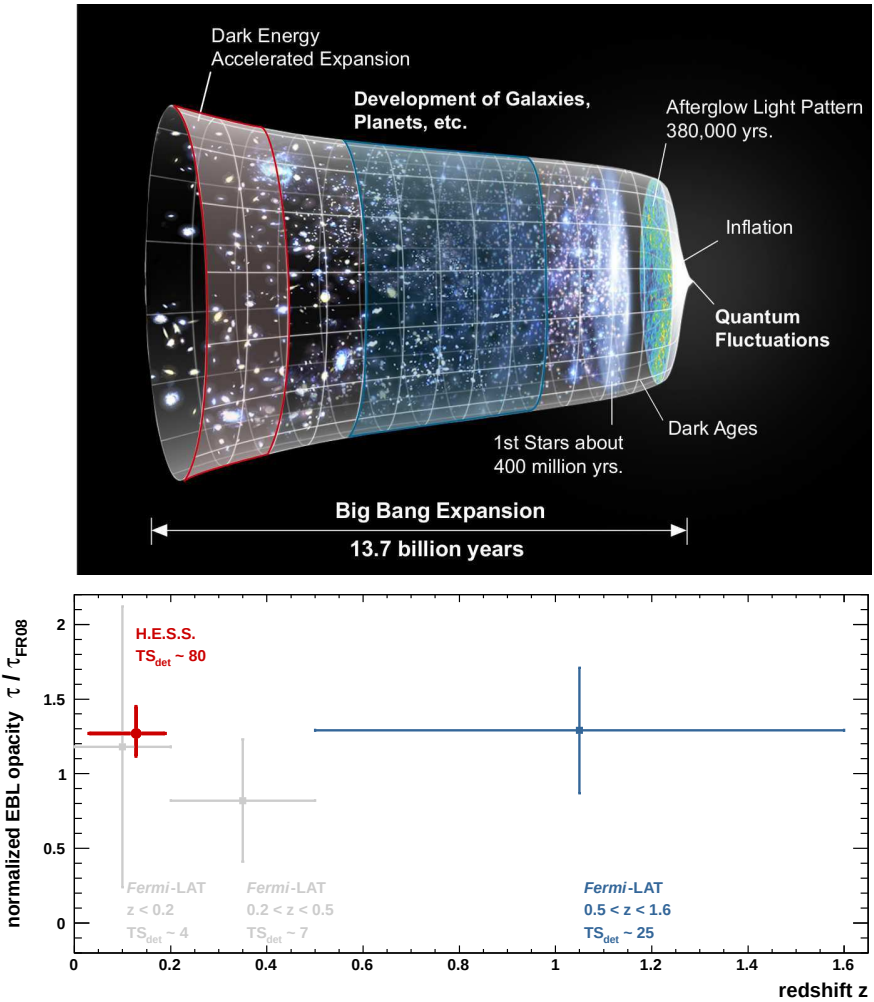

FIGURE 11. *Top panel*: schematic view of the current cosmological model. The past 2 Myrs ($z < 0.2$), in red, are probed by H.E.S.S., while the $4 - 9$ Myrs after the big bang ($0.5 < z < 1.6$, in blue) are probed by *Fermi*-LAT. *Bottom panel*: normalized EBL optical depth α vs redshift. The detection of the EBL is significant below $z < 0.2$ at VHE and between $0.5 < z < 1.6$ at HE.

its extremal values (to be conservative 1.0 and 1.6), while the limited knowledge of the instrument is accounted for adding quadratically a systematic uncertainty of 0.2 on the index and of 20% on the normalization.

Source	$\phi(1\text{ TeV})\times10^{12}$ $\text{cm}^{-2}\text{ s}^{-1}\text{ TeV}^{-1}$	Γ	χ^2/dof	$\mathcal{P}(\chi^2)$ %
1ES 0229+200	$3.1 \pm 0.3^{+1.1}_{-1.0}$	$1.62 \pm 0.16 \pm 0.27$	60.2 / 61	50
H 2356-309	$2.4 \pm 0.3^{+0.9}_{-0.8}$	$1.82 \pm 0.09 \pm 0.26$	70.2 / 62	22
1ES 1101-232	$5.4 \pm 0.6^{+2.4}_{-1.9}$	$1.43 \pm 0.10 \pm 0.27$	57.2 / 70	86
1ES 0347-121	$2.2 \pm 0.5^{+0.9}_{-0.7}$	$1.90 \pm 0.17 \pm 0.28$	33.0 / 36	61

TABLE 6. Intrinsic spectra of the four sources previously used by H.E.S.S. to constrain the EBL. The first uncertainty is statistical and the second one accounts for the EBL uncertainty and for the systematic of 20% on the flux and 0.2 on the index.

Strong constraints on the EBL could be derived in the previous studies of the H.E.S.S. collaboration (Aharonian et al. 2006b, 2007a,b), where a maximum slope of 1.5 is assumed (a natural value corresponding to an EDF index of 2 in an SSC model). The stringency of the constraints can be explained *a posteriori* since these sources have indeed intrinsic slopes between ~ 1.5 and ~ 2, as I show in the following. Such hard spectra are remarkable at VHE and stress out the efficiency of the particle acceleration by these BL Lac objects.

3.3.1.2. *Highly significant sources*

The second dataset on PKS 2005-489 is well described by a power-law model with an index of $2.48 \pm 0.08_{\text{stat}} \pm 0.21_{\text{sys}}$, softer than the spectra of the four previous sources and indicating that the peak of the emission in $\nu F_\nu = E^2 \text{d}N/\text{d}E$ occurs at relatively low energies (presumably below the threshold energy of this datasets of ~ 200 GeV). The dataset number *1* is composed of a larger number of events than the number *2* and is well described by a log-parabola (preferred at the 3σ level to a power law). The curvature is not detectable in the smaller

dataset probably because of the limited statistics and smaller energy range. Based on the curvature $\beta = 0.67 \pm 0.24_{\rm stat} \pm 0.04_{\rm sys}$ at 1 TeV and on the index $\alpha = 3.81 \pm 0.41_{\rm stat} \pm 0.21_{\rm sys}$, the peak energy in νF_ν (in log-log scale) can be derived from $\log(E[\mathrm{TeV}]) = (2-\alpha)/2\beta$, which reads in this case $\log_{10}(E[\mathrm{TeV}]) = -1.17 \pm 0.64_{\rm stat} \pm 0.26_{\rm sys}$. This locates the second peak of the SED between 15 GeV and 290 GeV, using only the statistical uncertainty, and between 5 GeV and 900 GeV using the statistical and systematic uncertainties.

With the aim of understanding the flux and spectral variations of PKS 2155-304 and Mrk 421, an exponential cut-off power-law model is fitted to each dataset. Though for a bunch of datasets this model is marginally preferred to a power law (e.g. PKS 2155-304 (*1, 2008*)) or too restrictive (e.g. PKS 2155-304 (*7*)), it enables the study of the intrinsic index and of the intrinsic cut-off energy of as a function of the flux level of the source. The fluxes at 1 TeV, the photon indices and the inverse of the cut-off energies are given in Table 7. In both case, a hardening of the spectrum with an increase of the flux is observed, though a fit of a linear function to the index vs $\ln \phi$ is only preferred at the $\sim 2\sigma$ level to a constant fit for the datasets on Mrk 421.

A fit of the inverse of the cut-off energies[7] with a constant matches the points on Mrk 421 with an average cut off of $7.3 \pm 1.1_{\rm stat} \pm 1.3_{\rm sys}$ TeV for a χ^2 probability of 94%. The systematic uncertainty on the cut-off energy is derived from the uncertainty on the EBL normalization and on the energy scale (10%). The same analysis yields a cut-off at $1.80 \pm 0.16_{\rm stat} \pm 0.4_{\rm sys}$ TeV, though with a worse χ^2 probability of 2%.

3.3.2. Multi-wavelength overview

One of the strength of the result derived in the previous section lies in the use of the data from a single experiment, not hampered by potential inter-calibration systematic effects. Nonetheless, one can check *a posteriori* the compatibility between the VHE spectra de-absorbed from the EBL and the spectra measured at HE, for which the absorption is negligible at $z < 0.2$.

[7]The inverse of the cut off is the parameter that is effectively fitted and the Gaussian uncertainty is associated to this quantity and not to the cut-off energy itself.

Source	ϕ(1 TeV)$\times 10^{12}$ cm^{-2} s^{-1} TeV^{-1}	Γ	$1/E_{\rm cut}$ TeV^{-1}	χ^2/dof
Mrk 421(*1*)	216 ± 9	2.43 ± 0.14	0.15 ± 0.05	21.9 / 32
Mrk 421(*2*)	345 ± 11	2.26 ± 0.11	0.14 ± 0.03	46.0 / 31
Mrk 421(*3*)	439 ± 13	2.11 ± 0.09	0.13 ± 0.03	34.8 / 29
PKS 2155-304(*2008*)	10.8 ± 1.8	2.57 ± 0.09	0.19 ± 0.18	22.0 / 38
PKS 2155-304(*1*)	17.8 ± 4.0	2.83 ± 0.11	0.20 ± 0.25	30.2 / 32
PKS 2155-304(*2*)	53 ± 11	2.53 ± 0.11	0.80 ± 0.25	25.5 / 28
PKS 2155-304(*3*)	120 ± 17	2.53 ± 0.07	0.87 ± 0.17	36.4 / 31
PKS 2155-304(*4*)	181 ± 37	2.45 ± 0.11	0.73 ± 0.21	19.7 / 21
PKS 2155-304(*5*)	244 ± 21	2.46 ± 0.05	0.40 ± 0.09	25.4 / 28
PKS 2155-304(*6*)	837 ± 92	2.02 ± 0.06	0.72 ± 0.11	30.3 / 22
PKS 2155-304(*7*)	1345 ± 157	2.01 ± 0.08	0.60 ± 0.11	22.7 / 14

TABLE 7. Intrinsic spectra of Mrk 421 and PKS 2155-304 for the datasets used in this study. For the sake of clarity, only statistical uncertainties are given.

3.3.2.1. *The four fantastics*

I have shown in Sect. 3.3 that the blazars 1ES 0229+200, H 2356-309, 1ES 1101-232 and 1ES 0347-121 are four fantastic accelerators, able to produce hard γ-ray spectra ($\Gamma \lesssim 2$) up to tens of TeV. The analysis of three and a half years of *Fermi*-LAT data show that the same characteristic is observed at HE. He analyzed *Fermi*-LAT data from MJD 54682 to MJD 55975 between 300 MeV and 300 GeV using instrumental response functions `P7SOURCE_V6` for a region of integration of size 15°. Only three of the four sources are detected in this energy range and I used the results of the analysis of Vovk et al. (2012) above 1 GeV for 1ES 0229+200, though they should certainly be taken with caution since D. Sanchez did not detect the source with more data and the updated calibration. In Fig. 12, I compare the photon indices derived at HE with *Fermi*-LAT data and the intrinsic indices derived in the previous section. The statistical uncertainty accounts for both HE and VHE limited statistics while the systematic uncertainty accounts for the limited knowledge on the VHE spectra and on the EBL.

Large negative values would indicate either that the intrinsic spectra are convex (pointing e.g. to the presence several components) or that the EBL effect is overestimated. Large positive values would reflect a concavity of the spectrum. A constant fit to the difference of indices for the four last points represents fairly well the data with a χ^2

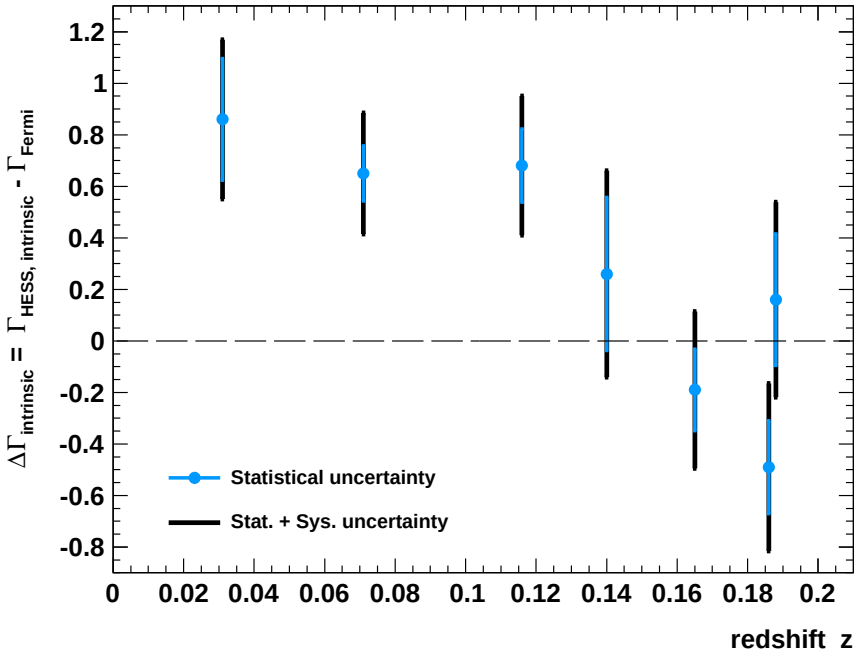

FIGURE 12. Preliminary intrinsic break measured with H.E.S.S. and *Fermi*-LAT after EBL de-absorption

probability of 42% for an average of $\Delta\Gamma = -0.12 \pm 0.17_{\mathrm{stat\ +\ sys}}$. The compatibility with zero shows the continuity of the processes responsible for the HE and VHE emissions and that the measured EBL level is in agreement with the sources intrinsic properties.

3.3.2.2. *Peaked emission of PKS 2005-489, PKS 2155-304 and Mrk 421*

A thorough study of the GeV-TeV connection has been carried out for PKS 2005-489, PKS 2155-304 and Mrk 421. Since these objects exhibit flux and spectral variability, simultaneous spectra are compared, which required for Mrk 421 to perform the analysis of the H.E.S.S. dataset acquired in 2010. The VHE spectrum of Mrk 421 in 2010 is well represented by an exponential cut-off power law (preferred at the 3σ level to a power law) with a χ^2 probability of 34%. The spectrum is quite similar to the one derived for Mrk 421(*1*) with a flux at 1 TeV

of $\phi(1\text{ TeV}) = 165.2 \pm 19.3\text{ cm}^{-2}\text{ s}^{-1}\text{ TeV}^{-1}$, a photon index of $\Gamma = 2.45 \pm 0.23$ and a cut-off energy defined by $1/E_{\text{cut}} = 0.17 \pm 0.06\text{ TeV}^{-1}$.

In the three cases, a smooth connection is found between the HE and the VHE spectra. One can note from Fig. 12 that an intrinsic break from HE to VHE can be measured for the three sources (simultaneous spectra are used), with an average value of $\Delta\Gamma = 0.71 \pm 0.15$ (where both statistical and systematic uncertainties are included). Since the intrinsic spectra derived with H.E.S.S. correspond to photon indices $\gtrsim 2$, the maximum of the intrinsic emission in νF_ν can be located with H.E.S.S. and *Fermi*-LAT data. At the time this manuscript is being written, the analysis is performed by D. Sanchez and a more extensive discussion will be presented in a forthcoming publication.

3.3.2.3. *Concluding remarks of the spectral studies*

The detection of the EBL imprint in the spectra of the blazars monitored with H.E.S.S. has a double impact. First, it enables a precise measurement of the COB over two decades of wavelengths, with a statistical uncertainty certainly inaccessible to *Fermi*-LAT, at least below $z \sim 0.5$. The peak amplitude of the COB at $z = 0$ is now known at the 20% level, only considering the VHE measurement. The room left for improvements and the potential consequences of such a measurement are discussed in Chapter 5. A precise measurement of the EBL absorption also allows the intrinsic spectra of VHE extragalactic sources to be derived, which significantly improves our knowledge of the broad band radiation emitted by these objects. The systematic uncertainties on the hardness of the intrinsic spectra are not dominated by the EBL uncertainty for nearby ($z \lesssim 0.2$) sources.

This study is an example of how knowledge on the astrophysics of a class of sources (intrinsic spectra), particle physics processes (pair creation) and cosmology (genesis and evolution of the COB) can be combined to accurately describe astronomical data.

Bibliography

Abdo, A. A., Ackermann, M., Ajello, M., et al. 2010, ApJ, 723, 1082

Aharonian, F., Akhperjanian, A. G., Barres de Almeida, U., et al. 2007a, A&A, 475, L9

Aharonian, F., Akhperjanian, A. G., Barres de Almeida, U., et al. 2007b, A&A, 473, L25

Aharonian, F., Akhperjanian, A. G., Bazer-Bachi, A. R., et al. 2006a, ApJ, 636, 777

Aharonian, F., Akhperjanian, A. G., Bazer-Bachi, A. R., et al. 2006b, Nature, 440, 1018

de Naurois, M. & Rolland, L. 2009, Astroparticle Physics, 32, 231

Domínguez, A., Primack, J. R., Rosario, D. J., et al. 2011, MNRAS, 410, 2556

Gilmore, R. C., Somerville, R. S., Primack, J. R., & Domínguez, A. 2012, MNRAS, 422, 3189

H.E.S.S. Collaboration, Abramowski, A., Acero, F., Aharonian, F., et al. 2010, A&A, 520, A83

Meyer, M., Horns, D., & Zechlin, H.-S. 2010, A&A, 523, A2

Meyer, M., Raue, M., Mazin, D., & Horns, D. 2012, arXiv:1202.2867

Piron, F., Djannati-Atai, A., Punch, M., et al. 2001, A&A, 374, 895

Reimer, A. 2007, ApJ, 665, 1023

The Fermi-LAT Collaboration. 2012, arXiv:1211.1671

Vovk, I., Taylor, A. M., Semikoz, D., & Neronov, A. 2012, ApJ, 747, L14

CHAPTER 4

Variability - minijets-in-a-jet statistical model

Blazars are characterized by some of the most surprising emission properties observed in any astrophysical source. Not only are they able to accelerate particles up to TeV energies but they can also exhibit extreme emission levels and hyper variability. Following C. Dermer (e.g. in Lott et al. 2012), the emission of an accreting object can be defined as extreme if the outflow varies faster than the Eddington limited inflow. For energy conservation reasons, this is necessarily a precarious state. I recall from Chapter 1.1.2.2 that if the energy is extracted from the accretion, the input power is limited by the Eddington luminosity $\mathcal{L}_{\rm Edd} = 4\pi GMm_pc/\sigma_{\rm T} \sim 1.26 \times 10^{47}(M/10^9M_\odot)$ erg s^{-1}. Calling $T_G = R_S/c = 2GM/c^3 \sim 0.98 \times 10^4(M/10^9M_\odot)$ s the light crossing time of the black hole, the quantity $\mathcal{L}_{\rm Edd}/T_G = 2\pi m_pc^4/\sigma_T \sim 1.28 \times 10^{43}$ erg s^{-2} is then a constant of Nature (independent of the mass of the object) and should set a strict upper limit on the variation rate $\Delta L/\Delta t$ of any observed luminosity. 3C 454.3 is one of the very few examples at HE of an extreme FSRQ (The Fermi-LAT collaboration 2011), with an isotropic luminosity change rate of $\sim 10^{46}$ erg s^{-2}.

A weaker criterion to characterize extreme emission states is hyper variability, i.e. variations in the flux of an object that apparently violate causality. Assuming that the minimum size involved in the surrounding of the super-massive black hole is R_S, then coherent emission can not vary faster than $T_G \sim 2.7(M/10^9M_\odot)$ hours. Hyper variability is defined by a violation of this criterion, sometimes called the causality argument. Strikingly, even objects such as the fastest gamma-ray bursts (GRB, see e.g. Piran 2004) are not hyper variable. Assuming a central mass of $\sim 30M_\odot$, their light-crossing time is approximately 0.1μs, two orders of magnitude below the minimum variation time scale for GRB. A couple of VHE blazars, such as the BL Lac objects Mrk 421 (e.g. Gaidos et al. 1996) and Mrk 501 (e.g. Albert et al. 2007) or the FSRQ PKS 1222+21 (Aleksić et al. 2011) are hyper variable.

PKS 2155-304 is one of the very few example of both a hyper variable and an extremely variable source. As such, it is one of the best laboratories to study the violent Universe. I describe in Sect. 4.1 the properties of the emission of this source during its most extreme period known at VHE. In Sect. 4.2, I develop a model that jointly accounts for the statistical, spectral and Fourier properties of the emission of this prototypical object.

4.1. The dramatic outbursts of PKS 2155-304

PKS 2155-304 is one of the brightest extragalactic sources of the southern sky at VHE or in the X-ray band. Its routine emission of a few tenths of C.U. has been long-term monitored with H.E.S.S. (see e.g. Aharonian et al. 2005a,b, 2009b), which has now accumulated more than 200 hours of data on this field of view. The period of 4 days between the 26 July and the 30 July 2006 (MJD 53944-53947) broke this routine, in particular with three runs taken on the 26 July that constitute "one of the most dramatic outburst seen from any TeV γ-ray source" (Longair 2010). The light curve of PKS 2155-304 above 200 GeV during these three runs is shown in Fig. 1.

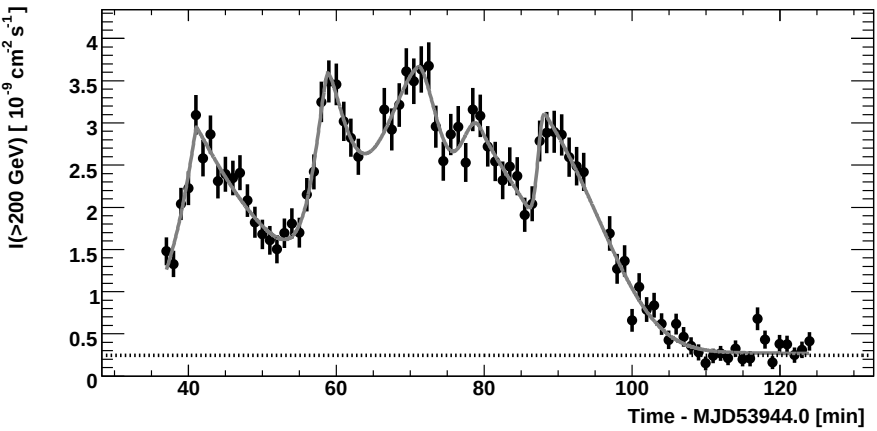

FIGURE 1. Integral flux of PKS 2155-304 above 200 GeV vs time during the dramatic outburst on the 26 July 2006. The data are binned in one minute intervals. The horizontal line represents the flux of the Crab Nebula. *Extracted from Aharonian et al. (2007)*

This high flux period at VHE and the concomitant multi-wavelength campaign have been extensively described in Aharonian et al. (2007, 2009a); H.E.S.S. Collaboration, Abramowski et al. (2010); H.E.S.S. Collaboration et al. (2012) and I only summarize the properties of the flux observed with H.E.S.S. in the following sub-sections.

4.1.1. Temporal properties

One of the most striking characteristic of the light curve shown in Fig. 1 is the typical time scale of the flux variations. An accurate estimation of this time scale is not straight forward and I describe in the following the method used by B. Giebels in Aharonian et al. (2007) to fit an appropriate model to these data, a method which I use in Chapter 5.3.1.

4.1.1.1. *Generalized asymmetric Gaussian fit*

The light curve of PKS 2155-304 during the dramatic outbursts can be interpreted as a series of bursts described with generalized asymmetric Gaussians $\mathrm{I}(t) = A \exp[-(|t - t_{\max}|/\sigma_{r,d})^{\kappa}]$, where $t_{\max}$ is the time maximum intensity of the burst A; σ_r and σ_d are the rise ($t < t_{\max}$) and decay ($t > t_{\max}$) time constants, respectively; and κ is a measure of the sharpness of the burst. The parameters σ_r and σ_d are highly correlated with κ and the appropriate rise and decay times from half to maximum amplitude are then computed as $\tau_{r,d} = [\ln 2]^{1/\kappa}\sigma_{r,d}$. The peak finding and fitting procedure reveals that the flux of PKS 2155-304 during this exceptional night is well described by a series of five bursts above a constant term as shown in Fig. 2.

4.1.1.2. *Shortest significant doubling time*

The parameters resulting from the fit of the light curve of PKS 2155-304 are given in Table 1.

The shortest rise time during these outbursts is $\tau_r = 67 \pm 44$ s (fifth peak), with a large uncertainty due to the 1 min temporal binning. The authors thus quote the shortest significant rise time as $\tau_{r\ HESS} = 173 \pm 28$ s. This time scale of ~ 3 minutes is at odds with the black hole light crossing time of ~ 3 hours[1], demonstrating the hyper variability of this object.

[1]The mass of the black hole hosted by PKS 2155-304 of $1 - 2 \times 10^9\ M_{\odot}$, is estimated from the correlation of supermassive black hole masses with the magnitude of the host in the R-band (Bettoni et al. 2003).

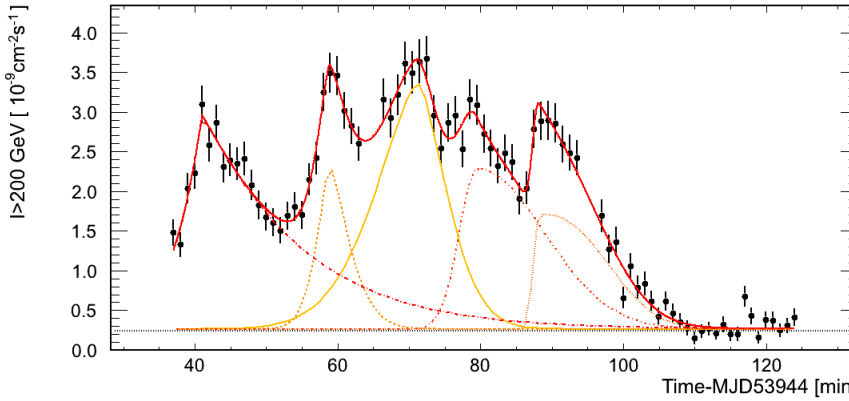

FIGURE 2. Integral flux of PKS 2155-304 above 200 GeV vs time during the dramatic outburst on the 26 July 2006. Five generalized asymmetric Gaussian functions are fitted to the data, which are binned in one minute intervals. *Courtesy of B. Giebels*

$t_{\max}$ [min]	A [10^{-9} cm^{-2} s^{-1}]	τ_r [s]	τ_d [s]	κ
41.0	2.7 ± 0.2	173 ± 28	610 ± 129	1.07 ± 0.20
58.8	2.1 ± 0.9	116 ± 53	178 ± 146	1.43 ± 0.83
71.3	3.1 ± 0.3	404 ± 219	269 ± 158	1.59 ± 0.42
79.5	2.0 ± 0.8	178 ± 55	657 ± 268	2.01 ± 0.87
88.3	1.5 ± 0.5	67 ± 44	620 ± 75	2.44 ± 0.41

TABLE 1. Results of the best χ^2 fit of the superposition of five bursts and a constant to the H.E.S.S. data. The constant term is $0.27 \pm 0.03 \times 10^{-9}$ cm^{-2} s^{-1} (1.1 C.U.) *Extracted from Aharonian et al. (2007)*

Using the EBL de-absorbed flux at 1 TeV of $\phi(1\text{ TeV}) \sim 1.3 \times 10^{-9}$ cm^{-2} s^{-1} TeV^{-1} derived in Chapter 3.3.1.2 (dataset number 7), I obtain an isotropic luminosity change in one doubling time of $\Delta L = 4\pi D_L^2 E^2 \phi(1\text{ TeV})/2 \sim 3.5 \times 10^{46}$ erg s^{-1}. The change of the apparent luminosity then occurs at a rate of $\Delta L/\tau_{r\ HESS} \sim 2 \times 10^{44}$ erg s^{-2}, an order of magnitude above the Eddington limited input. So, as stated in

the introduction of this chapter, PKS 2155-304 is both a hyper variable and an extreme VHE emitter.

4.1.2. Statistical properties

4.1.2.1. *Flux distribution*

The distribution of the logarithm of the flux of PKS 2155-304 as observed with H.E.S.S. between 2005 and 2007 is shown in Fig. 3. The interpretation of the July 2006 eruption as a "flaring" regime, compared to a routine "quiescent" regime, motivated the exclusion of the former in the left panel. The distribution of the flux is asymmetric and is well described with a log-normal distribution (H.E.S.S. Collaboration, Abramowski et al. 2010), i.e. with a Gaussian distribution of the logarithm of the flux.

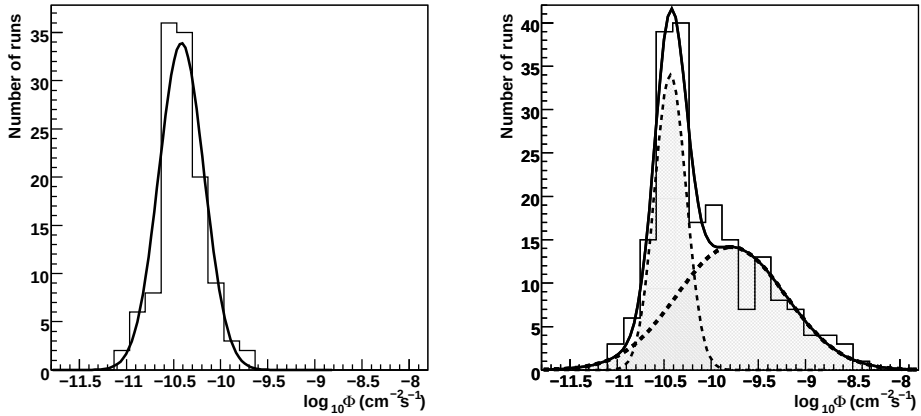

FIGURE 3. Distribution of the logarithm of the integral flux of PKS 2155-304 above 200 GeV, an entry corresponds to a run. *Left:* Data from 2005 to 2007 without the outburst period. *Right:* Data from 2005 to 2007 including the outburst period. *Extracted from H.E.S.S. Collaboration, Abramowski et al. (2010)*

The right panel of Fig. 3 shows the distribution of the logarithm of the flux of PKS 2155-304 between 2005 and 2007 including the data from the outburst. The sum of two Gaussian functions is fitted to the

data and the interpretation in term of a low quiescent state and a high flaring state seems appropriate.

4.1.2.2. *The R.M.S.-flux correlation*

The moments of the flux are closely related to the flux distribution. In the presence of instrumental uncertainties, a particular attention must be paid to the way they are estimated. The true variance V is especially biased by instrumental uncertainties σ_i and one can easily show (e.g. using a Gaussian field as in Appendix C) that the measured variance $V_{\rm mes}$ is the sum of the true variance and of the variance due to the uncertainties, i.e. $V_{\rm mes} = V + \sum_i \sigma_i^2$ where i indexes the data points. If the true variance dominates over the variance due to the uncertainties, one can compute an estimator of the true R.M.S. called the excess R.M.S. as $\sigma_{\rm XS} = \sqrt{V_{\rm mes} - \sum_i \sigma_i^2}$ (see also Vaughan et al. 2003, for the fractional and excess variance). This estimator of the true R.M.S. is only defined when the power in the intrinsic variance is larger than the variance due to uncertainties.

In H.E.S.S. Collaboration, Abramowski et al. (2010), the excess R.M.S. and the average of the flux of PKS 2155-304 are computed in 20 points wide windows with a temporal binning of 1 min (resp. 4 min) per point. A scatter plot of these sample R.M.S. and sample flux is shown in Fig. 4. A linear correlation is preferred to an absence of correlation at the 2σ level (resp. 4σ level) for the 1 min (resp. 4 min) temporal bins, as shown in the scatter plots with filled symbols. Studying a larger data set, with nonetheless an higher energy threshold, the authors show that for the two above-mentioned binnings a correlation is preferred at the 4σ level and 7σ level to an absence of correlation.

4.1.2.3. *The link between log-normality and the R.M.S.-flux relation*

The R.M.S.-flux relation can be explained as a consequence of a log-normal distribution of the flux (Uttley et al. 2005), but the reciprocal is not true! A log-normal flux ϕ is the exponential of an underlying random Gaussian variable x, so that $\phi = f(x)$, where f is the exponential function. A small fluctuation of x around x_0, δx, results in a small fluctuation of the flux ϕ around $f(x_0)$, $\delta\phi$, and the variance of

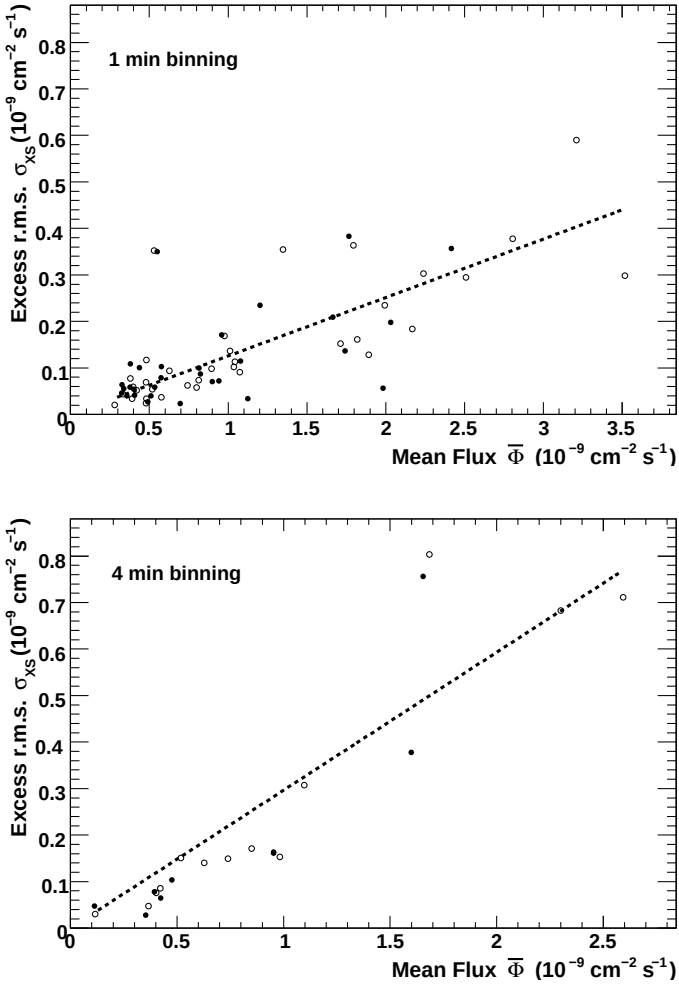

FIGURE 4. Excess R.M.S. versus flux of PKS 2155-304 above 200 GeV for a 1 min binning (*Top panel*) and 4 min binning (*Bottom panel*). The dashed lines are a linear fit to the full points. *Extracted from H.E.S.S. Collaboration, Abramowski et al. (2010)*

the flux is:

$$\delta\phi^2 = \left[\frac{\partial f}{\partial x}(x_0)\right]^2 \delta x^2 = [\exp(x_0)\delta x]^2 \propto f(x_0)^2 \tag{4.1}$$

Thus, the sample R.M.S. (square root of the left hand term) is proportional to sample flux (square root of the right hand term) if the flux is log-normal. This proposition remains valid for a large class of functions f, as I show in Sect. 4.2.1.2.

4.1.3. Spectral variability

4.1.3.1. *The flux-index relation*

In addition to flux variability, the blazar PKS 2155-304 exhibits an important spectral variability, as mentioned in Chapter 3.3. I show in Fig. 5 the variations of the intrinsic index of PKS 2155-304 as a function of its intrinsic flux at 1 TeV during the high-flux state, i.e. only including the data sets corresponding to the outburst period (*1* to *7*). Fitting the hardening of the index with an empirical function linearly varying with the logarithm of the flux $-\Gamma = a + b \log_{10} \phi(1 \text{ TeV})$ represents relatively well the data, with a χ^2 probability of 20% ($\chi^2/dof = 7.3/5$) and is preferred to a constant fit at the $\sim 9\sigma$ level by a likelihood ratio test.

The best-fit value of the proportionality coefficient is $b = 0.48 \pm 0.06$. Assuming the simplest variability scenario, i.e. a power law rotating around a swivel energy $E_{\rm swiv}$ where the flux $\phi_{\rm swiv}$ is fixed yields $\log \phi(E) = \log \phi_{\rm swiv} - \Gamma \times \log(E/E_{\rm swiv})$, i.e. $\log_{10}(E_{\rm swiv}[\text{TeV}]) = -1/b$, which would locate the swivel energy between 4 GeV and 14 GeV.

4.1.3.2. $F_{\rm var}$ *vs energy*

There is an interesting relation between the fractional variance and the energy as shown in Fig. 6. The correlation is parametrized by H.E.S.S. Collaboration, Abramowski et al. (2010) with a power-law function $F_{\rm var} \propto E^{0.2}$.

Within the simple "swivel energy" scenario where I assume that the underlying variable is the spectral index, the variance of the flux $\phi(E) = \phi_{\rm swiv}(E/E_{\rm swiv})^{-\Gamma}$ can simply be derived propagating a variation σ_Γ of the index:

$$\sigma^2_\phi(E) = \phi^2(E)\sigma^2_\Gamma \log^2(E/E_{\rm swiv}) \tag{4.2}$$

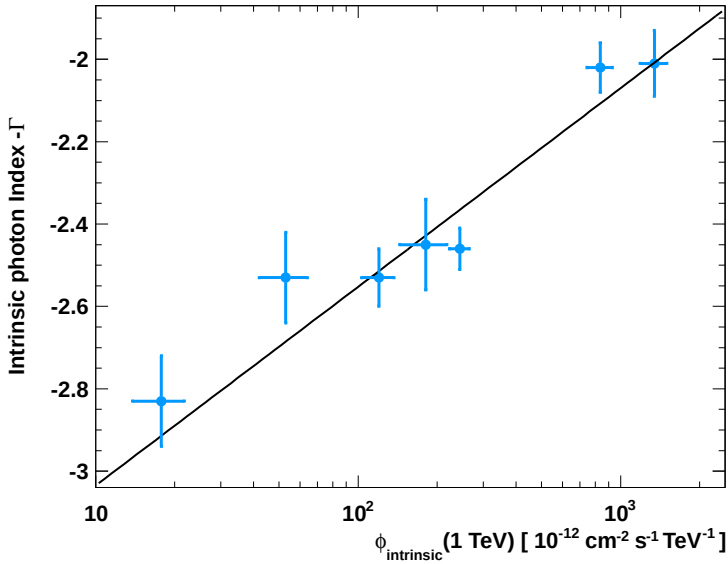

FIGURE 5. Photon index $-\Gamma$ vs EBL de-absorbed flux at 1 TeV, as derived in Chapter 3.3.1.2 for the high state of PKS 2155-304. The continuous line shows a fit of a function linear in $\log \phi$ to the data.

which, with a variation of the fractional variance $\sigma_\phi/\phi \propto \log E$, reproduces the increasing trend as function of energy. This model would be as good a representation of the data as the power-law fit shown in Fig. 6. Only a larger dynamical range in energy will allow the distinction.

4.1.4. Fourier properties

The last observable that I discuss is related to the properties of the outburst in the Fourier space. The power spectral density (PSD) of the light curve, defined as the square modulus of the Fourier transform, is indeed well modelled with a power law of index close to $\alpha = 2$, as shown in Fig. 7. Such an index corresponds to a so-called red-noise process; for reference, $\alpha = 0$ is referred to as white noise and $\alpha = 1$ as pink noise, or flicker noise.

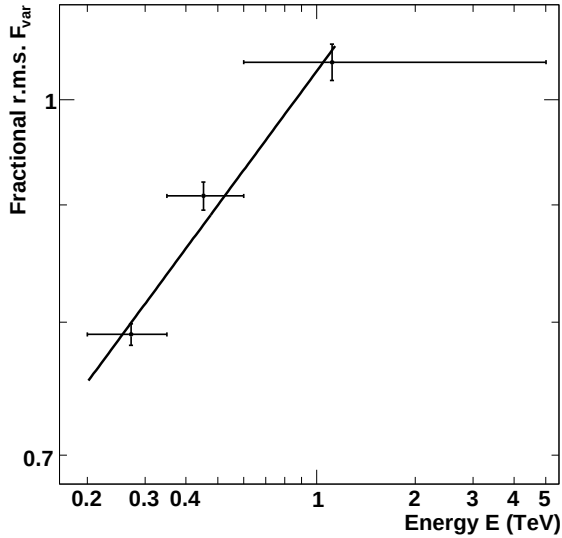

FIGURE 6. Fractional variance vs energy for the observation of PKS 2155-304 during the outburst. A fit of a power law to the data is shown by the continuous line. *Extracted from H.E.S.S. Collaboration, Abramowski et al. (2010)*

4.1.4.1. *Fourier spectrum of PKS 2155-304*

I define the studied light curve as the time series $\{t_i,\ \phi_i,\ \sigma_i\}$, where t_i are the dates when the fluxes ϕ_i are measured with an instrumental uncertainty σ_i. To compute the PSD, one usually subtracts the average flux μ to the time series, yielding $\phi'_i = \phi_i - \mu$, and then computes:

$$P(\nu) = A \times \left| \sum_{i=1}^{N} \phi'_i \mathrm{e}^{2i\pi\nu t_i} \right|^2 = A \left(\sum_i \phi'_i \cos(2\pi\nu t_i) \right)^2 + A \left(\sum_i \phi'_i \sin(2\pi\nu t_i) \right)^2 \tag{4.3}$$

where A is a normalization factor.

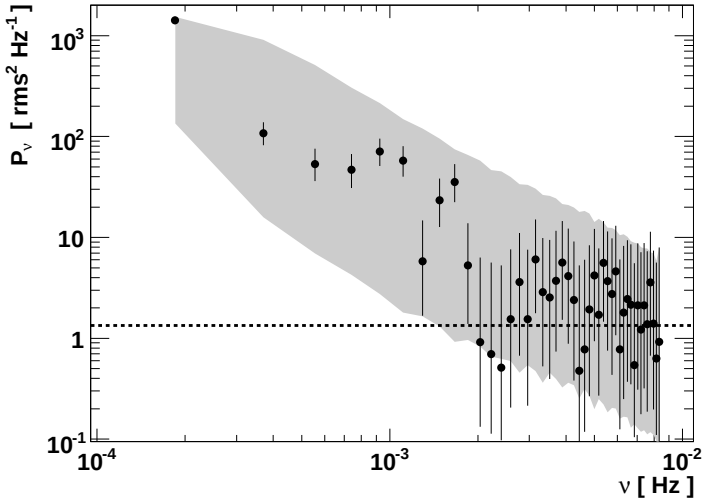

FIGURE 7. PSD of the light curve of PKS 2155-304 during the night of the 26 July 2006. The grey shaded area represents the 90% confidence interval for a red-noise process of index 2. *Extracted from Aharonian et al. (2007)*

The ideal case corresponds to an even number of points N and to a regular sampling of the time series $t_i = t_0 + i \times \delta t$, with $i \in \{1..N\}$. In this case, the Discrete Fourier Transform (DFT) is defined for the frequencies $\nu_k = \nu_{\min} + k \times \delta\nu$, where the step and the minimum frequency are the inverse of the light curve duration $\delta\nu = \nu_{\min} = 1/(t_N - t_1) = 1/T$ and the maximum frequency is set by the Shannon criterion $\nu_{\max} = 1/2\delta t$ (also called the Nyquist frequency), i.e. $k \in \{1..N/2\}$.

The normalization factor A can be set following the Parseval-Plancherel's theorem. The latter states that the integral of the PSD is proportional the variance V of the time series. Taking as a convention the equality

with the normalized variance reads:

$$\frac{V}{\mu^2} = \sum_{k=0}^{k_{\max}} P(\nu_k)\delta\nu = \frac{A}{T} \times k_{\max} \times \frac{1}{k_{\max}} \sum_{k=1}^{k_{\max}} \left| \sum_{i=1}^{N} \phi'_i \mathrm{e}^{2i\pi\nu_k t_i} \right|^2$$

$$= \frac{A}{T} \times k_{\max} \times \sum_{i=1}^{N} \phi'^2_i = \frac{A}{T} \times k_{\max} \times N \times V \tag{4.4}$$

which results in a normalization $A = N/k_{\max} \times T/\mu^2 N^2 = 2T/\mu^2 N^2$. This is the normalization of van der Klis, usually employed for the analysis of AGN and X-ray binaries (for a list of the various normalizations, see Appendix A of Vaughan et al. 2003).

Since the PSD depends on the flux, the instrumental uncertainties on the flux also result in an uncertainty on the PSD values, especially for VHE light curves where the count rates remain small. In Fig. 7, the error bars on the PSD are numerically computed varying the points of the light curves in their Gaussian error bars and computing the resulting variations in each frequency bin. I use in Appendix C an elegant method to compute these uncertainties in an analytical way. This obviously speeds up the computation, but above all it does not rely on the generation of random numbers.

4.1.4.2. *Experimental biases*

The uncertainties on the flux not only result in uncertainties on the PSD, but also distort it. A constant of amplitude $A\sum_i \sigma_i^2$ (see Appendix C) is added to the spectrum at each frequency, as represented in Fig. 7 with the dashed line. Above a given frequency, the information on the PSD is then lost and the red-noise characteristics no longer can be reconstructed.

One could think of fitting a power-law model exclusively on the low frequency part of the spectrum to reconstruct the Fourier index. Another instrumental effect, the sampling and windowing of the signal, prevents from such a simplistic approach. Considering the windowing: if the true signal $\hat{\phi}(t)$ is observed for a duration T, so that the observed signal is $\phi(t) = \hat{\phi}(t) \times \Pi_{0..T}(t)$ where Π is the rectangular function (1 in the interval, 0 elsewhere), then the Fourier transform (FT) of the observed signal is the convolution of a cardinal sine (FT of the rectangular function) with the FT of the true signal. This impacts primarily the steepest part of the spectrum (in linear frequency scale), which is

"smeared out", yielding a leakage of the power from low frequencies into the high-frequency domain (this effect is usually called spectral leakage).

The impact of the sampling, windowing and of the instrumental uncertainties are schematically represented in Fig. 8. The distorted PSD is represented in the bottom right panel, together with the dependence that would be obtained from a direct fit (black line). This illustrates the need for a forward-folding method, which starts from an ideal light curve (top left panel), applies the instrumental biases and compares the final result with the measurement.

The subtlety of the approach probably lies in generating the ideal light curve. Indeed, besides the scatter due to the statistical uncertainties, an intrinsic scatter is expected if the observed light curve is a realization of a stochastic process (e.g. red noise). The forward-folding Fourier analysis thus entails simulating a large number of ideal light curves for each set of tested parameters, in applying the instrumental distortions, and in comparing the "dirty" simulations with the observable (here the PSD) in order to retrieve the best set of underlying parameters.

4.1.4.3. *Forward-folding Fourier analysis*

The aperiodic, red-noise variability of AGN in the X-ray band has been discussed for almost 30 years and I refer the reader to the excellent discussion of Uttley et al. (2005) and reference therein for an extensive discussion of the topic. Red-noises are stochastic processes characterized by a power-law PSD, $P(\nu) \propto \nu^{-\alpha}$ with a Fourier index $\alpha > 1$. Within such a framework, the light curve that we observe is just one realization of the underlying process and the observed PSD is expected to show a great scatter around the underlying "true" PSD. To be more quantitative, for such a process, the real and imaginary part of the DFT are normally distributed with standard deviations of one hundred percent. Timmer & Koenig (1995) developed a simple method to generate realizations of such a random process. One defines an appropriate frequency binning $\{\nu_k\}_{k=1..k_{\rm max}}$ and a "true" PSD $P(\nu) \propto \nu^{-\alpha}$, and one draws $2k_{\rm max}$ random numbers ρ_k and ρ'_k with a Gaussian distribution of mean zero and standard deviation one. The DFT of the simulated light curve is then computed as:

$$\mathrm{DFT}(\nu_k) = \sqrt{P(\nu_k)/2} \times \rho_k + i \times \sqrt{P(\nu_k)/2} \times \rho'_k \tag{4.5}$$

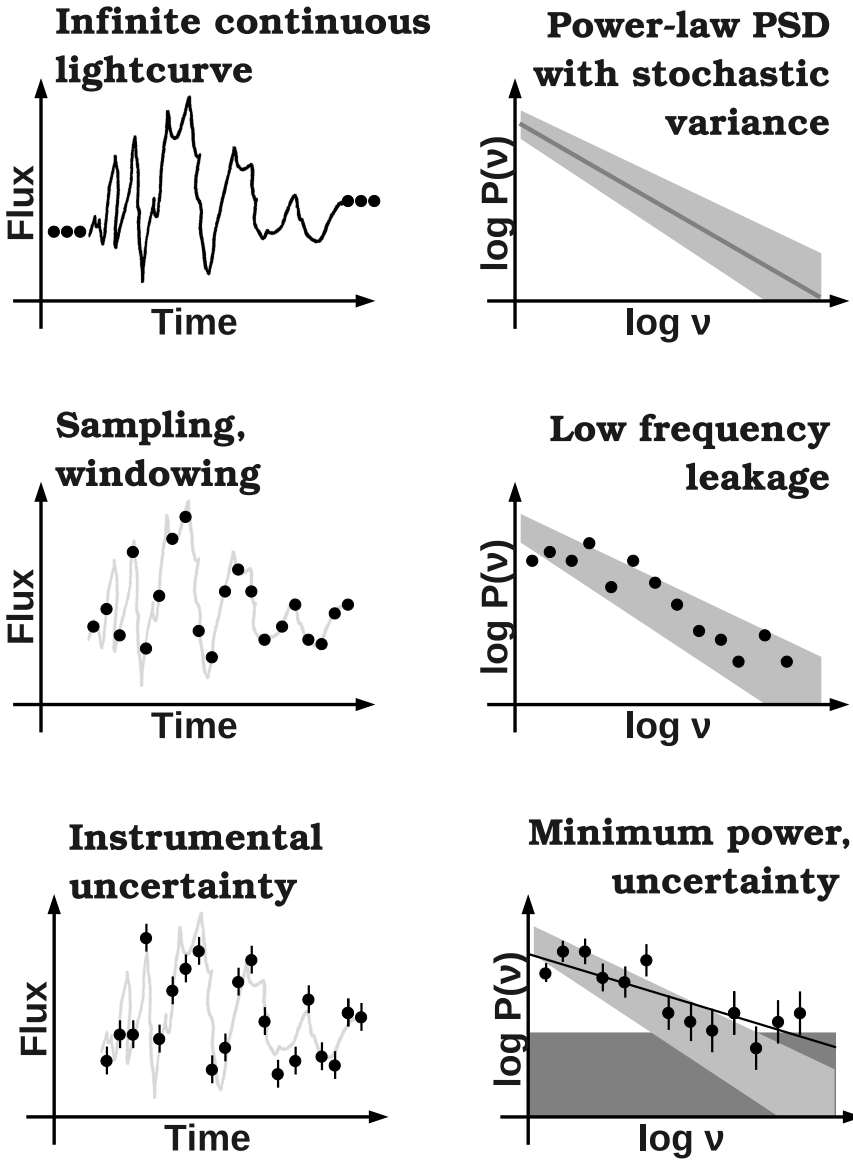

FIGURE 8. Schematic representation of the impact of the experimental effects on the PSD of a red-noise process.

so that $< |\mathrm{DFT}(\nu_k)|^2 >= P(\nu_k)$

A back Fourier transform algorithm, e.g. the FFT, enables the computation of a light curve that is one realization of the stochastic process. To minimize the spectral leakage, an extension of the low frequency part of the spectrum is required, i.e. the simulation of longer light curves than necessary (typically more than a factor 10, see e.g. Superina 2010). This approach generates a normally-distributed flux in the temporal space. It is not uncommon to find in the literature authors using the exponential of the light curves generated with the method of Timmer and König to simulate a log-normally-distributed flux.

Forward-folding Fourier analysis involves simulating realizations of a red-noise process for various sets of parameters (e.g. using the Fourier index α) and applying to the generated light curve the same biases as those that affect the observed light curve (sampling, windowing, instrumental uncertainties). This is the procedure that G. Superina followed in Degrange et al. (2008) using structure functions (a tool closely related to the PSD). She parametrized the power law with its normalization at 10^{-4} Hz and its index α. Assuming a log-normal process, i.e. using the exponential of the output of the method of Timmer and König, she reconstructed a Fourier index of $\alpha = 2.06 \pm 0.21$ (H.E.S.S. Collaboration, Abramowski et al. 2010).

I cross checked her results developing a forward-folding likelihood method based on the PSD. Using a log-log binning in the Fourier space, I define the probability density function of the true process affected by the instrumental biases by cumulating the probability density functions (pdf) of a large number (typically 10^4) of simulated Fourier spectra. The pdf of a single spectrum is simply given in each frequency bin ν_i by a normal distribution centred on the value of the simulated spectrum $P(\nu_i)$ and of standard deviation provided by the simulated instrumental uncertainty (as computed analytically in Appendix C). I parametrized the spectra only by their Fourier index and computed their normalization based on the measured variance. The method is linear, as shown in Fig. 9. This particular test corresponds to the simulation of normal light curves with a duration, a binning (1 min) and statistical uncertainties equivalent to those measured from PKS 2155-304 during the night of the 26 July 2006. The smallest statistical uncertainty on the

index that can be achieved with such a light curve is on the order of $\Delta\alpha = 0.4$ around $\alpha = 2$.

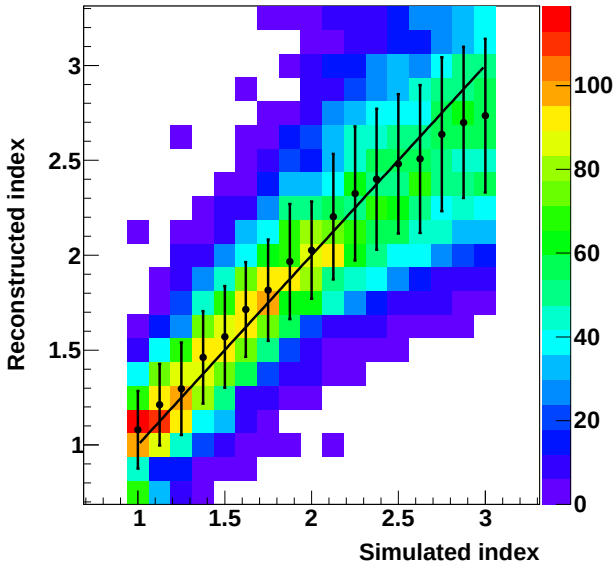

FIGURE 9. Reconstructed Fourier index vs simulated one using the forward-folding Fourier analysis described in the text. Each entry represents a simulation of a light curve equivalent to the big flare of PKS 2155-304. The continuous black line represents the identity function.

Studying the same data set as G. Superina (night of the outburst and the three following nights), binned on a 14 min time scale, I reconstruct a Fourier index of $\alpha_{\rm Norm} = 1.73^{+0.23}_{-0.14}$ for the simulation of a normal process and $\alpha_{\rm LogNorm} = 1.76^{+0.44}_{-0.21}$ for a log-normal process, in good agreement with the value derived with the structure functions.

4.2. Modelling of the outbursts

As mentioned in the introduction of this chapter, PKS 2155-304 is a fantastic laboratory for understanding the most violent processes in the Universe. The properties of its emission observed at VHE triggered a tremendous modelling effort (already $\sim$ 250 citations to the paper

"An Exceptional Very High Energy Gamma-ray Flare of PKS 2155-304" can be found on the NASA ADS as of September 2012). I add a model to this long list, which has the originality of putting aside the radiative processes at play in the emission of the γ rays. This model, which I call the minijets-in-a-jet statistical model, aims at showing that the statistical properties of the flux observed during the dramatic outburst can be generated inside the jet with an additive process and do not necessarily come from the disk, where multiplicative processes naturally emerge. It also conciliates the stochastic process responsible for the variations of the flux with the interpretation of the light curve as a series of bursts, which is an additive approach.

4.2.1. The additive/multiplicative dilemma

The large and fast variability of PKS 2155-304 is puzzling. The time scales involved in the emission are much shorter than the black hole light crossing time and are difficult to achieve in disks, as discussed by Narayan & Piran (2012). This points to a modulator of the emission that is relativistically boosted, naturally locating it inside the jet. The minimum variability time scale then goes down to $R/c\delta$, where R is the size of the region and δ his Doppler boost in the observer frame. A small size region and/or a large boost can then account for the minute time scale observed with H.E.S.S.. A wide class of models that have been developed to explain the emission of PKS 2155-304 are based on multiple region scenarios (see e.g. Ghisellini & Tavecchio 2008; Giannios et al. 2009), which would explain the successive bursts. The sum of the emission of each region is the quantity that we measure on Earth and it should tend to a Gaussian distribution invoking the central limit theorem (CLT). This conclusion is at odds with the observed skewed flux distribution.

On the contrary, inward propagating fluctuations in disks are expected to cumulate in a multiplicative way (see e.g. Arévalo & Uttley 2006) and create, as an avalanche, a log-normal distribution of the accretion rate that could modulate (as in McHardy 2008) the disk emission. This log-normality also finds its roots in the CLT: if one measures the quantity $y = \prod x_i$, then applying the CLT to $\log y = \sum \log x_i$, the distribution of $\log y$ is normal, i.e. y is log-normal. So multiplicative processes naturally generate log-normal distributions. A log-normally distributed variable moreover exhibits a linear R.M.S-flux correlation, as shown in Eq. (4.1), and as observed for PKS 2155-304.

A preliminary conclusion would be that fast variations point to a variability stemming inside the jet, where additive models are invoked, when the statistical properties of the flux indicate a multiplicative process, naturally generated in a disk. One can see that the crucial question of the jet-or-disk location of the emission modulator is closely related to a discussion of additive and multiplicative processes, which in turn is entirely based on a clincher: the CLT.

4.2.1.1. *The central limit theorem for physicists*

The CLT has a key role in the discussion of the additive vs multiplicative process that I discuss in the following and I briefly recall its demonstration (for physicists).

The only tools needed to demonstrate the CLT are the characteristic functions. The characteristic function $\varphi_X(t)$ of a random variable X can be defined as the Fourier transform of its pdf $f_X(x)$:

$$\varphi_X(t) = \int_{-\infty}^{+\infty} f_X(x) \exp(itx) \mathrm{d}x = \mathbf{E}[\exp(itX)] \tag{4.6}$$

where $\mathbf{E}$ is the expectation operator. This last equality is actually the definition of the characteristic function if the pdf is not defined. The derivatives of $\varphi_X(t)$ are closely linked to the moments of the random variable. For instance, the first derivative is:

$$\frac{\partial \varphi_X}{\partial t}(t) = \int_{-\infty}^{+\infty} ix f_X(x) \exp(itx) \mathrm{d}x = i\mathbf{E}[X \exp(itX)] \tag{4.7}$$

which reads for, t=0, $\frac{\partial \varphi_X}{\partial t}(0) = i\mathbf{E}[X]$, i.e. the first derivative evaluated at zero is, within a multiplicative term, the expectation of the random variable. Each derivative brings down a term ix and the k^{th} derivative of the characteristic function evaluated at zero is the k^{th} moment of the random variable:

$$\varphi_X^{(k)}(0) = i^k \mathbf{E}[X^k] \tag{4.8}$$

With this tool, one can show that the sum of a large number of random variables with finite average and variance tend to a normal distribution. I consider for simplicity[2] random variables X_j of mean

[2]A more general demonstration for X_i of average μ_i and standard deviations σ_i is easily achieved using the variable $Y_i = (X_i - \mu_i)/\sigma_i$.

$E[X^1] = \mu = 0$ variance $E[X^2] = \sigma^2 = 1$, a second order Taylor expansion of the characteristic function of each of this X_j yields:

$$\begin{aligned}\varphi_{X_j}(t) &= \varphi_{X_j}(0) + \varphi^{(1)}_{X_j}(0) \times t + \varphi^{(2)}_{X_j}(0) \times t^2/2 + o(t^2) \\ &= \mathbf{E}[1] + i\mathbf{E}[X^1] \times t + i^2\mathbf{E}[X^2] \times t^2/2 + o(t^2) \\ &= 1 - t^2/2 + o(t^2) \end{aligned} \tag{4.9}$$

Let now Z be the sum of these N independent variables normalized to $\sqrt{N}$ (the nice trick is here), i.e. $Z = \sum X_j/\sqrt{N}$. These variables are independent and the pdf of Z is the convolution of the pdfs of the $X_i/\sqrt{N}$, i.e. after Fourier transform, the product:

$$\begin{aligned}\varphi_Z(t) &= \prod \mathbf{E}[\exp(itX_j/\sqrt{N})] = \prod \varphi_{X_j}(t/\sqrt{N}) \\ &\sim \left(1 + \frac{-t^2/2}{N}\right)^N \to \exp(-t^2/2)\end{aligned} \tag{4.10}$$

which means that the characteristic function of Z tends to a Gaussian, for a large enough number of X_i. The pdf of Z is then the Fourier transform of a Gaussian, i.e. is itself a Gaussian. The sum of random variables with finite moments then tends to a Gaussian distribution. This demonstration of the CLT relies on the Taylor expansion performed in Eq. (4.9) and the moments of the summed quantities absolutely need to be finite.

4.2.1.2. *Pareto distributions*

Paretian variables are an example of random variable with infinite moments, in which case the CLT can not be applied. They are characterized by a probability density function following a power law of index $1 + \alpha$:

$$f_Y(y) = \frac{\alpha}{y^{1+\alpha}} \quad \text{for } y > 1 \tag{4.11}$$

One can for example try to compute the average of the variable as:

$$E[Y] = \int_1^{+\infty} y f_Y(y) \mathrm{d}y = \int_1^{+\infty} \alpha y^{-\alpha} \mathrm{d}y \tag{4.12}$$

which diverges for $\alpha \leq 1$. Similarly, the variance diverges for $\alpha \leq 2$.

The Pareto and the log-normal distributions share an interesting property: they are both the exponential of an underlying variable. While a log-normal variable is the exponential of a normal variable,

a Paretian variable is the exponential of an exponentially distributed variable (pdf $f_X(x) = \exp(-\alpha x)$, with $x \geq 0$). Indeed if $Y = g(X) = \exp X$, then:

$$\begin{aligned} \int f_X(x)\mathrm{d}x &= \int f_X\left(g^{-1}(y)\right)\frac{\partial g^{-1}}{\partial y}(y)\mathrm{d}y \\ &= \int \frac{\exp(-\alpha \log y)}{y}\mathrm{d}y = \int \frac{1}{y^{1+\alpha}}\mathrm{d}y \propto \int f_Y(y)\mathrm{d}y \end{aligned} \tag{4.13}$$

I followed in Sect. 4.1.2.3 the argument that Uttley et al. (2005) provide in their Appendix D, which shows that a log-normal variable follows a linear R.M.S.-flux relation. We can push their argument forward and extend it to Pareto distributions. Assuming that the quantity Y is a function of an underlying variable, say $Y = g(X)$, I showed in Eq. (4.1) that an R.M.S. proportional to the flux is equivalent to $(\partial g/\partial x)^2 \propto g(x)^2$, which is (one of) the definition of the exponential function. Thus, a flux proportional to its R.M.S. is equivalent to stating that the flux is the exponential of an underlying variable. So log-normal variables exhibit an R.M.S.-flux relation, and so do Paretian variables.

We have already solved part of the puzzle: it is not necessary for a flux to be log-normal in order to follow a linear R.M.S. flux relation.

4.2.1.3. *A generalized central limit theorem*

Pareto distributions do not have finite moments and their sum do not converge to a normal distribution, as would be expected from the CLT. A generalized central limit theorem (GCLT) has been established in the case of such heavy tailed variables. Apart from mathematical applications, this theorem is used in geophysics and in finance, where Pareto distributions are not uncommon (see, e.g., Zaliapin et al. 2005; Voit 2005). Following the GCLT, the sum of Paretian independent and identically distributed random variables tend to α-stable distributions. These distributions have the property (that can also be used as a definition) that if the variables X_i are α-stable, then their sum $Y = \sum a_i X_i$, where $\{a_i\}_i$ are constant multiplicative factors, also follows an α-stable distribution.

In general the pdfs of α-stable distributions do not have simple expressions and they are defined with their characteristic functions,

which depend on four parameters α, β, c and μ (note that I follow here the notations used e.g. in the GNU Scientific Library, but other parametrizations can be found in the literature):

$$\varphi_Y(t) = \exp\left[it\mu - |ct|^\alpha \left(1 - i\beta \mathrm{sign}(t) \tan(\frac{\pi}{2}\alpha)\right)\right] \tag{4.14}$$

where the term $\tan(\frac{\pi}{2}\alpha)$ is replaced with $-\frac{2}{\pi}\log|t|$ for $\alpha = 1$.

The parameters c and μ are, in the pdf space, a scale and a shift parameters, equivalent to the standard deviation and average for a Gaussian distribution. These parameters can be set for simplicity to one and zero, respectively. The parameter β quantifies the skewness of the distribution and equals one (maximum skewness) when considering the sum of positive Paretian variable (Zaliapin et al. 2005).

An algorithm that simulate a random variable following such an α-stable distribution can be found in the GNU Scientific Library[3]. I show in Fig. 10 the distribution of the logarithm of a random variable following a normalized maximally skewed α-stable distribution for $\alpha = 1.25$. This value is natural within the minijet-in-a-jet statistical model, corresponding to a photon index of 2 (the discussion remains valid for a wide range of values).

I perform in Fig. 10 a fit of a Gaussian to the distribution of the logarithm of the variable. The close agreement between the log-normal fit and the α-stable distribution over a large dynamical range (spanning two order of magnitudes around the maximum) is remarkable and it shows that unless an observation has a wider dynamical range in flux and as large statistics, it is almost impossible to distinguish the two distributions from each other.

We have solved a second point of the puzzle: an additive process can generate a flux distribution that has a large skewness and that closely resembles a log-normal distribution, despite not being multiplicative.

4.2.2. The minijets-in-a-jet statistical model

I develop a physical model that naturally generates a Pareto distribution of the flux of individual regions. This model is purely kinematic, i.e. I only describe the result of the motion of the physical system

[3] `double gsl_ran_levy_skew (const gsl_rng * r, double c, double alpha, double beta)`

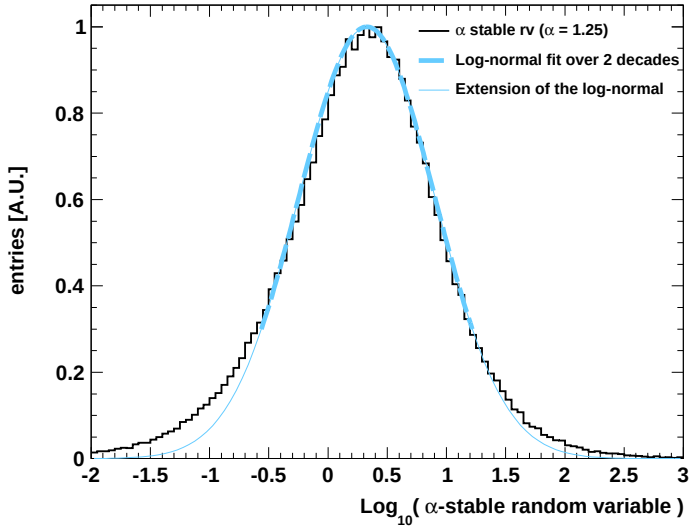

FIGURE 10. Simulated distribution of the logarithm of an α-stable distribution. The thick dashed blue line shows a Gaussian fit of the distribution spanning two decades around the maximum.

within special relativity, and not dynamical, i.e. the model does not rely on an acceleration mechanism or radiative processes. This simple framework can nonetheless be used within the context of dynamic models (which look for the origin of the radiation and/or variability) such as the needle-in-a-jet model of Ghisellini & Tavecchio (2008) or the jets-in-jet model of Giannios et al. (2009). The original idea emerged from the reading of the work of Narayan & Piran (2012), who study the short time-scales of flux variations within a reconnection and a turbulence scenario.

4.2.2.1. *Doppler factor of a single region, randomly oriented in a jet*

I show in Fig. 11 a schematic representation of the geometry of the system. An observer receives radiation from a jet, which is defined in the observer frame $\mathcal{R}_{\rm obs}$ by its velocity Σ (the speed of light is set to unity for the sake of clarity) and Lorentz factor $\Gamma = 1/\sqrt{1-\Sigma^2}$. The

angle offset between the line of sight and the jet axis is given by the parameter θ.

A minijet, e.g. a blob of plasma, is located inside the jet and is defined in the jet frame $\mathcal{R}_{\rm jet}$ by its velocity β and Lorentz factor γ. The conventional spherical angles, which I call ψ and φ, determine the orientation of the minijet with respect to the jet axis in $\mathcal{R}_{\rm jet}$. Finally, I assume that the emission is isotropic in the minijet frame.

I first aim at computing the Doppler factor of the emitting region in the observer frame. I already described in Chapter 1.1.2.1 the method I use to derive the Doppler factor: one just has to determine how the energy of a photon is transformed from the frame of isotropic emission to the observer frame. Writing, in $\mathcal{R}_{\rm minijet}$, the four-momentum as $[E_{\rm minijet}, p_{x\ \rm minijet}, p_{y\ \rm minijet}, p_{z\ \rm minijet}]$, noting that only the photons propagating along the line of sight are detected ($p_{y\ \rm obs} = p_{z\ \rm obs} = 0$) and calling E the energy measured in $\mathcal{R}_{\rm obs}$, the four-momentum transformation is just a series of rotations and Lorentz boosts:

$$\begin{bmatrix} E \\ E \\ 0 \\ 0 \end{bmatrix} = \begin{bmatrix} 1 & & & \\ & \mathrm{c}_\theta & \mathrm{s}_\theta & \\ & -\mathrm{s}_\theta & \mathrm{c}_\theta & \\ & & & 1 \end{bmatrix} \begin{bmatrix} \Gamma & \Gamma\Sigma & & \\ \Gamma\Sigma & \Gamma & & \\ & & 1 & \\ & & & 1 \end{bmatrix} \begin{bmatrix} 1 & & & \\ & 1 & & \\ & & \mathrm{c}_\varphi & \mathrm{s}_\varphi \\ & & -\mathrm{s}_\varphi & \mathrm{c}_\varphi \end{bmatrix}$$
$$\begin{bmatrix} 1 & & & \\ & \mathrm{c}_\psi & \mathrm{s}_\psi & \\ & -\mathrm{s}_\psi & \mathrm{c}_\psi & \\ & & & 1 \end{bmatrix} \begin{bmatrix} \gamma & \gamma\beta & & \\ \gamma\beta & \gamma & & \\ & & 1 & \\ & & & 1 \end{bmatrix} \begin{bmatrix} E_{\rm minijet} \\ p_{x\ \rm minijet} \\ p_{y\ \rm minijet} \\ p_{z\ \rm minijet} \end{bmatrix}$$

where c and s are the cosine and sine functions.

Since the inverse of a rotation of θ is a rotation of $-\theta$ and the inverse of a boost of velocity β is a boost of $-\beta$, this relation can be simply inverted as:

$$\begin{bmatrix} E_{\rm minijet} \\ p_{x\ \rm minijet} \\ p_{y\ \rm minijet} \\ p_{z\ \rm minijet} \end{bmatrix} = \begin{bmatrix} \gamma & -\gamma\beta & & \\ -\gamma\beta & \gamma & & \\ & & 1 & \\ & & & 1 \end{bmatrix} \begin{bmatrix} 1 & & & \\ & \mathrm{c}_\psi & -\mathrm{s}_\psi & \\ & \mathrm{s}_\psi & \mathrm{c}_\psi & \\ & & & 1 \end{bmatrix} \begin{bmatrix} 1 & & & \\ & 1 & & \\ & & \mathrm{c}_\varphi & -\mathrm{s}_\varphi \\ & & \mathrm{s}_\varphi & \mathrm{c}_\varphi \end{bmatrix}$$
$$\begin{bmatrix} \Gamma & -\Gamma\Sigma & & \\ -\Gamma\Sigma & \Gamma & & \\ & & 1 & \\ & & & 1 \end{bmatrix} \begin{bmatrix} 1 & & & \\ & \mathrm{c}_\theta & -\mathrm{s}_\theta & \\ & \mathrm{s}_\theta & \mathrm{c}_\theta & \\ & & & 1 \end{bmatrix} \begin{bmatrix} E \\ E \\ 0 \\ 0 \end{bmatrix}$$

This way, we have a simple expression of the energy in $\mathcal{R}_{\rm minijet}$ as a function of the observed energy. This relation defines the Doppler factor δ as $E_{\rm minijet} = \delta^{-1} E$ and after a bit of algebra, one gets:

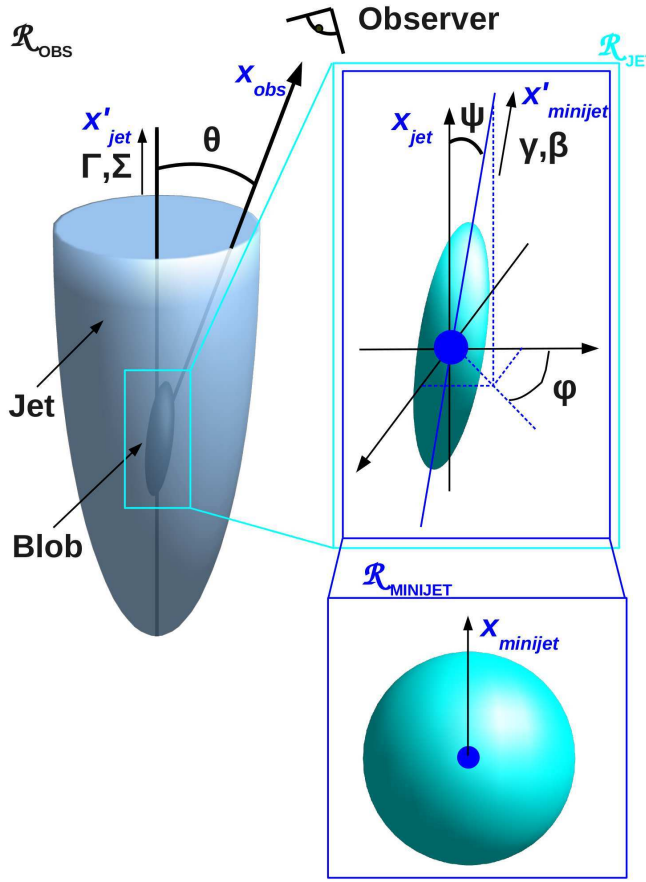

FIGURE 11. Schematic view of the geometry. The left side corresponds to the observer frame $\mathcal{R}_{\rm obs}$, in which the jet is tilted by angle θ from the line of sight (along $x_{\rm obs}$) and is boosted by a Lorentz factor Γ (velocity Σ) along $x'_{\rm jet}$. The minijet is defined by its Lorentz factor γ (velocity β), in the jet frame $\mathcal{R}_{\rm jet}$ (top right). The orientation of the minijet along $x'_{\rm minijet}$ compared to the jet axis in its rest frame, $x_{\rm jet}$, is defined by the spherical angles ψ and φ. The emission is assumed isotropic in the minijet frame $\mathcal{R}_{\rm minijet}$ (bottom right).

$$\delta = \frac{1}{\gamma\Gamma(1 + \Sigma\beta c_\psi - (\Sigma + \beta c_\psi)c_\theta) + \gamma\beta s_\theta s_\psi c_\varphi} \tag{4.15}$$

The Doppler factor is bounded and for a jet closely aligned with line of sight, the "blazar case", the extrema are:

$$\begin{aligned} \delta &\leq \frac{1}{\gamma\Gamma(1-\Sigma)(1-\beta)} \sim 4\Gamma\gamma \\ \delta &\geq \frac{1}{\gamma\Gamma(1-\Sigma)(1+\beta)} \sim \Gamma/\gamma \end{aligned} \tag{4.16}$$

where the $\sim$ corresponds to the ultra-relativistic limit.

One can note that for reasonable values of the Lorentz factor such as $\Gamma = 5$ and $\gamma = 5$, Doppler factors as high as $4\Gamma\gamma = 100$ can be achieved, which could easily explain the difference between the variability time scale of PKS 2155-304 (minute time scale) and its black hole light crossing time (hour time scale).

4.2.2.2. *Distribution of the emission for a single region*

I consider that the relevant variable is the orientation of the minijets inside the jet. Assuming that the underlying physical process results in an isotropy of the minijets in the jet frame, e.g. through the creation of plasma blobs in a random direction within a reconnection scenario or through the wandering of the velocity vector of the minijets, I can derive the distribution of the Doppler factor and the distribution of the flux. I analytically compute this distribution in the blazar case $\theta \to 0$ and I use numerical simulations otherwise.

Let $I(E)$ be the flux intensity at energy E (in photons per unit area per unit time), characterized by a non-thermal spectrum of index s (photon index s+1), so that the emitted spectrum is $I(E_{\rm minijet}) \propto E_{\rm minijet}^{-s}$. Since $I(E)/E^3$ is a Lorentz invariant, the observer measures:

$$I(E) = \delta^3 I(E_{\rm minijet}) = \delta^3 I(E/\delta) \propto \delta^{3+s} E^{-s} \tag{4.17}$$

The isotropic orientation of the minijets in $\mathcal{R}_{\rm jet}$ is defined by a uniform distribution of the angle φ between 0 and 2π and by a uniform distribution of $\mu = \cos\psi$ between -1 and 1. Expressing $I(E)$ as a function of φ and μ, one can *a priori* derive the intensity distribution. In praxis, an analytical solution can easily be found for $\theta = 0$, in which case the dependence on φ vanishes. The algebra is far more complicated when the object is misaligned but I numerically show in the following that the results derived in the particular case can be extended to a

wider class of objects. The intensity in the blazar case is:

$$I(E) \propto [\gamma\Gamma(1-\Sigma)(1-\beta\mu)]^{-3-s}\, E^{-s} \equiv (4\Gamma\gamma)^{3+s} g(\mu) E^{-s} \tag{4.18}$$

The factor $(4\Gamma\gamma)^{3+s}$ scales the function g so that:

$$g(\mu) = \left(\frac{(1+\Sigma)(1+\beta)}{4} \times \frac{1-\beta}{1-\beta\mu} \right)^{3+s} \leq 1 \text{ with } \mu \in [-1,1] \tag{4.19}$$

In the following, I call $I_N = g(\mu)$ the intensity normalized to its maximum. The pdf of I_N, $f_{\mathcal{I}}(I_N)$, is linked to the pdf of $\mu = \cos\psi$, $f_{\mathcal{C}}(\mu) = 1/2$ with $\mu \in [-1;1]$ via:

$$f_{\mathcal{I}}(I_N) = \left| \frac{\partial g^{-1}(I_N)}{\partial I} \right| f_{\mathcal{C}}\left(g^{-1}(I_N)\right) \tag{4.20}$$

where $g^{-1}(x) = \dfrac{1}{\beta} \times \left(1 - \dfrac{1+\Sigma}{2} \times \dfrac{1}{2\gamma^2} \times x^{-\frac{1}{3+s}}\right)$.

The probability density function of the normalized intensity is then:

$$f_{\mathcal{I}}(I_N) = \frac{1+\Sigma}{2\beta} \times \frac{1}{4\gamma^2(3+s)} \times \frac{1}{I_N^{1+\frac{1}{3+s}}} \tag{4.21}$$

i.e. the flux intensity follows a Pareto distribution of index $\alpha = 1/(3+s)$. Calling $\Gamma_{\rm phot}$ the photon index, the index of the Pareto distribution becomes $\alpha = 1/(2+\Gamma_{\rm phot})$ and using the natural value of $\Gamma_{\rm phot} = 2$ as derived for the intrinsic spectrum of PKS 2155-304 in the highest state, one gets $\alpha = 1.25$ (cf. example in Sect. 4.2.1.3).

The distribution holds for a non-beamed object ($\Gamma = 1$ and $\Sigma = 0$), as derived independently by Clausen-Brown & Lyutikov (2012) to model the flares of the Crab in the high-energy domain. It also holds for beamed objects misaligned from the line of sight, as shown in Fig. 12.

The distribution of the logarithm of the intensity $\propto \delta^{3+s}$ are generated by drawing two random numbers φ between 0 and 2π and $\mu = \cos\psi$ between -1 and 1. The conservation of the index of the Pareto distribution can be understood by neglecting the term $\gamma\beta s_\theta s_\psi c_\varphi$ in Eq.(4.15). In this case, the previous proof holds when varying the orientation of the jet with respect to the line of sight since the inverse of the Doppler factor remains a linear function of $\cos\psi$.

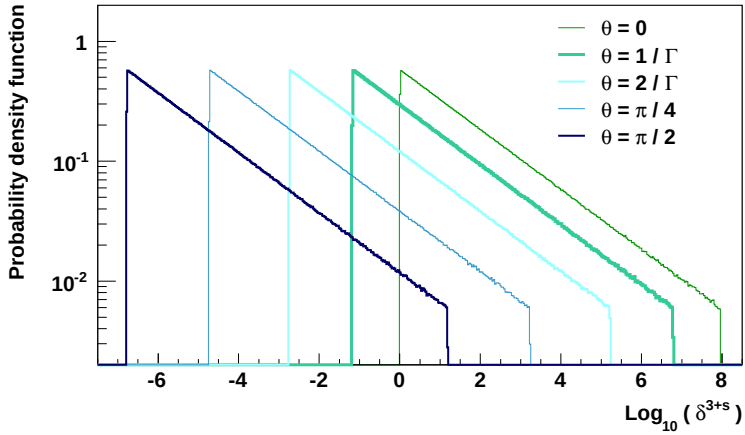

FIGURE 12. Distribution of the logarithm of the intensity of a minijet for various angles θ between the line of sight and the jet axis. The intensity is proportional to δ^{3+s}. The parameters of the simulations are $s = 1$, $\Gamma = 5$, and $\gamma = 5$.

4.2.2.3. *Flux distribution of the emission from a large number of regions*

I discussed in Sect. 4.2.1.3 the case of the sums of Paretian variables, which tend to α-stable distributions and can closely resemble log-normal distributions. One might worry that the cut-off in the distribution of the intensity affects the previous conclusions. Indeed, calling $I_{\max}$ and $I_{\min}$ the maximum and minimum intensity of a single region, one expects that the cut-off begins to play a role when the number of regions N becomes so large that $I_{\max} \ll N \times I_{\min}$. In our case $I_{\min} \sim (\Gamma/\gamma)^{3+s}$ and $I_{\max} \sim (4\Gamma\gamma)^{3+s}$, so that the break begins to play a role for $N \gg (2\gamma)^{6+2s} \sim 10^8$ (for $\gamma = 5$ and $s = 1$), a value which largely exceeds the number considered in the following.

I show in Fig. 13, the flux distributions that I simulated summing the contributions of N components, with $N \in \{1, 10, 30, 10^2, 3 \times 10^2, 10^3, 3 \times 10^3, 10^4\}$.

For $N \gtrsim 10^3$, the distribution of the logarithm of the flux can be described with a peak, followed by a power-law tail as expected for an α-stable distribution (Zaliapin et al. 2005; Nolan 2012). I show in

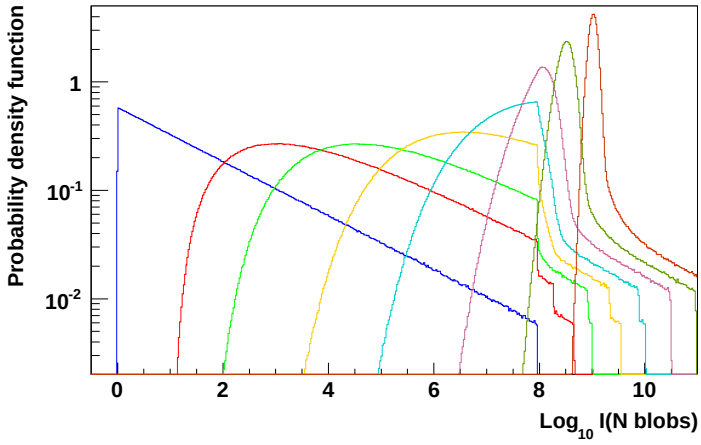

FIGURE 13. Distribution of the logarithm of the intensity of N independent and randomly oriented minijets. The number of minijets N increases from left to right with $N \in \{1, 10, 30, 10^2, 3\times10^2, 10^3, 3\times10^3, 10^4\}$. Even for a large number of regions, asymmetrical, tailed distributions are obtained.

Fig. 14 the distributions obtained for 3×10^3 and 10^4 minijets (note the linear y-axis compared to Fig. 13). I fit these distributions with the functions corresponding to a normal and log-normal flux, as represented with the dashed grey line and continuous black line respectively.

The distribution of the flux of the N minijets is neither normal nor log-normal but because of its skewness, the observed distribution, with limited statistics and a reduced dynamical range, could be interpreted as a log-normal distribution, even if it arises from an additive process and not from a multiplicative one.

4.2.2.4. *Back to the R.M.S.-flux relation*

I have shown in Sect. 4.2.1.2 that the R.M.S. is strictly proportional to the flux for a Paretian flux and one could expect this relation to vanish when summing the contribution of a large number of components. Interestingly, the linearity holds, certainly because the power-law tail of the distribution does not depend on the number of regions involved, as can be seen on Fig. 13. I illustrate this statement simulating light curves with 10^5 time steps for $N = 1$ and $N = 10^4$ minijets. I then

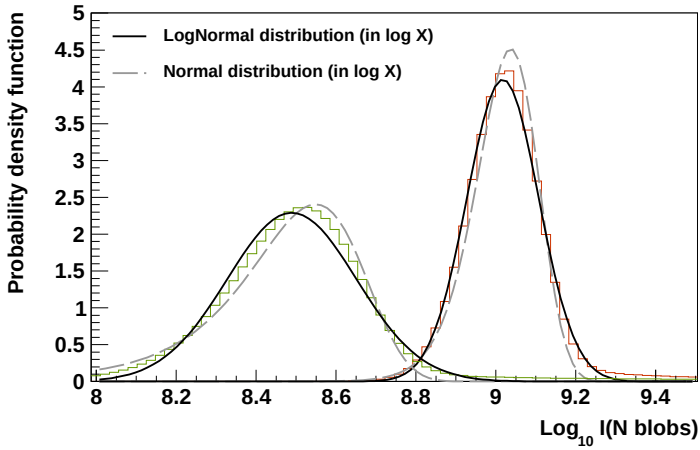

FIGURE 14. Distribution of the logarithm of the flux of N minijets for $N = 3 \times 10^3$ (left) and $N = 10^4$ (right), as in Fig. 13. The continuous black and grey dashed lines represent the best-fit with a log-normal and normal flux distributions, respectively.

compute the sample mean and the sample R.M.S. in 10 points wide windows. For the sake of clarity, I average the flux and the R.M.S. in 50 bins between the maximal flux and the minimal flux. The sample R.M.S. as a function of the sample flux is shown Fig. 15 for one minijet (top panel) and 10^4 minijets (bottom panel), where the error bars correspond to the standard deviation in each bin.

The positive x-intercept in the R.M.S.-flux relation that can be seen on the right panel in Fig. 15 corresponds to the peak of the flux distribution shown in Fig. 13. It could be interpreted as a constant component, such as the one assumed in the fit of the light curve of PKS 2155-304 (baseline at 1.1 C.U.). It corresponds within the minijets-in-a-jet statistical model to the value around which the average emissions of the minijets pile up.

4.2.3. Telegraph process and spectral assumption

I have shown that the statistical properties of the emission of PKS 2155-304 can be reproduced within the minijets-in-a-jet statistical model. The fast variability can also be accounted for with Doppler factors as

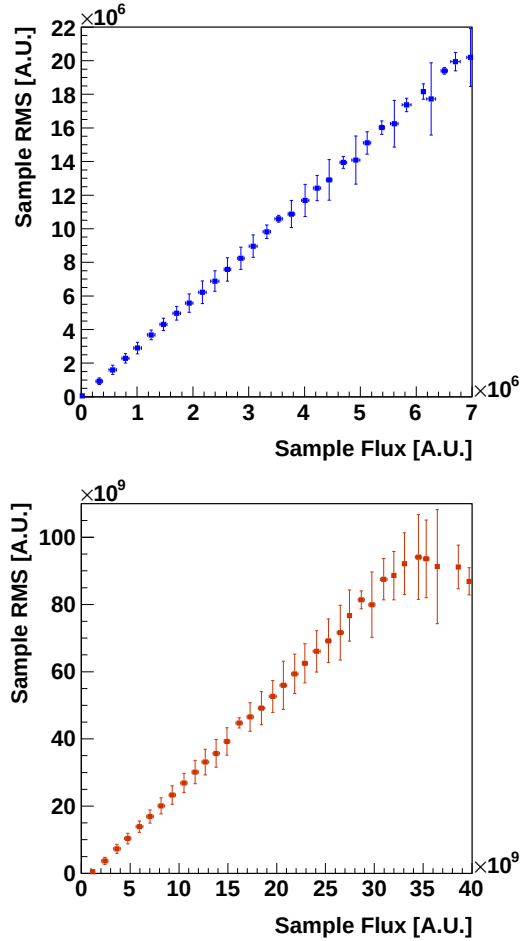

FIGURE 15. Sample R.M.S. as a function of the sample flux of $N = 1$ minijet (top) and the sum of $N = 10^4$ minijets (bottom). Linear relations are found in both cases, with a zero x-intercept in the first case and a positive one in the second.

large as $\delta_{\max} \sim 4\Gamma\gamma$ that allow for variations down to $R/c\delta_{\max}$, where R is the typical size of the emitting region in the minijet frame.

To model the time-dependent and energy-dependent observables, a process with a characteristic time and a spectrum with a characteristic

energy must be added to the modelling. I use very simple temporal and spectral prescriptions in the following and show that within this framework, the properties of the emission of PKS 2155-304 in the high state are naturally reproduced.

4.2.3.1. *Temporal and spectral prescriptions*

I aim at being as independent to a radiative model as possible and I assume, for the sake of simplicity, that all the emitting regions have the same photon spectrum. To reproduce the bump-like behaviour of the emission of blazars in $\nu F_\nu = E^2 \mathrm{d}N/\mathrm{d}E$, I assume that the photon spectrum of each minijet, in the minijet frame, is defined by:

$$\frac{\mathrm{d}N}{\mathrm{d}E} \propto E^{-\Gamma_{\mathrm{phot}}} \exp(-E/E_{\mathrm{cut}}) \tag{4.22}$$

where $\Gamma_{\mathrm{phot}} = 1.5$, i.e. on the order of the intrinsic spectral index derived in Chapter 3.3.2.1 for the "four fantastics". I define the cut-off energy as the reference energy, i.e. $E_{\mathrm{cut}} = 1$. In the following, the energies are then expressed in units of E_{cut}. Since the energy measured in the observer frame is affected by Doppler boosting ($\times\delta$), I also normalize the energy to the maximum Doppler factor $\delta_{\mathrm{max}} \sim 4\Gamma\gamma$.

The temporal prescription must introduce a time scale τ. In the context of minijets, this time scale can correspond to the typical reversal time, if one considers that the variations are due to a wandering of the individual velocity vectors, or to rate of magnetic reconnections.

To model the inertia of the physical process, i.e. the fact that the reversal of the minijet is not instantaneous, I employ a so-called generalized telegraph signal (see e.g. Dubkov & Malakhov 1978), which is a memoryless process that discontinuously changes of value at random times. Assuming that the jumps are independent, one can show that the probability to change of value after a period Δt is

$$P_0(\Delta t) = \exp(-\Delta t/\tau) \tag{4.23}$$

where τ is a positive constant. The PSD of such a process is then $P(f) \propto 1/(4\pi^2 f^2 + \tau^{-2})$, where f is the frequency. This process behaves as a white noise for $f \ll 1/\tau$ and as a red noise for $f \gg 1/\tau$.

The simulation of the generalized telegraph signal is quite straightforward. I attach a clock to each minijet in the jet frame. At each time step and for each minijet, I draw a random number between 0

and 1 and if this number exceeds the probability in Eq. (4.23), I draw a new orientation for the minijet and reset the clock, otherwise I simply increment the clock.

In the following, since the observed time differs from the time as measured by the clocks attached to each minijet in the jet frame, I account for the Doppler factor expressing the time in units of $\tau\delta_{\rm jet}$, where $\delta_{\rm jet} = 1/\Gamma(1 - \Sigma\cos\theta)$.

4.2.3.2. *Results*

I show in Fig. 16 the simulated evolution of the SED of 10^4 minijets, each following a Pareto distribution of the flux. The top panel represents the SED as seen by an observer and I focus on three energy bands in the following. The first energy band, in yellow, corresponds to the part of the spectrum that is below the peak, such as monitored with *Fermi*-LAT. The second and third bands, in green and violet respectively, are located close to the peak energy and correspond to the part of spectrum that H.E.S.S. would monitor.

The middle and bottom panels in Fig. 16 show the flux and the photon index as a function of time. One can already notice that the amplitude of the variations differ from band to band. In particular the small variations of the photon index as see by *Fermi*-LAT (Nolan et al. 2012; Abdo et al. 2010; Ackermann et al. 2011) are naturally reproduced in a scheme involving Doppler boosting. The properties derived for the minijets-in-a-jet statistical model obviously remain unchanged, as shown in Fig. 17, though the statistics are more limited for this specific simulation. The PSD of the three light curves are computed in Fig. 18. As expected from a telegraph process a f^{-2} behaviour is observed over most of the frequency range.

Finally, I show the spectral observables in Fig. 19. A hardening of the spectrum as a function of the flux level can be seen in the top panel. This simply corresponds to Doppler boosting: increasing the Doppler factor increases the intensity and the peak energy, the latter increasing the hardness of the spectrum. Noticeably, the fractional variance as a function of energy reproduces remarkably well the behaviour observed in PKS 2155-304 (cf. Fig. 6). The evolution of $F_{\rm var}$ with the energy is also linked to the concavity of the spectrum, i.e. to the progressive softening of the spectrum with an increasing energy.

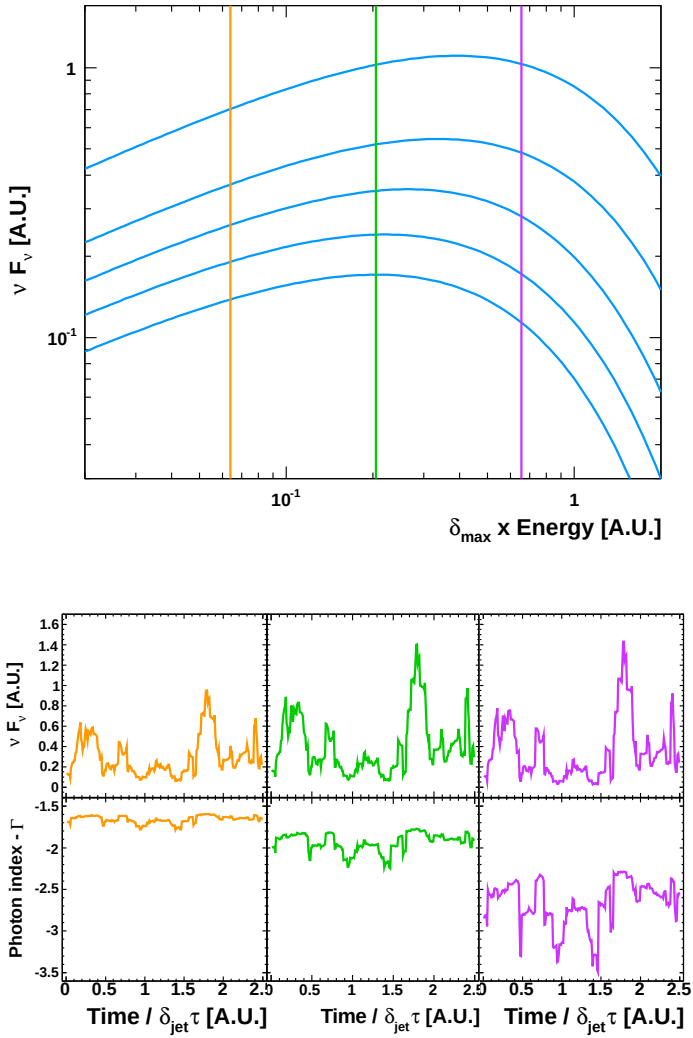

FIGURE 16. *Top panel*: SED at five instants, vs energy in units of the cut-off energy divided by the maximum Doppler factor. *Middle panels*: Light curves for the three energy bands shown above vs time, in units of the characteristic time scale τ multiplied by the jet Doppler factor. *Bottom panels*: Variations of the photon index vs time.

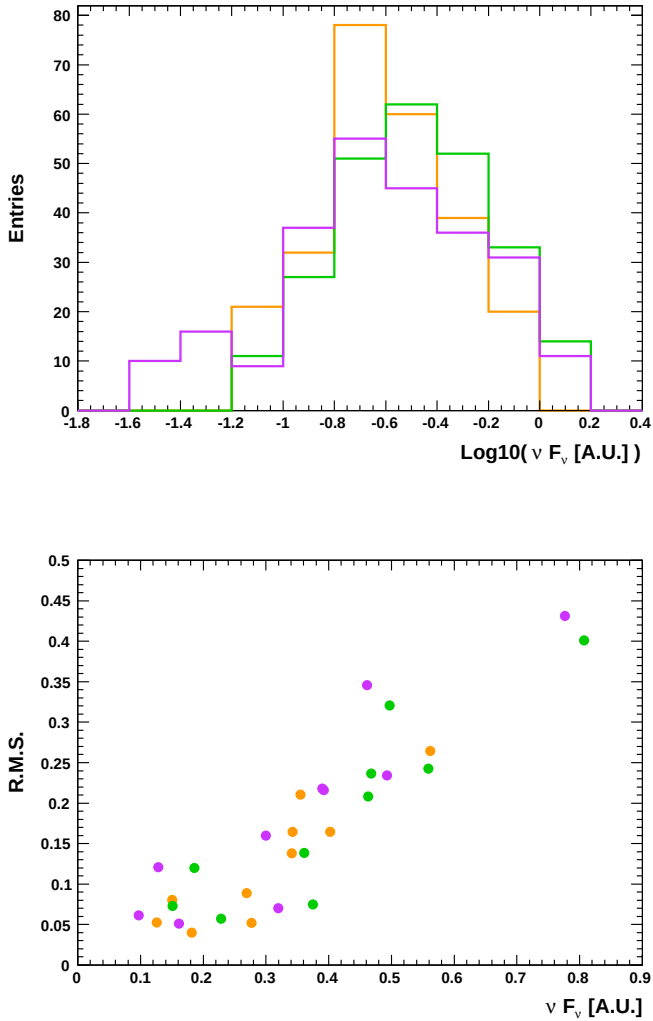

FIGURE 17. *Top panel*: Distribution of the logarithm of the flux for the three energy bands defined in Fig. 16. *Bottom panel*: R.M.S. flux relation computed in ten windows of 25 points for the three energy bands defined in Fig. 16.

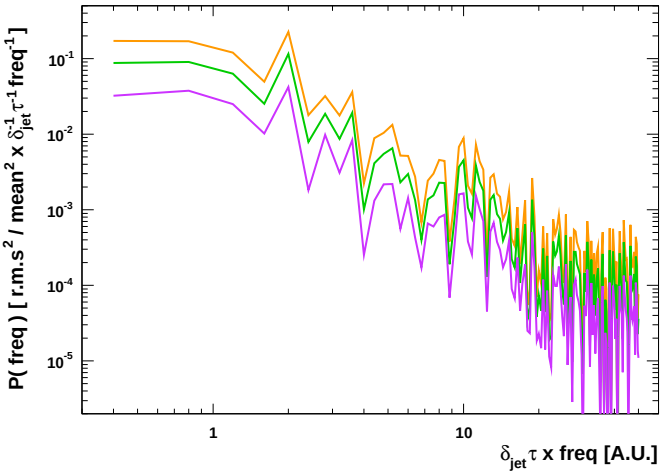

FIGURE 18. Power Spectral Densities of the light curves for the three energy bands defined in Fig. 16.

4.2.3.3. *Concluding remarks on the variability studies*

The dramatic outbursts of PKS 2155-304 constitute an extraordinary set of observables that remains difficult to model as a whole. I have shown in this chapter that, contrary to a common belief, the observed statistical properties of the emission do not necessarily advocate for a multiplicative process and that these observables can be reproduced within an additive model summing Pareto variables.

The minijets-in-a-jet statistical model is a kinematic representation of a relativistic turbulent medium that naturally generates Pareto flux distributions and reproduces the statistical properties of the emission of PKS 2155-304. The observed fast variability can also be explained by a series of two boosts yielding a shortening of times by two order of magnitudes, despite very reasonable Lorentz factors. With two simple and natural prescriptions that introduce a characteristic time scale and a typical energy, one can reproduce all the properties observed by H.E.S.S. during the dramatic outbursts of July 2006.

The potential evolutions of this model are diverse, since it can in principle be extended to any astrophysical sources where several boosted regions are involved. It is remarkable that Clausen-Brown &

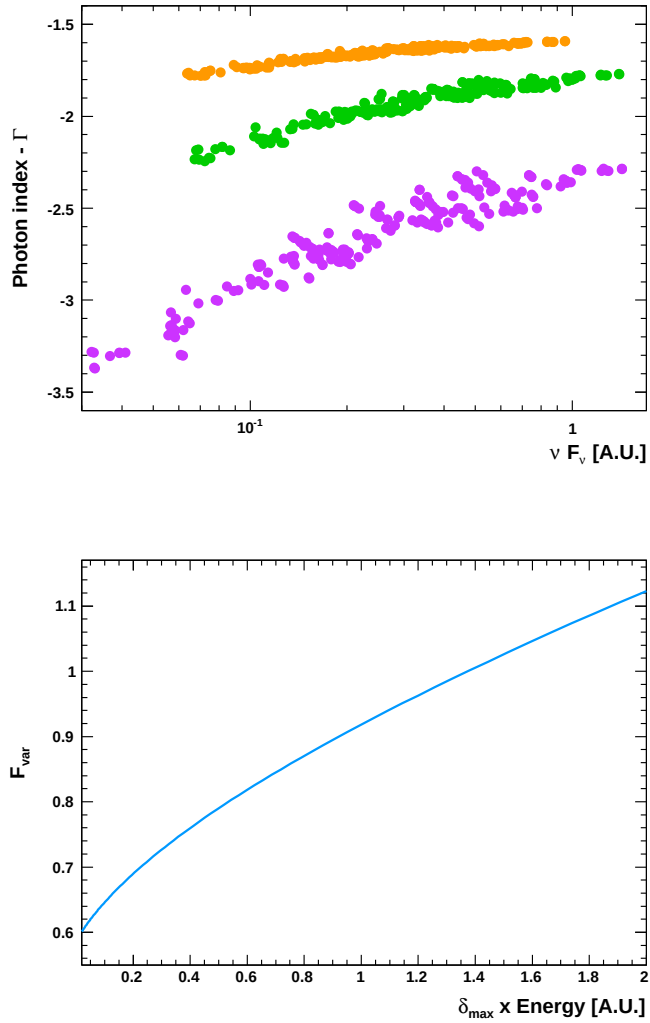

FIGURE 19. *Top panel*: Photon index vs flux for the three energy bands defined in Fig. 16. *Bottom panel*: Fractional variance vs energy.

Lyutikov (2012) recently derived a particular case of the minijets-in-a-jet statistical model to explain the flares of the Crab in the high-energy domain, though I am not sure that the moments of the flux that these authors stress out are the best quantities to compare to observations in the case of Pareto distributions (even if they are bounded Pareto distributions).

Giannios et al. (2010) invoked a minijets model to explain the fast variations in the emission of radio galaxies such as M 87. In such a scenario, a linear relation between the flux of the source and its R.M.S. as well as a skewed distribution of the flux could be revealed by long-term observation campaigns, such as the one described by Abramowski et al. (2012).

Plugging acceleration and radiative processes to this framework will certainly improve the understanding of the mechanisms at play in the violent Universe.

Bibliography

Abdo, A. A., Ackermann, M., Ajello, M., et al. 2010, ApJ, 710, 1271

Abramowski, A., Acero, F., Aharonian, F., et al. 2012, ApJ, 746, 151

Ackermann, M., Ajello, M., Allafort, A., et al. 2011, ApJ, 743, 171

Aharonian, F., Akhperjanian, A. G., Anton, G., et al. 2009a, A&A, 502, 749

Aharonian, F., Akhperjanian, A. G., Anton, G., et al. 2009b, ApJ, 696, L150

Aharonian, F., Akhperjanian, A. G., Aye, K.-M., et al. 2005a, A&A, 430, 865

Aharonian, F., Akhperjanian, A. G., Bazer-Bachi, A. R., et al. 2007, ApJ, 664, L71

Aharonian, F., Akhperjanian, A. G., Bazer-Bachi, A. R., et al. 2005b, A&A, 442, 895

Albert, J., Aliu, E., Anderhub, H., et al. 2007, ApJ, 669, 862

Aleksić, J., Antonelli, L. A., Antoranz, P., et al. 2011, ApJ, 730, L8

Arévalo, P. & Uttley, P. 2006, MNRAS, 367, 801

Bettoni, D., Falomo, R., Fasano, G., & Govoni, F. 2003, A&A, 399, 869

Clausen-Brown, E. & Lyutikov, M. 2012, arXiv:1205.5094

Degrange, B., Superina, G., Giebels, B., & Volpe, F. 2008, in Blazar Variability across the Electromagnetic Spectrum

Dubkov, A. A. & Malakhov, A. N. 1978, Radiophysics and Quantum Electronics, 21, 54

Gaidos, J. A., Akerlof, C. W., Biller, S., et al. 1996, Nature, 383, 319

Ghisellini, G. & Tavecchio, F. 2008, MNRAS, 386, L28

Giannios, D., Uzdensky, D. A., & Begelman, M. C. 2009, MNRAS, 395, L29

Giannios, D., Uzdensky, D. A., & Begelman, M. C. 2010, MNRAS, 402, 1649

H.E.S.S. Collaboration, Abramowski, A., Acero, F., et al. 2012, A&A,

539, A149
H.E.S.S. Collaboration, Abramowski, A., Acero, F., Aharonian, F., et al. 2010, A&A, 520, A83
Longair, M. S. 2010, High Energy Astrophysics
Lott, B., Dermer, C. D., & Escande, L. 2012, Journal of Physics Conference Series, 355, 012030
McHardy, I. 2008, in Blazar Variability across the Electromagnetic Spectrum
Narayan, R. & Piran, T. 2012, MNRAS, 420, 604
Nolan, J. P. 2012, Stable Distributions - Models for Heavy Tailed Data (Boston: Birkhauser), in progress, Chapter 1 online at academic2.american.edu/∼jpnolan
Nolan, P. L., Abdo, A. A., Ackermann, M., et al. 2012, ApJS, 199, 31
Piran, T. 2004, Reviews of Modern Physics, 76, 1143
Superina, G. 2010, PhD thesis, École polytechnique
The Fermi-LAT collaboration. 2011, arXiv:1102.0277
Timmer, J. & Koenig, M. 1995, A&A, 300, 707
Uttley, P., McHardy, I. M., & Vaughan, S. 2005, MNRAS, 359, 345
Vaughan, S., Edelson, R., Warwick, R. S., & Uttley, P. 2003, MNRAS, 345, 1271
Voit, G. 2005, The statistical mechanics of financial markets, ed. New York : Springer
Zaliapin, I. V., Kagan, Y. Y., & Schoenberg, F. P. 2005, Pure and Applied Geophysics, 162, 1187

CHAPTER 5

Perspectives

A bright future can be predicted for γ-ray astronomy with the planned instrumental progresses. I discuss in Sect. 5.1 the advances expected with the upgrade of current generation IACT, emphasizing the case of H.E.S.S. II, and I present the next generation instruments in this field, namely the Cherenkov telescope array (CTA). I then focus in Sect. 5.2 and Sect. 5.3 on two scientific topics, VHE cosmology and AGN variability, which will certainly be deeply explored with the new instruments.

5.1. Short-term and mid-term instrumental prospects

H.E.S.S. has now been operated for almost ten years and the concurrent instruments, MAGIC and VERITAS, have been under operation during more than five years. To maintain their capabilities, operations such as mirror refurbishment are necessary, as completed by H.E.S.S. for the four telescopes in late 2011.

One of the most anticipated improvement is the lowering of the energy threshold. The H.E.S.S. collaboration has chosen a radical approach to increase its sensitivity down several tens of GeV, by building the largest γ-ray telescope on Earth, as discussed in Sect. 5.1.1. Such an heterogeneous array of telescopes constitutes a good scale model for the next generation arrays, CTA, discussed in Sect. 5.1.2. The AGN science that will be addressed with H.E.S.S. II and CTA is detailed in Sect. 5.1.3.

5.1.1. The low-energy threshold of H.E.S.S. II

When the energy of the primary decreases, the number of Cherenkov photons produced by an atmospheric shower is drastically reduced and is more and more diluted in the night sky background. To counter this phenomenon, VERITAS has opted for an increased sensitivity to Cherenkov light with high quantum efficiency PMs. The other IACT

have opted for large collection area with two telescopes of 17 m diameter for MAGIC and a single telescope of 28 m diameter for H.E.S.S. II (vs. $12 - 13$ m for H.E.S.S. I and VERITAS).

5.1.1.1. *A 28 m diameter γ-ray telescope*

The second phase of H.E.S.S. entails adding a fifth large telescope, CT5, in the centre of the existing array. With a mirrored area of 596 m^2 and a focal length of 35 m, CT5, shown in Fig. 1, is the largest γ-ray telescope on Earth. A discussion of H.E.S.S. II capabilities can be found in de Naurois (2012).

FIGURE 1. Picture of CT5, the largest γ-ray telescope on Earth. *Credits: C. Foehr.*

As for CT1 to CT4, the structure is made of steel and is based on an alt-azimuth mounting. The large scale implies an overall weight of $\sim$ 580 tons, almost ten times heavier than the mid-size telescopes. Despite the tremendous inertia, a maximum speed of 200 °/min can

be achieved, enabling the positioning of the system anywhere in the sky in less than 2 minutes. A tracking accuracy down to the arcmin level is expected, but the weight of the camera (2.8 tons) and the large level arm sustained by the quadrupod cause elastic deformations of the structure. Two CCDs, one at the centre of the dish monitoring the camera and one monitoring the stars in the sky, are used to correct for these mechanical constraints. The absolute pointing is expected to be accurate down to $\sim$ 10 arcsec. The camera is equipped with an auto-focus system displacing it up to a few centimetres, to adapt to e.g. different zenith angle observations. It can also be unloaded from the structure with an automated system, for maintenance purposes.

The dish is made of 850 hexagonal mirror facets of 90 cm diameter, each equipped with two actuators for the alignment. Contrary to the H.E.S.S. I mirrors, arranged in a Davis-Cotton design to reduce the geometric aberrations, the mirrors of CT5 follow a parabolic shape which avoids the anisochronism caused by the former mounting, which could be as large as 9 ns for such a large size telescope.

5.1.1.2. H.E.S.S. *II electronics*

The camera has a 2 m diameter and covers a FoV of approximately 3.2^{o}, limited by geometric aberrations. This FoV is smaller than that of the H.E.S.S. I telescopes, a price to pay because of the high pixelation, with 2048 PMs, each covering 0.07^{o} in the sky, as shown in Fig. 2.

The main differences between the H.E.S.S. I cameras and the H.E.S.S. II camera concern the read-out electronics and the timing information on the shower. To overcome the limitations of the ARS of H.E.S.S. I, an ASIC called SAM (Swift Analogue Memory) has been developed, increasing the read-out speed by a factor of 10. The second-level trigger is handled similarly to H.E.S.S. I for the so-called hybrid events, which trigger CT5 and at least one of the four other telescopes. Below $\sim$ 50 GeV, H.E.S.S. I does not trigger at all. The second level trigger is then based on topological criterion, with a decision made in $\sim$ 50 μs (a FIFO buffers up to ten events to reduce the dead time). The reduced dead-time allows a 3-4 kHz trigger rate to be handled, twice faster than H.E.S.S. I capabilities.

In addition to the low and high gain signals, the timing information is also stored in the form of a *Time-Of-Maximum* and of a *Time-Above-Threshold*, within a 16 ns time window, for each pixel. Such pieces of information can be used to reconstruct the temporal development of

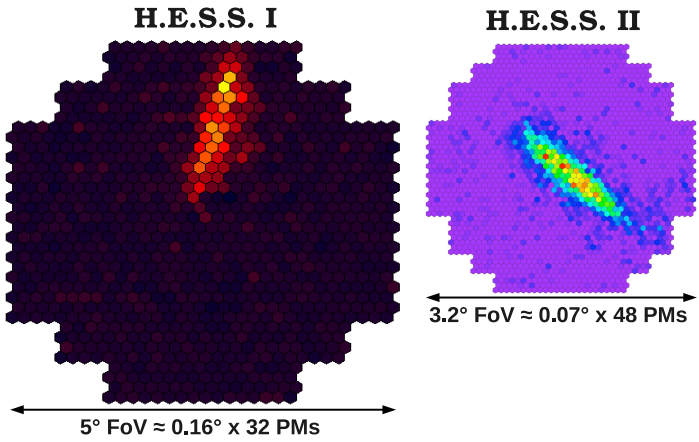

FIGURE 2. γ-like events seen by a H.E.S.S. I telescope (left) and the large size telescope CT5 (right). The images are roughly scaled to the FoV covered by each camera. *Extracted from the presentation of W. Hofmann at the Gamma2012 conference.*

the shower, which has proved useful in limiting the contamination by the NSB and in rejecting the hadronic background, as shown by the MAGIC collaboration in Aliu et al. (2009) (note that no significant improvement in stereoscopic mode was found within the VERITAS collaboration by Holder 2005). An analysis taking into account the timing information for both mono and hybrid events is not yet available, but an improvement of a factor 2 at $\sim$ 100 GeV in the effective area is expected, with an analysis energy threshold of $\sim$ 50 GeV. At these energies, the Earth magnetic field could begin to play a significant role, which will have to be fully understood in the analysis. Note finally that the poor correlation between discriminating parameters of the different analyses (*Hillas, Model 3D, Model++*) leaves some room for improvements, either through the use of multivariate analysis or through the development of more sensitive analysis methods.

5.1.2. The large effective area of CTA

Current generation IACT have partly explored the VHE sky. A full coverage at a sensitivity level on the order of the 1% C.U., i.e. on the order of the currently detected AGN, remains inaccessible, unless

extending the life time of the current instruments in an unreasonable way. Increased spectral and temporal capabilities are needed to improve, amongst others, our knowledge of the brightest VHE AGN (i.e. above a few % C.U.). VERITAS, MAGIC and H.E.S.S. have left little room for technological revolutions[1] and the challenge that the next generation arrays have to face is mostly a matter of scale.

Initially formed with the joint effort of the MAGIC and H.E.S.S. collaboration in 2005, the Cherenkov Telescope Array (CTA) project has now outgrown its European roots to group US, Indian, Brazilian and Japanese collaborators. The CTA collaboration represents more than 700 hundred participants from 50 laboratories in 25 countries. This project, well ranked in major scientific road maps, is extensively discussed in Actis et al. (2011). A special edition of the *Astroparticle Physics* journal on the science case is also on its way for publication. I briefly summarize the expected performances in the following, and refer the reader to the above-mentioned publications for more details.

5.1.2.1. *The CTA project*

The previous generation IACT detected a handful of sources. Current generation instruments have detected more than a hundred VHE emitters and have raised the interest of researchers from particle physics, astrophysics, cosmology and astronomy. The obvious goal of CTA is to gain another order of magnitude in terms of number of sources, i.e. to detect a thousand of them. This can only be achieved through a gain in sensitivity of a factor of 10 in the 100 GeV − 50 TeV energy range. Extending the energy range up to the highest energies ($\sim$ 100 TeV) and down to few tens of GeV should also largely impact the scientific topics addressed with CTA.

Two sites are planned, one in each hemisphere, to cover the entirety of the sky. Locating the arrays at different longitudes would moreover enable continuous monitoring of the sources at the frontier of the two observation domains. The southern array would be mostly dedicated to galactic science while the northern would mostly observe extragalactic sources. While for AGN the low-energy end of the VHE range

[1]With the potential exception of G-APDs (Geiger avalanche photo diods), also called SiPMs, and tested in the experiment FACT (Anderhub et al. 2011). These photo sensors indeed achieve quantum efficiencies up to 80 − 90%, roughly three times better than conventional PMs, allowing the energy threshold to be reduced without a large increase of the light collection area.

remains the most important one, as discussed in Sect. 5.1.3, galactic studies should benefit from the coverage up to ~ 100 TeV to answer the question of the maximum energy that can be reached by local cosmic accelerators.

An ideal array would be constituted of a huge number of large size telescopes, which would probe the lowest energies with their large collection area. The rare γ rays at the highest energies can be detected with an effective area on the ground above the square kilometre. An optimization in terms of cost nonetheless implies the use, as for H.E.S.S. II, of different types of telescopes. A typical example of array layout, with small size telescopes (SST), middle size telescopes (MST) and large size telescopes (LST), is shown in Fig. 3.

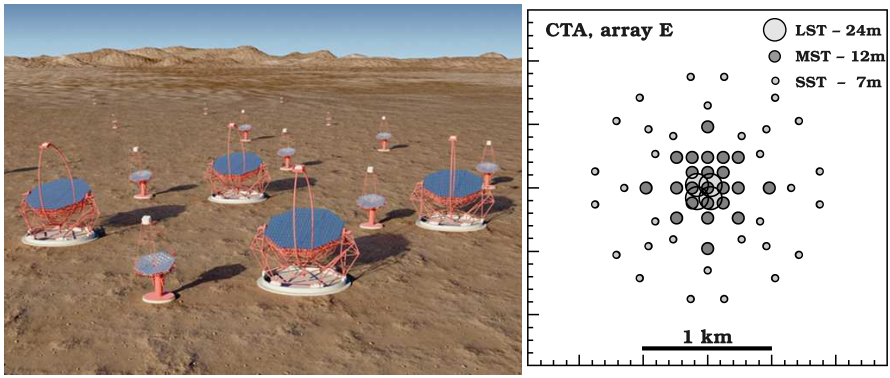

FIGURE 3. Typical layout of CTA telescopes. *Left:* Artistic view of the central part of the CTA array. *Credits: G. Pérez, UAC (SSM). Right:* Configuration E of the array as studied by the Monte Carlo group. *Adapted from Actis et al. (2011).*

With such an array (configuration E), the lowest energies are probed by the LSTs (typically 24 m diameter, in between H.E.S.S. II and MAGIC) which aim at covering 10% of the Cherenkov light pool and could observe a 5^o FoV with 0.09^o pixels. An alternative approach to a small number (here 4) of LSTs would be a dense array of MSTs (typically of 12 m diameter) with a similar light collection area, but the challenge for a such a system would lie in the trigger at the single telescope level, justifying the use of LSTs. In the low-energy range

(tens of GeV to a hundred GeV), the systematic uncertainty on the background estimation limits the sensitivity, introducing the need for deep and thorough calibration efforts.

MSTs, with a FoV of 8^o using 0.18^o pixels, should probe the intermediate energy range, 100 GeV − 10 TeV, with 23 elements roughly spaced by a hundred metres for the array E. With such a large area covered on the ground, the Cherenkov light pool of the showers would be for the first time fully contained by the array, allowing for high multiplicity events, i.e. events recorded by a large number of telescopes (five to ten in the energy range considered). The reconstructed energy and direction of these events should benefit a lot from these coincident observations. The improved angular resolution enables a reduction of the PSF (0.02^o for CTA vs 0.1^o for H.E.S.S.) and hence increases the rejection of the hadron and electron background, which limits the sensitivity in the intermediate energy range. An improved energy resolution (below 10%) in the 100 GeV − 10 TeV would have a dramatic impact on studies of spectral features, such as the imprint of the EBL.

Above 10 TeV, the main limitation is the effective area itself, i.e. the area covered on the ground. A total number of 32 SSTs spaced by $\sim$ 200 m, with a large FoV of 10^o and pixels of 0.25^o, could cover a ~ 3 km^2 area on the ground for the array E.

The construction of CTA is expected to start in 2015 and to last roughly ten years, noting that data acquisition can start as soon as the first telescope is installed. The cost of the two arrays is estimated to 150 M€, roughly a quarter of the cost of the *Fermi* satellite. Significant improvement in the engineering, construction and operation of the array are needed in comparison with current generation small scale IACT. The organization of the data access will also need a particular attention since CTA is planned to be an open observatory and will provide pre-processed events (accessible via e.g. Virtual Observatory tools).

5.1.2.2. *CTA observation strategy and capabilities*

The scheduling of the observations within an open structure and with a complex heterogeneous system such as CTA is not an easy task. Different strategies are shown in Fig. 4.

One of the legacies of CTA could be a full sky survey and a galactic survey with a deeper exposure than that performed by H.E.S.S. (Aharonian et al. 2006). The portion of the sky accessible by an array such

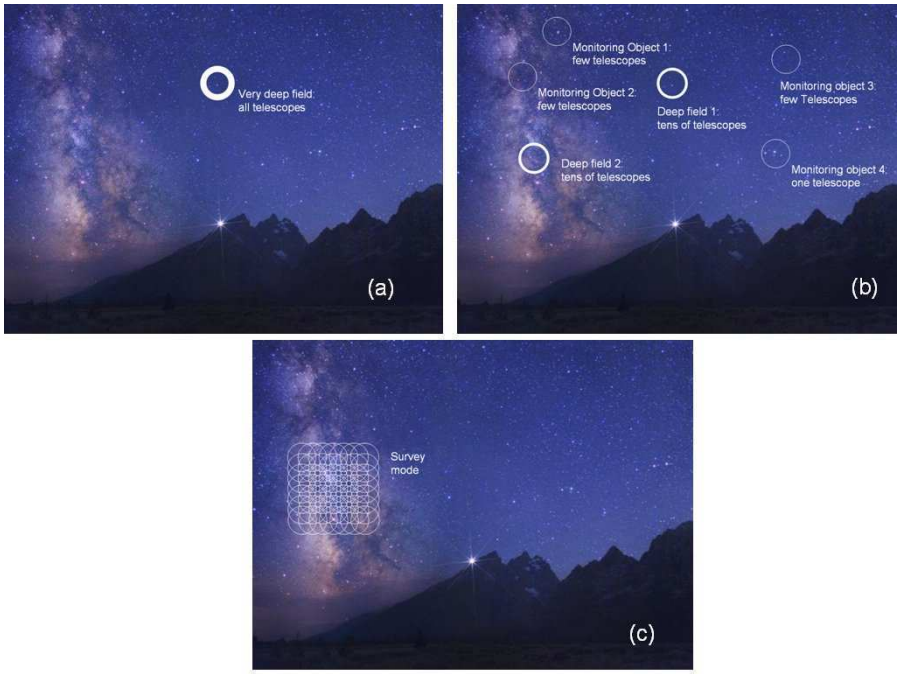

FIGURE 4. Different observation strategies for CTA. (a): Very deep field exposure using all the telescopes pointed toward the same direction. (b): Simultaneous study of faint sources with deep fields and monitoring of bright, potentially flaring, sources. (c): Survey mode. *Adapted from Actis et al. (2011).*

as CTA with a threshold energy below 100 GeV (zenith angle below 60°) corresponds to a quarter of the 4π steradians, which corresponds to 10^4 deg^2. Assuming a 5° FoV, a single pointing covers 20 deg^2 and 500 directions must be observed to cover the full accessible sky. Thus, with $\sim$ 250 hours dedicated to AGN in a year (see Fig. 2 for H.E.S.S.), each FoV can be observed during half an hour, corresponding to a sensitivity between 1 and 2% C.U. (Actis et al. 2011; Dubus et al. 2012), comparable with the current galactic survey of H.E.S.S., but carried out by CTA on the whole accessible sky. This sensitivity corresponds to the upper envelope of the red area shown in Fig. 5. Note that such a survey would not allow to detect sources such 1ES 1312-423 and

SHBL J001355.9-185406 as shown in Chapter 2.3. Deep field observations will be needed to discover a larger number of faint objects below the percent C.U..

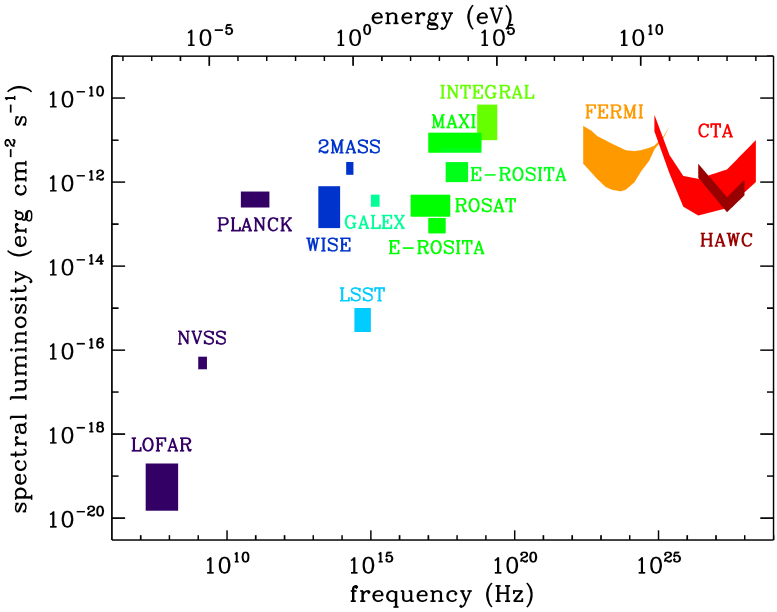

FIGURE 5. CTA sensitivity in survey mode within a multi-wavelength context. The CTA upper envelope correspond to the survey of a quarter of the sky at the % C.U. level (reachable in a year) and the lower envelope corresponds to the expected sensitivity of a Galactic plane survey. *Extracted from Dubus et al. (2012).*

The various current and future multi-wavelength sky surveys shown in Fig. 5 are more extensively discussed in Dubus et al. (2012). The reader is specifically referred to the sensitivity achievable with *Fermi*-LAT in 10 years (orange band, depending on the galactic latitude, see also Funk & Hinton 2012) which overlaps the CTA energy range between a few tens of GeV and 100 GeV. Another overlapping energy range is that of the high-altitude water Cherenkov gamma-ray observatory (HAWC, Sinnis et al. 2005), with an expected sensitivity after one to five years of operation shown as a dark red region. The large duty

cycle and sky coverage of HAWC and *Fermi*-LAT will be of uttermost interest in triggering pointings toward flaring objects in both low and high-energy ends of CTA.

5.1.3. AGN science with current and next generation IACT

The scientific topics that H.E.S.S. II and CTA will deal with have a large overlap. The main instrumental revolution for AGN studies is the lowering of the energy threshold. H.E.S.S. II will thus act, with a reduced sensitivity, as a path finder for CTA.

In the following, I group the main topics for VHE AGN studies in four sections: AGN unification, jets and their environment, variability, and VHE cosmology. More extensive discussions can be found in Actis et al. (2011), Giebels (2011) and in the special edition of Astroparticle Physics on CTA, particularly Sol et al. (2012), Reimer & Boettcher (2012) and Dubus et al. (2012). Note that I expose my contributions and opinions on cosmological and variability studies in Sect. 5.2 and Sect. 5.3.

5.1.3.1. *Can we constrain the AGN unification scheme?*

With a lower energy threshold and an increased sensitivity, the current and next-generation instruments can initiate VHE AGN population studies, which are for the moment still limited by the number of objects in each class (though some preliminary studies could be performed on the 34 HBLs detected so far). Using the sources in the 2LAC and 2FGL *Fermi*-LAT catalogue (Ackermann et al. 2011; Nolan et al. 2012), Sol et al. (2012) show that between 150 and 350 AGN could be detected in the all sky with 50 hours of CTA exposure on each target. The smallest estimate corresponds to sources with a known redshift, while a redshift distribution is assumed for the largest estimate. Such a large number of detection would at least triple the current AGN sample and one can expect, with a hundred of HBLs, to draw tendencies and better constrain the acceleration and emission processes at play in these objects.

Note that this extrapolation is based on *Fermi*-LAT sources and thus does not account for objects such as 1ES 0229+200, marginally detected at HE as discussed in Chapter 3.3.2.1. Assuming a given luminosity function for the blazar population, Dubus et al. (2012) estimate that a survey of a quarter of the sky with one hour on each FoV should reveal a total of ~ 20 AGN. This could bring to light more objects such

as the four fantastic discussed Chapter 3.3.2.1. With the large energy coverage of CTA, the question of the maximum energy to which AGN can accelerate particles could be partly answered (remember that for the four fantastic, the peak of the emission is not seen in the currently probed energy range).

In addition to HBLs, classes of objects that are for the moment marginally or not represented at all at VHE could be explored with H.E.S.S. II and CTA. The aim would be to test the blazar sequence, by extending the populations of IBLs, LBLs and FSRQs, to extend the population of VHE radio galaxies in particular to FR II objects and test the FR I / FR II distinction at VHE (can they be distinguished on a particle acceleration / beaming basis ?). The Seyfert galaxies will also be studied with H.E.S.S. II and CTA, the goal being the characterization of the transition between radio-loud and radio-quiet objects, and thus to address a crucial question within the AGN unification scheme: why do some AGN have apparent jets and others do not?

5.1.3.2. *Can we characterize the jet and its environment?*

The AGN emission at VHE is non-thermal and it certainly emerge from the jet, but the question of the precise location of the γ-ray emission remains widely debated. Even with its improved angular resolution, CTA will not be able to answer this question via imaging. With a PSF of 0.02^{o}, the best that can be expected for the location of the centroid is a resolution of ~ 10 arcsec. The closest VHE radio galaxies, for which the lateral view could enable a location, are Centaurus A ($z = 0.0018$) and M 87 ($z = 0.0042$), with redshifts corresponding to angular scales of ~ 40 pc/arcsec and ~ 90 pc/arcsec respectively. Thus only the location or the extension of the VHE emission on kpc scales could be tested.

But other observables can be used to constrain the location of the emission. Fast variations tend to place it close to the super massive black hole, in which case constraints on the magnetosphere and potentially on the mechanism that launches the jet could be derived. If γ rays are emitted within the BLR (below the pc scale), they could interact through pair creation with the HeII and HI recombination continua (in the UV), creating an absorption signature (a dip) at tens of GeV (Poutanen & Stern 2010). Such a signature would be a direct probe of the circum-nuclear material of AGN.

Variability in the γ-ray band correlated with motion / polarization change / flux change in the radio band led some authors to locate the emission on parsec scales in a few cases (see e.g. Agudo et al. 2011), though using HE and not VHE γ rays. The spectral and temporal improvement brought by CTA and H.E.S.S. II will certainly enlighten these crucial questions.

The jet properties themselves can certainly be partly investigated at VHE. Indeed, during outbursts such as those of PKS 2155-304 discussed in Chapter 4, the γ-ray luminosity dominates the total energy output of the AGN and is thus a constraining lower limit on the jet power. Studying the relation between the maximum γ-ray luminosity and the disk luminosity with a large population of AGN could certainly bring insights on the relation between the jet and the disk.

Finally, with an extended energy range and an improved spectral resolution, the spectra measured with H.E.S.S. II and CTA will refine the radiative constraints on the SED of AGN in the multi-wavelength context. This could decide the leptonic vs hadronic issue, which could be linked to the acceleration process and the jet launching, as discussed in Chapter 1.2.

5.1.3.3. *Can we further probe blazars variability?*

I discuss variability in more details in Sect. 5.3, but one can already mention the importance of the lowest energies, where *Fermi*-LAT can not probe fast events with its limited effective area. Extending relations such as F_{var} vs energy or studying spectrally resolved Fourier spectra and bi-spectra would certainly reveal interesting observables, which would not be hampered by the non strict simultaneity that multi-wavelength approaches sometimes suffer.

CTA could also resolve the variability of bright AGN in the "so-called" quiescent state. First, long-term monitoring campaigns, easily carried out with the mode (b) in Fig. 4, will improve our knowledge on the stochastic properties of the flux of AGN and characterize the duty cycles of quiescent/high states (if this question is meaningful in a stochastic framework). Then since, as I show in Sect. 5.3.1, CTA will be able to monitor a $\phi = 10$ C.U. flux at the $T = 1/10$ of minute time scale with a signal-to-noise ratio similar to that of the dramatic outbursts of PKS 2155-304 and since for a signal-dominated flux, this ratio is proportional to $\sqrt{\phi T}$, one can expect a 0.02 C.U. source to be monitored

with a similar accuracy on the hour time scale. Thus variability studies such as that for PKS 2155-304 will become routine analysis on at least a dozen of sources. Note that this number is certainly pessimistic, being only based on the current H.E.S.S. observations.

Finally, variability studies combined with an improved understanding of the energy dependency of the flux variations could bring further constraints on Lorentz invariance violation (LIV). Though the constancy of the speed of light is a cornerstone of special relativity, quantum effects are expected to play a role when approaching the Planck energy scale, implying an energy dependent speed. This can be tested with the highest energy γ rays, as done e.g. with the outbursts of PKS 2155-304 by H.E.S.S. Collaboration et al. (2011) and as extrapolated to CTA by Bolmont & Jacholkowska (2011). γ-ray bursts (Abdo et al. 2009) will certainly be alternative sources to AGN for such studies, probably yielding the most constraining limits.

5.1.3.4. *The first steps of VHE cosmology?*

I have already discussed in Chapter 3 the importance of VHE blazars, which allow a firm measurement of the second most intense cosmological background, the EBL. Attempts to constrain the intergalactic magnetic field (IGMF), which could have emerged in the early Universe, have also been recently led with these objects. The issue to solve is the following: what does happen to the electron-positron pairs created by the interaction of γ rays with the EBL?

If the IGMF is low enough, the pairs should be moderately deflected. For an initial γ ray of 1 TeV, each lepton carries away an energy of half a TeV, i.e. have Lorentz factors of $\gamma = 10^6$, and can upscatter the primary ambient photon field, the CMB at an energy $\epsilon_{\rm CMB} \sim 1$ meV, resulting in Comptonized photons of energy $E = \gamma^2 \epsilon_{\rm CMB} \sim 1$ GeV, in the Thompson regime. Thus there should be a pair echo of the ~ 1 TeV signal in the $\sim$ GeV energy range (see e.g. Taylor et al. 2011). This could be traced either as a real echo, for a variable source, or more simply as a bump in the GeV range in a steady state regime. Alternatively, if the magnetic field is strong enough, the pairs should be significantly deflected, resulting in an off-axis signal: a pair halo (see Aharonian et al. 1994). Given the angular resolution at HE, these halos are not expected to be resolved, but following the previous argument, initial 100 TeV γ rays should produce a ~ 100 GeV halo, which could be detected with VHE instruments. The pair halo technique is hampered by

a limited knowledge of the PSF. The pair echo limits are still discussed and could be invalidated on theoretical grounds by plasma instabilities in the electron-positron beam, preventing the Comptonization of the CMB and heating instead the intergalactic medium (see e.g. Broderick et al. 2012, and reference therein).

Attempts to constrain cosmological parameters, such as the Hubble constant H_0, using the absorption of the VHE emission of blazars have also been discussed, e.g. in Barrau et al. (2008). The idea is that for low redshifts, the EBL optical depth to γ rays is proportional to cz/H_0, where z is the redshift of the source. Using the spectrum of Mrk 501 measured by CAT and HEGRA and de-absorbing it with an decreasing H_0 (instead of with an increasing EBL normalization), the authors derive a lower limit on H_0, in agreement with the current constraints. Note that such an approach relies on a good knowledge of the EBL flux density, and unless refining the method, the constraints on the Hubble constant can not be disentangled from constraints on the EBL normalization, as derived in Chapter 3.

Finally, observations of blazars with H.E.S.S. II and CTA can also contribute to constrain the cosmological evolution of AGN. The *Fermi*-LAT collaboration has shown that FSRQs and BL Lac populations peak at different epochs, typically $z = 0.2 - 0.3$ for BL Lacs and $z = 1.0$ for FSRQs (Ackermann et al. 2011). The question of the evolution of blazars can certainly benefit from a larger energy coverage, which will extend the probe of the γ-ray Universe to larger redshifts. A related question is that of the extragalactic γ-ray background, which is presumably coming from the known γ-ray emitters, at least at the 70% level (Inoue & Totani 2009; Sol et al. 2012). A break in this diffuse background is expected above 100 GeV from interactions with the EBL (once again through pair creation) and the precise shape and location of this break depends on the evolution of the emitting population. The direct measurement of this background, at the level of a percent of the cosmic electron flux, will certainly be highly challenging for current and next-generation analyses, which could refine the background subtraction technique, by modelling this diffuse component itself, as in HE data analysis.

5.2. EBL-dependent prospects

I already exposed the current attempts of the community in VHE cosmology. In the following, I focus on the direct consequences of the method I developed in Chapter 3 and I perform in Sect. 5.2.1 the first redshift measurement at VHE, though for a source for which the spectroscopic redshift is already known, namely PKS 2155-304. This is mostly a feasibility study which represents good omens for VHE cosmology with H.E.S.S. II and CTA. Finally, I suggest in Sect. 5.2.2 potential improvements of the EBL measurements at VHE.

5.2.1. Measuring redshifts: toward cosmological constraints

I implemented everything needed to fit the redshift of a source in the software of H.E.S.S., down to the button to un-check in the GUI if one wants the redshift as a free parameter (by default the redshift of the source and the EBL normalization are fixed parameters). In ParisAnalysis, the minimization procedure is based on the Levenberg-Marquardt algorithm, which needs as inputs the derivative of the quantity to minimize. In our case, it involves the derivative of the flux as a function of redshift. Since the evolution of the absorption as a function of redshift is not analytical but is tabulated (up to $z = 1$ in our case), I added a row to the table in which I numerically computed the derivative of the optical depth.

With such a tool, the redshift of a source is just a parameter, exactly as the EBL normalization or a power-law index. I fit hereafter the redshift of PKS 2155-304 using the most constraining dataset for the EBL measurement (number *1*), for which the power law is a good representation of the spectrum and does not underestimate the curvature (using the χ^2 probability as a criterion). Since this dataset is the most constraining one for the EBL if one assumes the redshift of the source known, it should also lead to most stringent constraints on the redshift if one assumes the EBL normalization known.

For simplicity, and since I am just performing a feasibility study, I fix the normalization of the EBL model of FR08 to its best fit value, i.e. I use $\alpha_0 = 1.27$. The best fit parameters of the model and the covariance matrix V are:

$$\begin{array}{r} \phi(E_{\rm dec}) = 187 \pm 35 \\ \Gamma = 2.88 \pm 0.20 \\ \mathbf{z = 0.121 \pm 0.028} \end{array} \qquad V = \begin{bmatrix} 1220 & -6.71 & 0.982 \\ & 0.0381 & -0.00541 \\ & & 0.000811 \end{bmatrix} \tag{5.1}$$

where the flux is in units of 10^{-12} cm^{-2} s^{-1} TeV^{-1} and the decorrelation energy is $E_{\rm dec} = 420$ GeV.

Though the statistical uncertainty on the redshift is quite large, this measurement is in remarkably good agreement with the spectroscopic redshift $z = 0.116$. Note however that the parameters are highly correlated and writing the non-diagonal terms as $\rho\sigma_i\sigma_j$, one gets an anti correlation of amplitude $\rho = -0.97$. If one assumes that similarly the index is a 100% anti correlated with the EBL normalization and given the uncertainty on the index of $\sigma_\Gamma \sim 0.12$ from the EBL uncertainty, a scaling of the redshift statistical uncertainty yields an estimated systematic uncertainty due to the lack of knowledge on the EBL of 0.017. The latter includes the current statistical and systematic uncertainty on the EBL normalization and one can estimate that with VHE spectra, a redshift could hardly be measured with a precision better than 0.010.

I obviously used the best data set to perform this measurement and one could wonder if such a method can be employed with the spectra of unknown-z sources. I performed a preliminary analysis of the spectrum of PG 1553+113, which I do not present here because of its lack of conclusiveness, the statistics on the source being too small and the energy threshold too high to probe the unabsorbed part of the spectrum. This object should be a primary target of H.E.S.S. II and its measured spectrum will certainly be investigated in this way. Another interesting source could be PKS 0447-439, but with a few hundreds excess events compared to thousands for the dataset on PKS 2155-304, the resolution of the measurement would presumably be quite poor. Except for monsters such as PG 1553+113, redshift measurements of AGN at VHE will certainly mostly be performed with CTA.

5.2.2. Refining the EBL measurement

The current knowledge of the EBL is based on the interplay between modellings, direct measurements, lower limits from source counts, and indirect measurements with γ rays. Now that the detection of the EBL imprint at HE and VHE has been proven possible (cf. Chapter 3), γ-ray observatories should aim at extending the coverage of the measurement.

The $z = 0$ windows on cosmological backgrounds are shown in the top panel of Fig. 6, where the *Fermi*-LAT area corresponds to γ rays between 30 GeV and 500 GeV from sources uniformly distributed between $z \in [0.5, 1.6]$. The observation window of the high-frequency

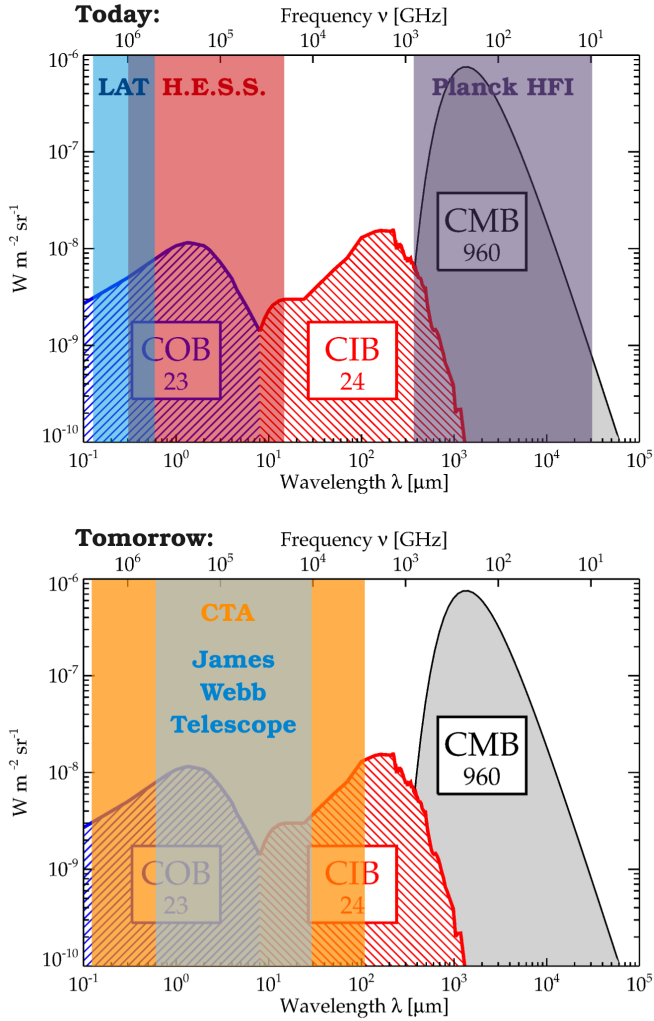

FIGURE 6. Wavelength windows on $z = 0$ cosmological backgrounds, as currently probed (top panel), and as CTA and the JWST will probe during the upcoming decade. *Backgrounds figures extracted from Dole et al. (2006).*

instrument (HFI), on board the Planck satellite (Planck Collaboration et al. 2011), is indicated with a purple area for reference.

The wavelength range covered with CTA is shown in orange in the bottom panel of Fig. 6, where the lower bound corresponds to sources at $z = 0.5$ above 50 GeV and the upper bound corresponds to 80 TeV γ rays. The EBL measurement will tremendously benefit from the James Webb Space Telescope (JWST, Gardner et al. 2006), which will observe the sky between 0.5 and 29 μm. The CTA measurement will probably suffer from much larger systematic uncertainties than the constraints that the JWST will derive from galaxy counts. A larger wavelength range will nevertheless be covered using γ rays, and an interesting synergy between groups of these different fields could certainly have a great impact on both cosmology and γ-ray astronomy.

With the low-energy extension that CTA and H.E.S.S. II will provide with respect to H.E.S.S. I, the period of the Universe where the EBL is probed will be extended up to at least $z = 0.5$, fully complementing the *Fermi*-LAT measurement. One could imagine that with a sufficiently large sample of sources, a redshift resolved study of the EBL opacity could be performed, allowing the photon density itself to be measured, instead of its cumulated distribution over the Universe history.

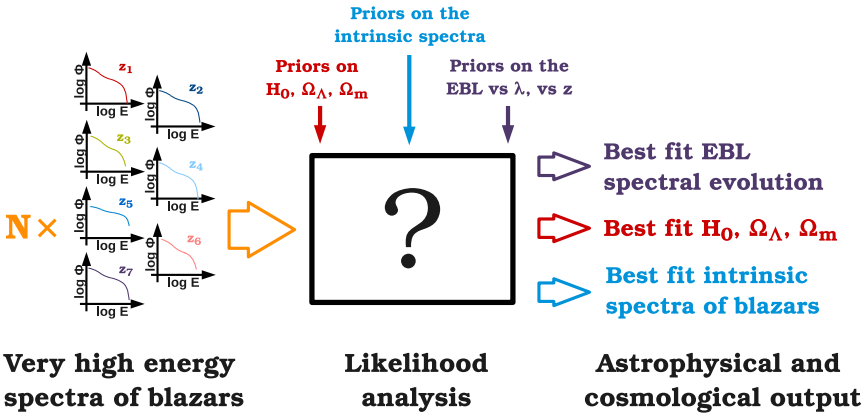

FIGURE 7. Schematic representation of the requirements of future EBL analysis, before studies of cosmological parameters can be performed.

Assuming that the EBL flux density is known well enough, one could in principle constrain cosmological parameters (in particular Ω_m and Ω_Λ), similarly to studies carried out with supernovae of type I A (Riess et al. 1998). The main difference lies in the use of the luminosity distance for super novae of type I A when the EBL absorption is related to the comoving distance $\int_0^z \mathrm{d}z' \frac{\mathrm{d}l}{\mathrm{d}z'}$. This difference could be of interest, making EBL absorption a non-redundant probe of the cosmological parameters complementary to studies exploiting the CMB, super novae of type I A or baryon acoustic oscillations. If we want to use the VHE spectra of blazars for such cosmological purposes, the current analyses will have to be re-designed, as suggested in Fig. 7. One could imagine to jointly fit a large number of VHE spectra from sources at different redshifts in order to measure the intrinsic spectra of the source, as well as the level of EBL density as a function of wavelength and redshift, but also constrain cosmological parameters such as the Hubble parameter, the density of matter, and the density of dark energy.

One hurdle has probably already been overcome with the use of splines by Mazin & Raue (2007) to describe the wavelength dependence of the EBL. A simple redshift dependency, e.g. in $(1+z)^\gamma$, could model the evolution in the restricted redshift range. Priors on the intrinsic spectra should certainly be based on smoothness (no inflection points) and could exploit the little spectral variability observed at HE, imposing e.g. low-energy extrapolations matching the *Fermi*-LAT hardness. All in all, it seems that most of the ingredients have already been developed. They must now be encompassed in a proper statistical framework and in an efficient analysis software, able to jointly fit the large number of spectra that CTA will acquire.

5.3. Variability studies

Variability is one of the key properties of blazars. As discussed in Chapter 4, probing the most extreme events allows the mechanisms at play in these accelerators to be better constrained. With improved capabilities, the next generation instrument will certainly extend the current studies both in terms of short time-scales coverage, as discussed in Sect. 5.3.1, and in terms of long-term monitoring, mentioned in Sect. 5.3.2.

5.3.1. Below the minute time-scale?

5.3.1.1. *Simulation*

CTA will have an increased sensitivity with respect to H.E.S.S., as well as a lower energy threshold. I show in Fig. 8 and Fig. 9 the impact of these improved capabilities[2] on the dramatic outbursts of PKS 2155-304.

To perform these simulations, I used the spectral modelling of the flux $F(E) = \mathrm{d}N/\mathrm{d}E$ derived for the multi-wavelength campaign carried out by H.E.S.S. and *Fermi*-LAT on the source in Aharonian et al. (2009). This enables the extension of the spectrum of the source down to the analysis threshold of CTA, around 50 GeV, by scaling up the H.E.S.S. integral flux $\Phi_{\mathrm{HESS}}(t)$ above 200 GeV, modelled with a series of five bursts on top of a constant. This scaling reads:

$$\Phi_{\mathrm{CTA}}(t) = (\Phi_{\mathrm{HESS}}(t) + \Psi(t)) \times \frac{\int_{E_{\mathrm{min\ CTA}}}^{+\infty} F(E)\mathrm{d}E}{\int_{E_{\mathrm{min\ HESS}}}^{+\infty} F(E)\mathrm{d}E} \tag{5.2}$$

where the high-energy bounds are reasonably taken as ∞ (sharp cut off in the spectrum). $\Psi(t)$ represents the additional noise, i.e. the measurement statistical uncertainties if the light curve simulated for CTA has the same properties in the Fourier space as the H.E.S.S. light curve. One can expect these properties to be extended. Indeed, with the improved sensitivity of CTA, smaller time scales and thus larger frequencies could be probed. In this case, $\Psi(t)$ is a realization of a red noise below the Nyquist frequency achieved with CTA and above the frequency at which the PSD of the H.E.S.S. signal enters the Poisson noise domain ($\nu_{\mathrm{brk}} = 1.6 \times 10^{-3}$ Hz). I employ the method of Timmer & Koenig (1995), generating a signal of null mean and of variance determined by the Parseval-Plancherel's theorem, i.e. for a power-law Fourier spectrum of index $\alpha = 2$:

$$V(\Psi) = V(\Phi_{HESS}) \times \frac{\int_{\nu_{\mathrm{brk\ HESS}}}^{\nu_{\mathrm{Nyq\ CTA}}} \nu^{-\alpha}\mathrm{d}\nu}{\int_{\nu_0}^{\nu_{\mathrm{brk\ HESS}}} \nu^{-\alpha}\mathrm{d}\nu} \tag{5.3}$$

[2] I used the effective area $A(E)$ simulated by Bernlöhr (2008) for the configuration D. The choice of the array (e.g. E or I) marginally impacts the temporal binning, at the 5% level.

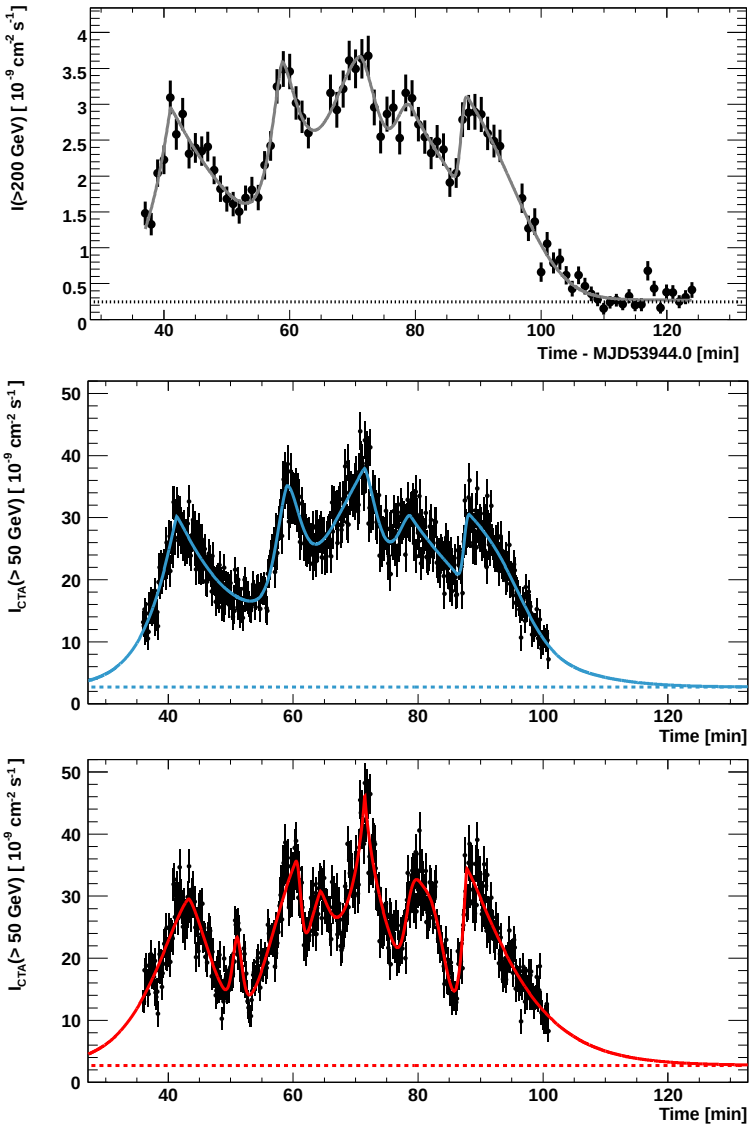

FIGURE 8. *Top:* Integral flux above 200 GeV of PKS 2155-304 monitored with H.E.S.S. vs time, with a 1 minute binning. *Middle and bottom:* Simulated integral flux above 50 GeV monitored with CTA vs time, with a 7.5 seconds binning. In the bottom panel, the PSD is extended up to the highest frequencies.

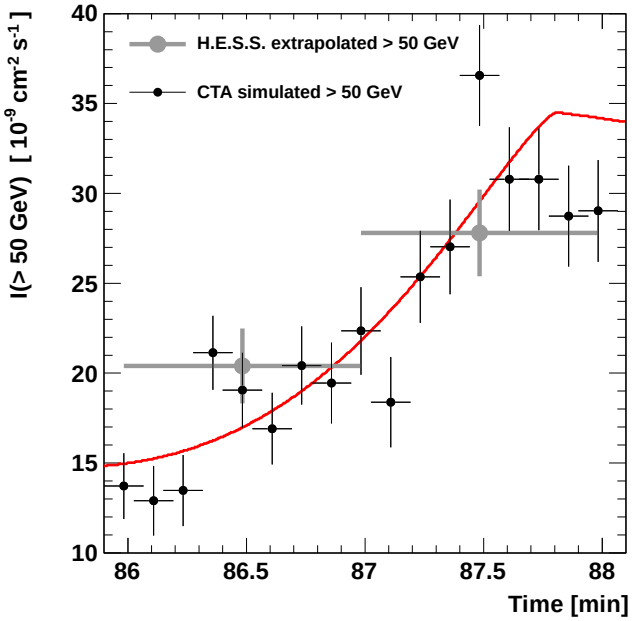

FIGURE 9. Integral flux of PKS 2155-304 above 50 GeV vs time seen by H.E.S.S. in gray and by CTA in black, corresponding to the second simulation in Fig. 8. Only the rise of the last peak in the light curve is shown.

Assuming a signal-dominated flux and for a Poisson distribution of events, the uncertainty on the flux on a temporal binning T is:

$$\sigma_{\Phi(>E_{min})} = \sqrt{\frac{\Phi_{\rm CTA}}{\left[\int_{E_{min}}^{+\infty} A(E)F(E)\mathrm{d}E \;/\; \int_{E_{min}}^{+\infty} F(E)\mathrm{d}E\right] \times T}} \tag{5.4}$$

where the temporal binning of the light curve is chosen to achieve an average significance of the simulated points equal to that of H.E.S.S.. Scaling up the integral flux, with the lowering of the energy threshold, and reducing the uncertainties, with the increase of the effective area, allow the flux to be sampled at the $T = 7.5$ second time scale. This represents almost a ten times increase in sampling rate (one minute for H.E.S.S.), as shown in the middle panel in Fig. 8 where the additional noise is simply due to the statistical uncertainties. The case of the extension of the PSD is shown in the bottom panel of Fig. 8.

5.3.1.2. *Results*

To determine the number of significant peaks and characterize their doubling rise and decay times (τ_r and τ_d), sharpness κ and amplitude A at the time $t_{\max}$, I use the same peak finding and fitting procedure as used for the actual H.E.S.S. data in Aharonian et al. (2007). The best fit parameters are given in Table 5.3.1.2. The additional red noise results in the apparition of short substructures, the second and fourth peak for the second simulation, while the number of significant peaks is conserved for the first one.

The parameters of the fit of the light curve simulated without an extension of the PSD can be directly compared to those measured with H.E.S.S.. Of particular interest are the rise and decay times, which allow the size of the emission region and its Doppler factor to be constrained with the causality argument. The average resolution $< \sigma_\tau/\tau >$ for H.E.S.S. is of 38% and goes down 17% with the first simulation. This decrease enable a significant measurement of the doubling time of the last peak $\tau_r = 60 \pm 18$ s, which should be compared with the shortest significant doubling time measured with H.E.S.S. of 173 ± 28 s. When extending the PSD, the additional variance results in even shorter time scales down to $\tau_r = 25 \pm 4$ s. Such short time scales would imply Doppler factors of several hundreds, which would question the interpretation in terms of bulk motion of the jet.

5.3.2. Long-term monitoring

5.3.2.1. *Long time scales*

Short time scales are of large interest because they directly probe the jet properties. On the other hand, there are growing pieces of evidence that the disk properties are probed on the long time scales. The most probing demonstration is certainly the relation shown in Fig. 10, derived from X-ray observations of stellar mass black holes (the microquasar GRS 1915+105 and the X-ray binary Cyg X-1), of Seyfert galaxies, and recently of blazars and radio galaxies (Marshall et al. 2009). With a forward-folding Fourier analysis, called PSRESP, McHardy et al. (2006) measure a transition in the PSDs of these object from a pink noise to a red noise behaviour. The inverse of the break frequency, $T_{\rm observed}$, scales linearly with $T_{\rm predicted} \propto M_{\rm BH}/\dot{m}_E$, where $M_{\rm BH}$ is the mass of the black hole and $\dot{m}_E$ is the accretion rate in Eddington units (assuming $\dot{m}_E \propto L_{\rm bol}/L_{\rm Edd}$).

$t_{\max}$ [min]	A [$10^{-9}\,\mathrm{cm}^{-2}\,\mathrm{s}^{-1}$]	τ_r [s]	τ_d [s]	κ
41.0	2.7 ± 0.2	173 ± 28	610 ± 129	1.07 ± 0.20
58.8	2.1 ± 0.9	116 ± 53	178 ± 146	1.43 ± 0.83
71.3	3.1 ± 0.3	404 ± 219	269 ± 158	1.59 ± 0.42
79.5	2.0 ± 0.8	178 ± 55	657 ± 268	2.01 ± 0.87
88.3	1.5 ± 0.5	67 ± 44	620 ± 75	2.44 ± 0.41

$t_{\max}$ [min]	A [$10^{-9}\,\mathrm{cm}^{-2}\,\mathrm{s}^{-1}$]	τ_r [s]	τ_d [s]	κ
41.4	26.7 ± 1.5	208 ± 13	452 ± 80	1.11 ± 0.17
59.1	16.8 ± 2.0	111 ± 14	138 ± 18	1.69 ± 0.63
71.5	32.7 ± 1.0	541 ± 106	186 ± 38	1.38 ± 0.27
78.8	23.8 ± 1.8	182 ± 36	784 ± 122	1.58 ± 0.81
88.3	11.9 ± 1.1	60 ± 18	513 ± 65	2.65 ± 0.40

$t_{\max}$ [min]	A [$10^{-9}\,\mathrm{cm}^{-2}\,\mathrm{s}^{-1}$]	τ_r [s]	τ_d [s]	κ
43.3	25.7 ± 1.1	202 ± 13	147 ± 13	1.42 ± 0.15
51.0	10.9 ± 1.6	32 ± 8	34 ± 6	1.85 ± 0.44
60.4	17.5 ± 2.0	210 ± 19	37 ± 8	2.19 ± 0.35
64.4	15.1 ± 2.0	124 ± 27	60 ± 11	1.32 ± 0.28
71.5	43.7 ± 1.6	74 ± 9	80 ± 6	0.80 ± 0.11
80.5	18.3 ± 1.7	108 ± 17	177 ± 17	2.99 ± 0.43
87.8	26.8 ± 1.8	25 ± 4	235 ± 12	1.27 ± 0.10

TABLE 1. Results of the best χ^2 fit of the superposition of bursts and a constant to the light curve. For the H.E.S.S. data, corresponding to the top table, the constant term is $0.27 \pm 0.03 \times 10^{-9}\,\mathrm{cm}^{-2}\,\mathrm{s}^{-1}$ ($1.1\mathrm{I}_\mathrm{Crab}$). *Extracted from Aharonian et al. (2007).* For the simulated CTA data, the constant term is fixed to $2.7 \times 10^{-9}\,\mathrm{cm}^{-2}\,\mathrm{s}^{-1}$.

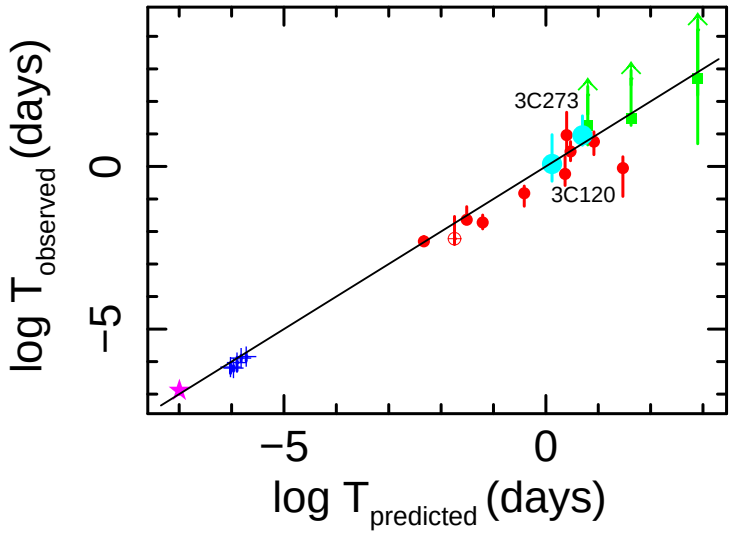

FIGURE 10. Break in the PSD vs time scale predicted from the accretion rate and the mass of stellar-size and super-massive black holes. The star and crosses correspond to GRS 1915+105 and to the different states of Cyg X-1, respectively. They are jointly fitted with the circles representing AGN, while the squares, for which only an upper limit on the break frequency could be derived, are not included. The light blue circles represent the blazar 3C 273 and the BLRG 3C 120. *Extracted from McHardy (2010).*

Involving the accretion rate, this remarkable relation points to a disk origin of the X-ray variability at low Fourier frequencies. Besides the black-hole mass and the accretion rate, another relevant parameter could be the spin of the black hole, which should affect the innermost stable orbit, with a faster rotation implying a smaller size / time scale. But the good quality of the fit does not suggest the need for additional underlying parameters, which could be interpreted as a clustering of the objects around a single value, e.g. maximum spinning system.

With CTA, long-term monitoring of bright blazars could be performed on yearly time scales with an hour sampling, allowing breaks to be measured from $\sim$ 10 h up to the month time scale. If the scaling

found in X rays can be extrapolated to VHE, then it could provide means for direct constrains on the accretion state of the most energetic blazars. Finally, since the fastest variability should originate from the jet while the longest seems to originate from the disk, CTA could open an unexplored window at VHE, with the study of the transition between the two modulation regimes.

5.3.2.2. *Flux distribution analyses*

With the ability to sample flux from ~ 10 C.U. for the most extreme outbursts down to the milli-C.U. level, CTA will perform measurements on a four decades dynamic range. We should begin to think about the data analysis techniques that can be used to compare large sets of flux measurements with theoretical distributions that significantly differ from normality. A distinction based on high order moments, such as the skewness or the kurtosis does not seem appropriate, because of the known large variations in the estimators of these quantities.

An alternative when studying skewed flux distributions could be a more systematic computation of maximum-likelihood estimators of the parameters of the underlying log-normal. These quantities, called μ^* and σ^* following Limpert et al. (2001), are the equivalent of the mean μ and standard deviation σ. Instead of characterising the distribution in terms of *plus or minus one std dev* ($\mu \pm \sigma$), the authors define it in terms of *times or divided by one logarithmic std dev* ($\mu^* \times/ \sigma^*$). The logarithmic mean reads

$$\mu^* = \exp\left(\frac{1}{n}\sum_{i=1}^{n}\ln\phi_i\right) = \left(\prod_{i=1}^{n}\phi_i\right)^{\frac{1}{n}} \tag{5.5}$$

i.e. is simply the geometric mean of the data. Similarly, the logarithmic std dev reads:

$$\sigma^* = \exp\sqrt{\frac{1}{n-1}\sum_{i=1}^{n}(\ln\phi_i/\mu^*)^2} \tag{5.6}$$

The impact of the flux uncertainty on these quantities could be determined, in a first approach, varying the points within their uncertainties. The way for establishing a proper estimator accounting for the statistical uncertainties, as the excess variance for non-skewed distributions, remains open. These parameters are certainly more meaningful that the usual average flux and fractional variance for skewed

flux distribution approaching log-normality. Moreover, one can test the deviation to a symmetric shape with the parameter σ^*. Limpert et al. (2001) consider that when σ^* is typically below $1.1-1.2$, it is difficult to distinguish normal and log-normal distributions, while above, log-normality seems a better description of the data (even if the notion of better for non-nested models is hard to properly define).

Numerical techniques to derive maximum-likelihood estimators of the parameters of α-stable distributions have also been developed, e.g. by Nolan (2001), mostly for the world of finance. One could imagine to adapt such approaches to astronomical data, properly accounting for the measurement uncertainties. This would allow approaches such as the minijets-in-a-jet statistical model to be tested. Some work remains to be done on these topics, but it seems that mathematics have already open the way for applications in geophysics and finance. Astronomers and high-energy physicists certainly have a great deal to bring to these ongoing efforts.

5.3.2.3. *Concluding remarks*

The perspectives of AGN studies with CTA and H.E.S.S. II are bright. VHE cosmology could become a prime tool for understanding the Universe and for constraining the intrinsic emission of distant sources. The generalization of variability studies will deepen the research around the crucial questions on the components of AGN, especially the jet, the black holes and the disk, as well as on their interplay. VHE astronomy has been build on the reunion of different communities, astronomers and particle physicists, who joined their skills to build the first generations of instruments. The field will certainly pursue in this path by developing the already growing interests of astrophysicists, cosmologists, geophysicists and mathematicians.

Bibliography

Abdo, A. A., Ackermann, M., Ajello, M., et al. 2009, Nature, 462, 331

Ackermann, M., Ajello, M., Allafort, A., et al. 2011, ApJ, 743, 171

Actis, M., Agnetta, G., Aharonian, F., et al. 2011, Experimental Astronomy, 32, 193

Agudo, I., Marscher, A. P., Jorstad, S. G., et al. 2011, ApJ, 735, L10

Aharonian, F., Akhperjanian, A. G., Anton, G., et al. 2009, ApJ, 696, L150

Aharonian, F., Akhperjanian, A. G., Bazer-Bachi, A. R., et al. 2007, ApJ, 664, L71

Aharonian, F., Akhperjanian, A. G., Bazer-Bachi, A. R., et al. 2006, ApJ, 636, 777

Aharonian, F. A., Coppi, P. S., & Voelk, H. J. 1994, ApJ, 423, L5

Aliu, E., Anderhub, H., Antonelli, L. A., et al. 2009, Astroparticle Physics, 30, 293

Anderhub, H., Backes, M., Biland, A., et al. 2011, Nuclear Instruments and Methods in Physics Research A, 639, 58

Barrau, A., Gorecki, A., & Grain, J. 2008, MNRAS, 389, 919

Bernlöhr, K. 2008, Astroparticle Physics, 30, 149

Bolmont, J. & Jacholkowska, A. 2011, in SF2A-2011: Proceedings of the Annual meeting of the French Society of Astronomy and Astrophysics, ed. G. Alecian, K. Belkacem, R. Samadi, & D. Valls-Gabaud, 529–533

Broderick, A. E., Chang, P., & Pfrommer, C. 2012, ApJ, 752, 22

de Naurois, M. 2012, Very High Energy astronomy from H.E.S.S. to CTA. Opening of a new astronomical window on the non-thermal Universe (TEL), http://tel.archives-ouvertes.fr/tel-00687872

Dole, H., Lagache, G., Puget, J.-L., et al. 2006, å, 451, 417

Dubus, G., Contreras, J. L., Funk, S., et al. 2012, arXiv:1208.5686

Funk, S. & Hinton, J. 2012, arXiv:1205.0832

Gardner, J. P., Mather, J. C., Clampin, M., et al. 2006, Space Sci. Rev.,

123, 485
Giebels, B. 2011, A contribution to gamma-ray astronomy of GeV-TeV Active Galaxies with Fermi and H.E.S.S. (TEL), http://tel.archives-ouvertes.fr/tel-00672596
H.E.S.S. Collaboration, Abramowski, A., Acero, F., et al. 2011, Astroparticle Physics, 34, 738
Holder, J. 2005, in International Cosmic Ray Conference, Vol. 5, International Cosmic Ray Conference, 383
Inoue, Y. & Totani, T. 2009, ApJ, 702, 523
Limpert, E., Stahel, W. A., & Abbt, M. 2001, BioScience, 51, 341
Marshall, K., Ryle, W. T., Miller, H. R., et al. 2009, ApJ, 696, 601
Mazin, D. & Raue, M. 2007, A&A, 471, 439
McHardy, I. 2010, in Lecture Notes in Physics, Berlin Springer Verlag, Vol. 794, Lecture Notes in Physics, Berlin Springer Verlag, ed. T. Belloni, 203
McHardy, I. M., Koerding, E., Knigge, C., Uttley, P., & Fender, R. P. 2006, Nature, 444, 730
Nolan, J. P. 2001, in Lévy Processes: Theory and Applications, ed. O. E. Barndorff-Nielsen, T. Mikosch, & S. I. Resnick, 379–400
Nolan, P. L., Abdo, A. A., Ackermann, M., et al. 2012, ApJS, 199, 31
Planck Collaboration, Ade, P. A. R., Aghanim, N., et al. 2011, A&A, 536, A1
Poutanen, J. & Stern, B. 2010, ApJ, 717, L118
Reimer, A. & Boettcher, M. 2012, arXiv:1208.5926
Riess, A. G., Filippenko, A. V., Challis, P., et al. 1998, AJ, 116, 1009
Sinnis, G., Smith, A., & McEnery, J. E. 2005, in The Tenth Marcel Grossmann Meeting. On recent developments in theoretical and experimental general relativity, gravitation and relativistic field theories, ed. M. Novello, S. Perez Bergliaffa, & R. Ruffini, 1068
Sol, H., Zech, A., Boisson, C., et al. 2012, Astroparticle Physics, submitted
Taylor, A. M., Vovk, I., & Neronov, A. 2011, A&A, 529, A144
Timmer, J. & Koenig, M. 1995, A&A, 300, 707

Conclusion

The last two decades have revealed an extragalactic γ-ray sky dominated by active galactic nuclei (AGN). These sources began to raise the interest of astronomers, astrophysicists, and cosmologists fifty years ago and they still have plenty of secrets to share. The non-thermal emission of the jets of AGN is particularly constrained by their flux in the γ-ray band, be it at high energy (HE, from tens of MeV up to hundreds of GeV) with pair-conversion satellites such as *Fermi*-LAT or at very high energy (VHE, from hundreds of GeV up to tens of TeV) with imaging atmospheric Cherenkov telescopes (IACT) such as H.E.S.S..

I have studied the AGN observed during the past decade with H.E.S.S., most of them having also been detected with *Fermi*-LAT after four years of operation. Because of the limited field of view (FoV) of IACT, a large fraction of the sky remains unexplored at VHE and regions of interest can be identified using the HE sky, entirely covered by *Fermi*-LAT. Though sometimes no source is detected in the targeted FoV, as shown with the preparation of the third publication of upper limits by the H.E.S.S. AGN group, this strategy keeps on expanding the list of known VHE AGN, which has recently exceeded a total of fifty sources. Twenty of them have been discovered with H.E.S.S. and I have personally contributed to the finding and the characterization of two of the faintest ones, 1ES 1312-423 and SHBL J001355.9-185406. Like most of the known VHE AGN, these objects are blazars, i.e. AGN with jets pointing toward the observer, and they belong to the high frequency peaked BL Lac class (HBL). I have analysed the H.E.S.S. data on these objects for the two publications (one cross-check and one main analysis). I have shown, in particular, that the reconstruction of the spectrum of 1ES 1312-423 is not biased by the unusual observation conditions (large offset). With the aim of modelling the emission of

this source, I have also gathered the archival and newly derived multi-wavelength data.

The simplest model matching the broad band spectrum of HBLs is the synchrotron self-Compton (SSC) scenario, where the VHE flux originates from the scattering of energetic electrons off a field of photons, generated by the very same electron population through synchrotron radiation in an ambient magnetic field. I have developed my own numerical code, following the state-of-the-art methods for an homogeneous, time-independent SSC model. My contribution to this field probably lies in a detailed discussion of the equipartition between the magnetic field and the electron population, a condition that should be met to minimize the energy budget. I established a set of parameters and a methodology to test the validity of equipartition and shown that it is strictly ruled out in the case of 1ES 1312-423. This finding seems to be applicable to a number of HBL, with the caveat that the population is still limited. If the SSC model is indeed a good representation of the spectral energy distribution of HBL objects, such constraints on the energetic balance could narrow down the acceleration processes at play in the jets of AGN.

Besides carrying informations on astrophysical jets, the γ rays emitted by blazars can be used to probe the second most intense cosmological background, namely the extragalactic background light (EBL), which conveys the integrated history of star and galaxy formation. VHE γ rays primarily interact though pair creation with the cosmic optical background (COB), the first of the two bumps of the EBL. The potential of VHE extragalactic observations for constraining the EBL had been realized since 1967 but a firm detection and measurement only came 45 years later. I used the spectra of the brightest objects detected with H.E.S.S., paying particular attention to potential intrinsic biases. I avoided the scatter due to spectral variability by grouping datasets on single sources by flux level and I fully accounted for intrinsic curvature by releasing the constraints on the functional form that were made in previous publications. Without any assumption on the intrinsic spectral parameters, I performed the first detection of the EBL signature in VHE spectra of blazars, significant at the 9σ level. I use this feature in the γ-ray band to measure the COB over two decades of

wavelength, with a peak amplitude known at the 20% level, including the systematic uncertainties, which were thoroughly studied.

Besides allowing the EBL absorption to be measured, the code that I implemented in the H.E.S.S. software allows the intrinsic properties of distant AGN to be determined. I thus derived the intrinsic spectra of PKS 2155-304, PKS 2005-489 and Mrk 421 and showed that this information combined with the spectra measured by *Fermi*-LAT enables to locate the peak of their emission. I also showed that 1ES 1101-232, 1ES 0229+200, 1ES 0347-121 and H 2356-309 are four fantastically efficient accelerators, with a hard HE spectrum extending above TeV energies. This demonstrates that the question of the maximum γ-ray energy that can be reached by blazars remains open in a few cases. I also implemented the tools to fit the redshift of a source for a given EBL absorption and I showed its capabilities by measuring for the first time a redshift at VHE, with a resolution of 30% for the data on PKS 2155-304. This result announces a bright future for γ-ray cosmology with the next-generation observatory CTA.

Besides the spectral characteristics, one of the most striking and still poorly understood properties of blazars is the tremendous variability that they sometimes exhibit. The most dramatic events ever observed from an AGN, at least at VHE, are the outbursts of PKS 2155-304, with flux variations unsustainable in a steady-sate regime, on time-scales as short as a few minutes (when the central object probably measures several light hours). These fast fluctuations pinpoint a jet origin of the variability, where relativistic effects can shorten the observed time-scales. I probed the variability on various time-scales in the Fourier space, using the power spectral density (PSD). I first showed that the instrumental uncertainty on the light curve can be propagated analytically in the Fourier space and I established simple formulas allowing a fast computation, which is more reliable than a Monte Carlo based approach. I have implemented a computation of the PSD and associated uncertainties within the H.E.S.S. software, together with minor tools such as the computation of the value of / limits on the excess variance, and a period-by-period binning for light curves. To account for the distortion of the PSD induced by the observational constraints (windowing, sampling), I have developed a forward-folding

Fourier analysis measuring the Fourier index of a light curve. This tool has confirmed the recently published results on PKS 2155-304, which were obtained with a different approach.

The unprecedented statistics on PKS 2155-304 has enabled the characterization of the statistical properties of the light curve measured with H.E.S.S., such as a highly skewed flux distribution and a correlation between the sample flux and the sample R.M.S.. These properties were usually attributed to multiplicative processes, expected in accretion disk, when additive processes are more commonly invoked in jets. I refuted the belief that additive models cannot reproduce such skewed distributions or linear R.M.S.-flux correlation by exposing the properties of Pareto distributions, which might be more common in finance and geophysics. I established a physical model which generates such distributions, where relativistically boosted emitting regions, called minijets, are randomly oriented in a boosted jet. The sum of the emissions, using a generalization of the central limit theorem, tends to an α-stable distribution, which shares the same properties as observed in the light curve of PKS 2155-304. I thus successfully interpreted the observed flux as a realization of a stochastic process, defined by the orientations of the minijets. In addition to the statistical properties, I showed that the red-noise behaviour, the flux-index correlation and the increase of the fractional variance with energy also find a natural explanation within this minijets-in-a-jet statistical model.

To conclude, I addressed the technical progresses achieved with H.E.S.S. II and expected for the next generation experiment CTA, which will result in a larger energy coverage and an unprecedented sensitivity. I discussed the expected impact on the AGN population and on our understanding of their jets. With these new instruments, variability modelling and γ-ray cosmology will probably enter an era of full maturity.

Épilogue

Les deux dernières décennies ont révélé un ciel extragalactique dominé en rayons γ par les noyaux actifs de galaxie (AGN). Ces sources attisent la curiosité des astronomes, des astrophysiciens et des cosmologues depuis maintenant cinquante ans, et elles ont encore de nombreux secrets à livrer. L'émission non thermique des jets d'AGN est tout particulièrement contrainte par leur flux en rayons γ, que ce soit à haute énergie (HE, quelques dizaines de MeV jusqu'à des centaines de GeV) avec les satellites à conversion de paires tels que *Fermi*-LAT, ou à très haute énergie (VHE, quelques centaines de GeV jusqu'à des dizaines de TeV) avec les télescopes atmosphériques à imagerie Cherenkov (IACT) tels que H.E.S.S..

J'étudie les AGN observés avec H.E.S.S. au cours de la dernière décennie, la plupart d'entre eux ayant aussi été détectés par *Fermi*-LAT après quatre ans de fonctionnement. Du fait du champ de vue limité des IACT, une grande fraction du ciel reste inexplorée à VHE et le ciel à HE, entièrement couvert par *Fermi*-LAT, peut être utilisé pour identifier les régions intéressantes. Il arrive qu'aucune source ne soit détecté dans le champ de vue ciblé, comme je l'ai montré avec la préparation de la troisième publication de limites supérieures par le groupe AGN de H.E.S.S.. Cependant, de telles stratégies ne cessent d'alimenter la liste des AGN connus à VHE, qui a récemment dépassé la barre des cinquante. Vingt de ces AGN ont été découverts par H.E.S.S.. J'ai personnellement contribué à la découverte et à la caractérisation de deux des plus faibles d'entre eux, 1ES 1312-423 et SHBL J001355.9-185406. Comme la majorité des AGN émettant à VHE, ces objets sont des blazars, i.e. des AGN dont le jet est pointé vers l'observateur, et ils appartiennent à la classe des BL Lac piquant à haute fréquence (HBL). J'ai analysé les données de H.E.S.S. sur ces objets pour préparer leur publication (en tant que vérification pour

l'une et analyse principale pour l'autre) et j'ai montré en particulier que la reconstruction du spectre de 1ES 1312-423 n'est pas biaisée par ses conditions d'observations inhabituelles (grand angle hors axe). Dans l'optique de modéliser l'émission de cette source, j'ai réuni les données multi longueur d'onde archivées et nouvellement obtenues.

Le modèle le plus simple permettant de comprendre l'émission des HBLs est le scénario synchrotron self-Compton (SSC), où l'émission à VHE provient de la diffusion d'électrons énergétiques sur un champ de photons, lui-même issu du rayonnement synchrotron des dits électrons dans un champ magnétique ambiant. J'ai développé mon propre code SSC, en suivant l'état de l'art en matière de modèle homogène et indépendant du temps. J'ai principalement contribué à ce domaine en menant une discussion détaillée de l'équipartition entre le champ magnétique et la population d'électrons, qu'on attend d'un système où le budget énergétique est minimal. J'ai établi un jeu de paramètres et une méthodologie pour évaluer la validité de l'équipartition et j'ai montré qu'elle était strictement rejetée dans le cas de 1ES 1312-423. Ce constat semble s'appliquer plus généralement aux HBLs, bien que l'échantillon d'objets étudiés soit encore limité. Si le modèle SSC est effectivement une bonne représentation de la distribution spectrale en énergie des HBLs, de tels bilans énergétiques de la zone émettrice pourraient contraindre les mécanismes d'accélération qui ont lieu au sein des jets des AGN.

Au delà de l'information qu'ils véhiculent sur les jets astrophysiques, les rayons γ émis par les blazars peuvent être utilisés pour sonder le deuxième fond diffus cosmologique le plus intense, appelé lumière de fond extragalactique (EBL) et contenant l'histoire intégrale de la formation d'étoiles et de galaxies dans notre Univers. Les rayons γ à VHE interagissent par création de paires avec le fond diffus optique (COB), une des deux composantes de l'EBL. Le potentiel des observations extragalactiques à VHE pour contraindre l'EBL a été relevé depuis 1967, mais une détection ferme ainsi qu'une première mesure ne sont arrivées que 45 ans plus tard. J'ai utilisé les spectres des sources les plus brillantes vues par H.E.S.S. et ai accordé une attention toute particulière aux biais potentiels liés à l'émission intrinsèque. J'ai minimisé la dispersion due à la variabilité spectrale en regroupant les lots de données

par niveau de flux, source par source, et j'ai entièrement pris en compte la courbure intrinsèque en relâchant les contraintes sur les formes fonctionnelles qui étaient imposées dans les précédentes publications. Sans avoir besoin de faire quelque hypothèse que ce soit sur les paramètres intrinsèques, je réalise la première détection de la signature de l'EBL dans des spectres de blazars à VHE, avec une significativité atteignant les 9σ. J'utilise cette signature en rayons γ pour contraindre le COB sur deux décades en longueur d'onde et mesurer l'amplitude du pic d'émission à 20% près, en incluant les incertitudes systématiques, qui ont été soigneusement étudiées.

En plus de permettre la mesure de l'EBL, le code que j'ai implémenté dans l'analyse de H.E.S.S. permet de déterminer les propriétés intrinsèques des AGN distants. J'ai ainsi obtenu les spectres intrinsèques de PKS 2155-304, PKS 2005-489 et Mrk 421, et j'ai montré que cette information, combinée aux spectres mesurés par *Fermi*-LAT, permet de localiser le pic de leur émission. J'ai aussi montré que 1ES 1101-232, 1ES 0229+200, 1ES 0347-121 et H 2356-309 sont quatre fantastiques accélérateurs, avec un spectre HE extrapolable au delà du TeV. Cela indique que la question de l'énergie maximale des rayons γ accessible au sein des blazars reste ouverte dans certains cas. J'ai enfin implémenté les outils nécessaires à l'ajustement du redshift d'une source pour un niveau d'absorption donné. J'ai mis en pratique ces outils et mesuré pour la première fois un redshift à VHE, avec une résolution de l'ordre de 30% pour les données de PKS 2155-304. Ce résultat est de bonne augure pour la cosmologie γ qui pourrait être développée avec la prochaine génération d'observatoires : CTA.

Au delà des caractéristiques spectrales, une des propriétés les plus frappantes et les moins comprises de l'émission des blazars est l'extrême variabilité dont il font parfois montre. L'événement le plus phénoménal jamais observé, du moins à VHE, est certainement l'éruption du blazar PKS 2155-304, avec des variations de flux intenables en régime permanent, à des échelles de temps aussi courtes que quelques minutes (quand l'objet central mesure plusieurs heures lumière). Ces échelles de temps indiquent que la variabilité de PKS 2155-304 trouve son origine dans le jet lui-même, où les effets relativistes semblent accélérer le déroulement des événements. J'ai sondé cette variabilité à diverses échelles de temps

dans l'espace de Fourier, en utilisant la densité spectrale de puissance (PSD). J'ai premièrement montré qu'on peut propager analytiquement les incertitudes instrumentales sur la courbe de lumière dans l'espace de Fourier et j'ai établi des formules simples permettant leurs calculs de manière rapide et sans avoir à recourir à des méthodes type Monte Carlo. J'ai implémenté le calcul de la PSD et de l'erreur associée dans les outils de H.E.S.S., avec d'autres menues fonctionnalités telles que le calcul de la variance en excès et de la limite supérieure sur cette quantité, ou l'échantillonnage à l'échelle de la période pour les courbes de lumière. Pour tenir compte des distortions de la PSD dues aux contraintes observationelles (échantillonage, fenêtrage), j'ai développé une analyse prenant en compte les biais instrumentaux dans l'espace de Fourier. J'ai ainsi mesuré l'indice de la loi de puissance de la PSD de PKS 2155-304 et j'ai confirmé les résultats récemment publiés.

La qualité sans précédent de la courbe de lumière de cet objet a permis la mesure par H.E.S.S. d'une large variété d'observables statistiques, telles qu'une distribution en flux fortement asymétrique et une corrélation entre flux et R.M.S. échantillonnés. Ces propriétés étaient généralement attribuées à des processus multiplicatifs, attendus dans les disques d'accrétion, alors que des modèles additifs sont plus communément utilisés dans les jets. J'ai réfuté l'idée que les modèles additifs ne peuvent pas reproduire de telles distributions de flux asymétriques ou encore de relations linéaires entre la R.M.S. et le flux, en exposant les propriétés des distributions de Pareto, qui sont peut-être plus connues des financiers ou des géophysiciens. J'ai établi un modèle physique qui génère de telles distributions, dans le cadre duquel des régions qui se meuvent à vitesse relativiste, les minijets, sont orientées de manière aléatoire dans un jet qui a lui même un mouvement relativiste dans le référentiel de l'observateur. À l'aide d'une généralisation du théorème central limite, on montre que la somme des émissions suit une loi α-stable, qui partage les propriétés du flux de PKS 2155-304 à VHE. J'ai ainsi interprété la courbe de lumière mesurée comme réalisation d'un processus stochastique, défini par l'orientation d'un grand nombre de minijets. En plus des propriétés statistiques, j'ai montré que le comportement en bruit rouge, la corrélation entre le flux et l'indice et l'accroissement de la variance fractionnelle avec l'énergie trouvent une explication naturelle dans ce modèle statistique

de minijets dans un jet.

Pour conclure, j'indique quelques uns des objectifs de l'astronomie γ extragalactique, à moyen et long terme. Les progrès techniques ayant mené à H.E.S.S. II et qui mèneront à la prochaine génération d'instruments CTA conduiront à une couverture en énergie accrue et à une sensibilité sans précédent. Je discute l'impact attendu sur la population d'AGN et sur la compréhension de leurs jets. Avec ces nouveaux instruments, la modélisation de la variabilité et la cosmologie γ connaitront certainement leur pleine maturité.

APPENDIX A

Reliability of the reconstruction at large offset

When targeting point-like sources, H.E.S.S. observations are usually performed in *wobble* mode, where the telescopes are oriented along a circle centred on the target. The usual value of $\sim 0.5^{\circ}$ for the radius of this circle is an optimum between a decrease of the radial acceptance for an increasing offset[1] and an increase of the number of regions used for background estimation[2].

I expose the results of the spectral analysis of the H.E.S.S. data on 1ES 1312-423 in Chapter 2.3.1.2 and the reader might be concerned about the impact of the observation conditions of this source on the reconstructed spectrum. 1ES 1312-423 is indeed in the same field of view as the actual target of the observations, Centaurus A. The distance between these two sources being on the order of 2°, the offset of 1ES 1312-423 with respect to the pointing direction has a similar value (average value of 1.91 ± 0.38, where the uncertainty is the R.M.S.), which corresponds to the edge of the H.E.S.S. cameras.

I study in the following the reliability of the chain analysis by selecting observations of the brightest source monitored with H.E.S.S., the Crab Nebula, recreating a situation similar to that of 1ES 1312-423.

A.1. Selection of the runs

I selected the runs on the Crab Nebula with the standard criteria in ParisAnalysis. Among the 123 runs available in January 2011, 13 correspond to observations where the angular distance between the pointing and the source is at least of 1.4°. I show in Fig. 1 the location

[1] The more inclined the telescope with respect to the source direction, the smaller the collection area.

[2] The larger the offset, the larger the distance between the camera centre and the ON source region.

of the source in the pointing frame for these runs. The color scale corresponds to the arrival directions of the γ-ray events and I normalized the maximum of this map to a value of one.

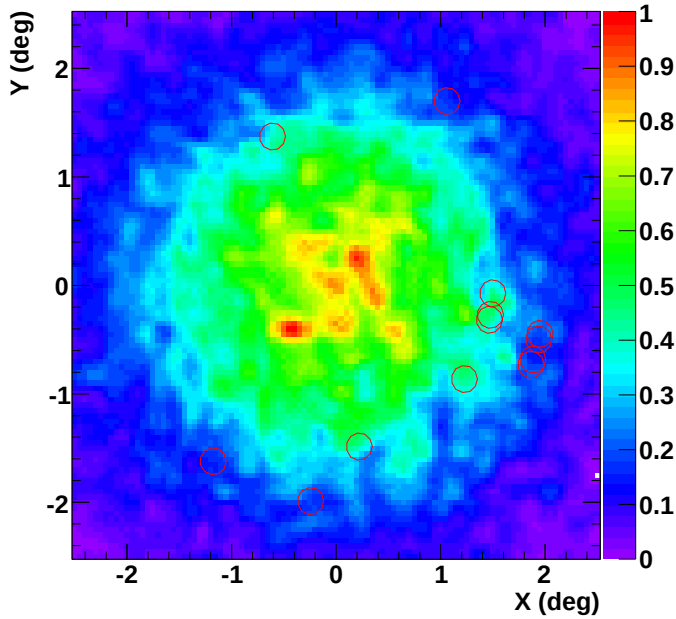

FIGURE 1. Location of the Crab Nebula in the pointing frame of the H.E.S.S. telescopes for the 13 runs at least 1.4° away from the origin.

To mimic the observation conditions of 1ES 1312-423, I selected the runs that cluster around a given direction in the camera frame. To be more precise, I used the 8 runs with X $>$ 1 deg and Y $<$ 0.5 deg, where the X-Y system is defined in Fig. 1. These runs have an average offset of $1.79 \pm 0.25^{\circ}$, comparable to that of 1ES 1312-423.

The acceptance map for these selected runs is compared the acceptance map of 1ES 1312-423 in Fig. 2. These maps are computed using the hadronic events, which are assumed to be uniformly distributed in the field of view, and I set the maximum to one.

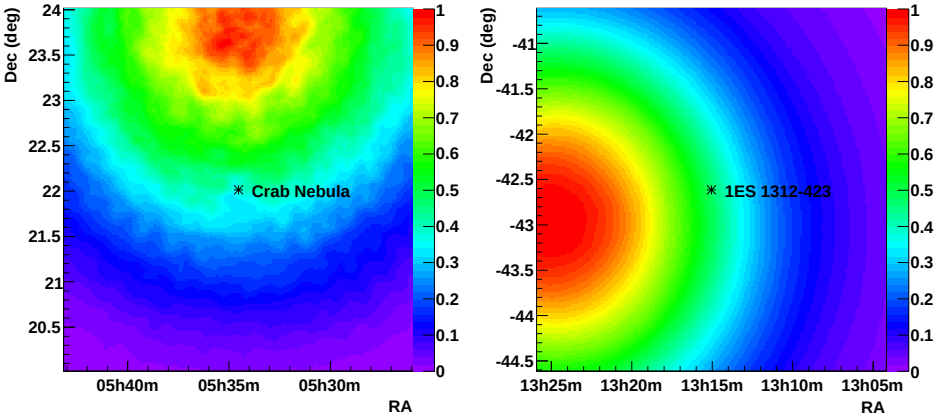

FIGURE 2. Normalised acceptance maps for the selected runs on the Crab Nebula (left) and for 1ES 1312-423 (right).

A.2. Reconstruction of the spectrum

I performed the spectral analysis of the 13 selected runs assuming a power-law spectrum, above the threshold energy of 430 GeV at 20% of the nominal acceptance. This model successfully represents the (relatively small amount of) data with a χ^2/dof of 42.9/34 ($\mathcal{P}_{\chi^2} = 14.2\%$). More complex models such as the log-parabola or the exponential cut-off power-law are not preferred at more than the 2σ level.

To allow for comparisons, I also fitted a power-law model on the full dataset (123 runs). Given the large amount of data and the known exponential cut off in the spectrum, this model obviously poorly represents the data ($\chi^2/dof = 290.3/74$). The energy range probed with this dataset is larger than the previous one, with an energy threshold at 20% of the nominal acceptance of 350 GeV due to the flatter average acceptance and with a maximum energy set to 40 TeV (when the maximum energy in the previous fit is at 24 TeV).

All these caveats mentioned, the spectra derived with the whole dataset and the selected runs are in good agreement, as shown in Fig. 3. Note that the slightly harder spectrum for the whole dataset certainly arise from the lower energy threshold. The astute reader will note a softer spectrum than published. This is certainly due, as mentioned

above, to the un-appropriate spectral model which poorly represents the data but allow for comparisons with the fit performed to the smaller dataset.

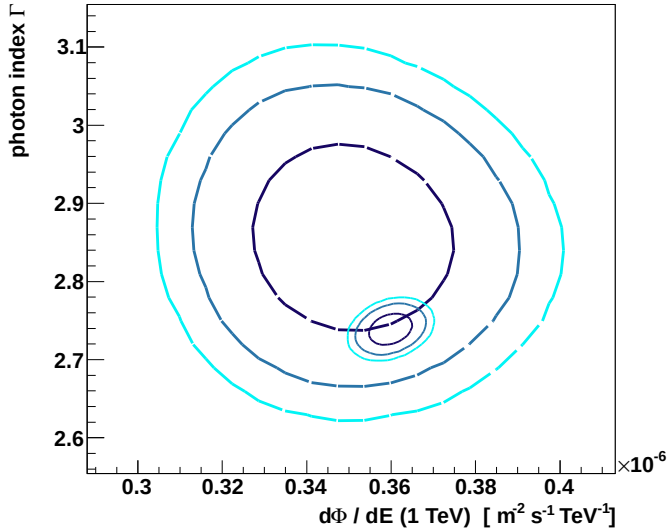

FIGURE 3. Confidence contours of the spectrum parameters of two Crab Nebula datasets at 1σ (light blue), 2σ (blue) and 3σ (dark blue) levels. The spectra are fitted with power laws, characterised by the differential flux at 1 TeV and the power law index Γ. The large dashed contours correspond to the selected runs and the solid line contours correspond to the whole Crab Nebula dataset passing standard quality cuts.

APPENDIX B

Appendix of the EBL study

B.1. Cross checks and systematic uncertainties

In this appendix, I study the systematic uncertainties on the EBL measurement performed with the H.E.S.S. data. Following the classification of Sinervo (2003), I identify two sources of systematics arising from "poorly understood features of the data or analysis technique" (class 2) and two sources of systematics arising "from uncertainties in the underlying theoretical paradigm" (class 3). I estimate the main class 2 systematic uncertainty with Monte Carlo simulated air showers passing through the whole chain analysis. The uncertainty on the energy scale due to the atmospheric conditions is accounted for with a toy model of the detector acceptance. Class 3 systematics are characterized in this study by the choice of EBL template model and the selection of the best intrinsic model for each data set. I compare the former with a concurrent modelling established by Domínguez et al. (2011) and I evaluate the impact of the latter with the data, testing *ad hoc* intrinsic models.

B.1.1. Analysis chain

I use Monte Carlo events triggering four telescopes (see, e.g., Aharonian et al. 2006, and reference therein for a description of the Monte-Carlo simulations), initially following a power law of photon index 2 (hardest simulated index). I create an artificial EBL attenuation by removing the events of the dataset with a probability corresponding to the EBL absorption at a redshift of $z = 0.1$. The data set studied is generated for a null azimuth and an off-axis angle of 0.5^{o}. The zenith angle of 18^{o} is close to the average zenith angle in the H.E.S.S. sky of PKS 2155-304, which is the source with the most important excess of γ rays in this study. The EBL optical depth normalization α is then reconstructed on sets of events following a spectrum

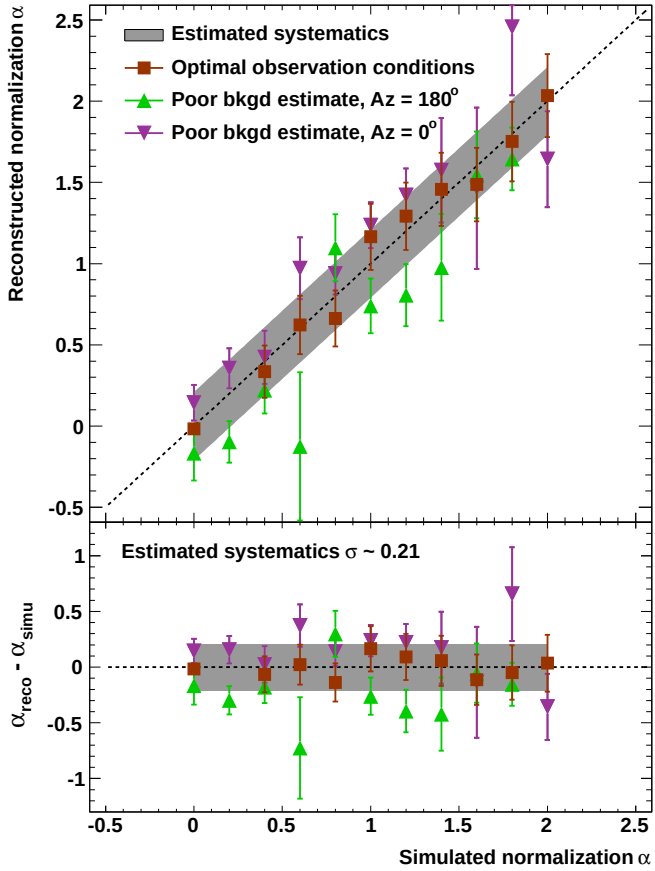

FIGURE 1. Reconstruction of the EBL normalization with Monte Carlo simulated air showers passing through the analysis chain. Three samples of Monte Carlo events are represented, the first one (orange squares) corresponds to the observation conditions of PKS 2155-304, the second and third (triangles) correspond to a poor background estimation. These two last sets are used to estimate the systematic uncertainty represented with the grey shaded area. *Top panel* : Reconstructed EBL normalization as a function of the simulated normalization. *Bottom panel* : Residuals, defined as the difference between the reconstructed and simulated optical depth normalizations.

$\phi(E) \propto E^{-2} \exp(-\alpha \times \tau(E,z))$, where $\tau(E,z)$ is the FR08 EBL opacity and z the redshift of the source.

The background is particularly important for the spectral fitting method described in Piron et al. (2001). I fixed it to a tenth of the signal - comparable to the value derived for the first data set on PKS 2155-304. The reconstructed EBL normalization α is represented in the top panel of Fig. 1 as a function of the simulated EBL normalization with orange squared symbols. The close match with the identity function, represented with the dashed line, strongly supports the reliability of the method employed.

The parameter that seems to affect the most the analysis chain is the background estimation, crucial for the above mentioned spectral fitting method. Imposing a background equivalent to a fiftieth of the signal[1], two samples of simulated events are studied for a null zenith and respective azimuths of 0^o and 180^o (the azimuth just indexes the data sets, since all azimuth angles are equivalent for a null zenith angle). The corresponding reconstructed EBL normalizations are represented with downward and upward triangles in the top panel of Fig. 1. The associated error bars represent statistical uncertainties, related to the limited size of the Monte Carlo samples (typically 10^4 events), that must be taken into account when estimating the systematic uncertainty. A first (a priori naive) evaluation of this systematic is the average difference $\alpha_{\rm reco} - \alpha_{\rm simu}$ represented in the bottom panel, which reads 0.17 and 0.20 for each sample. A second estimate can be the maximum variation in the measurement Δ associated with a Gaussian statistic, yielding a one standard deviation systematics $\Delta/\sqrt{12}$ (see, e.g., Sinervo 2003) of 0.19 and 0.21 respectively. The estimate that I choose is similar to the excess variance estimator developed by Vaughan et al. (2003) for variability. Assuming that the rms difference D between the simulated and reconstructed values is due to both statistical and systematic uncertainties, one would write $D^2 = \mathcal{V}(\alpha_{\rm reco} - \alpha_{\rm simu}) =< \sigma^2_{\rm stat} > +\sigma^2_{\rm sys}$, where $\mathcal{V}$ is the variance estimator. We thus define the systematic uncertainty estimate as :

$$\sigma_{\rm sys} = \sqrt{\mathcal{V}(\alpha_{\rm reco} - \alpha_{\rm simu}) - < \sigma^2_{\rm stat} >} \tag{B.1}$$

[1]For 10^4 signal events and 20 energy bins, this represents on average 10 background events per bin.

which reads 0.15 and 0.26 for each sample. The global systematic error using both samples, $\sigma_{\rm sys} = 0.21$, is represented by the gray shaded area in the top and bottom panels of Fig. 1. This systematics estimate is of the same order as the two mentioned before, though a bit larger, which suggests a possible slight overestimation.

To ensure that a point-to-point systematic effect does not mimic the EBL absorption as a function of energy, I perform the analysis on the whole Crab dataset (standard selection) with *Model++ Loose cuts*. Assuming that this source is located at a redshift of 0.1, the best fit EBL normalization is $\alpha = -0.07 \pm 0.01$ for an exponential cut off model with $\chi^2/dof = 155/96$, $\alpha = 0.19 \pm 0.05$ for a log-parabolic model but with a worse $\chi^2/dof = 192/96$. The slightly positive value for the log-parabola is not shocking since an exponential cut off is expected in the Crab spectrum. The slightly negative value for the exponential cut-off model reflects the systematics of H.E.S.S. above 50 TeV. The deviations from zero for the Crab Nebula are thus within the systematic uncertainty derived for the analysis chain.

B.1.2. Intrinsic model

The second systematic uncertainty arises from the choice of the model for the intrinsic spectra. This systematic is assessed with the data. I compare the total likelihood profile derived with a log parabola for each intrinsic spectrum on one hand and derived with an exponential cut-off power law on the other. This choice is purely arbitrary and reflects the maximal error that would be made if their was no objective criterion of selection of the intrinsic model. The corresponding likelihoods as a function of the EBL normalization are shown in Fig. 2, where the maximum is set to unity for clarity purposes. The two profiles are maximal for $\alpha_{\rm Expcut-off} = 1.36^{+0.09}_{-0.12}$ and $\alpha_{\rm LogParabola} = 1.12^{+0.15}_{-0.13}$. Using the last systematic estimator described in the Sect. B.1.1, the difference between these two values due to the statistics is estimated to 0.14 (variance due to uncertainties) and the deviation caused by the systematics is 0.10.

To ensure the reliability of the measurement, three other criteria of selection of the intrinsic model are tested. First, the model with the best χ^2 probability is selected (as in the main method) but the flattest likelihood profile is used in case of ambiguity (e.g. between a log-parabola and an exponential cut-off power law), yielding a normalization of 1.18 ± 0.18, preferred at the 8.9σ level to a null opacity. A

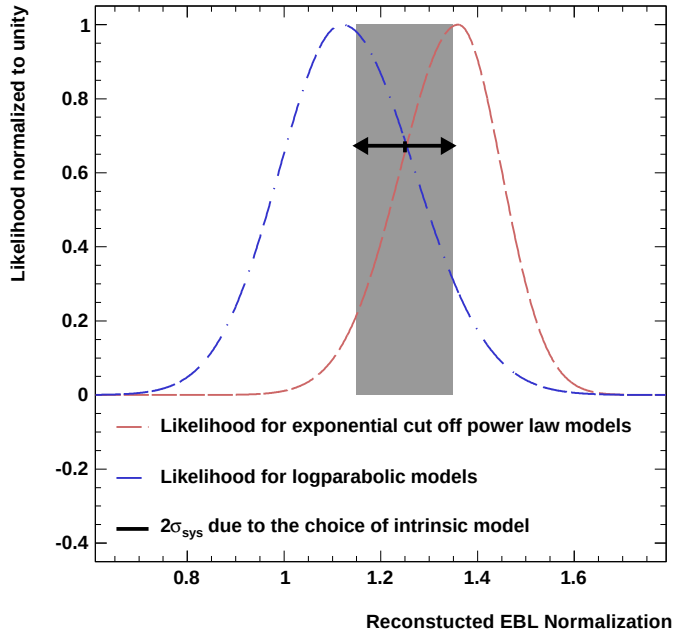

FIGURE 2. Likelihood profiles as a function of the normalized EBL opacity. The profiles are normalized to unity for clarity purposes. The dotted dashed curve is derived fitting log-parabolic intrinsic spectra to the data sets while the dashed curve is derived fitting exponential cut-off models. The gap between the two profiles due to the intrinsic spectral modelling is represented by the grey shaded area and the double arrow.

second approach consisted in choosing the simplest model as long as the next order is not preferred at the 2σ level (taking the flattest profile in case of ambiguity), yielding a normalization of 1.46 ± 0.11, preferred at the 14.3σ level to a null opacity. These two criteria do not change the intrinsic model for the data sets on 1ES 0229+200, 1ES 1101-232, Mrk 421 (*2*), PKS 2005-489(*1* and *2*) and PKS 2155-304 (*1*, *6* and *7*). A final test consisted in imposing the most complex model (an

exponential cut-off log parabola) to the other data sets, yielding a normalization of 1.29 ± 0.18, preferred at the 7.9σ level to a null opacity. The above-mentioned systematic uncertainty of 0.10 accounts for the slight changes induced by the selection method and the significance of the result remains almost unchanged.

It is worth noting that the particular attention paid to the intrinsic curvature of the spectra all along the analysis is not superfluous. The likelihood profile obtained assuming that the spectra are described by power laws is maximum for $\alpha_{\mathrm{PowerLaw}} = 2.01 \pm 0.07$. The value derived with such a basic spectral model is significantly above the nominal normalized EBL opacity because of the intrinsic curvature.

B.1.3. Energy scale and EBL model

The atmosphere is the least understood component of a Cherenkov experiment such as H.E.S.S.. It affects the absorption of the Cherenkov light emitted by the air showers. This absorption leads to a decrease of the number of Cherenkov photons arriving on the cameras and thus to a decrease of the reconstructed energy of the primary γ ray. The typical energy shift, on the order of 10% (Bernlohr 2000), does not affect the slope of a power-law spectrum, which is energy scale invariant, but impacts its normalisation. Indeed, for an initial spectrum $\phi(E) = \phi_0(E/E_0)^{-\Gamma}$, an energy shift δ yields a measured spectrum $\phi_{\mathrm{mes}}(E) = \phi_0[(1+\delta)E/E_0]^{-\Gamma} = \phi_0'(E/E_0)^{-\Gamma}$, where $\phi_0' = (1+\delta)^{-\Gamma}\phi_0$ is the measured spectral normalization. Since the spectral analysis developed in this study relies on the EBL absorption feature, which is a non energy scale invariant spectral model, I investigate the atmosphere absorption impact on the measured EBL normalization.

I develop a toy model of the detector and of the atmosphere effect to account for this effect. The detector acceptance $\mathcal{A}(E)$ is parametrized as a function that tends to the nominal acceptance value at high energies, as in Eq. (B.2) :

$$\log_{10}\mathcal{A}(E) = a \times [1 - b\exp(-c \times \log_{10} E)] \tag{B.2}$$

where $\mathcal{A}(E)$ is in m^2, the energy E is in TeV and $a = 5.19$, $b = 2.32 \times 10^{-2}$, $c = 3.14$, derived from the fit of the simulated acceptance. The number of events measured in an energy band $\mathrm{d}E$ is then simply $\mathrm{d}N/\mathrm{d}E = \mathcal{A}(E) \times \phi(E) \times T_{obs}$, where the observation duration T_{obs} is fixed to impose a total number of events of 10^6. Typical

event distributions for power law and EBL absorbed power law spectra are shown in the inset on Fig. 3. A logarithmic energy binning of $\Delta \log_{10} E = 0.1$ is adopted and the uncertainty on the number of events in each energy bin is considered to be Poissonian. To model the effect of the atmosphere on the EBL normalization reconstruction, I fit energy shifted distributions $\mathrm{d}N/\mathrm{d}E = \mathcal{A}(E) \times \phi(E_{\rm shift}) \times T_{obs}$ with a non-shifted model, i.e. $\propto \mathcal{A}(E) \times \phi(E)$, with $E_{\rm shift} = (1+\delta) \times E$ and $\phi(E) \propto E^{-\Gamma} \exp(-\alpha \times \tau(E,z))$. As mentioned above the effect on the index Γ is null because of the energy scale invariance. This is not the case for the specific energy dependence of the EBL opacity. A toy-model distribution which is energy shifted is shown in the top panel of Fig. 3 for a redshift $z = 0.1$ and an injected EBL normalization $\alpha = 1$, corresponding to FR08 EBL modelling. The residuals $\Delta \log_{10}(\mathrm{N_{events}})$ to the fit of a non shifted model are shown on the bottom panel.

The reconstructed and injected EBL normalizations differ by less than 0.05 for an energy shift of 10%, while the difference can go up to 0.11 for an energy shift of 25%. The standard atmospheric conditions required by the data selection motivates the use of the 10% energy shift[2] and thus of a systematic error due to Cherenkov light absorption of 0.05.

This toy model of the detector is also employed to compare independent EBL modelings. To probe a reasonable range of models, I use the lower and upper bounds on the EBL opacity derived by Domínguez et al. (2011) for the injected spectrum and I fit FR08 modelling to the event distribution. The variation in the reconstructed normalization is estimated to 0.06 for a redshift $z = 0.1$. I show in Fig. 4 that this systematic uncertainty can be propagated in the EBL SED space, given that the most constraining part of the spectrum is the region between $\sim$ 2 and $\sim$ 5 μm, responsible for the "wiggle" at VHE.

The small amplitude of the systematic effects of the atmosphere and of the EBL modelling choice (respectively 0.05 and 0.06) justify a posteriori the use of the simple framework described in this subsection and do not motivate a deeper investigation.

[2]Meyer et al. (2010) have even shown that a precision of 5% on the energy scale can be achieved with atmospheric Cherenkov telescopes.

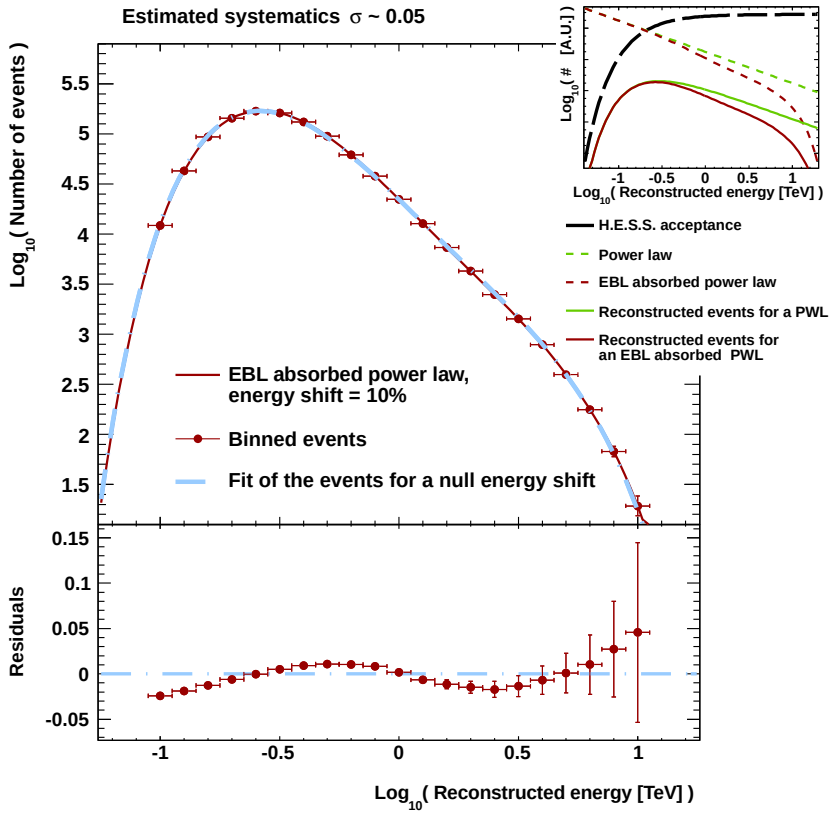

FIGURE 3. Toy model of the energy distribution of H.E.S.S. events. The inset in the top panel shows the detector acceptance (black line) and the expected distributions of events for a power law and an EBL absorbed power law (green and brown lines respectively). The injected spectra are shifted in energy to model the absorption of Cherenkov light by the atmosphere yielding the distribution of events shown in the top panel with brown filled circles. Fitting this distribution with a non shifted model enables the characterization of the atmospheric impact on the EBL normalization estimated to 0.05 for an energy shift of 10%. The residuals of the fit are shown in the bottom panel.

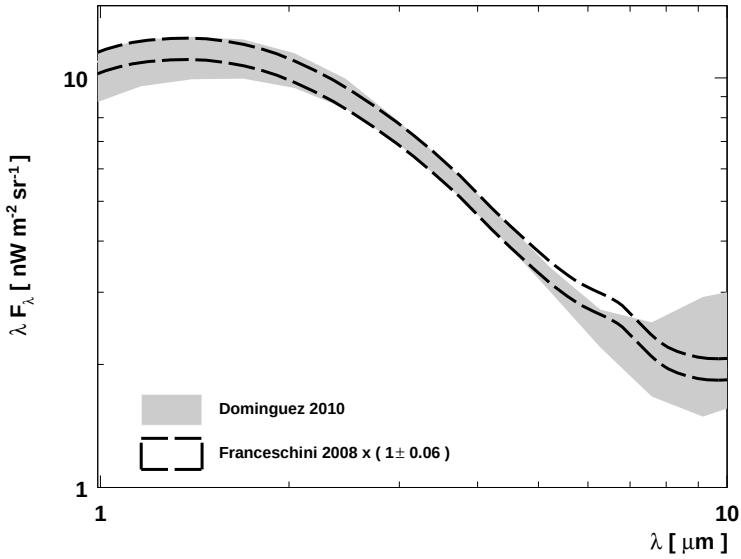

FIGURE 4. Comparison of the EBL modelings of FR08 and Domínguez et al. (2011) in the region of the SED responsible for the "wiggle" at VHE. The gray contour shows the 1σ confidence contour derived by Domínguez et al. (2011). The dashed lines represent the model of FR08 scaled by a factor 0.94 and 1.6, respectively.

B.1.4. Energy range covered

The last potential source of systematics investigated is the choice of the energy threshold applied in the analysis. This energy is the counterpart of the minimal acceptance above which events are kept, typically from 10 to 20% of the nominal acceptance value for a given set of observations. The impact of the threshold choice on the reconstructed EBL normalization for the dataset *1* on PKS 2155-304 is shown in Fig. 5. Except for an unreasonably low threshold at 1% of the nominal acceptance value, the reconstructed EBL normalization does not depend, within the uncertainties, on the threshold choice. The small threshold of 10% adopted in this study is motivated by an accurate reconstruction of the intrinsic spectrum.

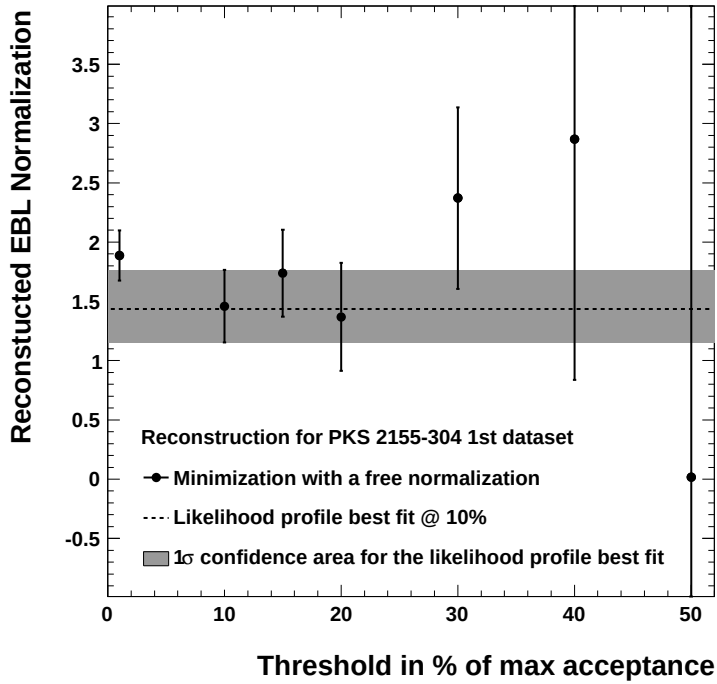

FIGURE 5. Reconstructed EBL normalization as a function of the analysis threshold, defined as a percentage of the nominal acceptance value. The blacks points correspond to the normalization derived for the first dataset on PKS 2155-304. The black line and gray shaded area correspond to the best fit EBL normalization and the uncertainty derived in this analysis with a threshold of 10%. Except for an unreasonably low threshold of 1%, the reconstructed EBL normalization does not depend of the threshold choice.

B.1.5. A glimpse at the wiggle

The signature of the EBL on H.E.S.S. spectra consists in a smoothly growing absorption with the energy but also of a characteristic "wiggle" around 1 TeV. The absence of this feature would certainly prevent a

detection of the EBL with TeV data since a smoothly decreasing spectrum could be modeled with a log-parabola or an exponential cut-off power law. Aiming at having a glimpse of this signature, the spectrum of H 2356-309 is fitted with log-log polynomials, as described in Eq. (B.3),

$$\phi(E) = \phi_0 E^{-\mathrm{a}-\mathrm{b}\ln\mathrm{E}-\mathrm{c}(\ln\mathrm{E})^2-\mathrm{d}(\ln\mathrm{E})^3} \tag{B.3}$$

where a and b are the usual spectral index and curvature, while c and d are the third and fourth order parameters. Fixing b = c = d = 0, one derives a power law; c = d = 0 denotes a log-parabola; the functions corresponding to d = 0 are of third order; the fourth order is characterized by a, b, c and d as free parameters. The four models are fitted to the data and the best fit functions are shown on Fig. 6. The 1σ confidence area (so called butterflies) are not shown for clarity purposes. We insist on the fact that the functions fitted on the data do not depend on an EBL model, these are just basic polynomials fitted to the data. I scale these polynomials by a factor $(E/E_0)^{\Gamma_{\mathrm{int}}}$, where E_0 is a reference energy and $\Gamma_{\mathrm{int}} = 1.8$ is the best fit intrinsic index, which enables a comparison with the EBL absorption.

For reference, the best fit EBL model is shown as a dashed line in Fig. 6, a vertical shift being applied for clarity purpose. There is a remarkable agreement between the fourth order model and the EBL absorption feature, which tends to support the idea that this wiggle is the engine driving the EBL detection. Obviously, this example is not a strong evidence of the EBL signature, statistically speaking the fourth order model is preferred at the 1.3σ level compared to the third order model or to the log-parabola.

A last remarkable point is the value of the equivalent χ^2 given in the table in Fig. 6. Indeed, the best fit of a fourth order model yields an equivalent χ^2 of 71.1 for 59 degrees of freedom. For comparison, the fit of a power law model absorbed with the EBL opacity scaled by α_0 yields a smaller equivalent χ^2 of 70.2 for 61 degrees of freedom. This shows that the parametrization adopted all along the analysis is a good one, first because it enables a comparison between different datasets and the characterization of the sources intrinsic spectra, but also because this EBL parametrization is the simplest one and does not rely on multiple parameters as polynomial fits do.

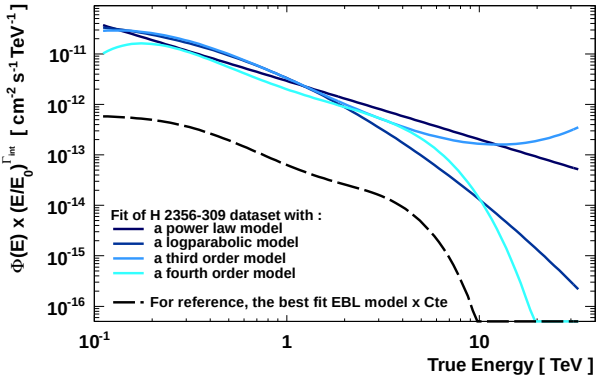

Model	χ^2 /dof	$\mathcal{P}(\chi^2)$
PWL	80.9 / 62	5.4%
LP	74.6 / 61	11.3%
Cubic	72.9 / 60	12.2%
Quartic	71.1 / 59	13.4%

FIGURE 6. On the left: Best fit models of H 2356-309 spectrum assuming a power law model, a log-parabola, a third order log-log polynomial and a fourth order model. In order to compare these results with the EBL absorption effect, the spectra are scaled by a factor $E^{\Gamma_{\rm int}}$, where $\Gamma_{\rm int} = 1.8$. For reference, the best fit EBL model derived with $\alpha_0 = 1.27$ is represented with a black dashed line, down shifted for clarity purpose. On the right : equivalent χ^2, number of degrees of freedom and χ^2 probability corresponding to each of the tested model.

B.2. Intrinsic spectral parameters

The intrinsic spectral parameters of the seven VHE sources used in the EBL study are given in Table 1.

Source	ϕ(1 TeV)	Γ	p	$c_{\phi\phi}$	$c_{\phi\Gamma}$	$c_{\phi p}$	$c_{\Gamma\Gamma}$	$c_{\Gamma p}$	c_{pp}
Mrk 421(*1*)	215.6	2.431	6.666	81.74	-0.2388	0.1949	0.02086	-0.006895	0.002504
Mrk 421(*2*)	345.2	2.263	7.127	124.8	0.2198	0.03411	0.01172	-0.00346	0.00113
Mrk 421(*3*)	438.9	2.113	7.871	179.4	0.3064	0.01255	0.008889	-0.002516	0.0007929
PKS 2005-489(*1*)	0.7681	3.807	0.6719	0.01835	-0.04836	-0.02227	0.1718	0.09411	0.05683
PKS 2005-489(*2*)	3.892	2.475	-	0.07837	-0.0165	-	0.005618	-	-
PKS 2155-304(*2008*)	10.77	2.566	5.176	3.143	-0.1513	0.3035	0.007551	-0.01412	0.03203
PKS 2155-304(*1*)	17.84	2.826	4.904	15.74	-0.442	0.9673	0.01281	-0.02632	0.06439
PKS 2155-304(*2*)	52.79	2.533	1.251	125	-1.162	2.738	0.0111	-0.02478	0.06382
PKS 2155-304(*3*)	119.9	2.530	1.143	289.9	-1.182	2.781	0.004948	-0.01102	0.02854
PKS 2155-304(*4*)	181.1	2.450	1.374	1349	-4.161	7.673	0.01322	-0.02306	0.04604
PKS 2155-304(*5*)	243.6	2.460	2.492	437.7	-0.9688	1.757	0.002244	-0.003749	0.007774
PKS 2155-304(*6*)	837.0	2.016	1.392	8456	-5.677	9.389	0.003992	-0.006117	0.01136
PKS 2155-304(*7*)	1345	2.011	1.655	2.475E04	-12.42	16.38	0.006522	-0.008062	0.01133
1ES 0229+200	3.104	1.623	-	0.09446	-0.02373	-	0.02433	-	-
H 2356-309	2.354	1.821	-	0.07559	-0.02339	-	0.008767	-	-
1ES 1101-232	5.408	1.426	-	0.351	-0.05107	-	0.01006	-	-
1ES 0347-121	2.176	1.898	-	0.2187	-0.07264	-	0.02744	-	-

TABLE 1. Intrinsic spectral parameters and covariance matrices for $\alpha = 1.27$. The first column indicates the dataset. The column 2, 3 and 4 show the spectral parameters, where the flux is given in units of 10^{-12} cm^{-2} s^{-1} TeV^{-1} and where p is either the cut-off energy in TeV, either the curvature parameter for the log-parabola describing PKS 2005-489(*1*) (in which case the reference energy is 1 TeV). The following columns give the parameters of the up-right corner of the covariance matrix (in the case of an exponential cut-off power law model, p refers to the inverse of the cut-off energy in the covariance matrix).

B.3. Lists of runs

This section is a book keeping of the run lists established for each data set used in the EBL study. The runs are selected with standard quality criteria and the run lists derived with ParisAnalysis are intersected with those derived with the German tool in hap.

B.3.0.1. *Mrk 421 (1)*

20259, 20260, 20294, 20295, 20296, 20314, 20315, 20316, 20317, 20338, 23668, 23695

B.3.0.2. *Mrk 421 (2)*

20234, 20235, 20276, 20277, 20293, 20335, 20336, 20337, 20382, 20384

B.3.0.3. *Mrk 421 (3)*

20357, 20358, 20359, 20360, 20381, 20383, 20385
56034, 56035, 56036, 56037, 56038, 56039, 56057, 56058, 56059, 56060, 56080, 56082, 56083, 56084

B.3.0.4. *Mrk 421 (2010)*

B.3.0.5. *PKS 2005-489 (1)*

21196, 21197, 21221, 21222, 21304, 21305, 21330, 21380, 21381, 21400, 21416, 21417, 21445, 21456, 21458, 21465, 21472, 21574, 21703, 21704, 22326, 22327, 22342, 22343, 22360, 22361, 22389, 22567, 22568, 22569, 22570, 22587, 22697, 22841, 22843, 22844, 22845, 22847, 22848, 22884, 22885, 22886, 22887, 22911, 22912, 22913, 22914, 23026, 27639, 27672, 27673, 27705, 27733, 27734, 27752, 27753, 27769, 27896, 27897, 27902, 27981, 28267, 28285, 28346, 28347, 28367, 28425, 28819, 28820, 28821, 28823, 28827, 28853, 28854, 28855, 28856, 28868, 28883, 28884, 28887, 28888, 28889, 28891, 28909, 28912, 28914, 28915, 28941, 28970, 28971, 28972, 28992, 28993, 29019, 29022, 33010, 33035, 33038, 33585, 33586, 33587, 33610, 33634, 33635, 33636, 34197, 34198, 34224, 34292, 34293, 34318, 34319, 34370, 34371, 34372, 34400, 34467, 34468, 34490, 34796, 34797, 34800, 34874, 34876, 34877, 34879, 34880, 34901, 34903, 34905, 34928, 34955, 39620, 39665, 39692, 39723, 39751, 39788, 39789, 39808, 39809, 39810, 40189, 40418, 40499, 40500, 40854, 40855, 40944, 41041, 41108, 45805, 45840, 45868, 45869, 45899, 47035, 47036, 47074, 47075, 48810, 48838, 48890, 51620, 51686, 52003, 52224, 52245

B.3.0.6. *PKS 2005-489 (2)*

21332, 21444, 22842, 22889, 22890, 22891, 22990, 23027, 27608, 27706, 27770, 27980, 28368, 28424, 28869, 28885, 28890, 28913, 28916, 28994, 29020, 29021, 33036, 33612, 34466, 51566, 51645, 51646, 51684, 51749, 51750, 52033, 52034, 52059, 52060, 52088, 52089, 52111, 52112, 52181, 52182, 52223, 52477

B.3.0.7. *PKS 2155-304 (2008)*

47741, 47742, 47743, 47744, 47747, 47748, 47751, 47752, 47805, 47806, 47807, 47808, 47809, 47810, 47811, 47829, 47830, 47831, 47835, 47836, 47837, 47855, 47856, 47857, 47858, 47859, 47861, 47862, 47863, 47865, 47888, 47889, 47890, 47891, 47892, 47912, 47913, 47914, 47915, 47916, 47917, 47946, 47947, 47948, 47949, 47950, 47973, 47974, 47975, 47976, 47977, 48029, 48030, 48053, 48054, 48055, 48056, 48057

B.3.0.8. *PKS 2155-304 (1)*

33694, 33695, 33696, 33767, 33768, 33769, 33770, 33771, 33901, 33927, 33928, 33929, 33990, 33991, 33993, 34004, 34005

B.3.0.9. *PKS 2155-304 (2)*

33667, 33668, 33671, 33772, 33894, 33895, 33896, 33897, 33898, 33899, 33900, 33930, 33931, 33992

B.3.0.10. *PKS 2155-304 (3)*

33773, 33774, 33801, 33812, 33813, 33814, 33815, 33816, 33817, 33841, 33853, 33854, 33855, 33856

B.3.0.11. *PKS 2155-304 (4)*

33775, 33799, 33800, 33810, 33811, 33819

B.3.0.12. *PKS 2155-304 (5)*

33793, 33795, 33796, 33797, 33809, 33820, 33821, 33822

B.3.0.13. *PKS 2155-304 (6)*

33787, 33791, 33792

B.3.0.14. *PKS 2155-304 (7)*

33788, 33789, 33790

B.3.0.15. *1ES 0229+200*

23241, 23242, 28351, 28352, 28375, 28376, 28377, 28432, 28435, 29000, 29001, 29002, 29027, 29028, 29029, 29092, 29093, 34202, 34228, 34230, 34233, 34266, 34267, 34268, 34269, 34270, 34298, 34299, 34300, 34301, 34325, 34378, 34379, 34380, 34381, 34382, 34408, 34410, 34411, 34474, 34478, 34497, 34811, 34812, 34884, 34885, 34886, 34887, 34910, 34912, 34913, 34934, 34935, 34936, 34963, 34964, 34987, 35011, 35845, 35846, 35847, 35859, 35860, 35861, 35881, 35882, 35883, 35884, 35885, 35895, 35896, 35934, 35950, 35951, 35967, 35984, 35985, 36004, 36005, 36026, 36027, 36082, 36083, 36102, 36126, 36264, 36315, 36316, 36317, 36328, 36329, 36341, 36342, 36358, 36412, 36459, 40922, 40955, 40956, 40985, 40986, 41022, 41023, 41171, 41172, 41173, 41195, 41196, 41197, 41249, 41250, 41274, 41275, 41277, 47329, 47330, 47386, 47423, 47424, 47463, 47466, 47525, 48345, 48361, 48362, 48363, 48395, 48396, 48397, 48398, 48422, 48423, 48424, 48446, 48447, 49261, 49262

B.3.0.16. *H 2356-309*

21223, 21224, 21250, 21277, 21279, 21280, 21333, 21354, 21382, 21383, 21414, 21415, 21431, 21446, 21466, 21478, 21727, 21754, 21755, 22344, 22345, 22363, 22377, 22392, 22571, 22572, 22574, 22588, 22589, 22590, 22892, 22894, 22895, 22896, 22916, 22917, 22918, 22994, 22996, 23028, 23029, 23054, 23055, 23056, 23073, 23075, 23122, 23226, 23237, 23261, 23262, 23274, 23275, 23500, 23501, 23503, 23521, 23522, 23538, 23539, 23541, 23542, 23543, 23553, 23569, 23570, 23571, 23633, 23634, 26189, 26191, 26212, 26213, 26244, 26245, 26248, 26249, 26265, 26269, 26296, 26298, 26299, 26300, 26302, 26346, 26348, 26349, 26350, 26352, 26423, 26424, 26425, 26428, 26497, 26498, 26499, 26501, 26502, 26503, 26703, 26704, 26705, 26977, 26978, 27027, 27064, 27089, 27090, 27091, 27115, 27132, 27133, 27163, 27165, 27166, 27187, 27188, 27205, 27206, 27208, 27260, 27261, 27294, 27295, 27297, 27298, 27330, 27332, 27342, 27343, 27360, 27641, 27674, 27676, 27677, 27708, 27709, 27710, 27735, 27737, 27738, 27772, 27773, 27774, 28348, 28349, 28370, 28371, 28372, 33570, 33571, 33592, 33593, 33618, 33640, 33644, 33672, 33673, 33675, 33699, 34297, 34471, 34493, 34494, 34929, 34930, 34931, 34933, 34956, 34957, 34959, 34960, 34983, 34984, 34986, 35005, 35006, 35008, 35009, 35010, 35051, 35052, 35053, 35099, 35101, 40305, 40336, 40394, 40395, 40424, 40452, 40475, 40476, 40508, 40529, 40550, 40558, 40559, 40560, 40638, 40639, 40640, 40649, 46384, 46410, 46411, 46412, 46440, 46441,

47136, 47137, 47183, 47231, 47261, 47262, 47293, 48812, 48823, 48853, 48870, 52503, 52534, 52535

B.3.0.17. *1ES 1101-232*

20333, 20379, 20380, 20432, 21037, 21038, 21060, 21061, 21067, 21068, 21069, 21070, 21071, 21072, 21073, 21077, 21078, 21079, 21080, 21081, 21082, 21097, 21098, 21099, 21100, 21101, 24425, 24427, 24428, 24429, 24430, 24431, 24432, 24433, 24434, 24435, 24436, 24439, 24440, 24441, 24442, 24444, 24446, 24447, 24448, 24449, 24450, 24451, 24459, 24460, 24461, 24462, 24465, 24466, 24467, 24468, 24469, 24470, 24477, 24478, 24479, 24480, 24481, 24483, 24484, 24485, 24486, 24495, 24496, 24497, 24498, 24500, 24501, 24503, 24504, 24505, 24521, 24543, 24544, 24545, 24546, 24547, 24558, 24559, 24560, 24561, 24577, 24578, 24579, 24580, 30047, 30889, 30891, 30892, 30920, 31350, 31351, 31352, 31353, 32317, 32318, 32343, 32368, 32369, 32370, 32371, 32372, 32373, 32399, 32400, 32401, 32402, 32427, 32428, 32429, 32430, 32451, 32452, 32453, 32454, 38044, 38045, 38096, 38097, 38098, 38127, 38128, 38129, 38169, 38214, 38215, 43965, 43966, 44005, 44006, 44043, 44044, 44045

B.3.0.18. *1ES 0347-121*

29685, 34383, 34475, 34476, 34477, 34498, 34499, 34500, 34515, 34516, 34517, 34610, 34611, 34622, 34917, 34965, 34966, 34967, 34968, 34991, 34992, 34993, 35014, 35015, 35016, 35060, 35061, 35062, 35063, 35231, 35232, 35233, 35234, 35252, 35253, 35254, 35259, 35435, 35436, 35551, 35552, 35897, 35899, 35935, 35936, 35937, 35938, 35939, 35986, 36007, 36029, 36103, 36318, 36330, 36343, 36359, 36393, 36413, 36414, 36460, 42136, 42160, 42161, 42192, 42223, 42224, 42225, 42250, 42251, 42285, 42674, 42675, 42694, 42695, 42746, 42747, 42811, 42841, 42865, 42866, 42886, 42887

Bibliography

Aharonian, F., Akhperjanian, A. G., Bazer-Bachi, A. R., et al. 2006, A&A, 457, 899

Bernlohr, K. 2000, Astroparticle Physics, 12, 255

Domínguez, A., Primack, J. R., Rosario, D. J., et al. 2011, MNRAS, 410, 2556

Meyer, M., Horns, D., & Zechlin, H.-S. 2010, A&A, 523, A2

Piron, F., Djannati-Atai, A., Punch, M., et al. 2001, A&A, 374, 895

Sinervo, P. 2003, in Statistical Problems in Particle Physics, Astrophysics, and Cosmology, ed. L. Lyons, R. Mount, & R. Reitmeyer, 122

Vaughan, S., Edelson, R., Warwick, R. S., & Uttley, P. 2003, MNRAS, 345, 1271

APPENDIX C

Instrumental uncertainty on the PSD

C.1. Estimating the PSD of one realization

Data associated to the flux of an astrophysical source are usually composed of N measurements $\hat{\Phi}(t_i) = \hat{\Phi}'_i$, at times t_i, over a duration T. A measurement uncertainty σ_i is associated to each $\hat{\Phi}'_i$.

The PSD of this time series measures the amount of variability at different temporal frequencies. To obtain this spectrum, one would first subtract the mean of the data μ from the signal, $\hat{\Phi}_i = \hat{\Phi}'_i - \mu$, and then compute the square modulus of its discrete Fourier transform:

$$\hat{P}(\nu) = A \times \left| \sum_{i=1}^{N} \hat{\Phi}_i \mathrm{e}^{2i\pi\nu t_i} \right|^2 \tag{C.1}$$

where A is a normalization factor, usually defined as $A = 2T/(\mu^2 N^2)$ (see e.g. Appendix A of Vaughan et al. 2003). The integral of $\hat{P}(\nu)$ is then the normalized variance V/μ^2, where V is the variance of the signal (theorem of Parseval-Plancherel).

Since $\hat{P}(\nu)$ is a function of $\{\hat{\Phi}_i\}_{i=1..N}$, which are themselves quantities with instrumental uncertainties, an uncertainty $\sigma_{\hat{P}(\nu)}$ is associated to the PSD. This uncertainty can be computed with simulations (as e.g. in Aharonian et al. 2007). For each point of the light curve, a random Gaussian number $\mathcal{N}(\hat{\Phi}_i, \sigma_i)$ is drawn, where $\mathcal{N}$ is the normal distribution, and the PSD of a "simulated" light curve can be computed. Repeating this operation n times and computing the standard deviation for each frequency leads to an estimation of the PSD uncertainty. This method requires a large number of PSD computation, with $n \sim$ few hundreds.

A direct propagation of uncertainties using Eq. (C.1) is biased as I show in the following, because of the non linear relation between $\hat{P}(\nu)$ and $\{\hat{\Phi}_i\}_{i=1..N}$. However, an unbiased analytical expression of $\sigma_{\hat{P}(\nu)}$ can be derived.

C.2. "Naive" propagation of the uncertainties

If F is a function of N uncorrelated measurements $\{\hat{\Phi}_i\}_{i=1..N}$, at times t_i, with associated uncertainties $\{\sigma_i\}_{i=1..N}$, then uncertainty σ_F on F is:

$$\sigma_F^2 = \sum_{i=1}^{N} \left(\frac{\partial F}{\partial \hat{\Phi}_i} \right)^2 \times \sigma_i^2 \tag{C.2}$$

Eq. (C.2) is rigorously valid if F is a linear function of $\{\hat{\Phi}_i\}_{i=1..N}$. Otherwise, this expression is an approximation based on a first order Taylor series expansion.

Applying Eq. (C.2) to the PSD:

$$\hat{P}(\nu) = A \left(\sum_i \hat{\Phi}_i \cos(2\pi\nu t_i) \right)^2 + A \left(\sum_i \hat{\Phi}_i \sin(2\pi\nu t_i) \right)^2 \tag{C.3}$$

The uncertainty $\sigma_{\hat{P}(\nu)}$ on the PSD would be:

$$\begin{aligned}
\sigma^2_{\hat{P}(\nu)\,\text{naive}} &= A^2 \times \sum_{i=1}^{N} 2\sigma_i^2 \left(\sum_j \hat{\Phi}_j \left(\cos(2\pi\nu t_i)\cos(2\pi\nu t_j) + \sin(2\pi\nu t_i)\sin(2\pi\nu t_j) \right) \right)^2 \\
&= 4A^2 \left(\sum_i \hat{\Phi}_i \cos(2\pi\nu t_i) \right)^2 \left(\sum_i \sigma_i^2 \cos^2(2\pi\nu t_i) \right) \\
&\quad + 4A^2 \left(\sum_i \hat{\Phi}_i \sin(2\pi\nu t_i) \right)^2 \left(\sum_i \sigma_i^2 \sin^2(2\pi\nu t_i) \right) \\
&\quad + 8A^2 \left(\sum_i \hat{\Phi}_i \cos(2\pi\nu t_i) \right) \left(\sum_i \hat{\Phi}_i \sin(2\pi\nu t_i) \right) \left(\sum_i \sigma_i^2 \cos(2\pi\nu t_i)\sin(2\pi\nu t_i) \right)
\end{aligned} \tag{C.4}$$

That is to say,

$$\begin{aligned}\sigma^{2\ \text{naive}}_{\hat{P}(\nu)} &= 2A\left(\sum_i \sigma_i^2\right)\hat{P}(\nu) \\ &+ 4A^2\left(\sum_i \hat{\Phi}_i \cos(2\pi\nu t_i)\right)\left(\sum_i \hat{\Phi}_i \sin(2\pi\nu t_i)\right)\left(\sum_i \sigma_i^2 \sin(4\pi\nu t_i)\right) \\ &+ 2A^2\left(\left(\sum_i \hat{\Phi}_i \cos(2\pi\nu t_i)\right)^2 - \left(\sum_i \hat{\Phi}_i \sin(2\pi\nu t_i)\right)^2\right)\left(\sum_i \sigma_i^2 \cos(4\pi\nu t_i)\right)\end{aligned} \tag{C.5}$$

I show in the following that this result is a good approximation when the uncertainty on the PSD is negligible with respect to the PSD value but is biased when it becomes dominant.

C.3. Using a Gaussian field

I develop in the following an elegant method to derive a proper estimation of the uncertainty on the PSD.

C.3.0.19. *Case of a single variable*

In the simple case of a single measurement $\hat{\Phi}_0$, with a Gaussian uncertainty σ_0, one can consider $\hat{\Phi}_0$ as the value taken by a random variable ρ normally distributed as $\mathcal{N}(\hat{\Phi}_0, \sigma_0)$. If $P(\rho)$ is the probability distribution of this variable, then :

$$P(\rho) \propto \mathrm{e}^{-\frac{(\rho-\hat{\Phi}_0)^2}{2\sigma_0^2}} \tag{C.6}$$

That is to say,

$$P(\rho) \propto \mathrm{e}^{-\frac{1}{2}(\rho-\hat{\Phi}_0)S^{-1}(\rho-\hat{\Phi}_0)} \tag{C.7}$$

where $S = \sigma_0^2$.

Let f be a function, linear or otherwise, of ρ, then the mean value and uncertainty of the quantity $f(\rho)$ are:

$$< f(\rho) >= \frac{\int d\rho P(\rho) f(\rho)}{\int d\rho P(\rho)} \tag{C.8}$$

$$\sigma_{f(\rho)} = \sqrt{< f(\rho)^2 > - < f(\rho) >^2} \tag{C.9}$$

C.3.0.20. *Case of N variables*

Generalizing to N uncorrelated measurements $\hat{\Phi}_i$, with Gaussian uncertainties σ_i, we consider N uncorrelated random variables ρ_i, distributed as $\mathcal{N}(\hat{\Phi}_i, \sigma_i)$. The associated probability distribution is:

$$P(\rho_1, ...\rho_N) \propto \mathrm{e}^{-\frac{1}{2}\ (\rho-\hat{\Phi})^t\ \mathbf{S}^{-1}(\rho-\hat{\Phi})} \tag{C.10}$$

where $(\rho - \hat{\Phi})^t\ \mathbf{S}^{-1}(\rho - \hat{\Phi}) = \sum_{ij}(\rho_i - \hat{\Phi}_i)S^{-1}_{ij}(\rho_j - \hat{\Phi}_j)$

and $S_{ij} = \delta_{ij}\sigma_i\sigma_j$ (δ_{ij} is the Kronecker symbol).

The mean value of a function F of $\{\rho_i\}$ is:

$$< F(\{\rho_i\}) >= \frac{\int d\rho_1..d\rho_N P(\rho_1..\rho_N)F(\rho_1..\rho_N)}{\int d\rho_1..d\rho_N P(\rho_1..\rho_N)} \tag{C.11}$$

This quantity can be expressed as a function of the moments of the Gaussian distribution, called the m–points correlation functions $< \prod_{i=1}^{m} \rho_i >$.

Wick's theorem gives a general expression of these moments. For example, the two and four points correlation functions are given in Eq. (C.12) and Eq. (C.13):

$$< \rho_i\rho_j >= S_{ij} + \hat{\Phi}_i\hat{\Phi}_j \tag{C.12}$$

$$\begin{aligned} < \rho_i\rho_j\rho_k\rho_l > = {} & \hat{\Phi}_i\hat{\Phi}_j\hat{\Phi}_k\hat{\Phi}_l + S_{ij}S_{kl} + S_{ik}S_{jl} + S_{il}S_{jk} \\ & + S_{ij}\hat{\Phi}_k\hat{\Phi}_l + S_{ik}\hat{\Phi}_j\hat{\Phi}_l + S_{il}\hat{\Phi}_j\hat{\Phi}_k \\ & + S_{jk}\hat{\Phi}_i\hat{\Phi}_l + S_{jl}\hat{\Phi}_i\hat{\Phi}_k + S_{kl}\hat{\Phi}_i\hat{\Phi}_j \end{aligned} \tag{C.13}$$

C.3.0.21. *Analytical estimate of the PSD uncertainties*

We consider a function F of $\{\rho_i\}$ defined as:

$$F(\{\rho_i\}) = A\left|\sum_i \rho_i \mathrm{e}^{2i\pi\nu t_i}\right|^2 \tag{C.14}$$

Then, using Eq. (C.12) and Eq. (C.1) :

$$\begin{aligned} < F(\{\rho_i\}) > &=< \left| A \sum_i \rho_i \mathrm{e}^{2i\pi\nu t_i} \right|^2 >= A \sum_{ij} < \rho_i \rho_j > \mathrm{e}^{2i\pi\nu(t_i - t_j)} \\ &= A \sum_{ij} \hat{\Phi}_i \hat{\Phi}_j \mathrm{e}^{2i\pi\nu(t_i - t_j)} + A \sum_i \sigma_i^2 \\ &= \hat{P}(\nu) + A \sum_i \sigma_i^2 \end{aligned} \tag{C.15}$$

The PSD and the mean of F differ only by a constant $A \sum_i \sigma_i^2$. Thus, $\hat{P}(\nu)$ and F have the same variance and the uncertainty $\sigma_{\hat{P}(\nu)}$ on the PSD can be expressed as the standard deviation of F:

$$\sigma_{\hat{P}(\nu)} = \sqrt{< F(\{\rho_i\})^2 > - < F(\{\rho_i\}) >^2} \tag{C.16}$$

Using Eq. (C.13), the left hand term can be developed as:

$$\begin{aligned} < F(\{\rho_i\})^2 > &= A^2 \sum_{ijkl} < \rho_i \rho_j \rho_k \rho_l > \mathrm{e}^{2i\pi\nu(t_i - t_j + t_k - t_l)} \\ &= A^2 \left| \sum_i \hat{\Phi}_i \mathrm{e}^{2i\pi\nu t_i} \right|^4 + A^2 \left| \sum_i \sigma_i^2 \mathrm{e}^{4i\pi\nu t_i} \right|^2 \\ &+ 2A^2 \left(\sum_i \sigma_i^2 \right)^2 + 4A^2 \left(\sum_i \sigma_i^2 \right) \left| \sum_i \hat{\Phi}_i \mathrm{e}^{2i\pi\nu t_i} \right|^2 \\ &+ 2A^2 \Re \left(\left(\sum_i \sigma_i^2 \mathrm{e}^{-4i\pi\nu t_i} \right) \left(\sum_i \hat{\Phi}_i \mathrm{e}^{2i\pi\nu t_i} \right)^2 \right) \end{aligned} \tag{C.17}$$

Using Eq. (C.15) to develop the right hand term and combining with Eq. (C.17) gives:

$$\begin{aligned} \sigma_P^2 &=< F(\{\rho_i\})^2 > - < F(\{\rho_i\}) >^2 \\ &= A^2 \left| \sum_i \sigma_i^2 \mathrm{e}^{4i\pi\nu t_i} \right|^2 + A^2 \left(\sum_i \sigma_i^2 \right)^2 + 2A \left(\sum_i \sigma_i^2 \right) \hat{P}(\nu) \\ &+ 2A^2 \Re \left(\left(\sum_i \sigma_i^2 \mathrm{e}^{-4i\pi\nu t_i} \right) \left(\sum_i \hat{\Phi}_i \mathrm{e}^{2i\pi\nu t_i} \right)^2 \right) \end{aligned} \tag{C.18}$$

The uncertainty on the PSD, $\sigma_{\hat{P}(\nu)}$ can be rewritten as:

$$\sigma^2_{\hat{P}(\nu)} = A^2 \left(\sum_i \sigma_i^2 \cos(4\pi\nu t_i) \right)^2 + A^2 \left(\sum_i \sigma_i^2 \sin(4\pi\nu t_i) \right)^2 + A^2 \left(\sum_i \sigma_i^2 \right)^2 + \sigma^{2\ \mathrm{naive}}_{\hat{P}(\nu)} \tag{C.19}$$

where $\sigma^{2\ \mathrm{naive}}_{\hat{P}(\nu)}$ is the uncertainty derived with a direct propagation of uncertainties.

C.4. Simulation check

The standard deviation in the PSD calculated from Eq. (C.5) and from simulations are compared in the left panel of Fig. 1 using the light curve of PKS 2155-304 during the dramatic outburst of the 26 July 2006. The top right part of the plot shows a tight correlation between the uncertainties. The validity of the Taylor expansion in this area is due to the small value of $\sigma_{\hat{P}(\nu)}/\hat{P}(\nu)$, which corresponds to the low frequency part of the PSD. When $\sigma_{\hat{P}(\nu)} \sim \hat{P}(\nu)$ (high frequency part of the PSD, bottom left in Fig. 1), this approximation is no longer valid and the propagated uncertainty is an underestimate of the simulated one.

The standard deviation in the PSD calculated from Eq. (C.19) and from simulations are compared in Fig. 1. For this light curve, the estimates are in close agreement.

The determination of the power spectrum, without error bars, requires the computation of two sums over the light curve points (see Eq. (C.3)). The determination of the uncertainties with the analytical method requires the computation of the three extra sums $\sum_i \sigma_i^2 \cos(4\pi\nu t_i)$, $\sum_i \sigma_i^2 \sin(4\pi\nu t_i)$ and $\sum_i \sigma_i^2$. Thus, the analytical determination of the uncertainties is equivalent to the computation of one and a half PSD. The simulation requires drawing N random numbers per light curve and computing n PSDs, where $n \sim$ few hundreds. The analytical method is therefore at least $\sim (n-2)$ times faster.

C.4.0.22. *Conclusion*

The measurement uncertainties on the flux are propagated to the Power Spectral Density. The main assumption is the Gaussianity of the uncertainties. The obtained formula allows a fast computation

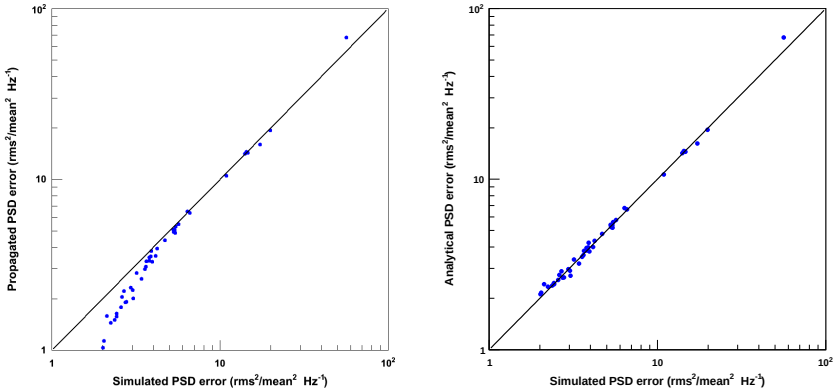

FIGURE 1. *Left :* Comparison between the PSD error bars obtained with a simple propagation of uncertainties and through simulations (n=500). The black line corresponds to the identity function y = x. *Right :* Comparison between the PSD error bars obtained with Eq. (C.19) and through simulations (n=500). The black line corresponds to the identity function.

of the PSD uncertainty and is consistent with that derived through simulation, as shown with the dramatic outburst of PKS 2155-304.

Bibliography

Aharonian, F., Akhperjanian, A. G., Bazer-Bachi, A. R., et al. 2007, ApJ, 664, L71

Vaughan, S., Edelson, R., Warwick, R. S., & Uttley, P. 2003, MNRAS, 345, 1271

Remerciements

Je me dois en premier lieu de remercier l'École doctorale de l'École polytechnique, ainsi que le laboratoire Leprince-Ringuet en la personne de son directeur Jean-Claude Brient et de ses directeurs adjoints présent, Pascal Paganini, et passé, Olivier Drapier, qui ont alimenté mon quotidien et mes virées scientifiques.

Mes remerciements vont ensuite aux membres de mon jury, les rapporteurs Frédéric Daigne et John Quinn pour leur lecture approfondie de ce manuscrit et leurs questions aiguisées, Régis Terrier et Christian Stegmann pour leur esprit critique et leur enthousiasme, ainsi que Martin Lemoine pour sa présidence magistrale.

Merci aux membres des collaborations H.E.S.S. et CTA avec qui j'ai pu échanger et qui se reconnaitront sûrement. Merci en particulier à ceux qui ont dirigé le groupe noyaux actifs de galaxie de H.E.S.S., Michael Punch, Martin Raue et Jean-Philippe Lenain. Ma reconnaissance va aussi à Werner Hofmann pour son accueil pendant ma visite au MPIK.

Toute ma gratitude va à mon directeur de thèse, Berrie Giebels, qui m'accompagne depuis un peu moins de trois ans. Cette thèse ne se serait pas si bien déroulée sans ses qualités scientifiques et humaines.

Je remercie chaleureusement les membres permanents ou temporaires du groupe d'astronomie gamma du LLR : Élodie Fillin-Martino pour sa joie de vivre, Shaobo Wang à qui je souhaite une très belle thèse, Yvonne Becherini pour nos nombreuses interactions, Hélène Laffon pour nos bavardages, François Brun pour nos pauses, productives et improductives, David Sanchez pour ses blagues salaces et notre collaboration sans faille, Philippe Bruel pour son humour qui ne manque pas

de cynisme, Pascal Fortin et Deirdre Horan pour avoir partagé leur bureau, leur quotidien et surtout leurs conseils avec moi, Steve Fegan pour nos nombreux et mouvementés échanges scientifiques, Bruno Khélifi et Mathieu de Naurois pour leur disponibilité, leurs connaissances et leur sympathie, Denis Bernard qui m'a particulièrement soutenu et motivé pendant cette dernière année, et enfin Gérard Fontaine et Bernard Degrange, dont les histoires scientifiques et personnelles, les connaissances encyclopédiques et l'insatiable curiosité ne cessent de me démontrer la beauté et les attraits de la recherche.

Merci à tous les membres du LLR, en particulier à Marc Louzir et Yannick Geerebaert à l'électronique, Eric Beyer, Emilia Becheva et Julien Tugler à l'informatique, Abdelhamid Khaled, Stephane Hormigos et Pascal Manigo à la mécanique, aux physiciens Alexandre Zabi, Frédéric Fleuret et Thomas Mueller, et aux thésards Nadir, David, JP, Ivo, Yacine et Benjamin.

Je souhaite vivement remercier Vincent Boudry, Julien Labaune et Rémi Lehe avec qui j'ai enseigné, ainsi que les élèves que j'ai encadré à l'École polytechnique et les futurs étudiants qui ne manqueront pas de lire ses remerciements pour y chercher une perle, comme je l'ai fait à leur époque.

Une petite pensée va à ceux qui m'ont aiguillé ou accompagné dans cette voie, mon professeur de spé Yannick Alméras, mes encadrants à l'ENS de Cachan, Emmanuelle Deleporte, Dominique Lagrost, François Treussart et tous les autres, mon éternel binôme et ami Morgan Delarue, et enfin mes responsables de stage auprès du LHC, Sophie Trincaz-Duvoid, puis Florian Beaudette, qui a aussi parrainé cette thèse.

Ces derniers mots vont à mes amis, à ma famille, à mes parents et beaux-parents, à mes (demi-)frères et sœurs, et à Solène.

Abstract

Fifty years after the discovery that quasars are extragalactic sources, their bright cores (AGN) and the jets that some of them exhibit still have plenty of secrets to share, particularly through observations in the γ-ray band. Above 100 GeV, Cherenkov telescopes such as H.E.S.S. have detected 50 AGN, mostly blazars, objects whose jets are pointed toward the observer. The detection of two faint ones, 1ES 1312-423 and SHBL J001355.9-185406, is described in this thesis. Their multi-wavelength spectra are reproduced with a synchrotron self-Compton model. The γ rays emitted by blazars are partly absorbed by the extragalactic background light (EBL), the second most intense cosmological background, which carries the integrated history of star formation. The first detection of this absorption above 100 GeV is performed, enabling the measurement of the EBL peak-amplitude in the optical band at the 20% level. In addition to these spectral studies, the fast flux-variations of blazars are investigated using the outbursts of PKS 2155-304 seen by H.E.S.S.. The observation of a skewed flux distribution and of an R.M.S.-flux correlation are interpreted within a kinematic model, where the emission is a realization of a stochastic process.

Résumé

Cinquante ans après la découverte de l'origine extragalactique des quasars, leurs noyaux (AGN) et les jets qu'ils montrent parfois nous réservent encore des surprises, en particulier dans le domaine des rayons γ. Au dessus de 100 GeV, les télescopes Cherenkov tels que H.E.S.S. ont détecté plus de 50 AGN, principalement des blazars, objets dont le jet pointe vers l'observateur. La détection de deux d'entre eux, 1ES 1312-423 et SHBL J001355.9-185406, est décrite dans cette thèse. Leurs spectres multi longueurs d'onde sont ajustés par un modèle synchrotron self-Compton. Les rayons γ émis par les blazars sont en partie absorbés par la lumière de fond extragalactique (EBL), deuxième composante cosmologique diffuse la plus intense, qui contient l'histoire intégrée de la formation d'étoiles. La première détection de cette absorption au dessus de 100 GeV est réalisée, conduisant à la mesure de l'amplitude du pic optique de l'EBL à 20% près. Finalement, les variations extrêmes du flux des blazars sont étudiées à l'aide des éruptions de PKS 2155-304 vues par H.E.S.S.. L'observation d'une distribution de flux hautement asymétrique et d'une corrélation R.M.S.-flux sont expliquées dans le cadre d'un modèle cinématique, où l'émission observée est une réalisation d'un processus stochastique.

Keywords High energy astrophysics, γ-ray astronomy: H.E.S.S., Active galactic nuclei: blazars, Cosmology: EBL, Variability: stochastic process

Mots clés Astrophysique des hautes énergies, Astronomie γ: H.E.S.S., Noyaux actifs de galaxie: blazars, Cosmologie: EBL, Variabilité: processus stochastique